The Electrochemistry of Hydrogen Sulfide in Room Temperature Ionic Liquids



Aoife O' Mahony

St John's College

University of Oxford

DPhil Thesis

Trinity Term 2010

Physical and Theoretical Chemistry

The Electrochemistry of Hydrogen Sulfide in Room Temperature Ionic Liquids

A Thesis Submitted for the Degree of DPhil in Physical and Theoretical Chemistry

by Aoife O' Mahony

St John's College, University of Oxford

Trinity Term 2010

The work presented in this thesis involves the use of room temperature ionic liquids (RTILs) as solvents in electrochemical experiments for the detection of hydrogen sulfide. The fundamentals of electrochemistry are presented, followed by an overview of RTILs in terms of their properties, applications and their behaviour as electrochemical solvents compared to conventional solvents. This is followed by an outline of electrochemical detection of various gases in aqueous, organic and ionic solvents. The results of 8 original studies are then presented as follows:

- The study of the electrochemical window of twelve different room temperature ionic liquids using cyclic voltammetry *vs.* an internal redox couple for two defined current densities, and observation of water uptake of different ionic liquids under different conditions using a Karl Fischer titrator.
- The reduction of hydrogen sulfide in various room temperature ionic liquids at a platinum electrode, measured using cyclic voltammetry. Also, solubilities and diffusion coefficients of hydrogen sulfide determined by potential step chronoamperometry.
- The oxidation of hydrogen sulfide in various room temperature ionic liquids at a platinum electrode measured using cyclic voltammetry and the simulation of the electrochemical signal using experimentally defined parameters.
- The disproportionation of N,N-dimethyl-p-phenylenediamine (DMPD) in room temperature

ionic liquids using cyclic voltammetry, and computational simulation of the voltammetry of DMPD using experimentally defined parameters to elucidate kinetic and thermodynamic data. DMPD was examined as a mediating species for hydrogen sulfide detection.

• The oxidation of catechol and dopamine in ionic liquids using cyclic voltammetry and observing adsorption effects when varying solvent anion. Catechol was examined as a mediating species for hydrogen sulfide detection.

• The electrochemical oxidation of NADH in ionic liquids using cyclic voltammetry and observing the "switching on or off" of the electrochemical signal when varying the solvent anion. NADH was examined as a mediating species for hydrogen sulfide detection.

• The mediated detection of hydrogen sulfide utilizing various mediating species in several ionic liquids using cyclic voltammetry, and the elucidation of the mediating mechanism of hydrogen sulfide in 3,5-tert-butyl-o-benzoquinone.

• The observation of the diffusion of ferrocene in an ionic liquid at ring-recessed disc microelectrode arrays in generator-collector mode using potential step chronoamperometry.

The results presented show that room temperature ionic liquids perform well as solvents in gas sensors, and could be viable alternatives to traditional organic solvents. Ionic liquids have also been observed to be tuneable in their reactions with analytes depending on the constituent cations and, in particular, anions. This tuneability is advantageous as specific combinations of cations and anions can be chosen to suit particular experiments.

Acknowledgements

First and foremost, I would like to thank my supervisor, Professor Richard G. Compton for the opportunity to work with him and for his guidance over the last three years. I have thoroughly enjoyed my time at Oxford and St. Johns, and that is in no small way due to Richard. He has been a great supervisor, and I have felt fully supported by him during projects, presentations and publications during my time here.

I would also like to thank my collaborators who have made the work in this thesis possible. Thank you Prof. Chris Hardacre and Dr. Leigh Aldous for providing the ionic liquid solvents. Thank you also to Denis, Edmund and Stephen, who simulated data and who I have had the pleasure of working and publishing with. Thank you to Honeywell for providing funding for the project.

There are several members of the group I would like to thank: Debbie for introducing me to the group and helping me through my first year in Oxford; Kass for being a wonderful friend over three years, living, working and getting into all kinds of scrapes with me, I definitely made a friend for life; Emma for online and personal shopping, being there when I needed a moan, and in particular, her latex wisdom; Fallyn for winning at tea, and the best effort at world Pimms drinking record I have ever attempted; Laura for being plagued by Part II students and great hugs; Juan, Denis, Chris, Edmund, Stephen, Ian and Martin (our ray of sunshine) for being great drinking buddies; and Neil for his neverending wisdom and ability to decipher. Also, all the Part II students and summer students who twisted my rubber arm to get up to no-good.

Finally I would like to thank my family: my mum and dad for loving and supporting me in all matters spanning my 27 years, I'm lucky to say they're proud of me no matter what I do; my

sister Ann who welcomed me to her home particularly the last 3 years, and didn't bat an eyelid when I cleared her wine stash; my brother Noel for always keeping an eye on me and picking me up from the airport on many an occasion; and my sister Chiara for being available for chats spanning hours when I needed to touch base. I'm so lucky to have you all.

Contents

Abstract ii

Acknowledgements iv

Table of Contents vi

Glossary xv

1 Introduction to Electrochemistry: Fundamentals and Methods. 1

1.1 Solid Electrode Electrochemistry at Metal Electrodes 1

1.1.1 Faradaic and Non-Faradaic Processes 2

1.1.2 The Nature of Electrode Reactions 3

1.1.2.1 Diffusion 6

1.1.2.2 Convection 8

1.1.2.3 Migration 9

1.1.3 Heterogeneous Electron Transfer 9

1.1.3.1 The Butler-Volmer Model 9

1.1.3.2 Electrochemical Reversibility 11

1.1.4 Homogeneous Processes 13

1.1.4.1 EC Mechanism 13

1.1.4.2 CE Mechanism 14

1.1.4.3 ECE Mechanism 14

1.2 The Electrochemical Cell 14

1.2.1 The Working Electrode 14

1.2.2 The Reference Electrode 15

1.2.3 The Counter Electrode 16

1.3 Introduction to Microelectrodes 16

1.3.1 Advantages of Microelectrodes 16
1.3.2 Diffusion Characteristics at Microelectrodes 18
1.4 Electrochemical Techniques 19
1.4.1 Cyclic Voltammetry 19
1.4.1.1 Voltammetry at Macroelectrodes 20
1.4.1.2 Voltammetry at Microelectrodes 22
1.4.2 Potential Step Chronoamperometry 23
References 26

2 Introduction to Room Temperature Ionic Liquids: Physical and Chemical Properties. 28

2.1 Introduction 28
2.2 Physical Properties of RTILs 30
2.2.1 Viscosity 32
2.2.2 Conductivity 34
2.2.3 Density 36
2.2.4 Thermal Stability and Negligible Volatility 36
2.3 Impurities and the Electrochemical Window of RTILs 39
2.4 Electrochemical Studies in RTILs 43
2.4.1 Mass Transport and Diffusion Coefficients 43
2.4.2 Electron Transfer Kinetics 46
2.4.3 Double Layer Capacitance 49
2.5 Applications of RTILs 50
2.5.1 Ionic Liquids in Academic Research 51
2.5.2 Ionic liquids in Industrial Applications 53

2.5.3 Gas Sensing in Ionic Liquids 54

References 54

3 Introduction to Gas Sensing. 59

3.1 A Brief History of Gas Sensing 59

3.2 Sensors for Detection of Oxygen and Carbon Dioxide 64

3.2.1 Detection of Oxygen and Carbon Dioxide in Room Temperature Ionic Liquids 67

3.3 Sensors for Detection of Ammonia 73

3.3.1 Electrochemical detection of ammonia in RTILs 75

3.4 Sensors for Detection of Hydrogen 79

3.4.1 Electrochemical detection of hydrogen in RTILs 80

3.5 Sensors for Detection of Sulfur Dioxide 83

3.5.1 Electrochemical detection of Sulfur Dioxide in RTILs 85

3.6 Sensors for detection of Hydrogen Sulfide 88

References 93

4 Experimental Methods. 97

4.1 Chemical Reagents and Ionic Liquids 97

4.2 Instrumentation 101

4.2.1 Electrodes and Potentiostat 101

4.2.2 Electrochemical Cell 101

4.2.3 Solutions and Gases 103

4.2.4 Karl Fischer Titrations 103

4.3 Sample Preparation 104

4.4 Microdisc Chronoamperometric Experiments 105

References 106

5 The Effect of Water as an Impurity on Room Temperature Ionic Liquids 108

5.1 Introduction 109

5.1.1 Water as an Impurity in RTILs 109

5.2 Results and Discussion 110

5.2.1 Karl Fischer Titrations 111

5.2.2 Cyclic Voltammetry of RTILs Exposed to Atmospheric Moisture at Different Temperatures 113

5.3 Conclusions 120

References 121

6 The Reduction of Hydrogen Sulfide in Room Temperature Ionic Liquids 122

6.1 Introduction 123

6.2 Results and Discussion 124

6.2.1 The Reduction of Hydrogen Sulfide in Various RTILs 124

6.2.1.1 Cyclic Voltammetry of H_2S in RTILs 124

6.2.1.2 Identity of Peaks (I), (II) and (III) 126

6.2.1.3 Potential Step Chronoamperometry 128

6.2.1.4 Reduction of H_2S in $[C_2mim][NTf_2]$: Additional Voltammetric Features 131

6.3 Conclusions 133

References 133

7 The Oxidation of Hydrogen Sulfide in Room Temperature Ionic Liquids **135**

7.1 Introduction . . . 136

7.2 Results and Discussion . . . 136

7.2.1 The Oxidation of Hydrogen Sulfide in Various RTILs . . . 136

7.2.1.1 Cyclic Voltammetry of H_2S in RTILs . . . 137

7.2.1.2 Simulation of Oxidation of H_2S in $[C_4mim][OTf]$ . . . 140

7.2.1.3 Comparison of Theory and Experiment for the Oxidation of H_2S 143

7.3 Conclusions . . . 150

References . . . 151

8 Kinetics and Thermodynamics of Redox Processes in Room Temperature Ionic Liquids: The Use of Voltammetry. The Disproportionation of Radical Cations of DMPD in $[C_4mim][BF_4]$. **153**

8.1 Introduction . . . 154

8.2 Theory . . . 156

8.2.1 Cyclic Voltammetry . . . 157

8.2.2 Computational Details . . . 158

8.3 Results and Discussion . . . 160

8.3.1 Chronoamperometry . . . 160

8.3.2 Cyclic Voltammetry . . . 161

8.4 Conclusions . . . 165

References . . . 165

9 The Electrochemical Oxidation of Catechol and Dopamine on Plat-

inum in $[C_2mim][NTf_2]$ and $[C_4mim][BF_4]$: Adsorption Effects in Ionic Liquid Voltammetry **168**

9.1 Introduction . . . 170

9.2 Results and Discussion . . . 171

9.2.1 Cyclic Voltammetry of Catechol in RTILs . . . 171

9.2.1.1 Catechol in $[C_2mim][NTf_2]$ . . . 171

9.2.1.2 Catechol in $[C_4mim][BF_4]$ . . . 175

9.2.2 Cyclic Voltammetry of Dopamine in RTILs . . . 179

9.2.2.1 Dopamine in $[C_2mim][NTf_2]$ . . . 179

9.2.2.2 Dopamine in $[C_4mim][BF_4]$ . . . 181

9.3 Conclusions . . . 184

References . . . 184

10 Selecting Room Temperature Ionic Liquids to Optimize Voltammetric Responses. The Oxidation of NADH in $[C_2mim][NTf_2]$ and $[C_4mim][PF_6]$ **187**

10.1 Introduction . . . 188

10.2 Experimental: Electrode Modification with PVF . . . 189

10.3 Results and Discussion . . . 190

10.3.1 The Oxidation of NADH in RTILs at Platinum Electrodes . . . 190

10.3.1.1 NADH in $[C_2mim][NTf_2]$ . . . 191

10.3.1.2 NADH in $[C_4mim][PF_6]$ . . . 192

10.3.2 Electrochemistry of NADH at PVF-modified Electrodes . . . 195

10.3.2.1 Modification of Platinum Electrode with PVF . . . 195

10.3.2.2 The Attempted Oxidation of NADH in $[C_2mim][NTf_2]$ and $[C_4mim][PF_6]$ at PVF-modified Electrodes . . . 196

10.4 Conclusions 199

References 200

11 The Mediated Detection of Hydrogen Sulfide in Room Temperature Ionic Liquids 202

11.1 Introduction 203

11.2 Experimental: Dissolving Mediators in RTILs 205

11.3 Results and Discussion 205

11.3.1 Attempted Detection of H_2S in RTILs Using Several Mediating Species . 206

11.3.2 The Successful Detection of H_2S in $[C_2mim][NTf_2]$ using 3,5-tert-butyl-o-benzoquinone as a Mediator 209

11.3.2.1 Reduction of H_2S in $[C_2mim][NTf_2]$ Using 3,5-tert-butyl-o-benzoquinone as a Mediator over Short Times 211

11.3.2.2 Oxidative and Reductive Features of H_2S in $[C_2mim][NTf_2]$ and 3,5-tert-butyl-o-benzoquinone Mediator over Long Times 214

11.3.2.3 The Mediated Detection of Low Concentrations of H_2S in RTILs 218

11.4 Conclusions 219

References 221

12 Micro arrays of ring-recessed disc electrodes in transient generator-collector mode: theory and experiment 223

12.1 Introduction 224

12.2 Theoretical model 226

12.2.1 The model of electrode surface 226

12.2.2 Mathematical model 227

12.3 Experimental and computational details 231
12.3.1 Instrumentation 231
12.3.2 Microdisc and Micro Array Chronoamperometric Experiments 231
12.3.3 Array fabrication procedure 232
12.3.4 Computational procedure 234
12.4 Results and Discussion 236
12.4.1 Isolated Ring-Recessed disc Electrodes: Theory 236
12.4.2 Effect of the Array Density 240
12.4.3 Array Characterisation 242
12.4.4 Experimental Validation 243
12.5 Conclusions 248
References 248

Glossary

Table 1: List of symbols commonly used throughout this thesis.

Symbol	Definition
Φ_m	electrostatic potential of the electrode
$\frac{d\phi}{dx}$	external electrical field
α	transfer coefficient defined in reductive direction
β	transfer coefficient defined in oxidative direction
δ_{dl}	diffusion layer thickness
ν	scan rate
τ	dimensionless time parameter
η	viscosity
κ	conductivity
ρ	density
Γ	surface coverage
Γ_{max}	maximum surface coverage
Θ	proportional coverage
σ	dimensionless scan rate
θ	dimensionless potential
A	area
c	concentration
$C_{x,t}$	concentration of electroactive species at distance x at time t
$C_{x,0}$	concentration of electroactive species at distance x at time = 0
$C_{0,t}$	concentration of electroactive species at electrode surface at time t
$C_{\mathrm{O}}*$	bulk concentration of O
C_{dl}	double layer capacitance
C	homogeneous chemical step
D	diffusion coefficient
D_{O}	diffusion coefficient of O
D_s	self diffusion coefficient
D_∞	hypothetical diffusion coefficient
e^-	electron
E	heterogeneous electron transfer step
E	potential
E_1	begin potential
E_2	end potential where voltammogram is reversed
$E_{1/2}$	half wave potential
E_0	standard electrode potential
$E_{\mathrm{a,D}}$	diffusional activation energy
E_{app}	applied potential
$E_{\mathrm{f}}{}^{\ominus}$	formal electrode potential
$(E - E_{\mathrm{f}}{}^{\ominus})$	
$E_{p,ox}$	oxidative peak potential
$E_{p,red}$	reductive peak potential
E_η	activation energy for viscous flow
$E_{a,D}$	activation energy of diffusion

Table 2: List of symbols commonly used throughout this thesis contd....

Symbol	Definition
ΔE_{pp}	peak-to-peak separation
F	Faraday constant (96485 C mol^{-1})
i	current
i_b	current for the backward process
i_c	charging or capacitative current
i_d	diffusion limited current in a chronoamperometric experiment
i_f	current for the forward process
i_p	peak current at a macroelectrode
i_{ss}	steady state limiting current
J	flux
J_d	diffusional flux
J_m	migratory flux
k_b	backward rate constant
k_B	Boltzmann constant (1.38×10^{-23} J K^{-1})
k_f	forward rate constant
k^0	standard heterogeneous rate constant
K_{eqm}	equilibrium constant
M	molar mass
n	number of electrons or a real integer > 0
n_{rd}	number of electrons transferred in the rate determining step
O	general solution species prone to undergoing a one-electron reduction
$[O]_0$	concentration of species O at the electrode surface
R	general solution species prone to undergoing a one-electron oxidation
R	universal gas constant (8.314 J mol^{-1} K^{-1})
$[R]_0$	concentration of species R at the electrode surface
r_d	radius of disk electrode
t	time
Δt	time interval
T	absolute temperature
T_0	ideal gas temperature
T_g	glass transition temperature
u	ionic mobility
x	direction
Δx	length interval
z	charge

Table 3: List of units commonly used throughout this thesis.

Unit	Definition
A	amp
atm.	atmospheric pressure
C	coulomb
cP	centipoise
cm	centimetre
eV	electron volt
J	joule
K	Kelvin
kV	kilo volt
M	molar mass
m	metre
mm	millimetre
mM	millimolar
mS	millisiemens
μm	micrometre
nA	nanoamp
nm	nanometre
ppb	parts per billion
ppm	parts per million
s	seconds
V	volt

Table 4: List of abbreviations commonly used throughout this thesis.

Abbreviation	Definition
A^-	solvent anion
BQ/H_2Q	benzoquinone/hydroquinone
CSV	cathodic stripping voltammetry
CV	cyclic voltammetry
ESR	electron spin resonance
EW	electrochemical window
3-D	three dimensional
DCM	dichloromethane
DEPD	*N*,*N*-diethylphenylene-1,4-diamine
DPPD	*n*,*N*-diphenyl-*p*-phenylenediamine
DNA	deoxyribonucleic acid
DMF	*N*,*N*-dimethylformamide
DMSO	dimethyl sulfoxide
ESR	electron spin resonance
Fc/Fc^+	ferrocene/ferricenium
GC	glassy carbon, gas chromatography
HA	proton solvated by solvent anion
HRP	horseradish peroxidase
IL	ionic liquid
IUPAC	International Union of Pure and Applied Chemistry
KF	Karl Fisher
LC	liquid chromatography
LSV	linear sweep voltammetry
MeCN	acetonitrile
MO	molecular orbital
MWCNTs	multi walled carbon nanotubes
NADH	nicotinamide adenine dinucleotide
NMR	nuclear magnetic resonance
OHP	outer Helmholtz plane
PANI	polyaniline
PTFE	polytetrafluoroethylene
PVC	polyvinylchloride
PVF	polyvinylferrocene
PZC	potential of zero charge
QUILL	Queen's University Ionic Liquids Laboratory

Table 5: List of abbreviations commonly used throughout this thesis contd....

Symbol	Definition
rds	rate determining step
RE	reference electrode
RTIL	room temperature ionic liquid
SHE	standard hydrogen electrode
SPE	screen printed electrodes
SWCNTs	single walled carbon nanotubes
TBAP	tetra-*n*-butylammonium perchlorate
TGA	thermogravimetric analysis
TMPD	N, N, N', N'-tetramethylphenylenediamine
THF	tetrahydrofuran
TSILs	task specific ionic liquids
UV	ultra violet
VTF	Vogel-Tammann-Fulcher
XPS	X-ray photoelectron spectroscopy
WE	working electrode

Chapter 1

Introduction to Electrochemistry: Fundamentals and Methods.

Electrochemistry is the area of chemistry concerning the chemical changes caused by the passage of an electric current or the production of electrical energy by chemical reaction. Such use of electrical measurement for analytical purposes has found a vast range of applications including environmental monitoring, industrial quality control and biomedical analysis. The two principal types of electroanalytical measurements are potentiometric and amperometric. Both types require at least two electrodes (conductors) and a contacting sample (electrolyte) solution, which constitute the electrochemical cell.[1] Electrochemical cells can be classified as electrolytic (when they consume electricity from an external source) or galvanic (if they are used to produce electrical energy). This work involves controlled-potential (potentiodynamic) techniques which deals with the study of charge-transfer process at the electrode-solution interface, and are based on dynamic (non-zero current) situations. Here, the electrode potential is being used to drive an electron-transfer reaction and the resulting current is measured. The advantages of controlled-potential techniques include high sensitivity, selectivity towards electroactive species, a wide linear range, portable and low-cost instrumentation, and a wide range of electrodes that allow a variety of unusual environments.

This Chapter will briefly outline some fundamental electrochemical principles, particularly those pertinent to the work presented in this thesis. For a more detailed account of the principles of electrochemistry, many competent textbooks are available.[1–8]

1.1 Solid Electrode Electrochemistry at Metal Electrodes

Solid electrode electrochemistry involves electron transfer between a metal or semiconductor and a chemical species in solution. The electrode/solution system can be divided into four

components: (1) The electrode; (2) the double layer: a layer of charged molecules having opposite charge to that of the electrode and specifically adsorbed onto the electrode surface; (3) the diffusion layer: a region of the solution dominated by an unequal charge distribution where the movements of the molecules are driven by diffusion; (4) the bulk solution: the rest of the solution where electro-neutrality exists.[6]

The attracted ions are assumed to approach the electrode surface and form a layer balancing the electrode charge. The overall result is two layers of charge (the double layer) and a potential drop which is confined to only this region (termed the outer Helmholtz Plane, OHP) of the solution.[9,10] The result is absolutely analogous to an electrical capacitor which has two plates of charge separated by some distance (d).

1.1.1 Faradaic and Non-Faradaic Processes

Two types of processes occur at electrodes. One type involves reactions in which charges are transferred across the metal-solution interface. Electron transfer causes oxidation or reduction to occur at a potential region that makes the electron transfer thermodynamically or kinetically favourable. Since such reactions are governed by Faraday's law, they are called Faradaic processes. Another process exists however, whereby no charge transfer occurs across the metal-solution interface even with changing potential. Since charge is not crossing the interface with a changing potential, the behaviour of the electrode-solution interface is analogous to that of a capacitor. At a given potential, there will exist a charge on the metal electrode, and an opposite charge in the solution. The charge on the metal represents an excess or deficiency of electrons and resides in a very thin layer on the metal surface. The charge in the solution is made up of an excess of either cations or anions in the vicinity of the electrode surface. This interface is called the electrical double-layer.

This double layer presents difficulties when using voltammetry for detection of very small

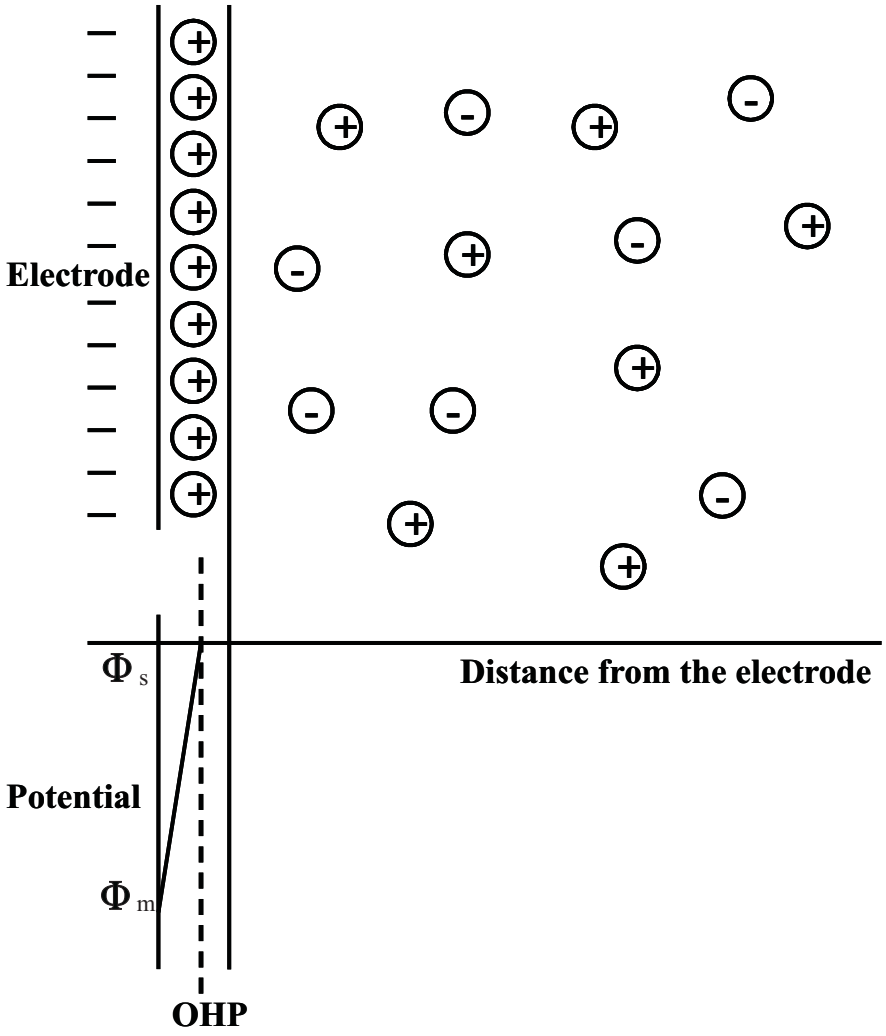


Figure 1.1: The double layer of an electrolyte solution at the electrode surface.

concentrations of analyte since this charging current interferes with the Faradaic current, which measures the analyte only. However, experimental conditions can be designed so that non-faradaic contributions can be minimised.

1.1.2 The Nature of Electrode Reactions

An electrode reaction is a heterogeneous chemical process involving the transfer of electrons to or from a surface, generally a metal or a semiconductor. The electrode reactions may be an anodic process whereby a species is oxidized by the loss of electrons to the electrode. By convention, the current density, I, for an anodic process is a positive quantity. Conversely, the

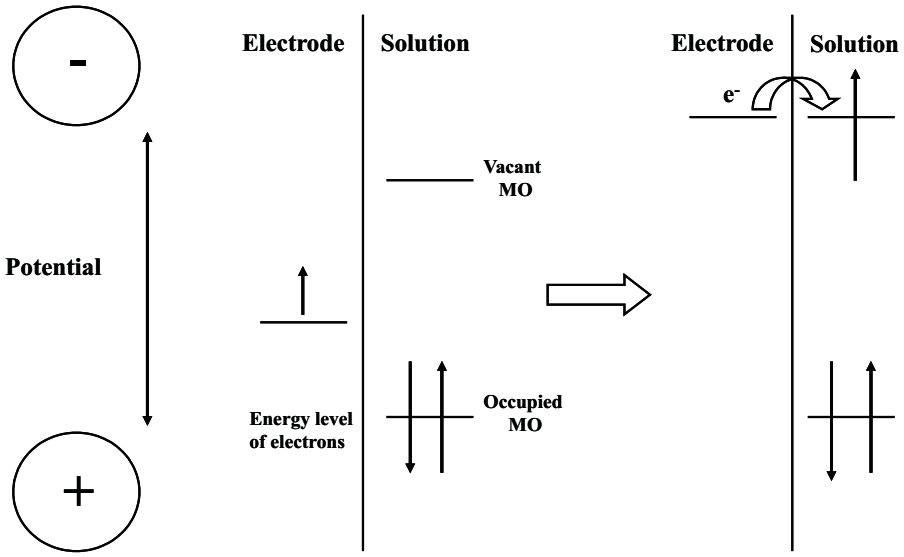


Figure 1.2: Potential effects on electrons.

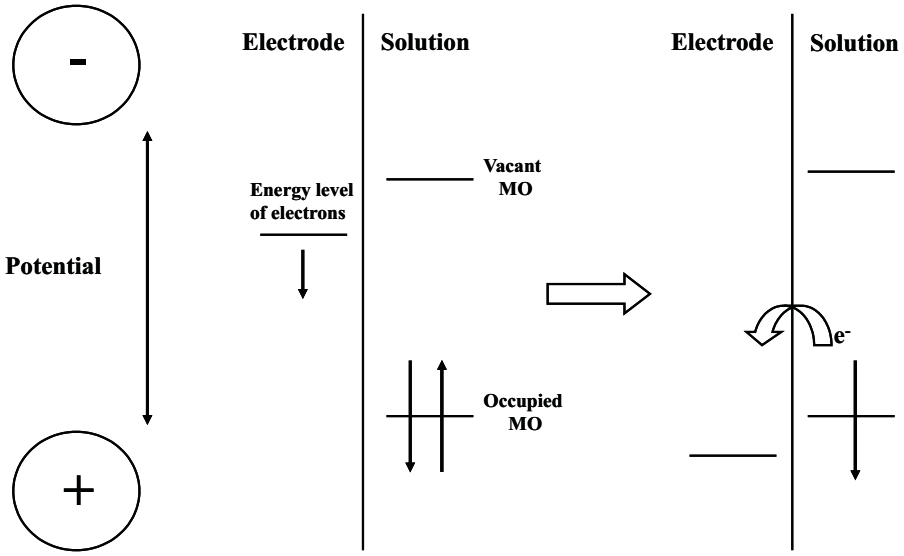


Figure 1.3: Oxidation of a species with electron transfer to electrode.

charge transfer may be a cathodic reaction in which a species is reduced by the gain of electrons and the current density is a negative quantity. An overall chemical reaction taking place in a cell is made up of two independent half-reactions, which describe the real chemical changes at the two electrodes. Each half-reaction responds to the potential difference at the corresponding electrode. For example, in an electrochemical cell with zinc metal (Zn) and a silver (Ag) wire covered with silver chloride (AgCl) immersed in a zinc chloride ($ZnCl_2$) solution, one half reaction

is the oxidation of Zn to Zn^{2+}, and the other half reaction taking place in the cell is the reduction of AgCl to Cl^- into solution and the formation of Ag metal.[7] This is represented in notation as follows:

$$Zn/Zn^{2+}, Cl^-/AgCl/Ag \tag{1.1}$$

where the slash represents a phase boundary, and a comma separates two components in the same phase.

Most of the time we are only interested in one of these reactions and the electrode at which it occurs is called the working electrode. To focus on it, we standardize the other half of the cell by using an electrode called the reference electrode, made up of phases having essential constant composition. Since the reference electrode has a constant make-up, its potential is fixed. Therefore, any changes to the cell are observable to the working electrode, so that we observe or control the potential of the working electrode with respect to the reference. By driving the electrode to more negative potentials the energy of the electrons is raised. They can reach a level high enough to transfer into vacant electronic states on species in the electrolyte. In that case, a flow of electrons from electrode to solution (a reduction current) occurs shown in Figure 1.2. Similarly, the energy of the electrons can be lowered by imposing a more positive potential, and at some point electrons on solutes in the electrolyte will find a more favourable energy on the electrode and will transfer there. Their flow from solution to electrode is an oxidation current, shown in Figure 1.3.

The critical potentials at which these processes occur are related to the standard potentials, $E^{\ominus}$, for the specific chemical substances in the system. Net rate of reaction and thus measured current may be limited by mass transport of the reactant or by the rate of electron transfer. Mass transport can be defined as the movement of material in an electrochemical cell. The mass transport in a solution can be due to three different mechanisms:

Diffusion: the transport of molecules in the body of the solution due to a concentration gradient,

Convection: mass transport due to mechanical forces such as stirring or temperature gradient. Convection was not a factor of mass transport as there was no stirring of the electrolyte solution, and temperature was kept constant,

Migration: the transport of charged species due to the presence of a potential gradient in the solution. Migration was not a factor of mass transport in this work as there was a large excess of supporting electrolyte in the system.

1.1.2.1 Diffusion

Diffusion arises from uneven concentration distributions and maximizes entropy by smoothing out inhomogeneities.[3] In this thesis, room temperature ionic liquids are used as solvents, and since they are composed entirely of ions, the mass transport and, consequently, the current depends only on diffusion. In this case the current (i) is directly proportional to the flux (J).

$$i = -nFAJ \tag{1.2}$$

where n is the number of electrons exchanged in the process, F is the Faraday constant (96485 C mol^{-1}), A is the area of the electrode (cm^2) and J is the flux (mol s^{-1} m^{-2}).

Considering the case of a planar electrode perfectly flat and of infinite dimensions the variation of concentration occurs only perpendicularly to the electrode surface. In this particular case the diffusion can be stated by Ficks first law.

$$J_{(x,t)} = -\frac{DdC_{(x,t)}}{dx} \tag{1.3}$$

where D is the mutual diffusion coefficient (m^2 s^{-1}) and $C_{(x,t)}$ is the concentration of the analyte

(mol L^{-1})

Combine Equations 1.2 and 1.3 to give an expression for the current response:

$$i = nFAD\frac{dC_{(x,t)}}{dx} \tag{1.4}$$

Hence, current is proportional to the concentration gradient of the electroactive species. Diffusional flux is concentration dependent shown in Equation 1.5:

$$\frac{dC_{(x,t)}}{dt} = D\frac{d^2C_{(x,t)}}{dx^2} \tag{1.5}$$

This equation shows the rate of change of concentration with time between points x and $(x+dx)$. To see the implications of these equations, imagine a voltammetric experiment involving the reduction of O to R at a planar electrode, where only O is initially present. The region within which O will convert to R during the experiment is the diffusion layer and is at the electrode surface. At the beginning of the experiment: $t = 0$, and the concentration is uniform throughout the solution so, $C_{\mathrm{O}(x,o)} = C_{\mathrm{O}(b)}$ at the electrode surface where $C_{\mathrm{O}(b)}$ is the concentration of the bulk solution. As time increases and potential changes to convert O to R, t $>$ 0 and at the electrode surface, $C_{\mathrm{O}(0,t)} = 0$. As the distance from the electrode surface increases, $x \rightarrow \infty$,[1] the concentration $\mathrm{C_{O(}}_{x,o)} \rightarrow \mathrm{C_O(b)}$, as less and less of O is being converted to R. These conditions result in a time-dependent concentration profile:

$$C_{\mathrm{O}(x,t)} = C_{\mathrm{O}}(b)(1 - \mathrm{erf}[\frac{x}{(4D_{\mathrm{O}}t)^{\frac{1}{2}}}]) \tag{1.6}$$

where erf is the Gauss error function described as:

$$\mathrm{erf}(x) = \frac{2}{\sqrt{\pi}}\int_0^x e^{-t^2}dt \tag{1.7}$$

whose derivative at $x = 0$ is:

$$\frac{dC}{dx}_{x=0} = \frac{C_{\mathrm{O}}(b)}{(\pi D_{\mathrm{O}} t)^{1/2}} \tag{1.8}$$

Substitute Equation 1.8 into Equation 1.4 to get the Cottrell equation:[11]

$$i(t) = -\frac{(nFD_{\mathrm{O}}\frac{1}{2}C_{\mathrm{O}}*)}{(\pi^{\frac{1}{2}}t^{\frac{1}{2}})} \tag{1.9}$$

where $i(t)$ is the Current at time t, n is the number of electrons involved in the process for each reagent molecule, $C_{\mathrm{O}}*$ is the bulk concentration of O (mol L^{-1}) and D_{O} = diffusion coefficient of O (m^2 s^{-1})

Equation 1.9 is the Cottrell equation which relates current to concentration with respect to time. This proportionality provides the possibility of using electrochemical processes as tools for the quantitative investigation of electro-active species in solution. This equation can be manipulated for different electrode geometries.

1.1.2.2 Convection

Convection is molecular movement caused when a mechanical force acts on solution.[3] There are two types of convection, natural and forced. Natural convection in solution can arise from thermal gradients or density differences in the solution. Thermal gradients arise as a result of the exo- or endo-thermicity of the process. Density differences occur as a result of the electrode reaction creating concentrations of products near the electrode surface of different density to those of reactants in bulk. Forced convection utilizes external forces such as gas bubbling, pumping or stirring. This can be deliberately introduced to suppress contributions of natural convection to give reproducible results over long timescales. Forced convection can be performed so as to produce well-defined hydrodynamic behaviour to allow quantitative and predictive flow

in a system, where concentration changes can be given by the velocity (v) of the solution:

$$\frac{d[B]}{dt} = -v_x \frac{d[B]}{dx} \tag{1.10}$$

1.1.2.3 Migration

Migration involves inducing movement of ions to or from the electrode with exertion of electrostatic force of charged species in the interfacial region caused by the existence of an external electrical field at the electrode/solution interface.[3] The migrational flux (j_m) is proportional to the concentration of target analyte ([A]) in the electric field:

$$j_m \propto -u[A]\frac{d\phi}{dx} \tag{1.11}$$

where u is the ionic mobility and $\frac{d\phi}{dx}$ is the external electrical field.

The effects of migration can be eliminated by using excess supporting electrolyte, a high concentration of charge carriers.

1.1.3 Heterogeneous Electron Transfer

We now examine the process of electron transfer between the analyte and the electrode surface. The potential of an electrode strongly affects the reactions occurring on its surface, so we now consider the relationship between the electrode potential and the faradaic currents produced from an electron transfer reaction in terms of electron transfer kinetics.

1.1.3.1 The Butler-Volmer Model

The Butler-Volmer model is a predictive model based purely on classical concepts, and while it has significant limitations, it is the most widely accepted and used treatment to rationalise heterogeneous electron transfer.[7] It was proposed independently by Butler[12] and Volmer,[13] the

electrochemists who contributed to its formation and experimental tests respectively, and is assumed for the work reported in this thesis.

To explain this model, we consider the simplest possible electrode process, wherein species O and R engage in a one-electron transfer at the interface, where species O is reduced to species R:

$$\mathrm{O} + e^- \underset{k_b}{\overset{k_f}{\rightleftharpoons}} \mathrm{R} \tag{1.12}$$

where k_f is the forward rate constant and k_b is the backward rate constant for the heterogeneous electron transfer. Current flow is proportional to the rate constant and the concentrations of O and R at the electrode surface. At a given potential, the overall current can be expressed as the sum of the currents for oxidation and reduction.

$$i = i_{\,b} + i_f = FAk_b[\mathrm{R}]_0 - FAk_f[\mathrm{O}]_0 \tag{1.13}$$

where $[\mathrm{R}]_0$ and $[\mathrm{O}]_0$ are the concentrations of species R and O at the electrode surface. The two rate constants, k_f and k_b can be expressed as follows:

$$k_f = k^0 exp\left(-\frac{\alpha F(E - E_f^{\ominus})}{RT}\right) \tag{1.14}$$

$$k_b = k^0 exp\left(\frac{(1-\alpha)F(E - E_f^{\ominus})}{RT}\right) \tag{1.15}$$

where k^0 is the standard electrochemical rate constant, (E - $E_f^{\ominus}$) is the overpotential (the difference between the equilibrium potential and the formal potential) and α is the transfer coefficient. The value of α ($0 < \alpha < 1$) reflects the sensitivity of the transition state between O and R. If α is close to 0, the transition state resembles O, and if α is close to 1, the transition

state resembles R. In general, α is close to $\frac{1}{2}$, suggesting an intermediate transition state between O and R.[3]

When we substitute Equation 1.14 and 1.15 into Equation 1.13 it produces the Butler-Volmer equation which describes the current dependence on the overpotential for a process which is controlled entirely by the electrode transfer kinetics:

$$i = FAk^0 \left([\mathrm{R}]_0 exp\left(\frac{(1-\alpha)F(E-E_f^{\ominus})}{RT} \right) - [\mathrm{O}]_0 exp\left(-\frac{\alpha F(E-E_f^{\ominus})}{RT} \right) \right) \tag{1.16}$$

This equation is very important as it predicts how observed current varies as a function of potential and transfer coefficient, and is widely used in the treatment of problems requiring an account of heterogeneous kinetics.

1.1.3.2 Electrochemical Reversibility

Reversibility gives an indication of the rate of electron transfer kinetics of a redox couple which is defined by the standard electrochemical rate constant, k^0. An electrochemically reversible system is one where k^0 is sufficiently fast that equilibrium is achieved on the timescale of the measurement and maintained as the potential is varied. In this case the Butler-Volmer equation can be simplified to the Nernst equation:[7]

$$E = E_f^{\ominus} + \frac{RT}{F} ln \frac{[\mathrm{R}]_0}{[\mathrm{O}]_0} \tag{1.17}$$

This equation relates the variation of electrolyte composition with electrode potential under equilibrium conditions.

However, if k^0 is slow, an electrochemically irreversible system occurs so that equilibrium cannot be achieved over the timescales of the measurement at potentials close to $E_f^{\ominus}$, and a

significant overpotential must be applied to induce a reaction. Systems displaying intermediate electrode kinetics are termed $quasi-reversible$. Marcus theory can predict k^0, and explains the difference in transfer kinetics for different systems.[14] Where a small change in the analyte geometry is required for transfer, k^0 is large and thus the system is reversible, whereas a large change in the analyte geometry for transfer to occur, k^0 is small and the system is electrochemically irreversible.[2] If the species O is reduced to species R, a large change in geometry (such as bond lengths and angles) may occur. The greater this change, the less energetically favourable the reaction, and the more electrochemically irreversible the system. For example, the reduction of $Fe(H_2O)_6{}^{3+}$ to $Fe(H_2O)_6{}^{2+}$ is quite sluggish, because while both species are structurally similar (octahedral), the bond lengths vary significantly increasing the energy barrier and decreasing k^0.[2] Conversely, if the species O is reduced to species R, and little change in geometry occurs, the reaction is more energetically favourable, and the system is more electrochemically reversible. For example, the reduction of $MnO_4{}^-$ to $MnO_4{}^{2-}$ proceeds relatively quickly since both species have the same structure (tetrahedral), equal bond angles, with only a slight decrease in bond length, therefore the energy barrier is easily overcome which increases k^0.[2] The contribution of the solvent of a system should also be considered in Marcus theory. The rearrangement of the solvent dipole between reactant and transition state geometry can affect the facility with which the reaction occurs.[2]

For irreversible reactions, one of the terms of the Butler-Volmer equation (1.16) can be neglected under extreme potentials. For these reactions, in the voltammogram, there is a region between the limiting current plateau and the equilibrium potential where current depends exponentially on potential, accordingly, for Equation 1.12 above, for the reduction of O to R:

$$ln|I_{red}| = -\frac{\alpha FE}{RT} + constant \tag{1.18}$$

where α can be calculated from a plot of $E\ vs.\ ln|I_{red}|$.[2]

1.1.4 Homogeneous Processes

In Section 1.1.3 we considered heterogeneous electron transfer reactions, but these can sometimes be accompanied by homogeneous reactions in solution, either preceding or following heterogeneous electron transfer. Testa and Reinmuth presented notation which dictates that the letter 'E' denoted a heterogeneous electron transfer, and the letter 'C' denotes a homogeneous chemical step.[15] The following are examples of the Testa-Reinmuth notation for a range of important mechanisms.

1.1.4.1 EC Mechanism

In the case of an EC mechanism, a chemical reaction follows the electron transfer step and forms a product which can then react further in a homogeneous reaction.

E: A - e^- $\rightleftharpoons$ A^+

C: A^+ + X^- $\rightleftharpoons$ AX

It can be anticipated that in the case of an EC reaction, the reaction is reversible at fast scan rates, however at slower scan rates, the reduction peak can lost due to the chemical reaction of electrochemically generated species A^+ (either with the solvent, the parent species or other species present in solution). A knowledge of the oxidative and reductive peak currents as a function of scan rate can therefore help determine the chemical reaction rate.

EC reactions are very common and well documented in literature. One such example is the oxidation of catechol in the room temperature ionic liquid $[C_4mim][BF_4]$[16] whereby after the oxidation of catechol to a doubly-protonated benzoquinone species, the anion of the ionic liquid abstracts the protons to form HBF_4. The mechanism is outlined in Chapter 9.

1.1.4.2 CE Mechanism

In the case of the CE mechanism, the electroactive species is generated by a chemical reaction which precedes the heterogeneous electrochemical reaction as follows:

C: $A \rightleftharpoons B$

E: $B + e^- \rightleftharpoons C$

1.1.4.3 ECE Mechanism

In the case of the ECE mechanism, initially an electrochemical oxidation or reduction occurs, this forms a chemically reactive species which can undergo a homogeneous chemical reaction to form a new electroactive species. This newly formed species is also electroactive and is thus capable of undergoing a further electron transfer as follows:

E: $A - e^- \rightleftharpoons A^+$

C: $A^+ + X^- \rightarrow AX$

E: $AX - e^- \rightleftharpoons AX^+$

1.2 The Electrochemical Cell

The type of electroanalytical measurement relevant to this work is potentiodynamic. It requires at least two electrodes (conductors) and a contacting sample (electrolyte) solution, which constitute the electrochemical cell. In this thesis a two-electrode cell was used with working and quasi-reference electrode.

1.2.1 The Working Electrode

The working electrode is the electrode that responds to the target analyte(s) and is termed the indicator.[6] A wide variety of working electrodes are now available. The most common working electrode materials utilize carbon. Originally the carbon paste electrode was developed but this

was soon replaced by more convenient and stable carbon-based working electrodes including those made from glassy carbon, pyrolytic carbon and porous graphite. Metals such as platinum, gold, silver, nickel, mercury, gold-amalgam and a variety of alloys are now also commonly used as working electrode materials.[7] The use of mercury-based electrodes presented a number of problems within and without the laboratory due to the toxicity of mercury. This has resulted in the banning of mercury use as an electrode material. Other disadvantages with mercury electrodes involve their instability when introduced to a flow system.

1.2.2 The Reference Electrode

The reference is the electrode that provides a stable and reproducible potential against which the potential of the working electrode is controlled and it should have the following properties: (1) It should be reversible and follow the Nernst equation; (2) Its potential should be stable over time; (3) Its potential should be independent from the temperature as much as possible. The most familiar reference electrode to electrochemists is the standard hydrogen electrode (SHE). Other reference electrode types are also in use. The silver/silver chloride reference electrode is preferred nowadays to the SHE for practical reasons. A similar reference electrode to the wet silver/silver chloride electrode is the mercury/mercurous chloride or calomel electrode.[8]

In this thesis, a quasi-reference electrode is used in a two-electrode set-up, generally a platinum wire or silver wire. The main advantage of using this type of electrode is that the solvent volume can be minimized to microlitre quantities, however disadvantages include the lack of stability of this system whereby a shift in potential at which redox active species appear at can occur over the course of an experiment. This however can be overcome by the use of an internal stable redox couple, whereby the peak potential of the electrochemically active analyte can be reported *vs.* this redox couple. In the case of this thesis, the IUPAC recommended ferrocene/ferricenium (Fc/Fc^+) redox couple is mostly used where peak potentials have been

reported.[17]

1.2.3 The Counter Electrode

A counter electrode is an electrode made of an inert material and has a large surface area compared with the working electrode. Its function is to carry the current from the working electrode. Due to the small currents observed in this thesis at a microdisc electrode, the reference electrode also acts as the counter.

1.3 Introduction to Microelectrodes

The use of microelectrode arrays dates back to 1942 when Davies and Brink measured the oxygen content in muscle tissue using small radii (25 μm) platinum microdisc electrodes.[18] This is the earliest use of microelectrodes reported. Despite the fact that microelectrode voltammetry has been in use for over 60 years, only in recent years their limitations and disadvantages, as well as the huge advantages, have been realized and understood. This in turn allows microelectrodes to fill a niche within the electrochemical field.[18] The development of microelectrodes within voltammetry has created the need to re-examine electrochemically induced diffusional processes. The effect of diffusional processes on current response over time of electrochemical experiments has been significantly altered. These altered hemispherical diffusion layers cause faster diffusion due to the multi-dimensional nature of this process, resulting in improved response time, greater sensitivity and greater current density.[8,19]

1.3.1 Advantages of Microelectrodes

Microelectrodes exhibit several other attractive and important properties that have expanded the possibilities of electrochemistry.[1] Because of the very small total currents at microelectrodes, it is possible to work in highly resistive solutions that would develop large ohmic (iR) drops with

conventional electrodes. The decreased ohmic distortions allow electrochemical measurements to be made in new and unique chemical environments that are not suitable to macroelectrodes. Microelectrode experiments have thus been reported in low-dielectric solvents, low-temperature glasses, gaseous and solid phases. In addition, more traditional systems can be studied with little or no deliberately added supporting electrolyte and with two-electrode systems. The greatly reduced double-layer capacitance of microelectrodes associated with their small area results in electrochemical cells with small RC time constants. For example, for a microdisc the RC time constant is proportional to the radius of the electrode. The small RC constants allow high-speed voltammetric experiments to be performed on the microsecond time scale and hence to probe kinetics of very fast electron-transfer and coupling-chemical reactions. Enhanced rates of mass transport of electroactive species result from the radial diffusion to the edges of microelectrodes. Such edge effects contribute significantly to the overall diffusion current. The rate of mass transport to and from the electrode increases as the electrode size decreases. As a consequence of the increase in mass transport rates and the reduced charging currents microelectrodes exhibit excellent signal-to-background characteristics in comparison to macroelectrodes. In addition, steady-state currents are rapidly attained and the contribution of convective transport is negligible.

Thus the consequences of properties of microelectrodes are as follows: (1) A steady state current for a faradaic process is attained very rapidly; (2) The faradaic-to-charging current ratio is improved, as the charging current decreases in proportion to the decreasing area of the electrode; (3) The ohmic drop of potential is decreased as the measured currents are very low; (4) The applied potential can be scanned rapidly because of suppressed charging current; (5) The signal-to-background ratio is greatly improved; (6) Small size of the electrodes permits measurements of very limited solution volumes.

1.3.2 Diffusion Characteristics at Microelectrodes

One of the biggest differences between microelectrodes and infinitely large planar electrodes is the radial component of diffusion.[1,2] Diffusion at microelectrodes is more complicated than that at macroelectrodes because edge effects must be taken into consideration. This is the component of radial diffusion and is outlined in Figure 1.4. When the time-scale of the voltammetric step is small enough, the current is given by the Cottrell equation (see Section 1.1.2.1), which describes linear diffusion to all electrodes. However, at longer times, steady-state currents resulting from non-linear diffusion are observed.

Composite electrodes couple the advantages of single microelectrodes with significantly higher currents due to larger surface areas. The surfaces of composite electrodes consist of uniform (array) or random (ensemble) dispersions of the conductor region. Similarly to single microelectrodes, at very short times, planar diffusion at each electrode in an array dominates the overall current collected and corresponds to the sum of the currents from each conductor region as described by the Cottrell equation.[11] As the diffusion layers grow out of the electrode area and radial diffusion sets in. Eventually, these individual diffusion layers come to merge and overlap, which causes a decrease in observed current because the supply of electroactive species to each electrode is hindered by its adjacent electrodes. Finally, when the diffusion zone overlap is at a maximum, planar diffusion is once again predominant where the total current is what is would be with a macroelectrode of the same area as outlined in Figure 1.4.

Hemispherical diffusion is the ideal scenario as the current measured is at the maximum at steady state. However, complete diffusional overlap significantly improves the signal-to-noise ratio as the signal is proportional to the surface area of the whole array while the noise is proportional only to the area of the electrodes.[1,2]

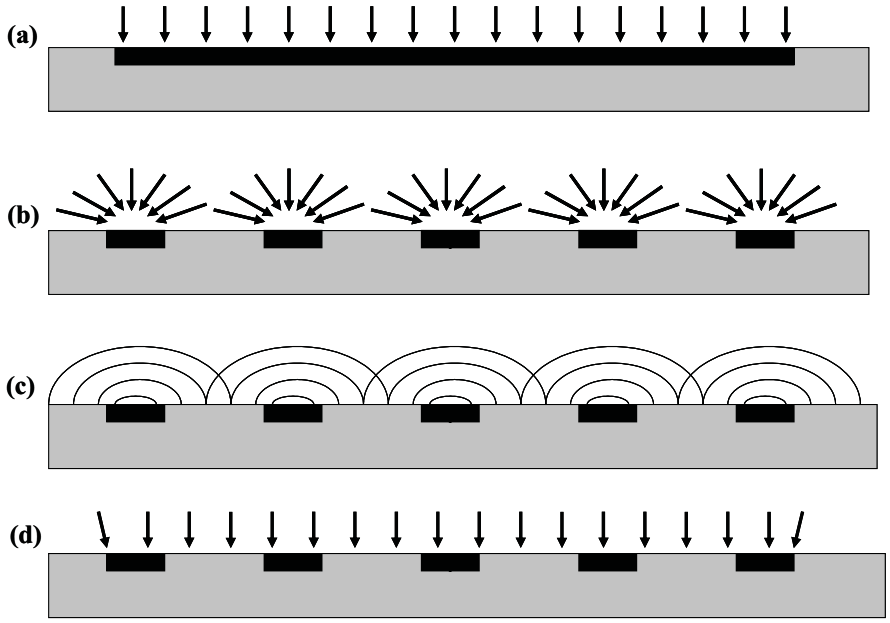


Figure 1.4: Comparison of linear diffusion at a macroelectrode (a: $\delta_{dl} << r_d$), radial diffusion at a microelectrode array at short times (b: $\delta_{dl} >> r_d$), onset of radial diffusional overlap at longer times (c) and diffusion overlap to produce planar diffusion at a microelectrode array at even longer times (d).

1.4 Electrochemical Techniques

There are many electrochemical techniques available to use. These include cyclic voltammetry and potential step chronoamperometry. These were the main techniques used in this work.

1.4.1 Cyclic Voltammetry

CV is the most widely used technique for acquiring qualitative information about electrochemical reactions. The power of CV results from its ability to provide key information on the thermodynamics of the redox process. CV is often the first experiment performed in electroanalytical study. In particular, it offers a rapid location of redox potentials of the electroactive species and evaluation of the effect of media and substrate upon the redox process and thus characterization of the target species.

CV is a potential sweep technique. It consists of linearly sweeping the electrode potential between two potential values, E_1 and E_2, and then reverses the sweep.[6,8] A large range of scan

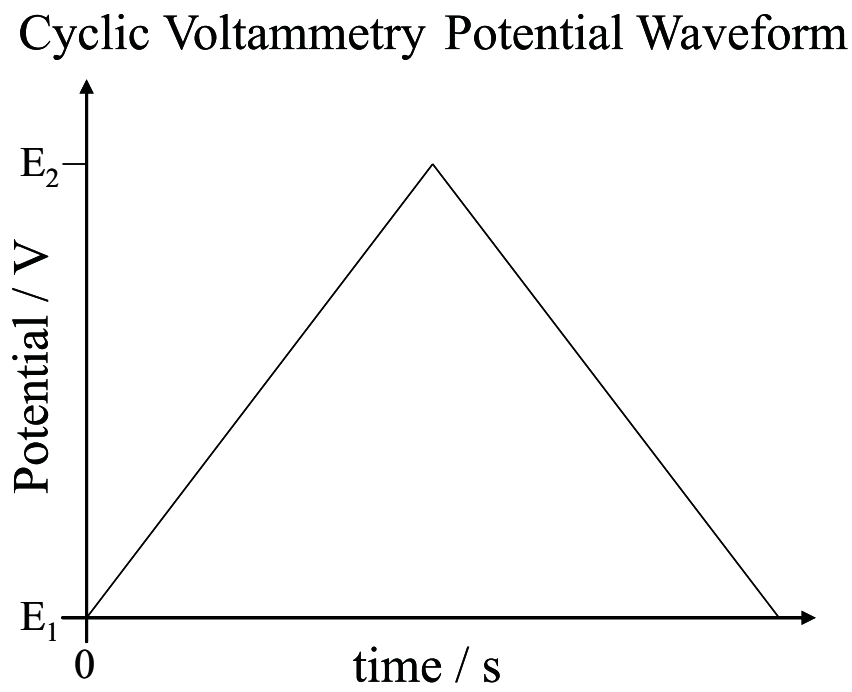


Figure 1.5: Schematic of Cyclic Voltammetry with potential *vs.* time.

rates can be used with this technique, from a few mV s^{-1} up to a few MV s^{-1}. The result of this experimental procedure is a current recorded continuously throughout the experiments. Graphically, the results are presented in a potential-current plot. The E *vs.* t waveform is presented in Figure 1.5. The most popular application of the CV in this work, is in the preliminary investigation of the redox characteristics of gases in solution at the platinum microdisc electrode, such as the i_p, (anodic and/or cathodic peak current), and the E_p (anodic and/or cathodic peak potential). Other widely used information given by CV includes reversibility, adsorption, number of electrons involved in the process and diffusion.[5]

1.4.1.1 Voltammetry at Macroelectrodes

Figure 1.6 shows three types of voltammetry observed at macroelectrodes: reversible, quasi-reversible and irreversible electron transfer.

In the case of reversible voltammetry, a potential is applied and initially, zero Faradaic current is observed. As the potential is swept positively, electron transfer is induced and the current

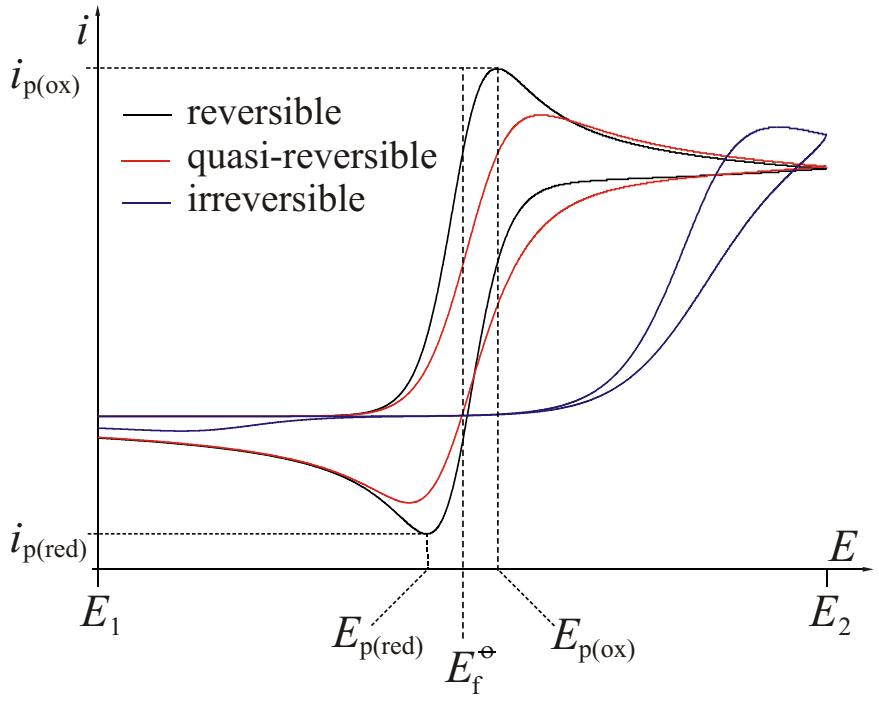


Figure 1.6: Cyclic voltammograms depicting reversible, quasi-reversible and irreversible systems.

increases as electroactive species is oxidised. As the potential is swept yet more positively, a maximum current is observed followed by a decrease since the diffusion layer becomes thicker and the analyte has further to diffuse to the electrode. The peak current at 298 K can be calculated using the Randles-Sevčik equation:[20,21]

$$i_p = (2.69 \times 10^5) n^{\frac{3}{2}} A D^{\frac{1}{2}} v^{\frac{1}{2}} c_{bulk} \tag{1.19}$$

where n is the number of electrons, A is the area of the electrode, D is the diffusion coefficient, v is the scan rate and c_{bulk} is the concentration of the electroactive species in bulk solution.

On reversing the voltammogram, the oxidised form of the analyte is present at a high concentration at the electrode surface and is reduced back which gives a voltammetric signal. For a fully reversible system, the forward and reverse maximum current signals are separated by $2.218\frac{RT}{nF}$ which corresponds to $\frac{57}{n}$ mV at 298 K.

In the case of quasi-reversible voltammetry, the peak separations are greater than $\frac{57}{n}$ mV at

298 K since the kinetics of electron transfer are slower than those of a reversible system. The peak currents are also smaller.

In the case of irreversible voltammetry, the broader wave shape is a result of sufficiently slow electron transfer, and accordingly, the peak current is less than that prediction in Equation 1.20. As well as this, a larger overpotential is required to drive the electron transfer so that the oxidation signal occurs at a more positive potential, and the absence of a back peak suggests that either the reversal of the electrochemical transfer occurs at a lower potential than that shown, or a chemical reaction occurs to consume the oxidised analyte preventing any further electrochemical activity. The peak current at 298 K can be calculated using the Randles-Sevčik equation:[20,21]

$$i_p = (2.99 \times 10^5)\alpha^{\frac{1}{2}} A D^{\frac{1}{2}} v^{\frac{1}{2}} c_{bulk} \tag{1.20}$$

where α is the transfer coefficient.

1.4.1.2 Voltammetry at Microelectrodes

For microelectrodes, where the radius of the electrode is $\leq$ 25 μm, the voltammetry has a sigmoidal shape outlined in Figure 1.7. At slow enough scan rates, this is a result of convergent diffusion and is termed steady-state voltammetry. It occurs because the rate of mass transport to the electrode surface is sufficiently fast so that the concentration of the electroactive species is continually replenished at the electrode surface over the whole potential range. The voltammogram is characterised by the limiting current, i_{ss}, and the half wave potential, $E_{\frac{1}{2}}$. For fast electrode kinetics, $E_{\frac{1}{2}}$ is close to the formal potential for the redox couple, in systems where the electrode kinetics are slow, $E_{\frac{1}{2}}$ deviates more so. The steady-state limiting current, i_{ss} can be used to electrochemically calibrate the radius of the electrode using the following equation:

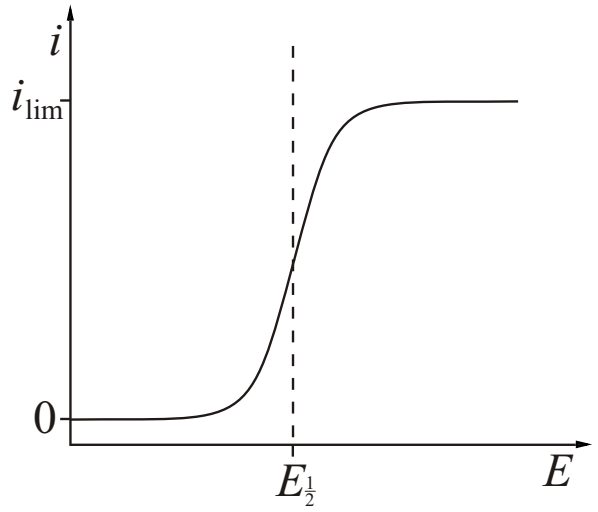


Figure 1.7: Steady-state voltammetry at a microdisc electrode.

$$i_{ss} = -4nFDcr \tag{1.21}$$

where F is the Faraday constant, c is concentration, D is the diffusion coefficient. As well as this, if radius of the electrode is known, this equation can be used to calculate diffusion coefficient of the electroactive species, but only under pure steady-state conditions. Therefore, it is noteworthy that planar diffusion can still be observed at microdisc electrodes at sufficiently fast scan rates or low diffusion coefficients. This feature is particularly pertinent to this thesis, since electrochemistry carried out in room temperature ionic liquids which are highly viscous and result in slow diffusion to the electrode surface. Therefore, the next electrochemical technique for the investigation of electroactive species in solution is of particular interest.

1.4.2 Potential Step Chronoamperometry

Potential step chronoamperometry is an electrochemical technique which studies the variation of current response of an analyte in solution at the electrode surface with time. In a system with an electrochemically active species in solution, the chronoamperometric technique steps the potential from an initial value, E_1 where no Faradaic current flows, to a higher value, E_2, a

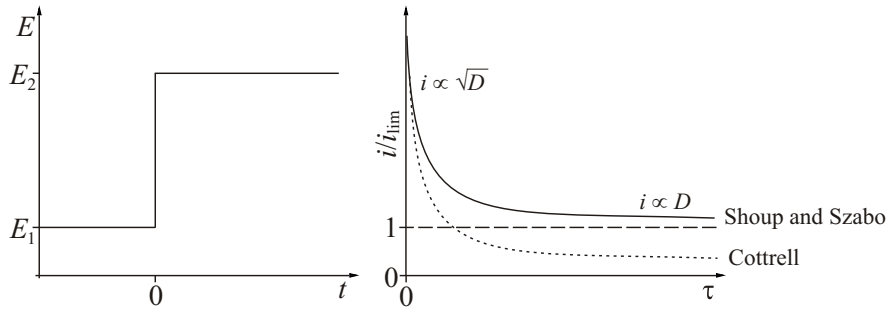


Figure 1.8: Potential waveform applied during potential step chronoamperometry and experimental output on microdisc electrode (Shoup and Szabo) compared to a macrodisc electrode (Cottrell).

potential at which oxidation or reduction of the species has occurred. A large current is initially recorded, which falls steadily with time due to depletion of the target analyte at the electrode surface. Figure 1.8 outlines the increase in potential step over time, and the decay of the current over time at a microdisc electrode denoted by the Shoup and Szabo wave[22] and the decay of current over time at a macrodisc electrode denoted by the Cottrell wave.[11]

For processes where planar diffusion dominates, the diffusion limited current, i_d tends to zero and is given by the Cottrell equation:[11]

$$i_d = \frac{nFAD^{\frac{1}{2}}c}{\pi^{\frac{1}{2}}t^{\frac{1}{2}}} \tag{1.22}$$

where n is the number of electrons transferred, F is the Faraday constant, A is the electrode area, c is the concentration of the electroactive species and t is the time. The diffusion coefficient of the target analyte can then be calculated from the slope of a linear relationship between i $vs.$ $\frac{1}{\sqrt{t}}$ which goes through the origin. The following boundary conditions exist for this relationship: (a) only species A is present in solution at $t = 0$, (b) the solution is sufficiently large so that the concentration of A approaches the bulk value at large distance from the electrode surface, and (c) the concentration of A is reduced to zero after the potential step.

For processes where convergent diffusion dominates, at longer times a more complex system

applies and two factors must be taken into account: initially, at very short times, planar diffusion dominates, whereby the current is proportional to the square root of the diffusion coefficient, outlined by the Cottrell equation above (Equation 1.22). At longer times, convergent diffusion applies where the transient decays to a limiting current, and the current is proportional to the diffusion coefficient, as opposed to Cottrellian behaviour. The current can then be described as a function of a dimensionless parameter, τ:[23]

$$i = 4nFr_dDcf(\tau) \tag{1.23}$$

where

$$\tau = \frac{4Dt}{r_d^2} \tag{1.24}$$

Hence, n is the number of electrons transferred, F is the Faraday constant, D is the diffusion coefficient, c is the initial concentration of the target analyte, r_d is the radius of the electrode and t is the time. Aoki and Osteryoung derived two different expressions for $f(\tau)$.[23] At short times when τ is less than 1.44:

$$f(\tau) = \sqrt{\frac{\pi}{4\tau}} + \frac{\pi}{4} + 0.094\sqrt{\tau} \tag{1.25}$$

whereas at longer times when τ is greater than 0.82:

$$f(\tau) = 1 + 0.71835\tau^{-\frac{1}{2}} + 0.05626\tau^{-\frac{3}{2}} - 0.00646\tau^{-\frac{5}{2}} \tag{1.26}$$

Shoup and Szabo[22] derived a single expression to describe the current over the entire range, with a maximum error of less than 0.6%:

$$f(\tau) = 0.7854 + 0.8862\tau^{-\frac{1}{2}} + 0.2146exp(-0.7823\tau^{-\frac{1}{2}}) \tag{1.27}$$

In some systems, double step potential chronoamperometry can also be performed to calculate the diffusion coefficient of the oxidative or reductive product of target analyte A. This involves stepping the potential from E_1 (point of zero Faradaic current) to E_2 (point after oxidation/reduction) and then back to E_1, measuring the decay for both processes. At microelectrodes, the first step can be analysed by the Shoup and Szabo expression outlined in Equation 1.27, and the second step by an exponentially expanding time grid described by Klymenko *et al.*[24]

Potential step chronoamperometry cannot however provide information of the electrode kinetics of a reaction since the position of the potential step, E_2 is selected to be more negative than the formal potential for the reduction process to ensure that mass transport is rate limiting.

This concludes the introduction to the fundamentals of electrochemistry. The processes discussed in this section are observed in the work presented in this thesis. The next Chapter will outline the electrochemical and practical aspects of room temperature ionic liquids, the electrolyte media selected for the work carried out in this thesis.

References

[1] Wang, J., Ed., *Analytical Electrochemistry*, Wiley, 2000.

[2] Compton, R. G. and Banks, C. E., *Understanding Voltammetry*, World Scientific, 2007.

[3] Fisher, A. C., Ed., *Electrode Dynamics*, Oxford University Press, Oxford, UK, 1996.

[4] Compton, R. G. and Sanders, G. H. W., Eds., *Electrode Potentials*, Oxford University Press, Oxford, UK, 1998.

[5] Kissinger, P. T. and Heineman, W. R., Eds., *Laboratory Techniques in Electroanalytical Chemistry*, Dekker, 1996.

[6] Pletcher, D.; Greef, R.; Peat, R.; Peters, L. M. and Robinson, J., Eds., *Instrumental Methods in Electrochemistry*, Horwood, 2001.

[7] Bard, A. J. and Faulkner, L. R., *Electrochemical Methods: Fundamentals and Applications, 2nd ed.*, John Wiley and Sons: New York, 2001.

[8] Skoog, D. A.; West, D. M.; Heller, F. J. and Crouch, S. R., Eds., *Fundamentals of Analytical Chemistry*, Thompson Brooks/Cole, 2004.

[9] von Helmholtz, H. L. F., *Ann. Physik*, 1853, **165**, 211–233.

[10] von Helmholtz, H. L. F., *Ann. Physik*, 1879, **243**, 337–382.

[11] Cottrell, F. G., *Z. Physik. Chem.*, 1903, **42**, 385–431.

[12] Butler, J. A. V., *Trans. Faraday Soc.*, 1924, **19**, 729–733.

[13] Erdey-Gruz, T. and Volmer, M., *Z. Physik. Chem.*, 1930, **150**, 203–213.

[14] Marcus, R. A., *Annu. Rev. Phys. Chem.*, 1964, **15**, 155–196.

[15] Testa, A. C. and Reinmuth, W. H., *Anal. Chem.*, 1961, **33**, 1320.

[16] Barnes, E.; O' Mahony, A.; Aldous, L.; Hardacre, C. and Compton, R. G., *J. Electroanal. Chem.*, 2010, **646**, 11–17.

[17] Rogers, E. I.; Silvester, D. S.; Poole, D. L.; Aldous, L.; Hardacre, C. and Compton, R. G., *J. Phys. Chem. C*, 2008, **112**, 2729–2735.

[18] Davies, P. W. and Brink, F., *Rev. Sci. Instruments*, 1942, **13**, 524–233.

[19] Bond, A. M., *Analyst*, 1994, **119**.

[20] Randles, J. E. B., *Trans. Faraday Soc.*, 1948, **44**, 327–338.

[21] Sevčik, A., *Collect. Czech. Chem. Commun.*, 1948, **13**, 349–377.

[22] Shoup, D. and Szabo, A., *J. Electroanal. Chem.*, 1982, **140**, 237–245.

[23] Aoki, K. and Osteryoung, J., *J. Electroanal. Chem.*, 1981, **122**, 19–35.

[24] Klymenko, O. V.; Evans, R. G.; Hardacre, C.; Svir, I. B. and Compton, R. G., *J. Electroanal. Chem.*, 2004, **571**, 211–221.

Chapter 2

Introduction to Room Temperature Ionic Liquids: Physical and Chemical Properties.

2.1 Introduction

RTILs are composed entirely of ions and exist in the liquid state at 298 K.[1] RTILs as a class typically contain a bulky organic cation that is weakly coordinated to an organic or inorganic anion.[2] For structures and a list of names, refer to Chapter 4. Weak coordination results in a reduction in the lattice energies and crystalline structure of the salt and, hence, lowers the melting point.[3] RTILs have attracted much attention recently as a replacement for traditional organic solvents as they possess many attractive properties. Among these properties are intrinsic ion conductivity, low volatility, high chemical and thermal stability, low combustibility and wide electrochemical windows.[2,4–10] The presence of an abundance of charge carriers means that when RTILs are used as solvents, no supporting electrolyte is required for electrochemical experiments, and this minimises waste. One would expect that intrinsic conductivity might allow faster mass transport of the analyte to the electrode surface, but the high viscosity of RTILs (*ca.* 1 to 2 orders of magnitude higher than conventional solvents) results in conductivities approximately similar to traditional organic solvents with added supporting electrolyte (eg. MeCN with 0.1M TBAP).[2] The low volatility of RTILs make them more environmentally attractive than volatile organic solvents, and thus they have been termed 'green solvents'.[9] The reduction and oxidation of the cations and anions accounts for the wide electrochemical window, so that a window of 5 to 6 V or more is not unusual for an ionic liquid.[7] The ability to vary the nature of the cation and the anion allows one to tune the solvents for a specific purpose and has given them the name 'designer solvents'.[4,6] This thesis is concerned with the use of RTILs for electrochemistry.

RTILs have been used in many electrochemical applications such as solar cells, electrochemical sensors, fuel cells, capacitors and in lithium batteries and are employed as solvents in electrochemical experiments.[11] Recently, electrodes modified with ionic liquids have been studied. It has been shown that it is possible to use ionic liquid formation on the electrode surface to form a liquid—liquid interface with an aqueous phase as an electroanalytical tool for quantitative anion detection[12–14] and could possibly replace previously used volatile organic solvents. The low volatility and high thermal stability of RTILs is also advantageous for gas detection and the development of robust gas sensors. A gas sensor lifetime is determined by how quickly the electrolyte dries up, and most conventional electrolytes (*eg.* H_2SO_4/H_2O) dry up quickly and thus cannot survive drastic temperature changes. Ionic liquids can sustain high temperature and pressure changes and remain physically and chemically unchanged.[15]

Ionic liquids can loosely be described in three main classes. The first class is based on haloaluminate anions such as $[AlCl_4]^-$.[16] However, the major drawbacks of these species was high sensitivity to moisture requiring them to be handled in a glovebox, which is not feasible for general experiments. The next generation of ionic liquids were more air- and water-stable and are based on $[BF_4]^-$ and $[PF_6]^-$ anions.[17] However these ionic liquids still absorb moisture changing the physical and chemical properties. At elevated temperatures, the presence of moisture in these ionic liquids can actually lead to hydrolysis which results in the formation of hydrogen fluoride. The third generation of ionic liquids are much more air- and water-stable than the previous two. In fact they are known for their hydrophobicity. Anions of these ionic liquids include $[NTf_2]^-$ and $[FAP]^-$ anions.[18] And finally, a more modern generation of ionic liquids are being synthesised which serve as catalysts or reagents for specific reactions. These are referred to as "'task-specific ionic liquids"'. The ions in these RTILs are modified with functional groups to give them a more specific role in a particular system.[19] These advances have led to a broader spectrum of applications for these species.

2.2 Physical Properties of RTILs

In Table 2.1 we report the physical and chemical properties of twelve RTILs and some conventional organic solvents from various authors. The table shows the twelve RTILs and their reported viscosity (η), conductivity (κ), density (ρ), melting point and decomposition temperature values. These are pertinent to the choice of electrochemical solvents.

Table 2.1: Physical properties of RTILs. *1 cP = 1 mPa·s.

RTIL	Viscosity η at 293 K / cP*	Conductivity κ at 293 K / mS cm^{-1}	Density ρ at 293 K / g cm^{-3}	Melting Point K	Decomposition[20] K
$[P_{14,6,6,6}][FAP]$	464	-	1.18[20]	223[6]	473
$[C_4mpyrr][NTf_2]$	89[21]	2.2[22]	1.40[20]	186[22]	583
$[C_6mim][FAP]$	74[18]	1.3[18]	1.56[20]	-	573
$[C_4mim][NTf_2]$	52[23]	3.9[23]	1.44[20]	219[6]	548
$[C_4dmim][NTf_2]$	105[21]	2.0[24]	1.42[20]	-	-
$[N_{6,2,2,2}][NTf_2]$	167[25]	0.7[26]	1.27[25]	219[6]	-
$[C_4mim][PF_6]$	371[27]	1.54[28]	1.37[27]	205[29]	573
$[C_2mim][NTf_2]$	34[23]	8.8[23]	1.53[20]	186[30]	553
$[C_4mim][BF_4]$	112[21]	1.7[28]	1.21[27]	191[6]	573
$[C_4mim][I]$	1110[31]	-	1.49[20]	201[6]	473
$[C_4mim][OTf]$	90[23]	3.7[23]	1.30[23]	191[32]	573
$[C_6mim][Cl]$	7453[18]	-	1.05[20]	188[6]	483
Acetonitrile	0.34[33]	0.79[33]	7.6*[33]	-	-
Dichloromethane	0.44[33]	1.33[33]	-	-	-
N,*N*-Dimethylformamide	0.92[33]	0.94[33]	4.0*[33]	-	-
Dimethylsulfoxide	1.99[33]	1.10[33]	2.7*[33]	-	-
Propylene carbonate	2.5[33]	1.21[33]	-	-	-

2.2.1 Viscosity

The viscosity of a solvent is an important electrochemical property, since high viscosities limit some applications and slow down the rate of diffusion-controlled chemical reactions.[34] Ionic liquids have viscosities comparable to that of oils, *i.e.* 1 to 2 orders of magnitude higher then conventional solvents. Table 2.1 outlines a list of the viscosities of some commonly used ionic liquids and conventional aprotic solvents. Viscosities of most ionic liquids are generally in the range of 30-450 cP at ambient temperature. The high viscosity of ionic liquids is a disadvantage for use in industrial processes since it limits transport to the sensing surface. Viscosities can be lowered by the addition of small amounts of organic cosolvents,[35] but this tends to cause the solvent to lose some of its favourable properties such as low-volatility and thermal stability. The diffusion coefficients of electrochemical species often reflect the different viscosities of RTILs where for sufficiently large molecules such as ferrocene or cobaltocene the diffusion coefficient is inversely proportional to the viscosity as implied by the Stokes-Einstein equation.[2]

The viscosity of RTILs is affected by the nature of both the cations and anions. The viscosity of ionic liquids is mainly due to van der Waals forces and hydrogen bonding.[34,36] The alkyl chain length of the imidazolium cations increases the liquids' viscosity due to a corresponding increase in van der Waals forces.[37] This result may seem counterintuitive as the associated electrostatic forces decrease as the side-chain length increases, however, the increasing contribution of weaker, non-associating dispersion forces dominates the trend.[8] Increased van der Waals forces result in more energy being necessary for molecular motions. Therefore longer alkyl substituents tend to give rise to more viscous RTILs.[31]

The nature of the anion also affects the viscosity of the ionic liquid, particularly through relative basicity and the ability to participate in hydrogen bonding. It is shown in Table 2.1 that the perfluorinated $[PF_6]^-$ and $[BF_4]^-$ anions form much more viscous ionic liquids due to strong H$\cdots$F interactions than those ionic liquids formed with the weakly basic $[NTf_2]^-$ anion,

in which the negative charge is quite delocalised over the two sulfoxide groups.[1] Differences in viscosities may also be caused by the size, shape and molar mass of the anion, with smaller, lighter and more symmetric anions leading to more viscous ionic liquids. For example, the increase in symmetry of anions such as $[PF_6]^-$ or $[BF_4]^-$ as compared to the anion $[NTf_2]^-$, as well as increased H-bonding, may contribute to the higher viscosity of RTILs incorporating these anions.[31,37] Table 2.1 shows that $[C_4mim][PF_6]$ and $[C_4mim][BF_4]$ have viscosities of 371 and 112 cP at 293 K, respectively, compared to $[C_4mim][NTf_2]$ which has a more bulky anion and a viscosity of 52 cP at 293 K. It is shown that the replacement of three fluorine atoms in the $[PF_6]^-$ anion by pentafluoroethyl-groups hugely decreases the viscosity of imidazolium ionic liquids, as can be seen when comparing $[C_4mim][PF_6]$ and $[C_6mim][FAP]$.[18] It has also been suggested that the addition of fluorine atoms to the imide anion increases viscosity due to an increase in van der Waals forces.[37]

The viscosities of ionic liquids are highly temperature dependent, with a 20 % change over 5 K not uncommon around room temperature.[38] Okoturo and VanderNoot[21] report the viscosities of twenty-three RTILs over a temperature range of 283 to 343 K. For most ionic liquids, those with asymmetrical cations without functional group on the alkyl chains, an Arrhenius relationship is approximately followed outlined by Equation 2.1.

$$ln\eta = ln\eta_\infty + \frac{E_\eta}{RT} \tag{2.1}$$

where η_∞ is the viscosity at infinite temperature, and E_η is the activation energy for viscous flow, R is the universal gas constant and T is the temperature.

Other RTILs, generally those with small, symmetrical, low molar mass cations closely follow the Vogel-Tammann-Fulcher relationship,[39–41] shown in Equation 2.2.

$$\eta = (A_\eta\sqrt{T})exp(-\frac{k_\eta}{T - T_g}) \tag{2.2}$$

where A_η and k_η are constants, T is the temperature and T_g is the glass transition temperature. Ionic liquids with small, symmetrical and low molar mass cations tend to give higher T_g values than ionic liquids with larger and higher molar mass cations. Some ionic liquids do not fit well to either equation.[21]

Literature data shows significant differences in reported viscosity values. The significant contribution of temperature may cause much of these discrepancies. However, the presence of impurities such as water, halides and oxygen, may also contribute to these differences, as well as differences reported for other physical properties which are later mentioned.

2.2.2 Conductivity

In electrochemical experiments, the conductivity of a solvent is of significant importance. RTILs have conductivities similar to those of organic solvents with added inorganic electrolytes (*eg.* DMSO + 0.1 M TBAP has a conductivity of 27 mS cm^{-1}).[1] Ionic liquids have advantages over traditional organic solvents as their conductivity is intrinsic, and they do not require the addition of a supporting electrolyte. The conductivity of a pure ionic liquid should depend on the mobility of the ions, which is influenced by the ion size, ion association, and particularly the viscosity.[18] In fact, the change in conductivity with composition in ionic liquids can be attributed almost directly to changes in the viscosity.[37] The high viscosity and large size of constituent ions result in reduced ion mobility and average conductivities. Conductivity generally decreases in the order of 1-alkyl-3-methylimidazolium > N,N-dialkylpyrrolidinium > tetraalkylammonium, attributed to the decrease in the planarity of the cationic core. The flatness of the imidazolium ring seems to allow a higher conductivity than does the tetrahedral nature of the ammonium salts, with the pyrrolidinium cation having an intermediate geometry.[1] This is apparent in Table 2.1, wherein the conductivities of $[C_4mim][NTf_2]$, $[C_4mpyrr][NTf_2]$ and $[N_{6,2,2,2}][NTf_2]$ decrease according to the order listed above (3.9, 2.2 and 0.7) mS cm^{-1}, respectively. While viscosity and conductivity

are generally inversely proportional, viscosity alone can not be held accountable for the variation in conductivity. Other factors should be considered such as anionic charge delocalisation and aggregation.[42]

It is expected that due to higher ionic mobility, smaller anions would form ionic liquids with higher conductivities.[43] The following general trend was observed for decreasing conductivity in the order: $[BF_4]^- > [NTf_2]^- > [OTf]^- > [FAP]^- > [PF_6]^-$,[44] though conductivity was found to be less dependent on the anion size with reports suggesting that larger anions had similar conductivity values for a given cation. However, when the conductivity was measured from the self-diffusion coefficients of the cation and anion, outlined in Equation 2.3, the values obtained were larger than those measured for a given RTIL:

$$\kappa = \frac{D_s q^2 c}{k_B T} \tag{2.3}$$

where D_s is the self-diffusion coefficient, q is the ionic charge, k_B is the Boltzmann constant, T is the temperature and c is the concentration of the ionic liquid charge carriers.

At increased temperatures, the conductivity increases, due to the increased mobility resulting from a decrease in viscosity.[26,45] The variation of ionic liquid conductivity with temperature follows the Vogel-Tammann-Fulcher relationship[26,38,43,46] (given below):

$$\kappa = A\sqrt{T}e^{-B(T-T_0)} \tag{2.4}$$

where κ is conductivity, A and B are empirically derived constants, and T_0 is the ideal glass temperature at which the conductivity drops to zero.

2.2.3 Density

Density of solvents is an important consideration for the development of certain types of batteries where weight issues are a concern. The density of an ionic liquid generally decreases with increasing length of alkyl chains in cations or anions.[8] Adding CH_2 groups to the alkyl chain on the imidazolium cation decreases the density since CH_2 is less dense than the imidazolium ring.[31] The density of RTILs increases with the molar mass of the anion in the approximate order $[BF_4]^-$ < $[OTf]^-$ < $[PF_6]^-$ < $[NTf_2]^-$ < $[FAP]^-$. In the studies of Huddleston *et al.*[31] it was noted that the densities of simple halide salts such as $[C_4mim][Cl]$ were lower than that of $[C_4mim][PF_6]$, which is reflected in Table 2.1 where $[C_6mim][Cl]$ is compared to $[C_4mim][PF_6]$ (1.05 g cm^{-3} compared to 1.37 g cm^{-3}). However, $[C_4mim][I]$ has a higher density than $[C_4mim][PF_6]$ (1.49 g cm^{-3} compared to 1.37 g cm^{-3}). Several researchers have recorded densities as a function of temperature and have reported an approximately linear decrease of density with temperature.[47–49]

2.2.4 Thermal Stability and Negligible Volatility

Ionic liquids are defined as salts having a melting point below 100^oC, and in order to use these molten salts as electrochemical solvents it is necessary to maintain the liquid phase over a wide temperature range.[50] Typical inorganic salts have high melting points (*ca.* 1000^oC) reflecting their high lattice energies, those strong electrostatic attractive forces between the ions.[51] For ionic liquids, van der Waals interactions, hydrogen interactions and π-π bonds must also be taken into account as well as electrostatic interactions. Accordingly, the structure of the ions that make up RTILs can alter these interactions which is directly effective in lowering the melting point of the salts. The structural components that affect the melting points include the ion radius, cation structure and anion structure.

For ions of equivalent charge, the electrostatic interaction of larger ions is weaker than that

of smaller ions. This is because the surface charge density decreases with increasing ion radius, and the separation between opposite ions increases with increasing ion radius. Therefore, due to the size of the component ions in ionic liquids, these salts show a lower melting point than other salts.[51] However, it should be noted that melting point does not only depend on electrostatic interactions. The $[N_{6,2,2,2}]^+$ cation is larger than the $[C_2mim]^+$ cation, yet $[N_{6,2,2,2}][NTf_2]$ has a higher melting point than $[C_2mim][NTf_2]$ outlined in Table 2.1. Since the delocalization of charge also contributes to lowering the electrostatic interaction, the existence of π electron orbitals is significant in lowering melting points.

The fact that most ionic liquids are composed of organic cations is attributed to weaker electrostatic interaction among component ions. The relationship between melting point and the basic structure of cations is significant in the liquidus range of ionic liquids. It is known that the imidazolium and pyridinium cations are aromatic, and these salts show relatively low melting points because of delocalized charge. The side chain bound to the cation also affects the melting point due to flexibility and volume effects. With respect to the imidazolium cation, with a carbon number from two to nine, these salts are liquid at room temperature. When the carbon number is zero or one, or greater than nine, the salts showed a higher melting point.[51] A liquid crystalline phase appeared for these salts with a carbon chain longer than nine which arises due to the orientational effect of the long alkyl chain. Symmetry is another factor that affects melting point. The salts with symmetrical ions usually show higher melting points than those with unsymmetrical ones. This phenomenon relates to the structural effect on crystallinity, whereby highly symmetrical ions are more efficiently packed onto the crystalline structure than unsymmetrical ones.

The anion species also has an effect on the melting point of ionic liquids. The low melting point is obtained with ions having weaker electrostatic interactions originating from negative charge delocalisation and stabilization by the electron-withdrawing effect of halogen atoms.

Non-halogenated anion-containing ionic liquids with low melting points are also available to a structural design incorporating lower anionic charge density. Larger anions generally form ionic liquids with lower melting points since lowering the surface charge densities of the anions also lowers the melting points. Where symmetry is concerned, more anions used are symmetrical, and there are few approaches where melting point has been lowered by using asymmetrical anions.[51]

Ionic liquids are thermally stable but do decompose at high temperatures. The decomposition temperature of ionic liquids depends on the component ion structure, similarly to other thermal properties. This does not however necessarily mean that ionic liquids can be used at any temperature below decomposition temperature. Therefore thermal stability is usually defined by the thermal gravimetric analysis (TGA) onset temperature[52] which is usually associated with weight loss.[53] The TGA onset temperature has the advantage of being easy to measure. It is clear from a TGA thermogram that some decomposition occurs at temperature less than the onset temperature. However this method has its limitations. This method yields temperatures whereby degradation, which is measured by the evolution of volatile degradants, is already well advanced and thus overestimates the real upper limit of thermal stability. There are many factors which can affect the reproducibility of this method, such as choice of crucible, additives or impurities and physical properties of some ionic liquids such as hydrophilicity.[53] Thermal stability studies designed to test the long-term stability of ionic liquids all indicate upper temperature limits well below the decomposition temperatures derived from fast scan TGA.[53]

Thermal decomposition temperatures decrease as the anion hydrophilicity increases, therefore one can conclude that drying improves the thermal stability of many RTILs. Halide anions reduce the thermal stability of ionic liquids, with decomposition occurring at least 373 K below corresponding RTILs with non-halide anions. Relative anion stabilities have been suggested by Huddleston *et al.* as $[PF_6]^- > [NTf_2]^- \approx [BF_4]^- >$ halides,[31] and Table 2.1 shows that this is

indeed the case. The ionic liquids [C_4mim][PF_6], [C_4mim][NTf_2] and [C_4mim][BF_4] have decomposition temperatures of 373 K higher than the corresponding halide ionic liquid [C_4mim][I]. Kroon *et al.* suggest that $[NTf_2]^-$ is more thermally stable than both $[PF_6]^-$ and $[BF_4]^-$, but agree that all of these anions are far more thermally stable than halides. Ionic liquids with the $[FAP]^-$ anion are also very thermally stable,[18] as can be seen from a decomposition temperature of 573 K for [C_6mim][FAP]. The decomposition temperature of RTILs also depends on the type of cation. The trend of thermal stability with respect to cation species appears to go as follows: phosphonium > imidazolium > tetraalkylammonium ≈ pyrrolidinium.[54]

The vapour pressure of ionic liquids is essentially zero under ambient conditions. They have been utilized as alternatives for traditional solvents for liquid-liquid extractions and are reusable.[55] Therefore ionic liquids have been recognized as non-volatile liquids at normal pressures. However, it is known experimentally that some ionic liquids can be distilled at elevated pressures.[51] Distillable ionic liquids can be prepared for separation of solvents and products.[56] These distillable ionic liquids have similar properties to regular ionic liquids, but are easily recovered and separated from products by low temperature distillation. They also have advantages associated with low cost of synthesis and high tuneable conductivities.

However, for the purposes of this work, the vapour pressure of ionic liquids is negligible since experiments are carried out within a temperature range far within the liquidus range of each of the ionic liquids used, and thus high temperature and low pressure studies are not necessary.

2.3 Impurities and the Electrochemical Window of RTILs

Ionic liquids generally exhibit a wide potential window which is highly desirable for applications as electrochemical solvents. This potential window range is equal to or slightly wider than that of conventional organic electrolytes, and is excessively larger than those accessible in aqueous electrolytes.[42] The potential window of ionic liquids is commanded not only by the chemical

structure of the materials used, but also the electrode material, sweep rate of the potential, temperature, atmosphere and solvent purity. Potential values are often referred against different quasi-reference electrodes, and thus data is difficult to compare with a high level of accuracy. The Fc/Fc^+ redox couple is helpful as an internal standard to define the electrochemical window for many ionic liquids. The potential window is usually evaluated using cyclic voltammetry (CV) or linear sweep voltammetry (LSV). When using CV it is noteworthy that the electrochemically oxidized or reduced products of the initial sweep may affect the voltammograms of the reverse sweep. LSV is not affected by this when fresh test solution and electrodes are employed for anodic sweep and cathodic sweep respectively, but reproducibility must be checked. Generally, anodic and cathodic limits are defined as the voltage where the current density reaches a certain value. The cut-off point is usually 1.0 mA cm^{-1}, as outlined in Chapter 5 when examining the potential window of several ionic liquids under various conditions. Cathodic and anodic limits of ionic liquids are attributed to the oxidative and reductive decompositions of the anions and cations respectively.[51] Ionic liquids having a potential window over 7 V have been reported making them favourable for application as electrolyte materials.[18,57]

The purity of an ionic liquid has a great influence on the size of the electrochemical window, and the nature of the electrode material may alter the decomposition potentials of the electrolyte.[42] For example, some RTILs are found to have shorter electrochemical windows on platinum than glassy carbon, likely due to catalytic activity of the platinum metal. Some general trends in electrochemical windows of RTILs have been observed depending on the nature of the ions. Quaternary ammonium and pyrrolidinium salts are known to be more stable towards reduction than the corresponding imidazolium salts due to cathodic stability of these species. The reduction of the imidazolium cation is related to the relatively high acidity of the C_2-H proton.[42] With respect to the anions, those which are anodically stable include $[PF_6]^-$, $[BF_4]^-$ and $[NTf_2]^-$. However, $[PF_6]^-$ and $[BF_4]^-$ are susceptible to hydrolysis which may release toxic

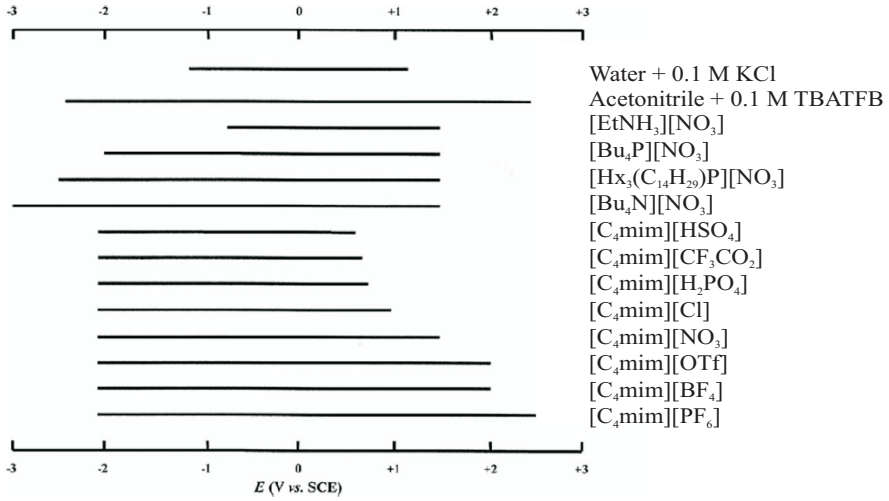


Figure 2.1: The electrochemical windows for some typical RTILs.[58]

hydrogen fluoride.[17] In this context, $[NTf_2]^-$ is favoured as a robust anion and has become widely used. A less widely used anion is trifluoro-tris(pentafluoroethyl)phosphate, $[FAP]^-$ which has been suggested to allow a substantial improvement of the anodic limit.[18] The electrochemical windows of some widely used ionic liquids are shown in Figure 2.1 which has been outlined by Plechkova *et al*.[58]

Additives such as halide ions or molecular solvents can greatly influence both the electrochemical window of an ionic liquid, and the outcome of electrochemical experiments.[1] Thus, where undesirable, it is necessary to identify and remove impurities such as these. The physicochemical properties of ionic liquids have been shown to be dramatically affected by the presence of impurities such as water and halides.

Halide impurities are generally introduced during the two-step synthesis used to manufacture many RTILs. In this reaction, the cation is formed by alkylation of an imidazole or amine using an alkyl halide. A metathesis reaction with an alkali metal or silver salt of the desired anion then forms the ionic liquids and a by product. If the second reaction does not go to completion, unreacted halide ions from the first step remain and must be removed in additional synthesis steps.[1] Halide impurities affect both the electrochemical window of the RTIL and the viscosity.

The presence of low levels of chloride causes a substantial decrease in viscosity of several ionic liquids, and since chloride ions are electroactive at potentials lower than those needed to oxidise heavily fluorinated constituent anions of ionic liquids, their presence lead to a narrowing of the electrochemical window of the ionic liquid. The presence of halide impurities can also have deleterious effects on electrochemical reactions using ionic liquids as electrolytes. Even trace quantities of halide anions will deactivate catalysts in some transition metal catalysed reactions, and may interfere with electrochemical processes underway.[53] Halide impurities can also act as stabilizing ligands, nucleophiles, or reactants depending on the chemical nature of the reaction.[16] Some synthetic methods utilize separation methods in an effort to remove these halide impurities and then wash the ionic liquid with water, which can be later removed.[16] This method however is not suitable for all ionic liquids but other solvents such as dried acetone can also be used.

The ionic liquids in this work are generally air- and water-stable. However, water is still absorbed into ionic liquids to some extent from the atmosphere. While no hydrolysis occurs generally in the ionic liquids in question, water impurities have been shown to decrease viscosity of an ionic liquid and decrease the electrochemical window.[42] The effect of water on the electrochemical window of ionic liquids is studied at length in Chapter 5, and thus will not be discussed in detail in this section. However, it is worth noting that not all new-generation ionic liquids are impervious to hydrolysis from the presence of water. Especially at elevated temperatures, ionic liquids with the $[PF_6]^-$ anion and the $[BF_4]^-$ anion are hydrolytically unstable.[59] The hydrolysis of these anions can results in the formation of hydrogen fluoride (HF),[17,59] a most unwanted impurity. It is also noteworthy that the presence of water can have dramatic effects on the diffusion coefficients of species in RTILs. Schröder *et al.* examined the diffusion coefficients of several species in $[BF_4]^-$- and $[PF_6]^-$-containing RTILs.[60] They noticed significant differences in the diffusion coefficients of ionic and neutral species in 'wet' RTILs. They explained this behaviour with the presence of a nanostructure in the 'wet' RTIL, analogous to concentrated

surfactant media. It causes neutral species to reside in the less polar regions of the RTIL and ionic species to undergo faster diffusion in the more polar, 'wet' regions.

Finally, another major impurity which is rather ubiquitous is oxygen. Because oxygen is electroactive, and is easily dissolved in ionic liquids, its removal is required before electrochemical experiments can be carried out to prevent any electrochemical interference.[42] The removal of oxygen is easily achieved through purging the ionic liquids under vacuum, or bubbling with argon for extended periods of time.

The presence of halide impurities in the ionic liquids in this work is not relevant, since ionic liquids received are of high purity and display featureless baselines when purged under vacuum until the onset of the oxidation and reduction of the anion and cation respectively. The presence of water in ionic liquids is examined in detail in Chapter 5, but in general, this can be mostly (but never fully) removed through purging under vacuum also.

2.4 Electrochemical Studies in RTILs

2.4.1 Mass Transport and Diffusion Coefficients

The diffusion coefficients of the constituent ions in ionic liquids have been measured generally by electrochemical means or by NMR methods.[16] The electrochemical methods measure the diffusion coefficient of an ion in the presence of a concentration gradient, ie. Fickian diffusion, while NMR methods measure diffusion coefficients in the absence of a concentration gradient, ie. self diffusion. It is apparent that component ions in ionic liquids find it difficult to diffuse compared to conventional solvents due to strong electrostatic interaction forces.[51] It is known that the difference in these diffusion coefficients are due to the higher viscosity of ionic liquids. In particular, the diffusion coefficients of ionic liquids containing fluorine anions are large due to stronger electrostatic forces. In the scope of this work however, it is mainly the diffusion of electroactive solutes in ionic liquids that is of significance.

The diffusion coefficient values of electroactive species commonly found in ionic liquids are about two orders of magnitude lower than those measured in conventional organic solvents, again due to higher viscosity. Diffusion coefficients are generally found to be inversely proportional to the viscosity in agreements with the Stokes-Einstein equation showing that ionic liquids behave like conventional solvents:[42]

$$D = \frac{k_B T}{p\pi\eta r} \tag{2.5}$$

where k_B is the Boltzmann constant, T is the absolute temperature, η is the viscosity, r is the hydrodynamic radius, and p is a constant. This relationship is found to be true for large molecules such as ferrocene or cobaltocene,[2] however for smaller molecules such as oxygen[61] (and other gases such as hydrogen sulfide,[15] sulfur dioxide[62] and hydrogen[11]), this relationship was not adhered to, likely due to the small size of these species. Since viscosity and diffusion coefficient are related in general, it follows that diffusion is highly sensitive to temperature, and this is outlined in the Arrhenius-type relationship outlined in Equation 2.6:

$$D = D_\infty e^{-\frac{E_{a,D}}{RT}} \tag{2.6}$$

where D_∞ is the hypothetical diffusion coefficient at infinite temperature, R is the universal gas constant and $E_{a,D}$ is the activation energy of diffusion.

True steady-state behaviour is required when calculating diffusion coefficients from limiting currents using cyclic voltammetry. In ionic liquids, because of the viscosity and resulting high diffusion coefficients, this can only be achieved at slow scan rates on small electrodes where spherical diffusion exists (*eg.* for diffusion coefficient of 10^{-11} m^2 s^{-1} at $\upsilon = 10$ mV s^{-1} and $r_d \leq 5$ μm) following the inequality:

$$\upsilon << \frac{RTD}{nFr_d^2} \tag{2.7}$$

where F is the Faraday constant and n is the number of electrons. The work carried out in this thesis is on a microelectrode which has the benefit of efficient mass transport, so that at low scan rates, steady-state voltammetry is observed, and at higher scan rates, transient voltammetry is observed. At low scan rates, the radius of the electrode is smaller than the diffusion layer thickness above it, therefore diffusion is described by the convergent model. At high scan rates, the radius of the electrode is larger than the diffusion layer thickness above it, and thus diffusion is described by a planar model. This intermediate behaviour makes it difficult to extract kinetic parameters from voltammetric data of electrochemically active species in ionic liquids. However, Barnes *et al.*[63] showed that the peak-to-peak separation of redox species in ionic liquids decreases with increasing scan rate in the transition from convergent to more planar diffusion, and this data can be used for simulation using the least-squares method to determine the value of k^0 across the entire range of scan rates.

A substantial dissimilarity in the diffusion coefficients between reactant and electrogenerated species can be observed in ionic liquids. This phenomenon was observed in the voltammetry of oxygen in ionic liquids[64] whereby the reduction peak of oxygen to superoxide was steady-state in nature dictated by convergent diffusion to the electrode surface, whereas the oxidation peak was highly transient in nature due to contributions from planar diffusion. This behaviour is attributed to the different diffusion coefficients of oxygen and superoxide in ionic liquids (1.5×10^{-10} m^2 s^{-1} and 4.7×10^{-12} m^2 s^{-1} respectively) resulting in a single voltammogram showing both steady-state and transient behaviour. This behaviour was also observed for larger molecules in ionic liquids such as TMPD,[65,66] ferrocene and cobaltocene.[2] This is due to the electrostatic interactions between the charged species and the ionic liquid component ions. However, another study revealed equal diffusion coefficients between initial uncharged analyte and

oxidatively charged analyte in ionic liquids. The diffusion coefficients of catechol, and its oxidised product, doubly-protonated o-benzoquinone were equal, suggesting that both species diffuse at the same rate through the ionic liquid media.[67] This may be attributed to the positive charge on the doubly protonated o-benzoquinone being substantially delocalised around the aromatic ring, so that ionic interactions between the oxidised species and the solvent would be diminished.

A method aside from voltammetry can be used to calculate the diffusion coefficient of electrochemically active species in ionic liquids, and that technique is chronoamperometry. If the radius of the electrode is known, then the diffusion coefficient D and concentration of analyte in solution n can be simultaneously determined using the Shoup and Szabo expression[68] which is incorporated into a fitting program.[69] This electrochemical technique has already been discussed in Chapter 1.

2.4.2 Electron Transfer Kinetics

There is not a straightforward transfer of kinetic processes when comparing ionic liquids to conventional solvents, possibly due to more varied physicochemical properties such as hydrogen bonding, π-π interactions, and ionic pair solvation effects due to the number of ions. Some work regarding kinetics of species in ionic liquids has been carried out,[63] but the amount of work carried out on kinetics does not correlate with the amount of work observing voltammetry only. The nature of ionic liquids affects the heterogeneous electron-transfer process. Kinetic of heterogeneous electron-transfers is slower by at least one order of magnitude in ionic liquids compared with conventional solvents with supporting electrolyte.[70] This is attributed to greater solvation of species in ionic liquids and to greater solvent reorganisation in highly ordered and viscous ionic liquid media.[70,71]

Investigations by Lagrost *et al.*[71] have observed the voltammetric reduction of substituted nitrobenzenes as well as aliphatic nitro-based compounds in MeCN and two ionic liquids ([C_4mim][NTf_2]

and $[N_{4,2,2,2}][NTf_2]$) using CV.

Electrochemical patterns in MeCN and both ionic liquids were similar for six nitro-based compounds examined, and the same radical anions were formed in all solvents through reduction. Some differences were apparent however. Smaller peak currents were observed in the ionic liquids compared to MeCN due to increased viscosity, and smaller diffusion coefficients were observed for the same reason. Also, larger peak-to-peak separation in ionic liquids were observed showing slower heterogeneous electron-transfers. Values of heterogeneous electron-transfer (k^0) were calculated using peak-to-peak separation values (ΔE_{pp}).

For five aromatic compounds, potentials shifted in the positive direction for ionic liquids compared to MeCN, relating to a higher stabilization of anion radical product by the ionic liquids cation through ion-pairing interactions. Stabilization appeared to be higher in ionic liquids with less bulky cations, and this was attributed to distance between charges on the cation and the radical anion. This shielding effect was observed for nitrobenzene analytes where a shift to more positive potentials became more noticeable for bulky cations (ammonium) than less bulky cations (imidazolium).

The k^0 value was measured at gold and glassy carbon electrodes. For some species examined, values of k^0 decreased by at least two orders of magnitude in ionic liquids compared to MeCN. These changes appear to be more pronounced for less sterically hindered nitro species than bulkier species. But contrary to this, heterogeneous electron-transfer kinetics for the aliphatic compound studied remained almost unchanged between the ionic liquids and MeCN, despite less steric hindrance. This may however be accounted for by experimental error. These outer sphere and solvation contributions are significant when observing heterogeneous electron-transfer kinetics in ionic liquids compared to conventional solvents when inner sphere contributions are not significant. However, when the inner sphere contributions are more significant, the k^0 values between ionic liquids and MeCN solvents show little difference, indicating that the solvent has

less of an effect on the heterogeneous electron-transfer rate than the actual analyte species. Such effects must be taken into consideration since some electrochemical processes that are fast in organic solvents become slow in ionic liquids unless they were already slow due to inner sphere reorganisation.

More recently, further studies have been carried out on the heterogeneous electron-transfer rate of species in ionic liquids, paying particular attention to the effect of size, or the hydrodynamic radius of species in theses solvents. Lagrost *et al.*[70,71] observed an effect of the hydrodynamic radius on the reorganisation of species in ionic liquids, however, more recent work shows that this is not the case. In the work carried out by Lagrost, ohmic drop and charging currents were not taken into account. The ohmic drop particularly in resistive solution would distort the voltammogram, accounting for experimental error observed above with respect to the aliphatic nitro-based compound. Further studies were carried out by Belding *et al.*[72] and Long *et al.*[73] to measure the kinetic parameters of species in a variety of ionic liquids.

Belding *et al.* carried out an extensive study of arenes and substituted anthracenes in various ionic liquids. Initially, the kinetic parameters of the species 9-phenylanthracene (9-PA) were examined in several ionic liquids at a microdisc platinum electrode using cyclic voltammetry for wave-shape analysis, and potential step chronoamperometry to calculate the diffusion coefficient of the species in the various RTILs. The merits of microelectrodes have already been discussed in Chapter 1, and it is known that the use of these electrodes substantially decreases ohmic drop and charging current. The k^0 value for 9-PA was calculated, and for each ionic liquid tested, showed no obvious relationship with hydrodynamic radius of the cations of the different ionic liquids. A variety of other anthracene species were also examined in one particular ionic liquid, and again the k^0 values calculated showed no dependence on the hydrodynamic radius of the species.

Further to this, Long *et al.* studied the electrochemistry of TMPD in several ionic liquids

using cyclic voltammetry and potential step chronoamperometry. From theoretical simulations, k^0 was calculated for TMPD in each ionic liquid. As expected, the k^0 value in ionic liquids was roughly one to two orders of magnitude higher in ionic liquids than for conventional solvents, but in contrast to previous studies, was found to be the same order of magnitude for TMPD in all ionic liquids, with a slight tendency to decrease with increasing viscosity due to slower diffusion. k^0 value were also calculated for several p-phenylenediamine-species in one ionic liquid, and no obvious relationship observed between k^0 and the calculated hydrodynamic radius, suggesting that the size of the analyte has no bearing on the heterogeneous electron-transfer rate in ionic liquids.

This newer data shows the effect of ohmic drop and the charging current on the elucidation of kinetic parameters in ionic liquids, and these factors must be taken into consideration when utilizing ionic liquids as solvents. In this thesis, microdisc electrodes have been used for all the experiments carried out, and thus the consideration of ohmic drop and charging currents are hugely diminished compared to those of macroelectrodes.

2.4.3 Double Layer Capacitance

The structure of the double layer of a solvent at the electrode-solvent interface is another important electrochemical property in ionic liquids. The variation of the double layer with potential can affect electrode processes. This effect is particularly significant when the concentration of the analyte species in the ionic liquid is low, so that the corresponding Faradaic current is low, causing the charging current to exert more significance. There are relatively few articles which deal with double layer studies in ionic liquids[45,74,75] and these suggest that ionic liquids possess double layer capacitances comparable to non-aqueous solvents with added supporting electrolyte.

Nanjundiah *et al*. carried out experiments to show relatively high double layer capacitance

values in some ionic liquids close to the point of zero charge (PZC) on mercury drop electrodes.[45] However, it was suggested that while similarities between ionic liquids and aqueous solvents at potentials close to the PZC exist, the Stern diffuse layer model[76,77] applied to aqueous systems is not suitable to describe the process in ionic liquids. Instead, a multi-layer model was proposed, in which alternating layers of cations and anions form in close proximity to the electrode to form layers of alternating positive and negative charge, in agreement with studies carried out on molten salts.[74] The excess charge on the ionic liquids can penetrate deeply into the liquid and is located several layers deep due to the close packing of ions.[74]

More recent studies show that maximum capacitance at the PZC is attainable if the ionic liquid is symmetrical, whereby the cations and anions are of similar size, and that as symmetry decreases, the capacitance curve becomes more complicated. Despite this, ionic liquids are still seen as suitable electrolytes in electrochemical double-layer capacitors due to thermal stability, wide electrochemical window, and high specific capacitance. However, the presence of impurities can significantly affect the structure of the double layer, and as with other properties, this makes it difficult to determine accurate capacitance values, so purity of the ionic liquids is of great importance.

2.5 Applications of RTILs

At least a million binary ionic liquids and 10^{18} ternary ionic liquids are potentially possible, compared to about 600 molecular solvents that are in use today.[78] This diversity at least, in principle, enables the solvent to be designed and tuned to optimize yield, selectivity, substrate solubility, product separation and even enantioselectivity. Therefore, it is no surprise that ionic liquids have found a plethora of applications in both academic research and industrial processes. A large range of water-stable ionic liquids allow for investigation of a greater variety of electrochemical processes and reduce the interference of side reactions. The electrochemical

behaviour of a select group of redox active compounds have been studied in ionic liquids and voltammetric responses have been compared to those seen already in more conventional solvents. Determination of diffusion coefficients in ionic liquids has consistently given values that are about 100 times smaller than in conventional solvents which is attributed to the higher viscosity of ionic liquids.

2.5.1 Ionic Liquids in Academic Research

A significant amount of work has been carried out observing the electrochemical behaviour of consistent redox systems such as metallocene derivatives.[1] The voltammetry of the Fc/Fc^+ couple is a good example of this, and in fact has been utilized as an internal redox reference system in ionic liquids.[2] The voltammetry of several aromatic compounds has also been examined in ionic liquids at a platinum electrode to elucidate thermodynamic and kinetic parameters to characterise the heterogeneous processes occurring.[1]

There are also applications for ionic liquids in organic synthesis. The ability of water-stable ionic liquids to dissolve a wide range of compounds while remaining immiscible with water enables their use as solvents in a number of organic synthetic reactions. One major application involves the use of organo-aluminate ionic liquids in reactions promoted by lewis acids where a mixture $AlCl_3$ and $[C_2mim][Cl]$ leads to an ionic liquid whose Lewis acidity is controlled by the amount of added $AlCl_3$.[79] This compound has been used as a solvent and Lewis catalyst for Friedel-Crafts acylations, alkylations, isomerations of alkanes and the alkylation of isobutane. Another application of ionic liquids in organic synthesis is their use as neutral solvents for use in the Diels-Alder reaction between cyclopentadiene and methyl acrylate. For many ionic liquids, Diels-Alder reactions led to significant rate enhancement, high yield and high selectivity.[79] Biphasic catalysis in ionic liquids is also attracting much attention since transition metal catalyst precursors are often soluble and stable in ionic liquids, whereas organic compounds

are either insoluble or easily separated by decantation, permitting the ionic liquid to be used again.

Ionic liquids provide an advantageous alternative to aqueous solvents due to their wide potential window allowing the electrodeposition of metals that are outside the potential range of aqueous solvents. The electrodeposition of copper has been carried out in $[C_2mim][BF_4]$ at platinum and tungsten electrodes.[1] While copper is not readily soluble in this ionic liquid, the addition of $[C_2mim][Cl]$ facilitated this dissolution. The electrodeposition of germanium has also been carried out for the investigation of semiconductors.

Ionic liquids can be considered to be polar solvents in most cases which makes them suitable for liquid-liquid extraction processes.[79] Partitioning data between some RTILs and water for organic solutes such as aniline, benzene and phthalic acid show a close correlation with that of the octanol-water system. RTILs have also shown reversible pH-dependent liquid-liquid partitioning which suggests them as potential replacements for toxic volatile organic compounds as solvents. RTILs can also be used to solubilize complex polar molecules such as cyclodextrins and glycopeptides and thus can be utilized as a stationary phase in gas chromatography (GC) where it acts as a low-polarity stationary phase to non-polar compounds, and a high-polarity stationary phase with strong proton donor groups.[79] Ionic liquids also possess other favourable properties of a stationary phase such as high viscosity and wetting ability.[80] Several groups have also reported using ionic liquids as mobile phase modifiers or running electrolytes to improve liquid chromatographic (LC) separations.[80]

A further use of ionic liquids in research involves the implementation of task-specific ionic liquids (TSILs) which are a sub-class of ionic liquids which possess utility beyond the scope of other ionic liquids.[19,81] By the incorporation of functional groups, these salts can act as catalysts and reagents in many processes such as synthesis, separations and electrochemical applications. Ionic liquids with viscosities much lower than currently used liquids are also being synthesised

for electrochemical applications.[82]

2.5.2 Ionic liquids in Industrial Applications

The favourable properties of ionic liquids have not gone unnoticed in the industrial world. Ionic liquids represent intrinsically excellent candidates for industrial applications compared to volatile organic solvents. Ionic liquids have been used as electrolytes in a variety of applications such as batteries, actuators, capacitors, fuel cells, solar cells, microelectrode sensors and electrosynthesis.[83] There is a very thorough publication by Plechkova *et al.* which outlines some major processes now underway by a variety of companies utilizing ionic liquids instead of conventional solvents.[58] I will outline two of these processes.

The BASIL^{TM} process is one of the most successful examples of the use of ionic liquid technology. BASIL^{TM} stands for Biphasic Acid Scavenging utilizing Ionic Liquids and is conducted by BASF. It is used for the production of the generic photoinitiator precursor alkoxyphenylphosphines. Originally, triethylamine was used to scavenge the acid that was formed in the course of the reaction, but it formed a dense insoluble paste making it difficult to handle. BASF replaced triethylamine with 1-methylimidazolium chloride which separates out of the reaction as a discrete phase. This new process has the advantages of being easy to handle, using a much smaller reactor, and increasing yield from 50% to 98%, as well as the ability to recycle the ionic liquid. This process is now carried out on a multi-ton scale proving that handling large quantities of ionic liquids is practical. BASF also utilize ionic liquids for breaking azeotropes, cellulose dissolution and aluminium plating.[58]

Another company, Degussa, is also developing ionic liquid technologies. They now use a new air product technology which is based on entrainment by the complexing of reactive gases in ionic liquids. It produces at least twice the performance of rival processes, which rely on the physical adsorption of gases on solids, and provides a method to deliver reactive and hazardous

gases in a safe and easily handled way, reducing risks and hazards in the workplace. The system is based on the Lewis acidity of basicity of the gases which are stored in Lewis base ionic liquids or Lewis acid ionic liquids respectively. This company also utilizes ionic liquids for processes involving paint additives, lithium ion batteries and pharmaceutical intermediates.

The publication by Plechkova *et al.* also documents a variety of other companies utilizing ionic liquids on a large scale in industrial processes.

2.5.3 Gas Sensing in Ionic Liquids

The most pertinent application of ionic liquids in this thesis is their use as electrolytes in gas sensors. The low volatility and thermal stability of RTILs render them advantageous media for the detection of gases and the development of stable and robust sensors.[1,17,84,85] Most conventional solvents cannot survive drastic temperature and pressure changes, therefore the lifetime of the sensor is limited by these factors. However ionic liquids remain physically and chemically unchanged within limits not possible for conventional solvents. The high viscosity of ionic liquids is a considerable drawback since this increases response time of a sensor, but modification of the sensor using a thin layer of ionic liquid can render these sensors comparable with the parameters of commercially available gas sensors.[17] Much work has been carried out constructing membrane-free gas sensors utilizing ionic liquids. Chapter 3 examines the development of gas sensors over the last few decades, and pays particular attention to the use of ionic liquids in gas sensing and the efforts to replace conventional solvents in practical gas sensors.

References

[1] Buzzeo, M. C.; Evans, R. G. and Compton, R. G., *ChemPhysChem*, 2004, **5**, 1106–1120.

[2] Rogers, E. I.; Silvester, D. S.; Poole, D. L.; Aldous, L.; Hardacre, C. and Compton, R. G., *J. Phys. Chem. C*, 2008, **112**, 2729–2735.

[3] Friere, M. G.; Santos, L. M. N. B. F.; Fernandes, A. M.; Coutinho, J. A. P. and Marrucho, I. M., *Fluid Phase Equilib.*, 2007, **261**, 449–454.

[4] Broder, T. L.; Silvester, D. S.; Aldous, L.; Hardacre, C. and Compton, R. G., *J. Phys. Chem. B*, 2007, **111**, 7778–7785.

[5] Ji, X.; Silvester, D. S.; Aldous, L.; Hardacre, C. and Compton, R. G., *J. Phys. Chem. C*, 2007, **111**, 9562–9572.

[6] Zhang, S.; Sun, N.; He, X.; Lu, X. and Zhang, X., *J. Phys. Chem. Ref. Data*, 2006, **35**(4), 1475–1517.

[7] Buzzeo, M. C.; Hardacre, C. and Compton, R. G., *ChemPhysChem*, 2006, **7**, 176–180.

[8] Jacquemin, J.; Husson, P.; Padua, A. A. H. and Majer, V., *Green Chem.*, 2006, **8**, 172–180.

[9] Kato, H.; Nishikawa, K. and Koga, Y., *J. Phys. Chem. B*, 2008, **112**, 2655–2660.

[10] Widegren, J. A.; Saurer, E. M.; Marsh, K. N. and Magee, J. W., *J. Chem. Thermodyn.*, 2005, **37**, 569–575.

[11] Silvester, D. S.; Aldous, L.; Hardacre, C. and Compton, R. G., *J. Phys. Chem. B*, 2007, **111**, 5000–5007.

[12] Wadhawan, J. D.; Schröder, U.; Neudeck, A.; Wilkins, S. J.; Compton, R. G.; Marken, F.; Consorti, C. S.; de Souza, R. F. and Dupont, J., *J. Electroanal. Chem.*, 2000, **493**, 75–83.

[13] Kakiuchi, T. and Tsujioka, N., *Electrochem. Commun.*, 2003, **5**, 253–256.

[14] Rozniecka, E.; Shul, G.; Sirieix-Plenet, J.; Gaillon, L. and Opallo, M., *Electrochem. Commun.*, 2005, **7**, 299–304.

[15] O' Mahony, A.; Silvester, D. S.; Aldous, L.; Hardacre, C. and Compton, R. G., *J. Phys. Chem. C*, 2008, **112**, 7725–7730.

[16] Wasserscheid, P. and Welton, T., Eds., *Ionic liquids in synthesis*, John Wiley and Sons, 2003.

[17] Shvedene, N.; Chernyshov, D. V. and Pletnev, I. V., *Russ. J. Gen. Chem.*, 2008, **78**, 2507–2520.

[18] Ignat′ev, N.; Welz-Biermann, U.; Kucheryna, A.; Bissky, G. and Willner, H., *J. Fluorine Chem.*, 2005, **126**, 1150–1159.

[19] Davis, J. H., J., *Chem. Lett.*, 2004, **33**, 1072–1077.

[20] http : //ildb.merck.de.

[21] Okoturo, O. O. and VanderNoot, T. J., *J. Electroanal. Chem.*, 2004, **568**, 167–181.

[22] MacFarlane, D. R.; Meakin, P.; Sun, J.; Amini, N. and Forsyth, M., *J. Phys. Chem. B*, 1999, **103**, 4164–4170.

[23] Bonhôte, P.; Dias, A.-P.; Papageorgiou, N.; Kalyanasundaram, K. and Grätzel, M., *Inorg. Chem.*, 1996, **35**, 1168–1178.

[24] Wang, Y.; Zaghib, K.; Guerfi, A.; Bazito, F. F.; Torresi, R. M. and Dahn, J., *Electrochim. Acta*, 2007, **52**, 6346–6352.

[25] Sun, J.; Forsyth, M. and MacFarlane, D., *J. Phys. Chem. B*, 1998, **102**(44), 8858–8864.

[26] MacFarlane, D. R.; Sun, J.; Golding, P.; Meakin, P. and Forsyth, M., *Electrochim. Acta*, 2000, **45**, 1271–1278.

[27] Seddon, K. R.; Stark, A. and Torres, M.-J., *ACS Symp. Ser.*, 2002, **819**, 34–39.

[28] Olivier-Bourbigou, H. Magna, L., *J. Mol. Catal. A*, 2002, **182183**, 419–437.

[29] Domanska, U. and Marciniak, A., *J. Chem. Eng. Data*, 2003, **48**(3), 451–456.

[30] Tokuda, H.; Hayamizu, K.; Ishii, K.; Susan, M. and Watanabe, M., *J. Phys. Chem. B*, 2005, **109**(13), 6103–6110.

[31] Huddleston, J. G.; Visser, A. E.; Reichert, W. M.; Willauer, H. D.; Broker, G. A. and Rogers, R. D., *Green Chem.*, 2001, **3**, 156–164.

[32] Tokuda, H.; Tsuzuki, S.; Susan, M.; Hayamizu, K. and Watanabe, M., *J. Phys. Chem. B*, 2006, **110**(39), 19593–19600.

[33] Lide, D. R., Ed., *Handbook of Chemistry and Physics: 76th Edition*, CRC Press, 1996.

[34] Weingartner, H.; Sasisanker, P.; Daguenet, C.; Dyson, P.; Krossing, I.; Slattery, J. and Schubert, T., *J. Phys. Chem. B*, 2007, **111**, 4775–4780.

[35] Wang, J.; Tian, Y.; Zhao, Y. and Zhuo, K., *Green Chem.*, 2003, **5**, 618–622.

[36] Endres, F. and Zein El Abedin, S., *PhysChemChemPhys*, 2006, **8**, 2101–2116.

[37] Fitchett, B. D.; Knepp, T. N. and Conboy, J. C., *J. Electrochem. Soc.*, 2004, **151**(7), E219–E225.

[38] McEwen, A. B.; Ngo, E. L.; LeCompte, K. and Goldman, J. L., *J. Electrochem. Soc.*, 1999, **146**, 1687–1695.

[39] Vogel, H., *Physik. Z.*, 1921, **22**, 645–646.

[40] Tammann, G., *Z. anorg. allgem. Chem.*, 1926, **158**, 1–16.

[41] Fulcher, G., *J. Am. Cer. Soc.*, 1925, **8**, 339–355.

[42] Hapiot, P. and Lagrost, C., *Chem. Rev.*, 2008, **108**, 2238–2264.

[43] Vila, J.; Varela, L. M. and Cabeza, O., *Electrochim. Acta*, 2007, **52**, 7413–7417.

[44] Endres, F.; MacFarlane, D. and Abbot, A., Eds., *Electrodeposition from Ionic liquids*, Wiley-VCH Verlag GmBH & Co. KGaA, 2008.

[45] Nanjundiah, C.; McDevitt, S. F. and Koch, V. R., *J. Electrochem. Soc.*, 1997, **144**, 3392–3397.

[46] Vila, L.; Gines, P.; Pico, J.; Franjo, C.; Jimenez, E.; Varela, L. and Cabeza, O., *Fluid Phase Equilib.*, 2006, **242**, 141–146.

[47] Gu, Z. and Brennecke, J., *J. Chem. Eng. Data*, 2002, **47**, 339–345.

[48] Dzyuba, S. V. and Bartsch, R. A., *ChemPhysChem*, 2002, **3**, 161–166.

[49] Fredlake, C.; Crosthwaite, J.; Hert, D.; Aki, S. and Brennecke, J., *J. Chem. Eng. Data*, 2004, **49**, 954–964.

[50] Krossing, I.; Slattery, J.; Daguenet, C.; Dyson, P.; Oleinikova, A. and Weingartner, H., *J. Am. Chem. Soc.*, 2006, **128**, 13427–13434.

[51] Silvester, D. S.; Rogers, E. I. and Compton, R. G., Wiley, 2008; chapter 13.2. in "Electrodeposition in Ionic Liquids".

[52] Wilkes, J. S., *J. Mol. Cat. A*, 2004, **214**, 11–17.

[53] Scammells, P. J.; Scott, J. L. and Singer, R. D., *Aust. J. Chem.*, 2005, **58**, 155–169.

[54] Kroon, M. C.; Buijs, W.; Peters, C. J. and Witkamp, G.-J., *Thermochim. Acta*, 2007, **465**, 40–47.

[55] Marsh, K. N.; Deev, A.; Wu, A. C.-T.; Tran, E. and Klamt, A., *Korean J. Chem. Eng.*, 2002, **19**, 357–362.

[56] MacFarlane, D. R. and Seddon, K. R., *Aust. J. Chem.*, 2007, **60**, 3–5.

[57] Galinski, M.; Lewandowski, A. and Stepnial, I., *Electrochim. Acta*, 2006, **51**, 5567–5580.

[58] Plechkova, N. V. and Seddon, K. R., *Chem. Soc. Rev.*, 2008, **37**, 123–150.

[59] Xue, H.; Verma, R. and Shreeve, J. M., *J. Fluorine Chem.*, 2006, **127**, 159–176.

[60] Schröder, U.; Wadhawan, J. D.; Compton, R. G.; Marken, F.; Suarez, P. A. Z.; Consorti, C. S.; de Souza, R. F. and Dupont, J., *New J. Chem.*, 2000, **24**, 1009–1015.

[61] Rogers, E. I.; Huang, X.-J.; Dickinson, E. J. F.; Hardacre, C. and Compton, R. G., *J. Phys. Chem. C*, 2009, **113**, 17811–17823.

[62] Barrosse-Antle, L.; Silvester, D. S.; Aldous, L.; Hardacre, C. and Compton, R. G., *J. Phys. Chem. C*, 2008, **112**, 3398–3404.

[63] Barnes, A. S.; Rogers, E. I.; Streeter, I.; Aldous, L. and Hardacre, C.and Compton, R. G., *J. Phys. Chem. B*, 2008, **112**, 7560–7565.

[64] Buzzeo, M. C.; Klymenko, O. V.; Wadhawan, J. D.; Hardacre, C.; Seddon, K. R. and Compton, R. G., *J. Phys. Chem. A*, 2003, **107**, 8872–8878.

[65] Evans, R. G.; Klymenko, O. V.; Price, P. D.; Davies, S. G.; Hardacre, C. and Compton, R. G., *ChemPhysChem*, 2005, **6**, 526–533.

[66] Rogers, E. I.; Silvester, D. S.; Jones, S. E. W.; Aldous, L.; Hardacre, C.; Russell, A. J.; Davies, S. G. and Compton, R. G., *J. Phys. Chem. C*, 2007, **111**, 13957–13966.

[67] Barnes, E. O.; O' Mahony, A. M.; Aldous, L.; Hardacre, C. and Compton, R. G., *J. Electroanal. Chem.*, 2010, **646**, 11–17.

[68] Shoup, D. and Szabo, A., *J. Electroanal. Chem.*, 1982, **140**, 237–245.

[69] Klymenko, O. V.; Evans, R. G.; Hardacre, C.; Svir, I. B. and Compton, R. G., *J. Electroanal. Chem.*, 2004, **571**, 211–221.

[70] Lagrost, C.; Carrié, D.; Vaultier, M. and Hapiot, P., *J. Phys. Chem. A*, 2003, **107**, 745–752.

[71] Lagrost, C.; Preda, L.; Volanschi, E. and Hapiot, P., *J. Electroanal. Chem.*, 2005, **585**, 1–7.

[72] Belding, S. R.; Rees, N. V.; Aldous, L.; Hardacre, C. and Compton, R. G., *J. Phys. Chem. C*, 2008, **112**, 1650–1657.

[73] Long, J.; Silvester, D. S.; Barnes, A. S.; Rees, N. V.; Aldous, L.; Hardacre, C. and Compton, R. G., *J. Phys. Chem. C*, 2008, **112**, 6993–7000.

[74] Graves, A. D. and Inman, D., *J. Electroanal. Chem. Interfacial Electrochem.*, 1970, **25**, 357–372.

[75] Ue, M.; Takeda, M.; Toriumi, A.; Kominato, A.; Hagiwara, R. and Ito, Y., *J. Electrochem. Soc.*, 2003, **150**, A499–A502.

[76] Bard, A. J. and Faulkner, L. R., *Electrochemical Methods: Fundamentals and Applications, 2nd ed.*, John Wiley and Sons: New York, 2001.

[77] Compton, R. G. and Banks, C. E., *Understanding Voltammetry*, World Scientific, 2007.

[78] Rogers, R. D. and Seddon, K. R., *Science*, 2003, **302**, 792–793.

[79] Dupont, J.; Consorti, C. S. and Spencer, J., *J. Braz. Chem. Soc.*, 2000, **11**, 337–344.

[80] Baker, G.; Baker, S. N.; Pandey, S. and Bright, F. V., *Analyst*, 2005, **130**, 800–808.

[81] Yoshizawa, M.; Narite, A. and Ohno, H., *Aust. J. Chem.*, 2004, **57**, 139–144.

[82] MacFarlane, D. R., *Aust. J. Chem.*, 2004, **57**, 111–112.

[83] Zhao, H., *Chem. Eng. Comm.*, 2006, **193**, 1660–1677.

[84] Pandey, S., *Anal. Chim. Acta*, 2006, **556**, 38–45.

[85] Silvester, D. S. and Compton, R. G., *Z. Phys. Chem.*, 2006, **220**, 1247–1274.

Chapter 3

Introduction to Gas Sensing.

3.1 A Brief History of Gas Sensing

Gas sensing has necessitated a significant body of work since the 1950s. Many reviews exist outlining different methods of gas sensing. Examples include electronic noses[1] which utilize conducting polymer arrays to predict human perception of odour for use in the food industry and environmental monitoring, chemiresistors[1,2] which utilize metal oxide-based semiconducting materials to detect carbon monoxide, methane, nitrogen dioxide and hydrogen sulfide, and others such as admittance sensors and optical sensors. The main type of gas sensors encountered in literature over the last 50 years utilize electrochemistry for detection[1–8] due to simplicity of set-up and the low cost associated with these sensors. Electrochemical gas sensors can be divided into two types, solid state electrolyte sensors which utilize potentiometric and amperometric techniques, and liquid state (protic and aprotic) electrolyte sensors which utilize voltammetric and potential step chronoamperometric techniques.

Sensors utilizing solid state electrolytes have mainly developed for used in the automotive industry for combustion control applications whereby they can withstand severe operating conditions and offer long-term stability, reliability and low cost.[6] These solid-state sensors are based on zirconia materials including ZrO_2, TiO_2 and SnO_2. These materials are doped with other oxides, and the corresponding sensors are designed as ceramic gas sensors. The properties of this zirconia species originate from the dopant (eg. Y_2O_3). In the solid solution of ZrO_2 and Y_2O_3, some Zr^{4+} ions are replaced by lower valency Y^{3+} so vacancies are created and ions can move in solid mixture, therefore the zirconia acts like a solid electrolyte which shows a change in conductivity when exposed to oxidizing or reducing gases. The advantages of these sensors

include robustness as they are completely solid state, as well as being lightweight and low cost. These are used to detect gases such as O_2, CO, NO_χ, SO_2 and H_2S. With more stringent pollution measures within the automotive industry, sensors such as these are necessary for detection of regulated and toxic industrial chemicals in the ppm to the ppb range. However, disadvantages to these sensors include restricted possibilities to distinguish between different gases.

The use of amperometry in solid state electrolyte sensors can overcome this lack of selectivity for different gases. A separation of different electrode reactions can be achieved with an externally applied voltage since the rates and directions of different electrochemical reactions depend strongly on the electrode potential, and this allows the detection of potentially separate components. Göpel *et al*. outlined how voltammetric methods can be used for simultaneous determination of O_2 and NO_χ gases by adjusting electrode geometry and working parameters in such a way that at the electrode only one process is taking place at any one time.[5] To increase selectivity, one sensor can contain several electrodes which are separated from the gas phase by the same solid state electrolyte so that the gas phase composition may be changed in a controlled way from one electrode to the next which results in high selectivities at individual electrodes. Therefore, single electrode amperometric sensors allow monitoring of several gases but only in periodic operation modes, whereas multi-electrode amperometric devices give fast responses and high selectivity allowing electrochemical filtering.

The other main type of gas sensor mentioned above is the liquid state electrolyte gas sensor which generally utilizes voltammetric and potential step chronoamperometric techniques. Probably two of the most well-known gas sensors in the last fifty years are the Clark cell for measuring oxygen in respiratory gas,[9] and the Stow and Severinghaus cell, for measuring carbon dioxide also in respiratory gas.[10,11] The history of these two sensors have been competently reviewed by Hahn in two separate publications,[3,4] and some of the points outlined in these works will be summarized here.

The basis of both of these sensors is to examine respiratory gas. Both inspiratory and expiratory gas exchange efficiency are reflected in blood gas measurements, the two gases of fundamental importance are oxygen and carbon dioxide. Therefore accurate, stable and reproducible blood gas sensors are needed in clinical practice. The traditional sensors developed for detection of these gases consists of two electrodes, liquid supporting electrolyte, and a polymer membrane to allow gas exchange between sample and electrolyte and avoid electrode fouling. Measurements are made voltammetrically where a potential is applied and faradaic current flows between the working and reference/counter electrode. This faradaic current is a function of the gas concentration. The electrolyte solution is typically an aqueous buffer solution with a neutral pH value.

The oxygen sensor was first described by Clark in a patent application.[9] Although the idea of isolating the cathode and anode behind a membrane to protect them from protein poisoning has been traditionally attributed to Clark, the idea actually came from Stow and co-workers in 1954.[10] This resulted in Clarks patent application being ruled invalid, despite the fact that his was the first design of oxygen sensor for use in whole blood. However the Clark sensor was still the most widely used sensor for clinical oxygen determination for forty years. The simplified reaction scheme for this sensor has been described by Hahn:[4]

$$O_2 + H_2O + 2e^- \rightarrow HO_2{}^- + OH^- \tag{3.1}$$

$$HO_2{}^- + H_2O + 2e^- \rightarrow 3OH^- \tag{3.2}$$

$$HO_2{}^- \overset{cat.\ \ decomp.}{\rightarrow} \frac{1}{2}O_2 + OH^- \tag{3.3}$$

where the $HO_2{}^-$ ion is either reduced to OH^-, catalytically converted back to oxygen, or transported into bulk solution. The amount of $HO_2{}^-$ decreases as voltage increases negatively. A Clark cell is shown in Figure 3.1.

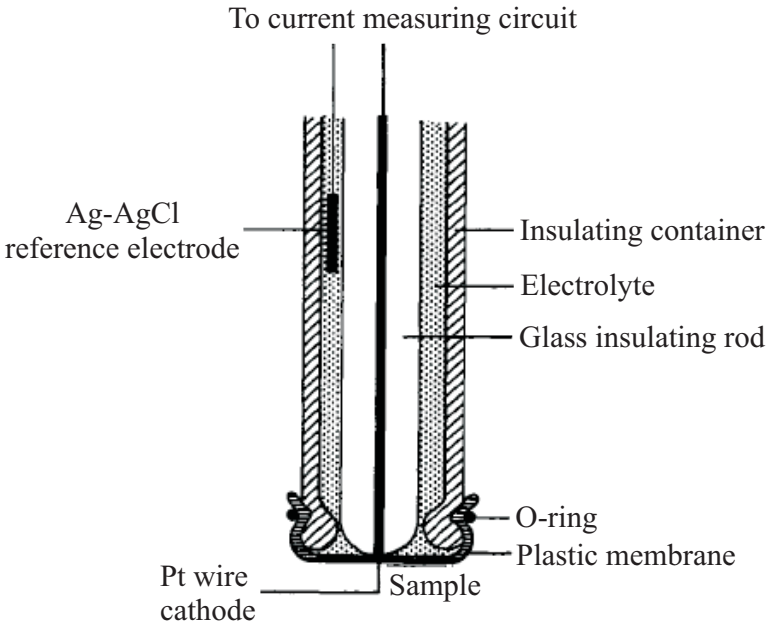


Figure 3.1: A schematic of a practical Clark cell (from Hahn 1987[3]).

The other major gas sensor mentioned above which has been developing over the last fifty years is the CO_2 sensor. The initial drive to push for the fabrication of this sensor in the fifties is said to be due to a polio epidemic that broke out in the United State of America, when the need for artificial ventilation was widespread.[3] It was vital to assess the effectiveness of artificial ventilation and this was achieved by various measurements of CO_2 in blood-gas at body temperature. The most effective sensor was proposed by Stow[10] who reported that a CO_2 sensor could be made by covering a pH electrode and a reference electrode with a rubber membrane over a thin layer of distilled water. Stow was the first to house both working and reference electrode behind a membrane. However, since this initial electrode was potentiometric, it was not stable to changes in pH of distilled water. This issue was rectified by Severinghaus[11] with the addition of a buffer (sodium bicarbonate). When CO_2 diffuses through the membrane

into the bicarbonate (electrolyte) solution, the equilibria in the system in the steady state are:

$$CO_2 + H_2O \rightleftharpoons H_2CO_3 \rightleftharpoons H^+ + HCO_3{}^- \tag{3.4}$$

A change in levels of CO_2 results in a change in pH and this corresponds to a potentiometric voltage change. The disadvantage to this measurement is the length of time it takes (*ca.* 60 s), and it cannot be used to simultaneously measure oxygen and carbon dioxide. Therefore, a large body of work exists attempting to improve detection of oxygen and carbon dioxide, achieve simultaneous detection of both species, and study the effect of different electrodes and electrolytes on the detection of these gases.

The work described above on a sensor for oxygen and carbon dioxide, paved the way for the fabrication of electrochemical sensors to detect other gases. This is a growing concern due to the tightening of regulations of gas emissions in all industries, and in the effort to understand the clinical aspects of these gases. In the next five sections of this Chapter, I will give some examples of the studies and advances of sensor fabrication for the following gases: oxygen, carbon dioxide, hydrogen, ammonia, sulfur dioxide and hydrogen sulfide. The presence of these gases has implications in medicine, industry, the environment and advances in technology.

3.2 Sensors for Detection of Oxygen and Carbon Dioxide

There is a wide selection of literature for the detection of oxygen and carbon dioxide, mainly for clinical reasons.[12–19] These works mainly focus on the simultaneous detection of oxygen and carbon dioxide, as well as other anaesthetic gases. The following will outline some chronological advances in this field with respect to advances in electrodes and electrolytes.

By the mid-sixties, the effect of solvent in the Clark cell for detection of oxygen had not yet been widely evaluated. Due to the reduction products of oxygen being either peroxide or water, the protic nature of the solvent would have significant influence on the electrochemical behaviour. Therefore, the electrochemistry of oxygen and its reduction product, superoxide, was investigated at several electrodes in DMSO.[12] This solvent provides an aprotic system that is different from the traditional aqueous system and provides a means of studying the effect of electrode material on the reduction of oxygen. The reduction of oxygen was carried out in DMSO with supporting electrolyte at both platinum and mercury electrodes. At the platinum electrode a single reduction signal was observed as well as a shoulder peak on the reductive signal for the solvent. At the mercury electrode however, two distinct reduction signals were observed. These signals were examined using chronoamperometry which showed that each step was a one-electron reduction and that the process was diffusion controlled. Sawyer *et al.*[12] summarized this voltammetry in the following scheme:

$$O_2 + e^- \rightarrow {O_2}^- \tag{3.5}$$

$${O_2}^- + e^- \rightarrow {O_2}^{2-} \tag{3.6}$$

This was one of the first observations of oxygen voltammetry in aprotic solvents, which eliminated further reaction due to protons. This also led to further work examining the effect of water on oxygen reduction.

In 1969, Fujinaga *et al*. examined the solubility and polarographic behaviour of oxygen in air-saturated DMSO with varying amounts of water.[13] They observed that the first one-electron reduction wave corresponding to formation of superoxide in DMSO solution, changed to a two-electron process with the addition of water due to protonation. The rate of protonation was potential-dependent and also dependent on the concentration of supporting electrolyte. They also calculated the diffusion coefficients of oxygen in mixed DMSO-water solvent using the solubility and polarographic data obtained.

Another observation of the electrochemical behaviour of oxygen in aprotic solvents was the adsorption of molecular oxygen on alloys of mercury with platinum, gold, iridium and rhodium from solutions in MeCN, DMF and DMSO.[14]

In 1982, a new type of membrane electrode for the determination of carbon dioxide in DMSO where its concentration was determined amperometrically was described by Albery *et al*.[15] They observed that the electrochemical reduction of carbon dioxide was a more direct method than that used in current carbon dioxide electrodes outlined previously by Stow and Severinghaus[10,11] which rely on effect of CO_2 on pH. The mechanism is as follows:

$$2CO_2 + 2e^- \rightarrow {C_2O_4}^{2-} \tag{3.7}$$

$$2CO_2 + 2e^- \rightarrow CO + {CO_3}^{2-} \tag{3.8}$$

The first problem encountered with this method was that oxygen reduces more easily at the electrode than CO_2 and thus interfered with the measurement. However, they used a metallised membrane as an electrochemical filter for removal of O_2, allowing the CO_2 to pass through. Furthermore, the O_2 current on the metallised membrane could be measured and was proportional to the concentration of O_2 and thus it was possible to construct a membrane electrode of the Clark type which measures both O_2 and CO_2.

This work has augmented in recent years to improve the simultaneous detection of O_2, CO_2 as well as include simultaneous detection of N_2O, an anaesthetic gas which could potentially interfere with detection of the former two gases. In a large body of work that spans ten years, in five parts, Hahn *et al.* have presented the simultaneous detection of the three gases at microelectrodes in aprotic solvents.[16,17,20–22] They begin by presenting work on a practical sensor which is developed to measure O_2 and CO_2 simultaneously in medical applications and operates well in the presence of anaesthetic agents at gold microdisc cathodes in DMSO in the ranges commonly found in medical practice. They use steady-state voltammetry to achieve this simultaneous detection whereby both gases are always present in analysed samples, and the O_2 reduction product (O_2^-) does not react with CO_2 or any other reaction products as there is insufficient time under steady state conditions prevailing at microelectrodes for these reactions to take place homogeneously near the electrode surface.

The work culminates in the use of potential step chronoamperometry techniques which remove any deleterious cross-interference reactions when N_2O is added to the mixture. Chronoamperometric studies in DMSO yield the following observations: (i) reductive signals are enhanced for CO_2 and N_2O with stepwise addition of oxygen; (ii) reductive signals are enhanced for O_2 with stepwise addition of CO_2; (iii) no significant change was observed for limiting current of N_2O with increase of CO_2 concentrations; (iv) CO_2 reductive signal shifts initially with the presence of N_2O, but increasing CO_2 concentration causes the signal to shift back to the former position; (v) no signal enhancements are observed for O_2 with the addition of N_2O, indicating no cross-interference between those species. Therefore, simple algorithms are employed to determine the concentrations of both CO_2 and N_2O from several chronoamperometric transients.

Finally, some work has been carried out by Compton *et al.*, building on previous literature, to theoretically model the electrochemical behaviour of O_2 and CO_2 in aprotic solvents at microdisc electrodes. This begins with the electroreduction of CO_2 in DMSO at a gold micro-

electrode using linear sweep voltammetry and cyclic voltammetry.[18] Previous literature shows the electroreduction to follow the mechanism outlined in Equations 3.7 and 3.8. The mechanism proposed by Compton *et al*. for CO_2 reduction in DMSO is as follows:

$$CO_2(\text{bulk}) \overset{k_d}{\rightarrow} CO_2(\text{surface}) \overset{k_1}{\rightarrow} {CO_2}^{\bullet -}(ads) + CO_2 \overset{k_2,slow}{\rightarrow} {CO_2}^{2-} \overset{e^-,fast}{\rightarrow} \text{products} \qquad (3.9)$$

where k_d is the rate of diffusion, and k_1 and k_2 are the rates of the follow up reactions. This mechanism shows that the rate determining step is the reaction of ${CO_2}^{\bullet -}$ with CO_2. The numerical simulation of the experimental voltammograms permit the extraction of kinetic data such as the charge transfer coefficient.

Section 3.1 and this section show the evolution of gas sensing over the last fifty years, and are a good indication of the process by which advances are made. These two previous sections have paid particular attention to the evolution of gas sensors for O_2 and CO_2, since a large body of work exists outlining these gas sensors, and thus the evolution of gas sensing is best illustrated by these particular gases, as well as the fact that subsequent electrochemical gas sensors are based on these models. We next examine work carried out using room temperature ionic liquids as electrolytes in O_2 and CO_2 gas sensing.

3.2.1 Detection of Oxygen and Carbon Dioxide in Room Temperature Ionic Liquids

The continued research on O_2 and CO_2 in various solvents continued, but for other reasons than clinical or combustive ones. The selective oxidation of compounds has become important in manufacturing chemicals. Typically these reactions are conducted at high temperatures with the use of catalysts, but with increased environmental awareness, greener alternatives are called for. Therefore, the exploration of chemical synthesis by electrochemical means has been investigated.

One important reaction in this research is the generation of the superoxide ion ($O_2^{\bullet -}$) in different solvents.[23] This section looks at this process in room temperature ionic liquids.

The detection of oxygen in ionic liquids began in 1990 when Carter *et al.* reported the voltammetric behaviour of dioxygen in a basic, room-temperature chloroaluminate molten salt, 1-ethyl-3-methylimidazolium chloride mixed with $AlCl_3$.[24] The attributes and advantages of using RTILs are already discussed in Chapter 2, and thus will not be repeated in this section. Suffice to say, much interest has arisen in their use in recent years. Carter *et al.* used cyclic staircase voltammetry (CSV) at a glassy-carbon (GC) disc electrode to observe the reduction of O_2 in this ionic liquid. They observed a signal reduction wave within a specified voltammetric window for a range of sweep rates, and that transport of O_2 in the system was diffusion controlled, but that some adsorption of O_2 was occurring at the GC electrode surface which caused passivation of the electrode following continuous voltammetric cycling. They concluded that the working electrode surface was passivated by both formation of insulating products at the surface during cycling, and the slow oxidation of the electrode surface at open circuit. Thus, stable superoxide formation was not achieved at this juncture preventing the use of superoxide as a reagent in further reactions.

About ten years later, AlNashef *et al.* presented work showing that the superoxide ion could be generated via a one-electron electrochemical reduction (see Equation 3.5, Section 3.2) in ionic liquids using CV in the absence of impurities, and that this ion was stable. These experiments were carried out in both MeCN, and the ionic liquid $[C_4mim][PF_6]$.[25] They observed a reduction peak in the presence of oxygen, and a corresponding oxidation peak, which showed a chemically reversible reaction, and that this solvent was capable of supporting the electrochemical generation of a stable superoxide ion. The peak currents were proportional to the square root of the scan rate showing that the process was diffusion controlled.

This group also carried out work observing the activation of CO_2 by the superoxide ion

in RTILs as a possible route to electrochemical production of chemicals. It was shown that at increased partial pressures of both O_2 and CO_2, the electrochemical generation of both is increased. In the case of CO_2, at increased partial pressure, the reaction rate increased shown by an increase in the reduction signal, but in the presence of $O_2^{\bullet -}$, the oxidation signal of reduced CO_2 decreased. This suggests that the electrochemically generated superoxide ion in the RTIL is stable and reacts with CO_2 to possibly yield a carboxylating agent. This development is promising in the area of chemical synthesis, and showcases well the advantages of using RTILs as solvents for these processes.

Of course, these observed advantages of the use of RTILs for electrochemical reduction of O_2 and CO_2 did not go unnoticed for those wanting to fabricate an O_2 sensor. The Compton group has carried out a large body of work investigating the properties and possibilities of electrochemistry of O_2 and CO_2 in RTILs.[26–32] The electrochemical reduction of O_2 was investigated in a series of RTILs at platinum and gold electrodes.[26,27] The aim of the study was to carry out a comprehensive investigation of the electro-generation of stable superoxide in various RTILs and characterize the heterogeneous kinetics for this process. Chronoamperometry allowed for the determination of the diffusion coefficient of O_2, as well as the diffusion coefficient of the electrogenerated superoxide, and these values for various RTILs at various electrode materials are presented in Table 3.1.

In Table 3.1, the values for diffusion coefficient (D) and concentration (c) for O_2 and $O_2^{\bullet -}$ are presented for two different RTILs. The higher viscosity of $[N_{6,2,2,2}][NTf_2]$ compared to $[C_2mim][NTf_2]$ due to structural variation in the cationic components results in significantly different diffusion coefficients of oxygen and superoxide.

Table 3.1: Comparison of the diffusion coefficients of O_2 and $O_2^{\cdot -}$ in two different RTILs at a gold microdisc electrode at 293 (± 3) K.

RTIL	D_{oxygen}	$D_{\text{superoxide}}$
[Emim][NTf_2]	7.3×10^{-10} m^2 s^{-1}	2.7×10^{-10} m^2 s^{-1}
[$N_{6,2,2,2}$][NTf_2]	1.5×10^{-10} m^2 s^{-1}	4.7×10^{-12} m^2 s^{-1}

Evans *et al.* took this work further to examine the the behaviour of O_2 and $O_2^{\bullet -}$ in both quaternary ammonium RTILs, similar to [$N_{6,2,2,2}$][NTf_2] shown in Table 3.1, and quaternary phophonium ions (for structure, see Chapter 4). The reduction of O_2 proceeded reversibly via the loss of one-electron to yield the superoxide radical in quaternary ammonium RTILs which was stable and values for diffusion coefficients were comparable to those in Table 3.1. However in the quaternery phosphonium RTILs, the presence of the weakly acidic phosphonium ion rendered superoxide unstable, and behaviour intermediate between one-electron reduction of O_2 in aprotic solvents and two-electron process observed in aqueous solution was observed. Therefore, studies of the electrochemistry of O_2 in RTILs continued in those that allowed for the stable formation of the superoxide radical.

Further studies outline the electrochemistry of O_2 in RTILs at different temperatures, specifically focusing on diffusion coefficients. As already mentioned in Chapter 2, the viscosity of RTILs alters with temperature, and this in turn alters the diffusion coefficient of the species in the RTIL. In order to fabricate a practical sensor for O_2 in RTILs, using chronoamperometry to find the concentration of the analyte, there must be a basis for predicting the diffusion coefficient within a range of temperatures.[28,29] Table 3.2 presents diffusion coefficients and solubilities for the reduction of oxygen under different temperatures using potential-step chronoamperometry in six RTIL solvents. An approximate relationship was observed when analyzed in terms of the Stokes-Einstein equation in all RTILs. This data can be useful for calculating concentration of O_2 in a practical gas sensor, as the chronoamperometric technique yields the concentration of the gas, and if diffusion coefficient at the atmospheric temperature is known, then that concentration

value becomes more accurate.

Table 3.2: Viscosity (cP), diffusion coefficient ($\times 10^{-10}$ m^2 s^{-1}) and solubility (mM) from Shoup and Szabo[33] analysis of potential step chronoamperometry for the reduction of O_2 at varying temperatures on Au microdisc.

RTIL		293 K	298 K	303 K	308 K	313 K	318 K
$[C_4mim][NTf_2]$	η	52	47	41	34	29	-
	D	7.95	8.76	10.44	11.77	13.41	15.88
	c	2.7	3.1	2.9	2.9	2.9	2.7
$[C_4mpyrr][NTf_2]$	η	89	70	64	54	46	-
	D	4.60	5.49	6.38	7.41	8.66	9.36
	c	3.7	3.6	3.7	3.7	3.6	3.8
$[C_4dmim][NTf_2]$	η	105	88	73	61	52	-
	D	4.30	5.05	5.74	6.79	8.27	8.95
	c	3.4	3.6	3.7	3.7	3.6	3.8
$[C_4mim][BF_4]$	η	112	92	78	65	56	-
	D	1.26	1.79	2.21	2.29	2.91	3.29
	c	4.9	4.1	4.1	4.5	4.0	4.2
$[C_4mim][PF_6]$	η	201	173	149	127	109	-
	D	1.78	2.50	2.98	3.54	4.49	5.97
	c	2.8	3.0	3.0	2.7	2.4	2.8
$[N_{6,2,2,2}][NTf_2]$	η	252	192	149	116	92	73
	D	4.25	4.55	5.29	6.00	7.02	7.98
	c	3.9	3.9	3.9	3.8	3.7	3.9

Observations of CO_2 in RTILs has not been as well documented as that of O_2. However, studies have been carried out with respect to reduction of CO_2 in RTILs and have yielded some interesting results. Previously in this section, the interaction of CO_2 with $O_2^{\bullet -}$ was observed in RTILs, and this reaction increased with increasing partial pressure. AlNashef *et al.* postulated that this interaction may yield a carboxylating agent.[23] Buzzeo *et al.* explored this reaction further. They observed the reduction of O_2 in the presence of CO_2 by cyclic voltammetry at a gold microdisc electrode in two RTILs. Cyclic voltammetry of O_2 showed an increase in the reductive wave and the diminishing of the oxidative wave in the presence of CO_2, indicating

that the generated superoxide rapidly reacts with carbon dioxide. The kinetics of the reaction between the $O_2^{\bullet-}$ and the CO_2 were investigated, and best-fit simulation was used to suggest the mechanism below:

$$2O_2 + 2e^- \rightarrow 2{O_2}^{\bullet-} \tag{3.10}$$

$$2{O_2}^{\bullet-} + CO_2 \overset{k,slow}{\rightarrow} {CO_4}^{\bullet-} \tag{3.11}$$

$${CO_4}^{\bullet-} + CO_2 \rightarrow {C_2O_6}^{\bullet-} \tag{3.12}$$

$${C_2O_6}^{\bullet-} + {O_2}^{\bullet-} \rightarrow {C_2O_6}^{2-} + O_2 \tag{3.13}$$

The elucidation of the mechanism may assist the synthesis of chemicals in the future using the stable superoxide ion. Other studies of CO_2 in RTILs explore the interaction of CO_2 with RTILs. Barrosse-Antle showed that gaseous CO_2 is almost irreversibly absorbed by the RTIL $[C_4mim][Ac]$ (where $[Ac]^-$ = acetate) in which it undergoes a chemically irreversible reduction suggesting a means for removal of CO_2 from greenhouse gases.[31] The same author showed the the introduction of CO_2 into RTILs can alter the viscosity of the solvent, making it less viscous, due to the solubility of the CO_2 in the solvent.[32]

In conclusion, the last three sections have taken us on a journey of gas sensing for O_2 and CO_2, in a variety of media, at a variety of surfaces, for a variety of reasons, and have illustrated the evolution of gas sensing over the last fifty years. The next four sections will briefly outline methods of gas sensing for other targets, and will finish with an outline of sensing H_2S, which is the target analyte in this work.

3.3 Sensors for Detection of Ammonia

The necessity to fabricate a gas sensor for ammonia stems from clinical, industrial, domestic and environmental applications. Medical application of ammonia detection include detection in the breath of patients indicating liver disease,[34] as well as presence of ammonia in blood for monitoring of renal control.[35] Industrial and environmental issues with ammonia frequently go hand in hand. Ammonia is often found in waste waters discharged from a variety of industrial and agricultural activities.[36] It can be formed from the biodegradation of organic nitrogen species which are found in sewage and fertilizers, and have adverse effects on oxygen balance in the aquatic environment. Ammonia is also a target gas in applications like leakage control in refrigeration systems and air conditioners. It also forms and stabilizes ambient polluting aerosols.

The use of flow cells using membrane electrodes for detection of ammonia has been quite popular. Meyerhoff *et al.*[35] have described the development of a simple, accurate and sensitive flow injection analysis system for the determination of ammonia using potentiometry. They utilized a tubular flow-through ion-selective polymer membrane electrode to detect the concentration of ammonium ions formed in the internal electrolyte buffer stream as the sample is passed through a gas dialyzer. The potentiometric peak heights were recorded and found to increase with increasing concentration of ammonia. This system was optimized for the analysis of blood samples, and was found to be sensitive, reproducible and inexpensive.

Another flow injection method for detection of ammonia was described by Van Son *et al.* using spectrophotometry.[37] This flow injection method allowed ammonia to diffuse through a gas-permeable membrane, causing an absorbance change of an acid-base indicator solution (bromothymol blue). The resulting absorbance change was measured spectrophotometrically in a flow-through cell and the response was found to be linear in the concentration range examined. This particular sensor was used to test total ammonia concentration in canal-water in

Amsterdam and was found to be sensitive, selective and robust.

An advancement was made on this work using this type of sensor in work describing a flow-through system using pH ion-sensitive field-effect transistor.[38] This type of sensor was based on semiconductors which replaced the spectrophotometric detection system, and thus allows miniaturization of this sensor. It operates by converting ammonium to ammonia which diffuses through a microporous hydrophobic membrane into an ammonium chloride recipient stream forming a pH buffer which is monitored by the semiconductor detector. A linear response to concentration of ammonia was achieved and this system was implemented to analyse samples of the Llobregat river in Catalonia, Spain.

While the above monitoring of ammonia has involved a regular collection of samples which are taken to the laboratory for analysis, Andrew *et al*. developed an automated technique for on-line analysis using again, flow injection methods. Their method utilizes the diffusion of gaseous ammonia from an alkaline sample stream, through a microporous membrane into bromothymol blue indicator stream, with the resulting colour change measured photometrically using an LED, similar to the Van Son method[37] mentioned above. The monitor had a linear response to ammonia and was tolerant of acidic samples. The stability of the monitor was demonstrated over an eight day period of continuous operation in the laboratory, and actual on-line results showed good correlation with laboratory analysis.

The amperometric detection of ammonia has been recently popular at various electrode surfaces such as single-walled carbon nanotubes,[39] multiwalled carbon nanotubes[40] and more conventional materials such as glassy carbon, boron-doped diamond, and graphite electrodes.[34]

Zhang *et al*. presented a fabrication method to make a chemical gas sensor using single walled carbon nanotubes (SWCNTs) electrochemically functionalized with polyaniline (PANI).[39] This sensor was tested for on-line monitoring of ammonia gas using cyclic voltammetry. The fabrication method allows the creation of arrays of individually addressable sensors, each functionalized

with a different substance (than PANI), and thereby displaying different sensor characteristics. For ammonia sensing, the results showed superior sensitivity to SWCNT gas sensors previously tested, as well as good reproducibility upon repeated exposure to ammonia.

The use of multi-walled carbon nanotubes (MWCNTs) was also explored as a sensor for ammonia.[40] Ji *et al*. showed that, while attempting to detect ammonia at a basal plane pyrolytic graphite electrode in propylene carbonate, intercalation occurred between the electrode and electrolyte. However, when the surface was modified with MWCNTs, quantitative voltammetric responses were observed for the oxidation of ammonia. The same group also observed the direct oxidation of ammonia at the glassy carbon electrode in propylene carbonate, and presented useful analytical voltammetric responses for the electrochemical oxidation of ammonia showing the glassy carbon electrode to be a near-optimal choice for electrode substrate for an ammonia gas sensor.[34] The group also presented a mechanism for the electrochemical oxidation of ammonia. The suggested that it occurs as an ECE mechanism (discussed in Chapter 1):

$$E : 4\mathrm{NH_3} + 3\mathrm{e^-} \rightarrow 3{\mathrm{NH_4}}^+ + \frac{1}{2}\mathrm{N_2(g)} \tag{3.14}$$

$$C : {\mathrm{NH_4}}^+ \rightleftharpoons \mathrm{NH_3} + \mathrm{H^+} \tag{3.15}$$

$$E : \mathrm{H^+} + \mathrm{e^-} \rightarrow \frac{1}{2}\mathrm{H_2(g)} \tag{3.16}$$

As with O_2 and CO_2, a new breed of electrolyte known for favourable properties, as well as selective reactions based on identity of component ions, RTILs, have also been tested as electrolytes for ammonia detection.

3.3.1 Electrochemical detection of ammonia in RTILs

The employment of non-aqueous solvents for electrochemical investigation offers the advantages of wider electrochemical window and good solubility. In particular, room temperature ionic

liquids (RTILs) possess these traits as well as others (see Chapter 2) which render them ideal for use as solvents in electrochemical gas sensing.

The fabrication of a gas sensor for ammonia in various solvents at various surfaces, has been discussed in Section 3.3. This section will outline some of the work carried out in detecting ammonia in RTILs.

The direct electrochemical oxidation of ammonia has been examined previously in propylene carbonate at a glassy carbon electrode.[40] Buzzeo *et al.*[41] examined the direct oxidation of ammonia in both organic solvent DMF and the RTIL $[C_2mim][NTf_2]$. The corresponding voltammetric responses were shown to be similar in both solvents and a linear response of the limiting current against the concentration of ammonia was observed in both solvents. Analysis of the voltammetric response at a platinum microdisc electrode yielded a mechanism already observed for the oxidation of ammonia at the glassy carbon electrode in propylene carbonate outlined in Section 3.3 in eqns 3.14, 3.15 and 3.16. The linear response to concentration of the analyte demonstrates a possible analytical utility of the approach.

This work was continued by Giovanelli *et al.*[42] who presented a novel methodology for the electrochemical determination of ammonia, based on its interaction with hydroquinone (QH_2) in both DMF, and $[C_2mim][NTf_2]$. It showed that ammonia reversibly removes protons from the hydroquinone molecules which allows an oxidative process that yields a new wave at less positive potentials that can be used to fingerprint, and quantify ammonia. The behaviour was explained as follows:

$$QH_2 + 2NH_3 \rightleftharpoons 2NH_4{}^+ + Q^{2-} \tag{3.17}$$

$$Q^{2-} \rightleftharpoons Q + 2e^- \tag{3.18}$$

where ammonia acts as as a proton acceptor, drawing off protons from the hydroquinone

molecules to form the more energetically favourable ammonium ions. Upon the addition of ammonia to the hydroquinone, the voltammetry shows a new wave attributed to the oxidation of the deprotonated hydroquinone. Analysis of this wave shows a linear response with concentration of ammonia, thereby demonstrating the analytical utility of this approach. Favourable limits of detection were achieved, and the signal appears at a lower potential thus decreasing the number of possible electrochemical interferents. This reaction was further investigated mechanistically[43] at the glassy carbon electrode in propylene carbonate to elucidate various kinetic parameters of the reaction, and thus increase understanding of the process.

Finally, a detailed study was carried out by Ji *et al.*[44,45] to study the mechanism of the oxidation of ammonia in several RTILs with different anions, namely, $[C_4mim][BF_4]$, $[C_4mim][OTf]$, $[C_2mim][NTf_2]$ and $[C_4mim][PF_6]$. The cyclic voltammetry obtained allowed the proposal of a revised mechanism for ammonia oxidation in RTILs to Equations 3.14, 3.15 and 3.16 presented in Section 3.3 and mentioned above. This work has also helped to define a pK_a scale in ionic liquids and furthered work in analytical sensing of ammonia. The revised mechanism is as follows:

$$NH_3(g) + 2A^- \rightarrow \frac{1}{2}N_2(g) + 3HA + 3e^- \tag{3.19}$$

$$HA + NH_3(g) \rightleftharpoons {NH_4}^+ + A^- \tag{3.20}$$

$$HA + e^- \overset{rds}{\rightarrow} A^- + Pt(H) \rightarrow A^- + \frac{1}{2}H_2(g) \tag{3.21}$$

$${NH_4}^+ + e^- \overset{rds}{\rightarrow} NH_3 + Pt(H) \rightarrow NH_3 + \frac{1}{2}H_2(g) \tag{3.22}$$

where A^- = the unprotonated anion(s) which is formed first, followed by ${NH_4}^+$. This is valid in four of the RTILs, except for $[PF_6]^-$ where ${NH_4}^+$ is formed first. In all cases, the protonated anions, HA, and ammonium ion, ${NH_4}^+$ are thought to be in equilibrium and the position of

equilibrium can be altered by changing the nature of the RTIL anion. This work shows the tuneability and selectivity of RTILs in electrochemical reactions, and has implications for the use of RTILs in gas sensing.

3.4 Sensors for Detection of Hydrogen

Molecular hydrogen is an important species in the fields of fuel combustion, electrochemical cells, and as a hydrogenation agent for industrial processes and organic synthesis. For these reasons, the electrochemical properties of hydrogen need to be established. Particularly with the newer use of hydrogen as a fuel, sensors for the detection of hydrogen are important.

The electrochemical oxidation of hydrogen has been studied on platinum and palladium surfaces in protic solvents such as H_2O. The electrochemical detection of hydrogen was carried out by Will[46] on a platinum electrode in a sulfuric acid solution and it was noted that the reaction mechanism consists of the diffusion of molecular hydrogen followed by dissociation and ionization. The diffusion characteristics were later studied further with respect to oscillatory kinetics at a platinum electrode in trifluoroacetic acid,[47]but relatively little literature has been published in aprotic solvents. Barrette *et al.*[48] observed the reversible oxidation of H_2 in a variety of aprotic solvents such as DMSO, DMF and MeCN. Initially, the anodic peaks observed however were not reproducible and not linear with the concentration of H_2, but when the electrodes were activated electrochemically at potentials more positive than the initial peaks, the H_2 oxidation peak changed from a shape characteristic of an electrochemically quasi-reversible process to one for a nearly reversible one-electron transfer. In all solvents, except MeCN, reversible waves with peak currents were found to be linear with increasing concentration of H_2, allowing, in principle, the basis for a H_2 sensor. Daniele *et al.*[49] have also investigated the electrochemical oxidation of H_2 in several organic polar solvents. By carrying out the electrogeneration of anhydrous perchloric acid, and assuming the following reaction:

$$HClO_4 + A + 2e^- \rightleftharpoons HA^- + {ClO_4}^- \tag{3.23}$$

where A = solvent, the half-wave potential for the reversible H^+/H_2 system could be related to

the bulk solvent basicity, which could be a basis for measuring hydrogen concentration.

More recently, the electrochemical oxidation of H_2 was observed in RTILs in an effort to fabricate an amperometric sensor which incorporates all the advantages of using RTILs as solvents.

3.4.1 Electrochemical detection of hydrogen in RTILs

The oxidation of hydrogen has been studied by cyclic voltammetry in a range of RTILs with different cations and anions.[50] The absence of oxidation peaks within the potential limits of many experiments carried out on gold microdiscs suggests that H_2 is electrochemically inactive on gold, as gold is part of a group of metals of high hydrogen overpotential.[51] On platinum microdiscs, hydrogen shows varying voltammetric behaviour, ranging from nearly electrochemically and chemically reversible to chemically irreversible depending on the anion of the chosen IL and the contrasting interactions of protons. It was anticipated that the oxidation occurs *via* the following reaction:

$$H_2 - 2e^- + 2A^- \rightleftharpoons 2HA \tag{3.24}$$

where the proton formed upon oxidation of H_2 reacts with the solvent anion (A^-) and the product HA is either stable or unstable. In most ILs, solvation of the proton formed during the oxidation of H_2 occurs, and depending on whether this species is stable or not, reversible or irreversible voltammetry is observed.

Studies in $[C_n\text{mim}][NTf_2]^-$-based ILs (where $n = 2$ or 4) show stable and reproducible voltammetry which was quasi-reversible at all scan rates. Similar behaviour was also observed in $[N_{6,2,2,2}][NTf_2]$ and $[P_{14,6,6,6}][NTf_2]$. However in $[C_4\text{mpyrr}][NTf_2]$, chemically irreversible voltammetry observed indicates that the product of oxidation is unstable, and the formation of platinum oxides occurs at potentials before that of hydrogen oxidation.

"Activation" of the electrode produced an interesting effect, whereby the quasi-reversible behaviour observed on non-activated electrodes became nearly reversible as seen previously by

Barrette *et al.* in aprotic media.[48] In this IL, and other $[NTf_2]^-$ ILs, the oxidation product $HNTf_2$ is formed. This product is stable and easily reduced to H_2.

Hydrogen oxidation was then studied in RTILs with varying anions.[52] In $[C_4mim][OTf]$ and $[C_4mim][PF_6]$, partially reversible waves were observed suggesting that the products H[OTf] and $H[PF_6]$ formed, respectively, between the IL anion and the proton formed from the oxidation of H_2 is stable enough to be detected voltammetrically. Both $[C_4mim][BF_4]$ and $[C_6mim][Cl]$ produced voltammetry that was less reversible with much reduced reduction peaks, suggesting that reaction products $H[BF_4]$ and HCl (or possibly $[HCl_2]^-$) are formed, which are unstable on the voltammetric timescale. Upon activation, the waveshapes for $[C_4mim][OTf]$ and $[C_4mim][PF_6]$ become almost fully reversible, as seen previously for $[NTf_2]^-$ RTILs whilst in $[C_4mim][BF_4]$ and $[C_6mim][Cl]$ the voltammetry remains only partially reversible, confirming the instability of $H[BF_4]$ and HCl in this medium.

The diffusion coefficient, D and solubility, c of H_2 on an activated platinum electrode was determined from analysis of chronoamperometric transients using Shoup and Szabo[33] approximations, and the values obtained in a range of RTILs are reported in Table 3.3.

Table 3.3: Diffusion coefficient and solubility data[53] for H_2 in various RTILs at 298 K, obtained from Shoup and Szabo[33] analysis of chronoamperometric transients.

RTIL	D /m^2 s^{-1}	c /mM
$[C_2mim][NTf_2]$	5.5×10^{-10}	4.2
$[C_4mim][NTf_2]$	8.8×10^{-10}	3.3
$[C_6mim][FAP]$	3.4×10^{-10}	6.6
$[C_4mim][OTf]$	3.6×10^{-10}	4.3
$[C_4mim][BF_4]$	2.2×10^{-10}	5.2
$[N_{6,2,2,2}][NTf_2]$	3.2×10^{-10}	7.2
$[C_4mim][NO_3]$	1.0×10^{-10}	4.8
$[C_4mim][PF_6]$	1.5×10^{-10}	5.1
$[P_{14,6,6,6}][NTf_2]$	2.9×10^{-10}	7.9
$[C_6mim][Cl]$	0.13×10^{-10}	9.7

The results suggest that H_2 is more soluble in IL media than more conventional solvents. For this reason, the method shows great promise for analytical determination of hydrogen in Clark-

cell type gas sensors.[41] At increasing temperatures, the peak current of hydrogen oxidation increases due to a decrease in viscosity. The more steady-state oxidation peak, compared to the more transient reduction peak suggests a larger diffusion coefficient for the solvated proton (HA) than for H_2.

3.5 Sensors for Detection of Sulfur Dioxide

The monitoring of SO_2 is of great importance with respect to environmental pollution, occupational health and industrial emission control, especially with increased regulation.[54] SO_2 has been linked to respiratory problems, particularly in asthmatics as well as being thought to contribute to increased mortality.[55] SO_2 is mainly produced by burning sulfur-containing substances such as coal and fuel-oil, but also comes from natural reactions such as volcanic eruptions and forest fires. SO_2 in the atmosphere is changed into sulfuric acids that cause acid rain, which is hugely damaging to vegetation and buildings.[56] The reduction of SO_2 is industrially important for operation of lithium/sulfur oxide batteries, and the manufacture of dithionite salts which are a common industrial reducing agent.[57]

The reduction of SO_2 has been thoroughly studied in aprotic solvents.,[57–61] as well as protic solvents[56] and potentiometrically in solid-state electrolyte sensors.[62,63] The reduction of sulfur dioxide in DMF has been investigated by means of cyclic voltammetry and chronoamperometry at a gold electrode.[58] These techniques suggest that SO_2 is reduced by one electron to give several species. The one-electron reduction of SO_2 proceeds as follows:

$$SO_2 + e^- \rightleftharpoons {SO_2}^- \tag{3.25}$$

which yields a species that is free to react with non-reduced SO_2 in the following reaction:

$$n SO_2 + {SO_2}^- \rightleftharpoons (SO_2)_2{SO_2}^- \tag{3.26}$$

Reduced SO_2 also undergoes a dimerization reaction to form dithionite as follows:

$$2{SO_2}^- \rightleftharpoons {S_2O_4}^{2-} \tag{3.27}$$

The electrochemical behaviour of SO_2 in DMF has also been studied at the platinum electrode.[59] The conclusion drawn showed that SO_2 undergoes an irreversible one-electron reduction to form the anion radical $SO_2^{\bullet -}$ which then dimerises to form $S_2O_4^{2-}$, and that an intermediate complex was formed, $(SO_2)_2SO_2^{\bullet -}$, similar to that in Equation 3.26.

Further experiments carried out on the reduction of SO_2 in DMSO at a hanging drop mercury electrode, also showed the formation of the $S_2O_4^{2-}$ dimer, and showed it as a stable reaction product.[60] The reproduciblilty of the voltammetry was good, but a linear response with increasing SO_2 was not observed. Further work carried out in DMF at the HDME electrode showed that the choice of solvent and electrolyte could affect the reaction mechanism whereby the stability of the $S_2O_4^{2-}$ dimer decreases with increasing basicity.[57] These systems so far have not been viable for the fabrication of a sensor for SO_2.

However, recently, the fabrication of an electrochemical sensor for SO_2 has been realised. A sensor based on a porous Au-solid polymer electrolyte sensing electrode in direct contact with the gas has been described.[64] This sensor is based on a precious metal-solid polymer electrolyte electrode, which is composed of a porous metal electrode chemically deposited or vacuum-deposited onto one side of a solid polymer electrolyte, which acts as the sensing electrode for gas determination. The sensing electrode is placed in direct contact with the gas, and the solid polymer electrolyte acts an internal electrolyte solution where the counter and reference electrodes are placed. This configuration is shown to give a fast response and higher sensitivity than cells employing gas-permeable membranes, such as those for Clark cells. The internal electrolyte solution is aqueous and responds to the SO_2 by forming the SO_4^{2-} ion and protons. Under this regime, very low detection limits are attainable, the values lying in the low-ppb region for SO_2. This is quite an improvement over previous gas sensors, and the limits of detection are comparable to conventional methods in environmental monitoring. Further work of this nature was carried out on a nano-Au-assembled electrode for SO_2 sensing in a range of different aqueous

electrolytes of different pH (0.1 M HCl, 0.1 M H_2SO_4, 0.1 M NaOH) using cyclic voltammetry.[56] Similar reaction mechanism were observed as those previously mentioned[64] whereby in acidic solution, the SO_4^{2-} ion as well as protons were formed. It was found however, that increasing the basicity of the electrolyte solution by using 0.1 M NaOH, caused the formation of the SO_3^{2-} ion, which yielded the biggest current response. This work shows all the advancement in the fabrication of a practical gas sensor for SO_2. The issue with aqueous electrolyte solutions however is their volatility, which is why work has been carried out to observe the electrochemical characterization of SO_2 in RTILs.

3.5.1 Electrochemical detection of Sulfur Dioxide in RTILs

The reduction of SO_2 has more recently been studied *via* cyclic voltammetry on Pt (10 μm diameter) in the ionic liquids [C_4mim][NO_3], [C_2mim][NTf_2], [C_4mim][BF_4], [C_4mim][PF_6] and [C_6mim][Cl] and peak assignments have been made on the basis of the experimental results obtained and literature data.[55] A reduction signal was observed, corresponding to the following process:

$$SO_2 + e^- \rightleftharpoons SO_2^{\bullet -} \tag{3.28}$$

which changes from steady-state at slow scan rates to transient behaviour as the scan rate is increased; similar behaviour is observed in all ILs. The diffusion coefficient and solubility of SO_2 in each IL was obtained by potential step chronoamperometry methods and the values are reported in Table 3.4.

Table 3.4: Chronoamperometric data obtained from theoretical fitting to the Shoup and Szabo[33] expression for the electrochemical reduction of SO_2 in different ionic liquids at 298 K.

RTIL	D /m^2 s^{-1}	c /mM
[C_2mim][NTf_2]	8.7×10^{-9}	230
[C_4mim][BF_4]	7.9×10^{-10}	1600
[C_4mim][NO_3]	4.8×10^{-10}	3000
[C_4mim][PF_6]	4.4×10^{-9}	438
[C_6mim][Cl]	3.1×10^{-10}	3500

The values suggest that the Stokes-Einstein relationship between solvent viscosity and diffusion coefficient is not followed, as observed previously for other gases in the same medium.[29,53,55]

On the reverse potential sweep, at least two oxidation signals are observed, one more prominent, followed by a small shoulder signal. In [C_4mim][NO_3] only, closer inspection of the voltammetry reveals a third oxidation signal at more negative potentials than the other two previously mentioned oxidation signals. The electrochemistry of 1 %, 10 % and 100 % SO_2 was analysed voltammetrically to assist with the assignation of peaks in the oxidative region, and values of 8.1×10^{-11} and 7.3×10^{-11} m^2 s^{-1} for diffusion coefficient were determined for 10 % and 1 % SO_2, respectively, with solubilities of 2100 and 340 mM, respectively, from chronoamperometric transients.

Using DigiSim[65] and an EC mechanism, based on that denoted in eqns. 3.29 to 3.31, involving the interaction of the imidazolium RTIL and the anion radical, the reduction of SO_2 in [C_4mim][NO_3] was simulated.

$$SO_2 + e^- \overset{k^0}{\rightleftarrows} {SO_2}^{\bullet -} \tag{3.29}$$

$${SO_2}^{\bullet -} + \text{solvent} \overset{k_f}{\rightarrow} {SO_2}^{\bullet -} \cdots \text{solvent} \tag{3.30}$$

$${SO_2}^{\bullet -} \cdots \text{solvent} \overset{k^0}{\rightleftarrows} SO_2 + e^- \tag{3.31}$$

The theoretical results allow assignment of the first oxidation signal to be the oxidation of solvated ${SO_2}^{\bullet -}$. The second oxidation signal is assigned to the oxidation of either ${S_2O_4}^{2-}$ or

$S_2O_4^{\bullet-}$, both commonly identified in aprotic media.[57–61] The latter oxidation signal, present at a more negative potential is thought to be stabilised by the solvent, and is attributed to the oxidation of unsolvated $SO_2^{\bullet-}$.

Collection of diffusion coefficient and solubility values at different temperatures revealed an increase of rate of diffusion with a decrease in solubility as the temperature increased. Analysis of this data in terms of the Arrhenius relationship allowed calculation of the diffusional activation energy of SO_2 in $[C_4mim][NO_3]$. A value of 10 kJ mol^{-1} was determined.

The RTILs studied were found to be highly sensitive to SO_2 gas, as observed by the high solubility, which suggests that this class of solvents, especially $[C_4mim][NO_3]$ may be a viable solvent in gas sensing applications.

3.6 Sensors for detection of Hydrogen Sulfide

Hydrogen sulfide is a well-known hazardous pollutant which is found naturally in coal pits, sulfur springs, oil and gas wells. It presents a serious hazard to the health of living organisms when encountered in elevated concentrations.[66] According to safety standards,[67] exposure to concentrations as low as 10 ppm can lead to personal stress, and at concentrations higher than 250 ppm, it is detrimental to human health and may eventually cause death. H_2S is produced along with methane in many natural gas fields. In fact, natural gas can contain up to 90% H_2S, whereupon it is referred to as dirty gas.[68] H_2S is also produced from hydrodesulfurizaton of crude oils.[69] Therefore, it is essential to develop fast-response hydrogen sulfide gas sensors that can quickly and accurately measure the presence of this gas.

Similar to O_2 and CO_2 sensors, the fabrication of a sensor for H_2S of the potentiometric type has been carried out using solid-state electrolytes.[70] The electrochemical cell uses a Na^+-solid electrolyte and a PbS working electrode to record H_2S concentration changes. The change in potential was linear with the concentration of H_2S, however this sensor does suffer from interference of other gases.

The voltammetric detection of H_2S in liquid electrolyte has also been well documented, particularly on platinum electrodes.[71–78] The majority of this work observed the *oxidation* of H_2S at platinum electrodes. Some of the earliest observations suggested that anodic oxidation of H_2S is one method of coating the electrode with sulfur. Najdeker *et al*. observed the oxidation of H_2S in 0.1 M H_2SO_4 at platinum electrodes using cyclic voltammetry.[71] They ascribed an anodic wave to the formation of platinum sulfide, and a further wave at a more positive potential to the formation of elemental sulfur, and suggested a series of mechanisms to describe this oxidation. This observation was later confirmed by Ramasubramanian at a platinum electrode in aqueous sulfide solutions using cyclic voltammetry and electron diffraction.[72] The mechanism likely follows the pathway:

$$2\mathrm{Pt} + \mathrm{H_2S} \rightleftharpoons \mathrm{Pt-SH} + \mathrm{Pt-H_{(ads)}} \tag{3.32}$$

$$\mathrm{Pt-SH_n} \rightleftharpoons \mathrm{Pt-S} + n\mathrm{H^+} + n\mathrm{e} \tag{3.33}$$

A study was also undertaken to observe the effect of H_2S on platinum in aqueous electrolyte (H_3PO_4) over a range of temperatures.[76] The authors found as before, that H_2S poisons the platinum electrode suface forming a sulfide layer which was observed by a decrease in anodic current with continued cyclic voltammetry. The extent of this poisoning was found to decrease with increasing temperature, but increase with increasing potential, and that at sufficiently high potentials, a layer of adsorbed elemental sulfur formed on the electrode surface.

Evans *et al.*[73] also observed the electrochemical behaviour of H_2S on platinum surfaces in aprotic electrolytes such as MeCN. This work again observed the poisoning of the platinum electrode surface on exposure to H_2S in aprotic solvent, and also observed some of the reductive electrochemistry for H_2S which showed a large "steady-state" peak followed by a transient oxidative peak on the reverse sweep, but did not suggest the identity of the peaks. Banks and Winnick[77] conducted experiments for removing H_2S at high temperatures in purified molten Na_2S/K_2S on a graphite working electrode in the presence of hydrogen gas. They found high cathodic currents which were "steady-state" at low scan rates, becoming more transient at higher scan rates. Further experiments were carried out in molten sulfide on a graphite working electrode to examine the kinetics of H_2S.[75] Using potential step chronoamperometry, the oxidative and reductive currents of H_2S were examined, and overpotential ranges were noted as well as the reaction orders for each process. Berberova *et al.* examined the anodic currents of H_2S at platinum in nonaqueous solutions (MeCN) in an effort to form the unstable radical cation $H_2S^{\bullet+}$ for organic synthesis.[78]

It was Opekar *et al.* who starting examining the amperometry of H_2S for use as a gas

sensor.[74] In their work, they preconcentrated H_2S onto a silver working electrode in 0.1 M KOH electrolyte solution, and used cathodic stripping voltammetry (CSV) to determine the concentration of H_2S adsorbed onto the electrode. The magnitude of the CSV peak was found to be linear with concentration of H_2S within a certain range. More recently, Horn *et al*. presented a Clark-type sensor for H_2 (mixed with air) at a Pt spiral electrode which allows for rapid analysis in environmentally realistic conditions.[79] This sensor utilizes the direct amperometric oxidation of H_2S in phosphate buffer solution. A significant advantage of this system is the prevention of interference from other gases, *eg*. H_2. Detection limits of this sensor were 2-20 ppm, limits matching industrial sensors currently on the market.[80] The response time for this sensor was shown to be <200s, and the system was seen to be operational over a long time. The use of other electrode materials has been explored also in recent years in an effort to fabricate a practical gas sensor for H_2S which does not suffer the drawbacks of surface poisoning as platinum does. The electrochemistry of H_2S has been studied at a nickel hydroxide macro- and microdisc electrodes in 0.1 M NaOH alkaline solution.[81] This work examines the possibility of oxidising nickel hydroxide, the product of which would undergo catalytic reduction by sulfide ions which would again be electrochemically oxidised to produce the analytical signal. The actual electrode then acts as a mediating species. The oxidative wave scaled with concentration of sulfide and gave a favourable limit of detection, which allowed the development of a simple and cheap design for an electrochemical cell for determination of gaseous H_2S.

The detection of H_2S in aqueous media utilizing a mediating species dissolved in the electrolyte solution has attracted much attention. There exists a large body of work in which the reaction of electrochemically generated quinoid derivatives with sulfide has been investigated as a method of detecting the latter. Upon applying a suitable anodic potential, oxidation of the mediating species will occur to provide the corresponding quinone. The addition of sulfide will result in the formation of the thiol derivative which itself will be redox active. Reoxida-

tion of this species will result in an increase in the oxidation current beyond that of the initial current of the mediating species alone. This work has been carried out using glassy carbon electrodes in acetate and phosphate buffer solutions using cyclic voltammetry for the mediating species DMPD,[82] DEPD,[83] and DPPD,[84,85] as well as hydroquinone, aminophenol, catechol and dopamine[86] and at screen printed electrodes as well as a glassy carbon electrode. In each case, the response of the current scaled linearly with the concentration of sulfide. This shows a versatile strategy for detection of sulfide in aqueous solution. The structural and functional diversity of the compounds investigated emphasizes the generic nature of the reaction, and the use of inexpensive and commercially available reagents is a bonus for the fabrication of a practical H_2S sensor.

The use of ferrocene derivatives as mediating species in aqueous electrolyte solution for detection of H_2S using cyclic voltammetry and square wave voltammetry has also been well documented. These do not act in the same way as the quinoid mediating species however. In the case of the ferrocene derivatives, they undergo an electrocatalytic reaction with sulfide and thiol species. The ferrocene is first oxidized to the ferricenium ion, which is subsequently homogeneously reduced back to ferrocene by the sulfide species. This regenerated ferrocene can then be again oxidized at the electrode surface to produce the analytical signal.[87] This method has been explored in aqueous solvents in a range of systems: at platinum electrodes using ferrocene sulfonates at the mediator;[87] at basal plane pyrolytic graphite, glassy carbon and boron-doped diamond electrodes using poly(vinyl)ferrocene as the mediating species;[88] at basal plane pyrolytic electrode using a vinylanthracene and vinylferrocene-containing copolymer as the mediating species;[89] at boron-doped diamond using ferrocene sulfonates as the mediating species.[90] The signal of the ferrocene species increased linearly with increasing sulfide concentration. The detection limits in these studies also compare favourably with previous studies for the electro-catalytic determination of H_2S, again, offering a cheap and sensitive practical gas

sensor for H_2S.

Finally, mediating species of the benzoquinone variety have been used to detect H_2S at a glassy carbon electrode in acetate buffer.[81] The use of this species is pertinent to the body of work to follow in this thesis. In the case of these species, exposure to H_2S results in a chemical reaction to form an adduct which itself is electroactive, except unlike the quinoid species, this new adduct results in a new voltammetric signal. This new signal itself is a method for detection of H_2S. Also, since the mediating species is being consumed, the decrease in its signal is also a method of detection of H_2S. This represents a new voltammetric detection method for H_2S detection in aqueous solution.

In this work, the electrochemistry of H_2S is studied at the platinum electrode in RTILs. Earlier Chapters outline the direct detection of H_2S at the electrode in RTILs, and later Chapters outline the use of various species as mediators for detection of H_2S in RTILs, most of which were not successful, but one of which was. As an aside, the electrochemistry of several of these mediating species have not previously been observed in RTILs, and were thus studied in this media.

The use of RTILs as solvents for H_2S has been previously documented, but only with respect to solubility.[69,91] To the best of my knowledge, the work that follows is the first attempt at observing the reduction and oxidation of H_2S in RTILs.

It is worth mentioning that the solubility of H_2S in various solvents has attracted much attention.[66,92–96] This property of H_2S has also been studied in RTILs and results are compared to those of more conventional solvents, outlined in Chapter 6.

References

[1] Bakker, E. and Telting-Diaz, M., *Anal. Chem.*, 2002, **74**, 2781–2800.

[2] Janata, J. and Bezegh, A., *Analytical Chemistry*, 1988, **60**, 62R–74R.

[3] Hahn, C. E. W., *Clin. Phys. Physiol. Meas.*, 1987, **83**, 3–38.

[4] Hahn, C. E. W., *Analyst*, 1998, **123**, 57R–86R.

[5] Göpel, W.; G., R. and M, R., *Solid State Ionics*, 2000, **136-137**, 519–531.

[6] Docquier, N. and Candel, S., *Prog. Energy Combust. Sci.*, 2002, **28**, 107–150.

[7] Knake, R.; Guchardi, R. and Hauser, P. C., *Anal. Chim. Acta*, 2003, **475**, 17–25.

[8] Hammond, M. H.; Johnson, K. J.; Rose-Pehrsson, S. L.; Ziegler, J.; Walker, H.; Caudy, K.; D., G. and Tillett, D., *Sens. Actuators B*, 2006, **116**, 135–144.

[9] Clark, L. C., *Trans. Am. Soc. Int. Artif. Organs*, 1956, **2**, 41–48.

[10] Stow, R. W.; Baer, R. F. and Randall, B., *Arch. Phys. Med. Rehabil.*, 1957, **38**, 646–650.

[11] Severinghaus, J. W. and Bradley, A. F., *J. Appl. Physiol.*, 1958, **13**, 515–52.

[12] Sawyer, D. T. and Roberts Jr, J. L., *J. Electroanal. Chem.*, 1966, **12**, 90–101.

[13] Fujinaga, T.; Izutsu, K. and Adachi, T., *Bull. Chem. Soc. Japan*, 1969, **42**, 140–145.

[14] Lund, W. and Peover, M. E., *J. Electroanal. Chem.*, 1970, **25**, 19–25.

[15] Albery, W. J. and Barron, P., *J. Electroanal. Chem.*, 1982, **138**, 79–87.

[16] Hahn, C. E. W.; McPeak, H.; Bond, A. M. and Clark, D., *J. Electroanal. Chem.*, 1995, **393**, 61–68.

[17] Floate, S. and Hahn, C. E. W., *J. Electroanal. Chem.*, 2005, **583**, 203–211.

[18] Welford, P. J.; Brookes, B. A.; Wadhawan, J. D.; McPeak, H.; Hahn, C. E. W. and Compton, R., *J. Phys. Chem. B.*, 2001, **105**, 5253–5261.

[19] Wadhawan, J. D.; Welford, P. J.; Maisonhaute, E.; Climent, V.; Lawrence, N. S.; Compton, R. G.; McPeak, H. B. and Hahn, C. E. W., *J. Phys. Chem. B*, 2001, **105**, 10659–10668.

[20] Hahn, C. E. W.; McPeak, H. B. and Bond, A. M., *J. Electroanal. Chem.*, 1995, **393**, 69–74.

[21] Hahn, C. E. W. and McPeak, H., *J. Electroanal. Chem.*, 1997, **427**, 179–188.

[22] McPeak, H.; Bond, A. M. and Hahn, C. E. W., *J. Electroanal. Chem.*, 2000, **487**, 25–30.

[23] AlNashaf, I. M.; Leonard, M. L.; Matthews, M. A. and Weidner, J. W., *Ind. Eng. Chem. Res.*, 2002, **41**, 4475–4478.

[24] Carter, M. T.; Hussey, C. L.; Strubinger, S. K. D. and Osteryoung, R. A., *Inorg. Chem.*, 1991, **30**, 1149–1151.

[25] AlNashaf, I. M.; Leonard, M. L.; Kittle, M. C.; Matthews, M. A. and Weidner, J. W., *Electrochem. and Solid State Lett.*, 2001, **4**, D16–D18.

[26] Buzzeo, M. C.; Klymenko, O. V.; Wadhawan, J. D.; Hardacre, C.; Seddon, K. R. and Compton, R. G., *J. Phys. Chem. A*, 2003, **107**, 8872–8878.

[27] Evans, R. G.; Klymenko, O. V.; Saddoughi, S. A.; Hardacre, C. and Compton, R. G., *J. Phys. Chem. B*, 2004, **108**, 7878–7886.

[28] Rogers, E. I.; Huang, X.-J.; Dickinson, E. J. F.; Hardacre, C. and Compton, R. G., *J. Phys. Chem. C*, 2009, **113**, 17811–17823.

[29] Huang, X.-J.; Rogers, E. I.; Hardacre, C. and Compton, R. G., *J. Phys. Chem. B*, 2009, **113**, 8953–8959.

[30] Buzzeo, M. C.; Klymenko, O. V.; Wadhawan, J. D.; Hardacre, C.; Seddon, K. R. and Compton, R. G., *J. Phys. Chem. B*, 2004, **108**, 3947–3954.

[31] Barrosse-Antle, L. E. and Compton, R. G., *Chem. Comm.*, 2009, pages 3744–3746.

[32] Barrosse-Antle, L. E.; Hardacre, C. and Compton, R. G., *J. Phys. Chem. B*, 2009, **113**, 2805–2809.

[33] Shoup, D. and Szabo, A., *J. Electroanal. Chem.*, 1982, **140**, 237–245.

[34] Ji, X.; Banks, C. E. and Compton, R. G., *Electroanalysis*, 2006, **18**, 449–455.

[35] Meyerhoff, M. E. and Fraticelli, Y. M., *Anal. Lett.*, 1981, **14**, 415–432.

[36] Andrew, K. N.; Worsfold, P. J. and Comber, M., *Anal. Chim. Acta*, 1995, **314**, 33–43.

[37] Van Son, M.; Schothorst, R. C. and Den Boef, G., *Anal. Chim. Acta*, 1983, **153**, 271–275.

[38] Alegret, S.; Alonso, J.; Bartroli, J.; Del Valle, M.; Jaffrezic-Renault, N. and Duvault-Herrera, Y., *Anal. Chim. Acta*, 1990, **231**, 53–58.

[39] Zhang, T.; Nix, M. B.; Yoo, B.-Y.; Deshusses, M. A. and Myung, N. V., *Electoanalysis*, 2006, **18**, 1153–1158.

[40] Ji, X.; Banks, C. E.; Hu, G.; Crossley, A. and Compton, R. G., *Electroanalysis*, 2006, **18**, 2141–2147.

[41] Buzzeo, M. C.; Giovanelli, D.; Lawrence, N. S.; Hardacre, C.; Seddon, K. R. and Compton, R. G., *Electroanalysis*, 2004, **16**, 888–896.

[42] Giovanelli, D.; Buzzeo, M. C.; Lawrence, N. S.; Hardacre, C.; Seddon, K. R. and Compton, R. G., *Talanta*, 2004, **62**, 904–911.

[43] Ji, X.; Banks, C. E.; Silvester, D. S.; Wain, A. J. and Compton, R. G., *J. Phys. Chem. C*, 2006, pages A–I.

[44] Ji, X.; Silvester, D.; Aldous, L.; Hardacre, C. and Compton, R., *J. Phys. Chem. C*, 2007, **111**(26), 9562–9572.

[45] Ji, X.; Banks, C. E.; Silvester, D. S.; Aldous, L.; Hardacre, C. and Compton, R. G., *Electroanalysis*, 2007, **19**, 2194–2201.

[46] Will, F. G., *J. Electrochem. Soc.*, 1963, **110**, 145–151.

[47] Conway, B. E. and Novak, D. M., *J. Phys. Chem.*, 1977, **81**, 1459–1468.

[48] Barrette, William C., J. and Sawyer, D. T., *Anal. Chem.*, 1984, **56**, 653–657.

[49] Daniele, S.; Ugo, P.; Mazzocchin, G. A. and Bontempelli, G., *Anal. Chim. Acta*, 1985, **173**, 141–148.

[50] Silvester, D. S.; Aldous, L.; Hardacre, C. and Compton, R. G., *J. Phys. Chem. B*, 2007, **111**, 5000–5007.

[51] Dong, H.; Feng, R.; Ai, X.; Cao, Y.; Yang, H. and Cha, C., *J. Phys. Chem. B*, 2005, **109**, 10896–10901.

[52] Del Sesto, R. E.; Corley, C.; Robertson, A. and Wilkes, J. S., *J. Organometallic Chem.*, 2005, **690**, 2536–2542.

[53] Silvester, D. S.; Rogers, E. I. and Compton, R. G., Wiley, 2008; chapter 13.2. in "Electrodeposition in Ionic Liquids".

[54] Morrin, A.; Moutloali, R. M.; Killard, A. J.; Smyth, M. R.; Darkwa, J. and Iwuoha, E. I., *Electoanalysis*, 2004, **16**, 1944–1948.

[55] Barrosse-Antle, L.; Silvester, D. S.; Aldous, L.; Hardacre, C. and Compton, R. G., *J. Phys. Chem. C*, 2008, **112**, 3398–3404.

[56] Li, H.; Q., W.; Xu, J.; Zhang, W. and Jin, L., *Sens. Actuators B*, 2002, **87**, 18–24.

[57] Gardner, C. L.; Fouchard, D. T. and Fawcett, W. R., *J. Electrochem. Soc.*, 1981, **128**, 2345–2350.

[58] Martin, R. P. and Sawyer, D. T., *Inorg. Chem.*, 1972, **11**, 2644–2647.

[59] Magno, F.; Mazzocchin, G. A. and Bontempelli, G., *Electroanal. Chem.*, 1974, **57**, 89–96.

[60] Bruno, P.; Caselli, M. and Treini, A., *J. Electroanal. Chem.*, 1980, **113**, 99–111.

[61] Potteau, E.; Levillain, E. and Lelieur, J.-P., *J. Electroanal. Chem.*, 1999, **476**, 15–25.

[62] Gauther, M. and Chamberland, A., *J. Electrochem. Soc.*, 1977, **124**, 1579–1583.

[63] Skeaff, J. M. and Dubreuil, A. A., *Sens. Actuators B*, 1993, **10**, 161–168.

[64] Hodgson, A. W. E.; jacquinot, P. and Jauser, P. C., *Anal. Chem.*, 1999, **71**, 2831–2837.

[65] Rudolph, M.; Reddy, D. P. and Feldberg, S. W., *Anal. Chem.*, 1994, **66**, 589A–600A.

[66] Koschel, D.; Coxam, J.-Y. and Majer, V., *Ind. Eng. Chem. Res.*, 2007, **46**(4), 1421–1430.

[67] Xu, J.; Wang, X. and Li, C., *Electrochem. Solid-State Lett.*, 2006, **9**(7), H53–H56.

[68] Xu, Q.; Wang, R.; Kiyobayashi, T.; Kuriyama, N. and Kobayashi, T., *J. Power Sources*, 2006, **155**, 167–171.

[69] Pomelli, C.; Chiappe, C.; Vidis, A.; Laurenczy, G. and Dyson, P., *J. Phys. Chem. B*, 2007, **111**(45), 13014–13019.

[70] Bukun, N.; Dobrovolsky, Y.; Levchenko, A.; Leonova, L. and Osadchii, E., *J. Solid State Electrochem.*, 2003, **7**, 122–124.

[71] Najdeker, E. and Bishop, E., *J. Electroanal. Chem.*, 1973, **41**, 79–87.

[72] Ramasubramanian, N., *J. Electroanal. Chem.*, 1975, **64**, 21–37.

[73] Evans, J.; Blount, H. and Ginnard, C. R., *J. Electroanal. Chem.*, 1975, **59**, 169–175.

[74] Opekar, F. and Bruckenstein, S., *Anal. Chem.*, 1984, **56**(8), 1206–1209.

[75] White, K. and Winnick, J., *Electrochim. Acta*, 1985, **30**, 511–519.

[76] Chin, D. T. and Howard, P. D., *J. Electrochem. Soc.*, 1986, **133**(12), 2447–2450.

[77] Banks, E. K. and Winnick, J., *J. Appl. Electrochem.*, 1986, **16**, 583–590.

[78] Berberova, N. and Shinkar, E., *Russ. Chem. Bull.*, 2000, **49**, 1178–1184.

[79] Horn, J. J.; Mccreedy, T. and Wadhawan, J. D., *Anal. Meth.*, 2010, **2**, 1346–1354.

[80] http : //www.citytech.com/index.html.

[81] Giovanelli, D.; Lawrence, N. S.; Jiang, L.; Jones, T. G. J. and Compton, R. G., *Anal. Lett.*, 2003, **36**, 2941–2959.

[82] Lawrence, N. S.; Davis, J.; Jiang, L.; Jones, T.; Davis, S. and Compton, R. G., *Analyst*, 2000, **125**, 661–663.

[83] Lawrence, N. S.; Thompson, M.; Davis, J.; Jiang, L.; Jones, T. G. J. and Compton, R. G., *Mikrochim. Acta*, 2001, **137**, 105–110.

[84] Thompson, M.; Lawrence, N. S.; Davis, J.; Jiang, L.; Jones, T. G. J. and Compton, R. G., *Sens. Actuators, B*, 2002, **87**, 33–40.

[85] Lawrence, N. S.; Jiang, L.; Jones, T. G. J. and Compton, R. G., *Anal. Chem.*, 2003, **75**, 2054–2059.

[86] Lawrence, N. S.; Davis, J.; Jiang, L.; Jones, T.; Davies, S. and Compton, R., *Electroanalysis*, 2001, **13**, 432–436.

[87] Lawrence, N. S.; Tustin, G. J.; Faulkner, M. and Jones, T. G. J., *Electrochim. Acta*, 2006, **52**, 499–503.

[88] Robinson, K. and Lawrence, N. S., *Electrochem. Commun.*, 2006, **8**, 1055–1061.

[89] Robinson, K. and Lawrence, N. S., *Electroanalysis*, 2006, **18**, 677–683.

[90] Banks, C. E.; Yashina, A. S.; Tustin, G. J.; Lafitte, V. G. H.; Jones, T. G. J. and Lawrence, N. S., *Electroanalysis*, 2007, **19**, 2518–2522.

[91] Jou, F.-Y. and Mather, A., *Internat. J. Thermophys.*, 2007, **28**, 490–495.

[92] King, M. B. and Al-Najjar, H., *Chem. Eng. Sci.*, 1977, **32**, 1241–1246.

[93] Short, I.; Sahgal, A. and Hayduk, W., *J. Chem. Eng. Data*, 1983, **28**, 63–66.

[94] Hayduk, W. and Pahlevanzadeh, H., *Can. J. Chem. Eng.*, 1987, **65**, 299–307.

[95] Lliuta, M. A. and Larachi, F., *J. Chem. Eng. Data*, 2007, **52**, 2–19.

[96] Duan, Z.; Sun, R.; Liu, R. and Zhu, C., *Energy & Fuels*, 2007, **21**(4), 2056–2065.

Chapter 4

Experimental Methods.

This Chapter outlines the chemicals and instrumentation used in the thesis presented, as well as the experimental procedures and voltammetric techniques employed. Descriptions of any procedures specific to particular experiments are outlined in the relevant Chapters.

4.1 Chemical Reagents and Ionic Liquids

The chemicals used in this thesis are listed in Table 4.1 and some structures are shown in Figure 4.1.

Table 4.1: Chemicals used for experiments reported herein along with commercial supplier and purity

Chemical Name	Formula/ Abbreviation	Supplier	Purity
Ferrocene	$Fe(C_5H_5)_2$/Fc	Aldrich	98%
Tetra-n-butylammoniumperchlorate	TBAP	Aldrich	99%
Acetonitrile	MeCN	Fischer Scientific	99.99%
Bistrifluoromethanesulfonimide	$H(NTf_2)$	Fluka	95%
Sulfur	S	Aldrich	99.98%
Hydrogen Sulfide	H_2S	CK Gas Products	99.99%
Hydrogen Sulfide	H_2S	CK Gas Products	1.01%
N,N-Dimethyl-p-phenylenediamine	DMPD	Aldrich	97%
Catechol	$C_6H_4(OH)_2$	Aldrich	99+%
Dopamine Hydrochloride	$C_8H_{11}NO_2$.HCl	ALFA	99+%
Nicotinamide adenine dinucleotide (reduced)	NADH	Aldrich	99+%
Polyvinylferrocene	PVF	Polysciences	-
Potassium ferrocyanide	$K_4[Fe(CN)_6]$	BDH	-

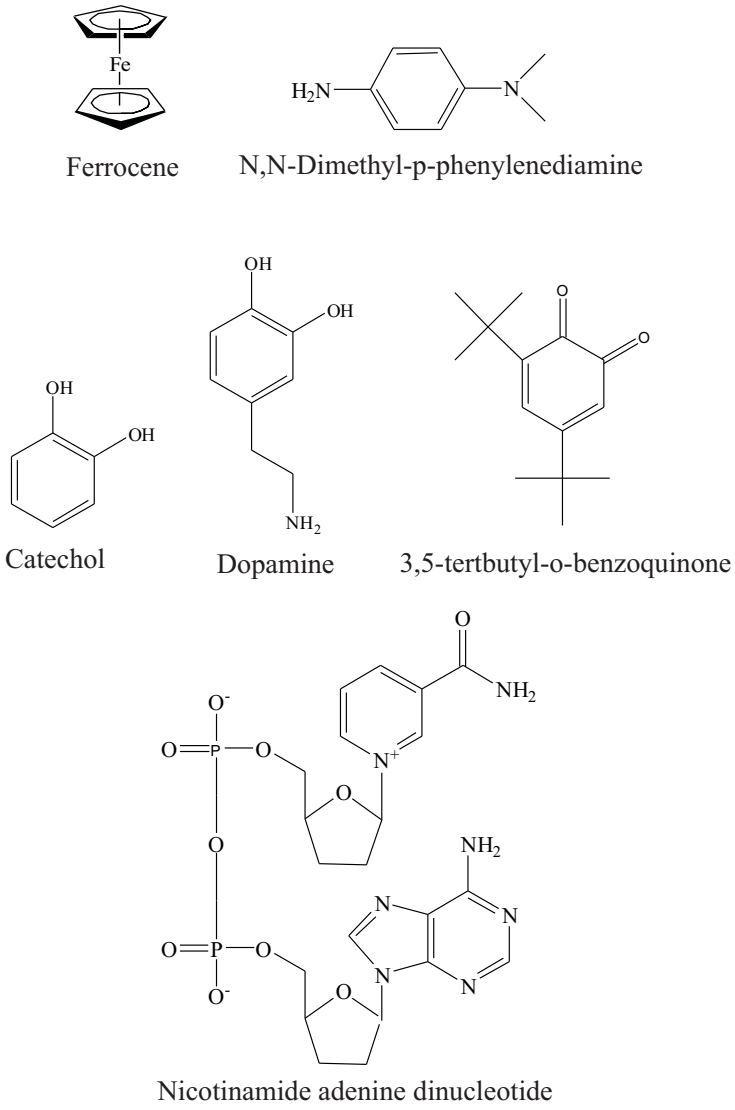


Figure 4.1: Structures of chemicals used in this thesis.

The RTILs used in this thesis are listed in Table 4.2 and the structures of the cations and anions are shown in Figure 4.2.

Table 4.2: RTILs used in this thesis (references to literature synthesis procedure)

RTIL Name	Formula	Supplier	η /cP
1-Ethyl-3-methylimidazolium bis(trifluoromethanesulfonyl)imide	$[C_2mim][NTf_2]$	prepared by QUILL procedure: Bonhôte *et al.*[1]	20[1]
1-Butyl-3-methylimidazolium bis(trifluoromethanesulfonyl)imide	$[C_4mim][NTf_2]$	prepared by QUILL procedure: Bonhôte *et al.*[1]	34[1]
1-hexyl-3-methylimidazolium tris(pentafluoroethyl)trifluorophosphate	$[C_6mim][FAP]$	prepared by QUILL procedure: Ignat'ev *et al.*[2]	7456[1]
N-Butyl-*N*-methylpyrrolidinium bis(trifluoromethanesulfonyl)imide	$[C_4mpyrr][NTf_2]$	prepared by QUILL procedure: MacFarlane *et al.*[4]	89[3]
1-Butyl-3-methylimidazolium trifluoromethanesulfonate	$[C_4mim][OTf]$	donated by Merck KGaA	90[1]
1-Butyl-2,3-dimethylimidazolium bis(trifluoromethanesulfonyl)imide	$[C_4dmim][NTf_2]$	prepared by QUILL procedure: Bonhôte *et al.*[1]	105[3]
1-Butyl-3-methylimidazolium tetrafluoroborate	$[C_4mim][BF_4]$	donated by Merck KGaA	112[3]
1-Butyl-3-methylimidazolium hexafluorophosphate	$[C_4mim][PF_6]$	donated by Merck KGaA	201[3]
N-Hexyltriethylammonium bis(trifluoromethanesulfonyl)imide	$[N_{6,2,2,2}][NTf_2]$	prepared by QUILL procedure: Bonhôte *et al.*[1]	252[3]
1-Butyl-3-methylimidazolium nitrate	$[C_4mim][NO_3]$	prepared by QUILL procedure: Cammarata *et al.*[6]	266[5]
Tris(*p*-hexyl)tetradecylphosphonium tris(pentafluoroethyl)trifluorophosphate	$[P_{14,6,6,6}][FAP]$	donated by Merck KGaA	464[7]
1-butyl-3-methylimidazolium iodide	$[C_4mim][I]$	donated by Merck KGaA	1110[8]
1-hexyl-3-methylimidazolium chloride	$[C_6mim][Cl]$	donated by Merck KGaA	7456[1]

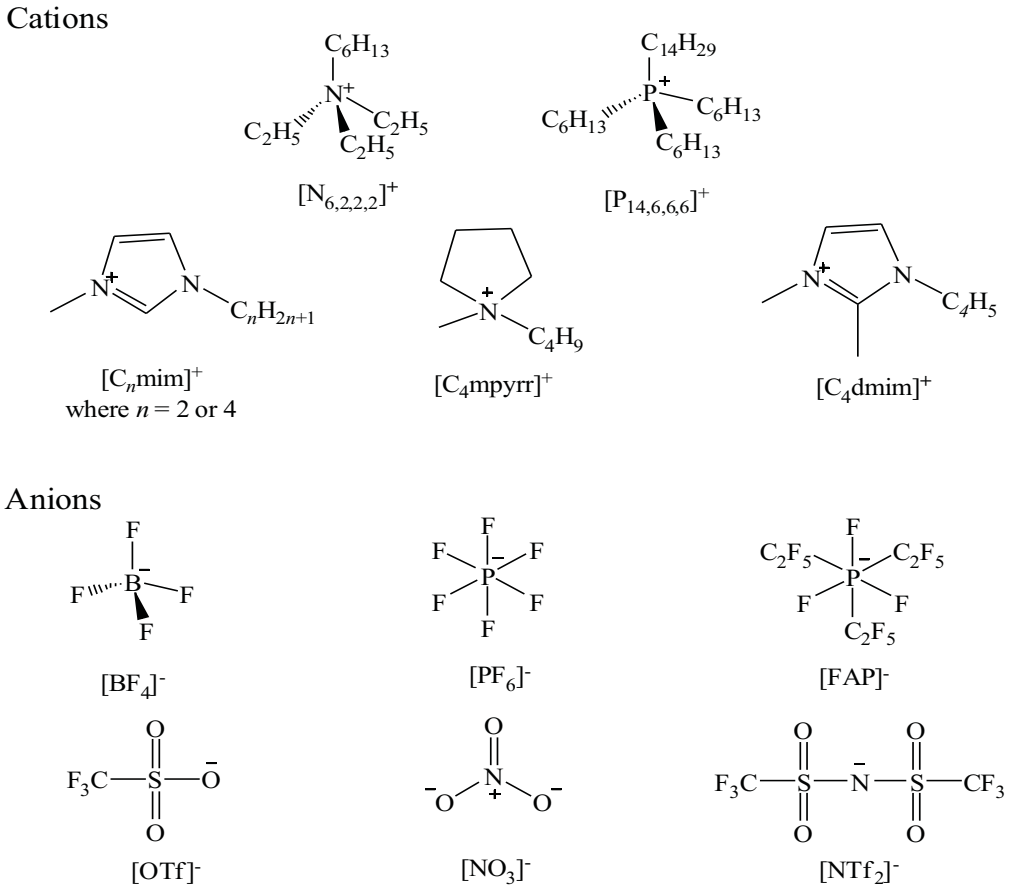


Figure 4.2: Structures of cations and anions of RTILs used in this thesis.

Some of the RTILs were kindly donated by the commercial supplier, Merck. Many were kindly donated by Queens University Ionic Liquid Laboratory (QUILL) and were synthesised and characterised by Dr. Leigh Aldous.

$[C_2\text{mim}][NTf_2]$, $[C_4\text{mim}][NTf_2]$, $[C_4\text{mpyrr}][NTf_2]$, $[C_4\text{dmim}][NTf_2]$ and $[N_{6,2,2,2}][NTf_2]$ were prepared according to standard literature procedures.[1,4] The synthesis of $[C_4\text{mim}][NO_3]$ was adapted from a previously published procedure.[6] The synthetic method used for halide RTILs involves the metathesis of a halide salt[9] ($[C_4\text{mim}][I]$ and $[C_6\text{mim}][Cl]$).

$[C_4\text{mim}][BF_4]$, $[C_4\text{mim}][PF_6]$ and $[P_{14,6,6,6}][FAP]$ were kindly donated by Merck KGaA and used as received without further purification.

$[C_4\text{mim}][OTf]$ was also kindly donated by Merck KGaA but first diluted with CH_2Cl_2 before being passed through a column consisting of alternating layers of neutral aluminium oxide and

silica gel to remove acidic impurities.

4.2 Instrumentation

4.2.1 Electrodes and Potentiostat

All electrochemical experiments were performed using a computer-controlled μ-Autolab potentiostat (Eco-Chemie, Netherlands). A conventional two-electrode system was used, typically with a platinum electrode (10 μm diameter), or a gold electrode (5 μm diameter) as the working electrode, and a 0.5 mm diameter platinum (or silver) wire as a quasi-reference electrode. The platinum microdisc working electrode was polished on soft lapping pads (Kemet Ltd., U.K.) using alumina powder (Buehler, IL) of size 5.0, 1.0 and 0.3 μm. The electrode diameter was calibrated electrochemically by analyzing the steady-state voltammetry of a 2 mM solution of ferrocene in MeCN containing 0.1 M TBAP, with a diffusion coefficient for ferrocene of 2.3×10^{-5} cm^2 s^{-1} at 298 K.[10]

4.2.2 Electrochemical Cell

The two electrode system employed in this thesis were housed in a glass cell "T-cell" shown in Figure 4.3, designed for investigating microsamples of ionic liquids under a controlled atmosphere.[11,12] The working electrode was modified with a section of disposable micropipette tip to create a small cavity above the disc into which a drop (20 μL) of ionic liquid was placed. The working electrode was then inserted into the bottom of the T-cell and the circuit completed by introduction of the platinum (or silver) quasi-reference electrode through the top of the cell. All joints were sealed with vacuum grease to ensure a closed system throughout. Prior to experiment, the RTIL solution was purged under vacuum (Edwards High Vacuum Pump, Model ES 50) for *ca.* 90 minutes, which served to remove trace atmospheric moisture naturally present in the RTIL.

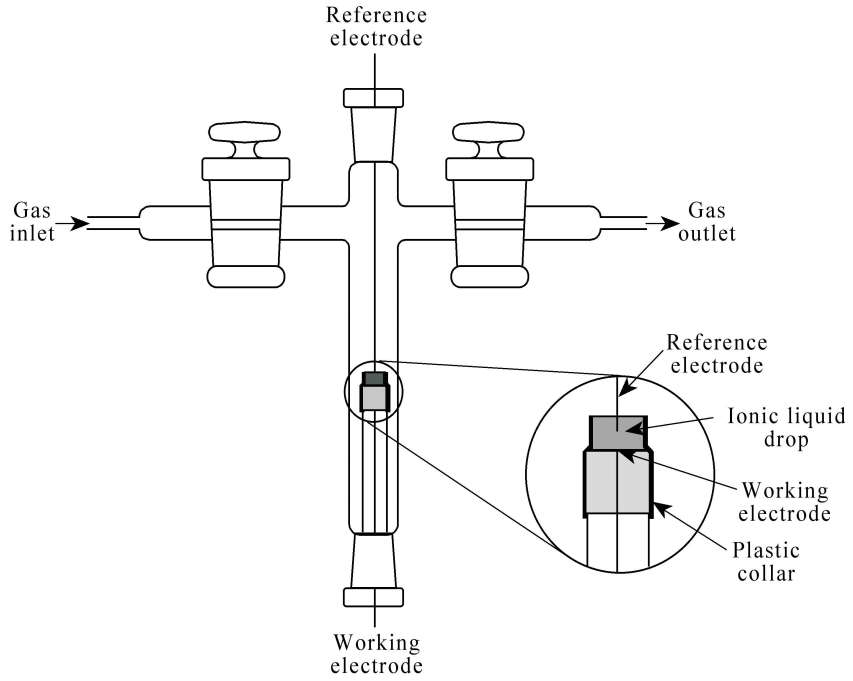


Figure 4.3: T-Cell for electrochemical gas experiments.

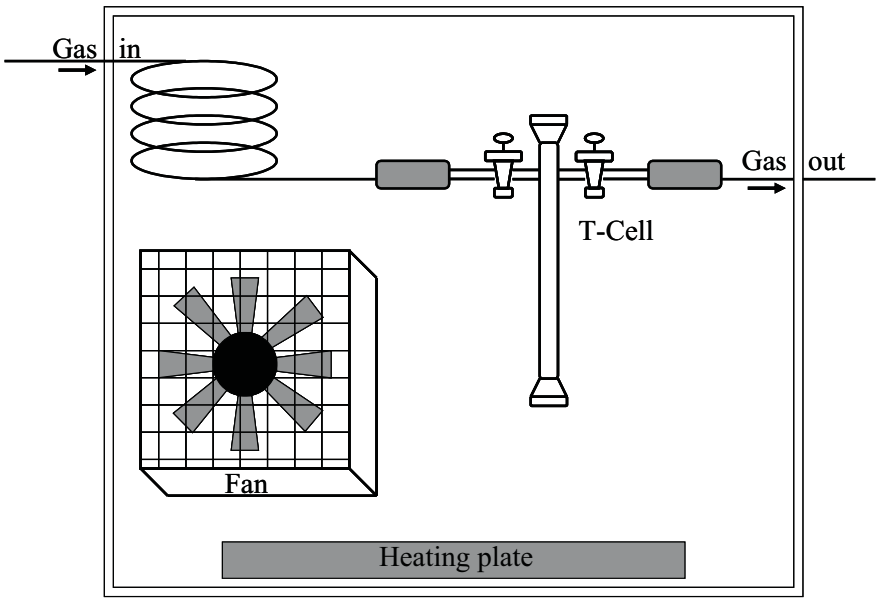


Figure 4.4: Faraday Cage for electrochemical gas experiments.

All experiments were performed inside a fume cupboard, in a thermostatted box (previously described by Evans *et al.*)[13] which also functioned as a Faraday cage shown in Figure 4.4. The temperature was maintained at 298 (± 1.0) K.

4.2.3 Solutions and Gases

For experiments using an internal reference couple, a solvent evaporation technique was employed. A stock solution of Fc was made in MeCN to a known concentration (typically 10 mM) and 20 μL was pipetted into the cell containing 20 μL of RTIL solution. The MeCN was evaporated under vacuum to leave a known concentration of electroactive species in solution.

Gaseous experiments were carried out in the T-cell. When the ionic liquid was purged under vacuum (0.5 Torr) for *ca.* 90 minutes, and the baseline showed no presence of impurities, hydrogen sulfide, H_2S, gas was introduced (*via* PTFE tubing) through one arm of the cell. The gas was allowed to diffuse through the sample for *ca.* 30 minutes to obtain maximum peak currents, which were monitored over a period of time to ensure that true equilibrium was obtained. An outlet line (made of PTFE) led from the other end of the cell into a fume cupboard.

4.2.4 Karl Fischer Titrations

All Karl Fischer Titrations were performed using a Cou-Lo Aquamax KF Moisture Meter in conjuction with Cou-Lo Formula A Coloumetric Anode Solution and Cou-Lo Formula C Coulmoetric Cathode Solution (GRScientific, UK) shown in Figure 4.5. Each RTIL sample was injected into the titrator using a 100 μl glass syringe with 7 cm needle (SGE, UK). The syringe was flushed with methanol several times and then flushed with the ionic liquid to be titrated. The RTIL was then injected into the titrator, and a reading of water content was obtained. The Cou-Lo Aquamax uses the coulometric principle, whereby the water present in the sample is coulometrically titrated to a predefined end point at which there is a minute excess of free iodine present. Stoichiometrically, one mole of water will react with one mole of iodine, so that 1 mg of water is equivalent to 10.71 C of electricity. Combining the coulometric technique with Karl Fischer titration, the Aquamax titrator determines the water content of the sample by measuring the amount of electrolysis current necessary to produce the required iodine. This is



Figure 4.5: Karl Fischer Titrator.

an absolute technique which does not require calibration of the reagents. Water content is given by Aquamax KF standard W/w calculation mode.

Result (ppm) = $\frac{microgram\ count}{W-w}$

Where W = total weight of sampler + sample (mg)

and w = tare weight of empty sampler (mg)

4.3 Sample Preparation

The data reported in Chapter 5 was obtained from RTILs tested for water content. The RTILs were subject to the following pre-treatments: vacuum-dried, wet or used straight from the bench-top under atmospheric conditions. The atmospheric samples were used without any attempt at drying or purification. The vacuum-dried samples were purged under vacuum for 24 h, while stirring continuously at a temperature of 333 K. The wet samples were prepared as follows: 1 mL of ionic liquid and 1 mL of deionised water were added to a small glass tube, shaken and allowed to stand for approx. 24 h. Any water that did not mix with the RTILs was removed and the layer of ionic liquid titrated. For each measurement, the ionic liquids were kept at a

temperature of 298 K.

4.4 Microdisc Chronoamperometric Experiments

Chronoamperometric transients were achieved using a sample time of 0.01 s. After pre-equilibration for 20 seconds, the potential was stepped from a position of zero current to a chosen potential after the reductive peak, and the current was measured for 5 s. The software package Origin 7.0 (Microcal Software Inc.) was used to fit the experimental data. The equations proposed by Shoup and Szabo[14] (below) were imported into the non-linear curve fitting function, and the computer was instructed to perform 100 iterations on the data.

$$I = -4nFDcr_{\mathrm{d}}f(\tau) \tag{4.1}$$

$$f(\tau) = 0.7854 + 0.8863\tau^{-\frac{1}{2}} + 0.2146\exp(-0.7823\tau^{-\frac{1}{2}}) \tag{4.2}$$

$$\tau = \frac{4Dt}{{r_{\mathrm{d}}}^2} \tag{4.3}$$

where n is the number of electrons transferred, F is the Faraday constant, D is the diffusion coefficient, c is the initial concentration of parent species, r_{d} is the radius of the disc electrode, and t is the time. The equations used in this approximation are sufficient to give D and c within an error of 0.6 %.

The value for the radius (previously calibrated) was fixed, and a value for the diffusion coefficient and the product of the number of electrons and concentration was obtained after optimization of the experimental data.[13,16] The best fit is achieved using the Origin 7.0 software package nonlinear least squares fitting, which is based on the Levenberg-Marquardt algorithm. Using the nonlinear least squares fitter, one can fit a function, such as the Shoup and Szabo equations[14] to experimental data using user-defined fitting functions such as a fixed electrode

radius. Further information can be obtained from the 'Origin Reference' tool in Origin 7.0.

Double potential step chronoamperometric transients were achieved using a sample time of 0.01 s. The solution was pretreated by holding potential at a point of zero current for 20 s, after which the potential was stepped to a position after the oxidative peak for catechol, and the current was measured for 5 s. The potential was then stepped back to a point of zero current, and the current response measured for a further 5 s. In order to extract diffusion coefficients and solubility data from these transients, the first potential step was fitted as before using the a nonlinear curve fitting function in the software package Origin 7.0 (Microcal Software Inc.) following Equations 4.1, 4.2 and 4.3 as proposed by Shoup and Szabo. To model the second potential step, a computer simulation program (described by Klymenko *et al.*)[16] was employed. Values of D and nc obtained from Shoup and Szabo[14] analysis of experimental data were input into simulation software and values of D for the reverse step were varied until the best fit between theoretical and experimental data was achieved. The best fit is achieved using the weighted sum of squared differences between the experimentally measured and theoretical currents. Further details of this fitting program are outlined by Klymenko *et al.*[16]

References

[1] Bonhôte, P.; Dias, A.-P.; Papageorgiou, N.; Kalyanasundaram, K. and Grätzel, M., *Inorg. Chem.*, 1996, **35**, 1168–1178.

[2] Ignat′ev, N.; Welz-Biermann, U.; Kucheryna, A.; Bissky, G. and Willner, H., *J. Fluorine Chem.*, 2005, **126**, 1150–1159.

[3] Okoturo, O. O. and VanderNoot, T. J., *J. Electroanal. Chem.*, 2004, **568**, 167–181.

[4] MacFarlane, D. R.; Meakin, P.; Sun, J.; Amini, N. and Forsyth, M., *J. Phys. Chem. B*, 1999, **103**, 4164–4170.

[5] Seddon, K. R.; Stark, A. and Torres, M.-J., *ACS Symp. Ser.*, 2002, **819**, 34–39.

[6] Cammarata, L.; Kazarian, S. G.; Salter, P. A. and Welton, T., *PhysChemChemPhys*, 2001, **3**, 5192–5200.

[7] http : //ildb.merck.de.

[8] Huddleston, J. G.; Visser, A. E.; Reichert, W. M.; Willauer, H. D.; Broker, G. A. and Rogers, R. D., *Green Chem.*, 2001, **3**, 156–164.

[9] Pereiro, A. B.; Verdia, P.; Tojo, E. and Rodriguez, A., *J. Chem. Eng. Data*, 2007, **52**, 377–380.

[10] Sharp, M., *Electrochim. Acta*, 1983, **28**, 301–308.

[11] Schröder, U.; Wadhawan, J. D.; Compton, R. G.; Marken, F.; Suarez, P. A. Z.; Consorti, C. S.; de Souza, R. F. and Dupont, J., *New J. Chem.*, 2000, **24**, 1009–1015.

[12] Silvester, D. S.; Aldous, L.; Hardacre, C. and Compton, R. G., *J. Phys. Chem. B*, 2007, **111**, 5000–5007.

[13] Evans, R. G.; Klymenko, O. V.; Price, P. D.; Davies, S. G.; Hardacre, C. and Compton, R. G., *ChemPhysChem*, 2005, **6**, 526–533.

[14] Shoup, D. and Szabo, A., *J. Electroanal. Chem.*, 1982, **140**, 237–245.

[15] Rees, N. V.; Klymenko, O. V.; Coles, B. A. and Compton, R. G., *J. Electroanal. Chem.*, 2002, **534**, 151–161.

[16] Klymenko, O. V.; Evans, R. G.; Hardacre, C.; Svir, I. B. and Compton, R. G., *J. Electroanal. Chem.*, 2004, **571**, 211–221.

Chapter 5

The Effect of Water as an Impurity on Room Temperature Ionic Liquids

The effect of water content on RTILs was studied by Karl Fischer titration and cyclic voltammetry in the following ionic liquids: $[P_{14,6,6,6}][FAP]$, $[C_4mpyrr][NTf_2]$, $[C_6mim][FAP]$, $[C_4mim][NTf_2]$, $[C_4dmim][NTf_2]$, $[N_{6,2,2,2}][NTf_2]$, $[C_4mim][PF_6]$, $[C_2mim][NTf_2]$, $[C_4mim][BF_4]$, $[C_4mim][I]$, $[C_4mim][OTf]$, and $[C_6mim][Cl]$. Karl Fischer titrations were carried out to determine the water content of RTILs for vacuum-dried, atmospheric and wet samples. The anion in particular was found to affect the level of water uptake. The hydrophobicity of the anions adhered to the following trend: $[FAP]^- > [NTf_2]^- > [PF_6]^- > [BF_4]^-$ > halides. Cyclic voltammetry shows that an increase in water content significantly narrows the electrochemical window of each ionic liquid. The electrochemical window decreases in the following order: vacuum-dried > atmospheric > wet at 298 K > 318 K > 338 K. The anodic and cathodic potentials *vs.* the Fc/Fc^+ internal reference couple are also listed under vacuum-dried and atmospheric conditions. The data obtained may aid the selection of an RTIL for use as a solvent in electrochemical applications.

5.1 Introduction

5.1.1 Water as an Impurity in RTILs

Water is considered to be one of the most significant impurities in RTILs as it is ubiquitous, and even hydrophobic RTILs absorb some from the atmosphere.[1] The effect of water on RTILs has been studied regarding properties such as viscosity, conductivity and electrochemical window. It has been shown that an increase in water content in an ionic liquid leads to a decrease in viscosity, accounting for many of the discrepancies in experimental viscosity measurements.[2,3] Viscosity values are related to conductivity values, since a decrease in viscosity enhances the mass transport of analyte to the electrode surface. Therefore, a change in the water content of an ionic liquid will also affect conductivity; as water content increases so does conductivity.[1] The relationship between water content and density of an RTIL has also been studied, and it has been shown that an increase in water content causes a decrease in the density of an ionic liquid. A decrease in viscosity and subsequent increase in conductivity may appear to be advantageous. However, an increase in water content results a reduction in the electrochemical window of an ionic liquid.[4] The narrowing of the electrochemical window occurs at both the cathodic and anodic limits. The process responsible for this is likely water electrolysis.[5] It has been reported that ionic liquids containing the $[PF_6]^-$ and $[BF_4]^-$ anions can exhibit the largest electrochemical window, but such anions are susceptible to hydrolysis when in contact with water and can result in the undesirable evolution of hydrogen fluoride.[6] With this in mind, studies have been carried out to examine which RTILs have the greatest water uptake. In particular, Ignat'ev *et al.* have studied several ionic liquids containing the $[FAP]^-$ anion, a hydrophobic anion that is immiscible with water.[7] The water uptake for $[FAP]^-$ RTILs is much less than that for RTILs containing other anions such as $[NTf_2]^-$ and $[PF_6]^-$. In fact, the level of water uptake in $[PF_6]^-$-containing RTILs has been shown to have interesting effects on the diffusion properties of analyte species within.[5]

This Chapter provides numerical data on the water contents and effect of water on the electrochemical windows of several RTILs. RTILs, whether they are hydrophobic or hydrophilic in nature, can absorb considerable amounts of water, which changes their physical and chemical properties.[5] This is of particular interest where electrochemical sensing is concerned. RTILs have been particularly well documented as solvents for gas sensing for gases such as O_2,[8] NO_2,[9] H_2,[10] SO_2[11] and H_2S.[12] The uptake of water from any source decreases the wide electrochemical windows of RTILs and can limit their use as sensing solvents. RTIL-modified electrodes at a liquid—liquid interface with aqueous solution has also been studied over the last number of years[13–15] to substitute volatile organic solvents with more thermally stable RTILs. The effects of water on RTILs would be of particular interest in this field. In this Chapter, we will show the extent of water uptake of several RTILs, as well as its effect on the electrochemical window of ionic liquids. This provides information to aid the selection of RTILs as solvents for electrochemical experiments.

5.2 Results and Discussion

In this Chapter, we present numerical data on the water content of twelve RTILs calculated using the Karl Fischer titration method. This data gives an indication of the hydrophobicity or hydrophilicity of each RTIL. We also present data showing the effect of water on the electrochemical window of twelve RTILs. The electrochemical window is calculated *vs.* the Fc/Fc^+ internal redox couple.[16] The limits of the electrochemical window are at current densities of 1 mA cm^{-2} and 5 mA cm^{-2}. These current densities are small to give a realistic indication of a suitable electrochemical window of RTILs for use as solvents for sensing at low concentrations of analyte.

5.2.1 Karl Fischer Titrations

We examined the water content of twelve RTILs with different cations and anions. The water content of each ionic liquid was obtained using a Karl Fischer Titrator. Each RTIL was tested for water under three types of conditions: atmospheric, vacuum-dried, and wet. The atmospheric samples were those used straight from the bench without any attempt at drying or purification. The vacuum-dried samples were purged under vacuum for 24 h while stirring continuously at a temperature of 333 K. The wet RTILs were mixed with water in a glass tube and allowed to stand for 24 h. The measured water contents are presented in Table 5.1 and are organized in order of increasing hydrophilicity of air-equilibrated samples. It should be noted that the first RTIL listed in Table 5.1 was tested for water content under atmospheric conditions only, as too little sample was left over for further tests.

Table 5.1: Water content$^{\phi}$ of twelve RTILs in atmospheric, vacuum-dried and wet conditions at 298 K. Atmospheric: used straight from the bench without any attempt at drying or purification. Vacuum-dried: dried under vacuum for 24 h at 333 K while continuously stirring. Wet: mixed with equal parts of water for 24 h, immiscible water layer was decanted off.

RTIL	Atmospheric/ppm	Vacuum-dried/ppm	Wet/ppm
$[P_{14,6,6,6}][FAP]$	328	-	-
$[C_4mpyrr][NTf_2]$	406	133	11,407
$[C_6mim][FAP]$	417	203	3068
$[C_4mim][NTf_2]$	491	144	5680
$[C_4dmim][NTf_2]$	504	295	9868
$[N_{6,2,2,2}][NTf_2]$	1150	167	8200
$[C_4mim][PF_6]$	2119	268	24,194
$[C_2mim][NTf_2]$	3385	105	19,940
$[C_4mim][BF_4]$	5083	119	Miscible
$[C_4mim][I]$	11,349	1050	Miscible
$[C_4mim][OTf]$	15,227	250	Miscible
$[C_6mim][Cl]$	61,049	2231	Miscible

$^{\phi}$Water content given by Aquamax KF standard W/w calculation mode.
Result (ppm) = $\frac{microgram\ count}{W-w}$
Where W = total weight of sampler + sample (mg)
and w = tare weight of empty sampler (mg)

The miscibility of RTILs with water is determined to a large extent by the anion. The $[FAP]^-$ RTILs appear to be quite hydrophobic and immiscible with water. The water uptake of $[FAP]^-$ RTILs is generally less than those containing the $[NTf_2]^-$ anion and much less than those containing the $[PF_6]^-$.[7] This is shown in Table 5.1, where $[P_{14,6,6,6}][FAP]$ and $[C_6mim][FAP]$ have two of the three lowest water content values in atmospheric conditions. RTILs containing anions such as $[NTf_2]^-$ and $[PF_6]^-$ are also immiscible and present a phase split in water at room temperature.[17,18] The water uptake of RTILs containing the $[NTf_2]^-$ anion are also relatively low (compared to other anions) in atmospheric conditions. Each IL containing the $[NTf_2]^-$ cation (with the exception of $[C_2mim][NTf_2]$) has lower water content levels than the $[PF_6]^-$ ionic liquid, and some have water content levels comparable to the very hydrophobic $[FAP]^-$ RTILs. Halide, $[BF_4]^-$ and $[OTf]^-$ ionic liquids are miscible with water and this trend is evident in Table 5.1; the halide, $[BF_4]^-$ and $[OTf]^-$ RTILs have the highest water content in atmospheric conditions. $[OTf]^-$ likely hydrogen-bonds strongly to water due to the presence of the $[SO_3]^-$ group and therefore has a high water content.

The identity of the anion appears to be a main factor in controlling the extent to which RTILs can be dried. The third column of Table 5.1 shows the water content of each IL under vacuum-dried conditions. The general trend of hydrophobicity of ionic liquids containing the $[FAP]^-$, $[NTf_2]^-$ and $[PF_6]^-$ anions is observed. However, it is interesting to note that the water content of $[C_4mim][OTf]$ and $[C_4mim][BF_4]$ after vacuum drying is comparable with the more hydrophobic ionic liquids, while the RTILs containing halide anions still contain over 1000 ppm water after drying. The fourth column of Table 5.1 shows the water content of wet RTILs. As before, a general trend of hydrophobicity of RTILs containing $[FAP]^-$ and $[NTf_2]^-$ anions is observed. There is an exception to this trend; $[C_4mpyrr][NTf_2]$ has a water content level higher than expected from its atmospheric water content. It is also noteworthy that even though $[C_4mim][OTf]$ and $[C_4mim][BF_4]$ were seen to have a lower water content than anticipated after

vacuum drying, they are miscible with water under saturated conditions, which is expected. Therefore, hydrophobicity of anions here follow the general trend: $[FAP]^- > [NTf_2]^- > [PF_6]^- > [BF_4]^- >$ halides, as previously suggested in the literature.[19–21]

The cation of an ionic liquid also affects its hydrophobicity and hydrophilicity. Hydrophobicity of an ionic liquid increases with increasing alkyl chain length.[18] This trend is observed in atmospheric conditions for $[C_4mim][NTf_2]$ and $[C_2mim][NTf_2]$ which have water content values of 491 ppm and 3385 ppm respectively at 298 K. This trend has also been observed with respect to $[BF_4]^-$ imidazolium RTILs, where the alkyl chain of $[C_nmim]^+$ with $n < 6$ is water soluble.[19]

The experimentally-obtained values in Table 5.1 are not in perfect agreement with literature values for water content of dried or saturated RTILs.[19] However, miscibility values of halide and $[BF_4]^-$ RTILs with water are in agreement with the literature.

5.2.2 Cyclic Voltammetry of RTILs Exposed to Atmospheric Moisture at Different Temperatures

The effect of water on the electrochemical window of twelve RTILs was examined using cyclic voltammetry on a Pt microelectrode (diameter 10 μm) *vs.* Pt quasi reference electrode at scan rate of 100 mV s^{-1}. Figure 5.1 shows the full electrochemical windows on platinum for four RTILs ($[C_2mim][NTf_2]$, $[C_4mim][OTf]$, $[C_4mim][BF_4]$ and $[C_4mim][PF_6]$) under vacuum-dried, atmospheric, wet conditions at increasing temperatures (see Chapter Experimental for definitions). In vacuum-dried conditions, little or no atmospheric moisture was present resulting in a redox window free of voltammetric features. In atmospheric conditions, the electrochemical windows were found to decrease, and the reduction of atmospheric oxygen was seen at a potential between -1.0 V and -1.5 V. Finally, water was added into the cell to create a wet atmosphere around the RTIL. With the addition of water into the cell, the amount of moisture uptake of the RTILs increased significantly as seen by the narrowing of the electrochemical windows in

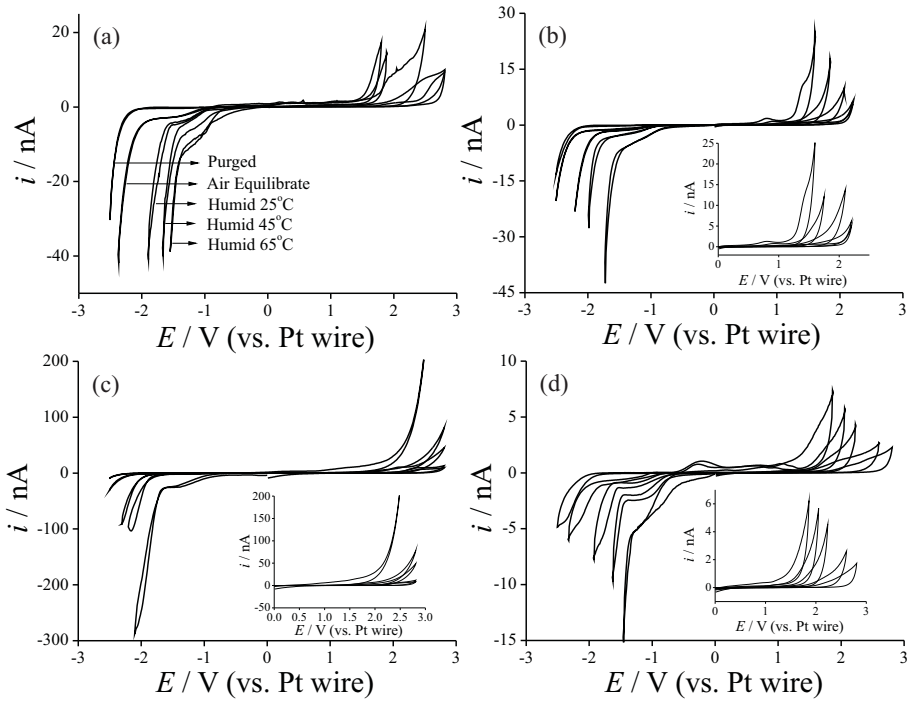


Figure 5.1: Effect of water on the electrochemical window of (a) $[C_2mim][NTf_2]$, (b) $[C_4mim][OTf]$, (c) $[C_4mim][BF_4]$, and (d) $[C_4mim][PF_6]$ with increasing water content for vacuum-dried, atmospheric, and wet conditions. Wet conditions are measured at temperatures (298, 318 and 338) K. CV carried out on 10 μm Pt Electrode *vs.* Pt wire (0.3 mm). No Fc/Fc^+ internal reference present in scans below (Fc/Fc^+ internal reference is present for numerical data). Each scan is taken at 100 mV s^{-1}.

Figure 5.1. This behaviour is known and has been observed previously by Silvester *et al.* They presented the voltammetry of $[C_4mim][OTf]$ and showed a decrease in the electrochemical window from vacuum-dried conditions to atmospheric conditions.[4] In this Chapter, in all twelve RTILs, a reduction in the electrochemical window was observed with increasing temperature.

The insets to Figure 5.1 show the anodic scan only of $[C_4mim][OTf]$, $[C_4mim][BF_4]$ and $[C_4mim][PF_6]$. The voltammograms were typically scanned from 0.0 to +2.8 V *vs.* a Pt quasi-reference electrode under the same conditions as the redox scans above. These anodic scans show little difference to the redox scans in the same electrochemical window, however, it is apparent from Figure 5.1(d), that the reverse of the redox scans (particularly for higher temperatures) at 1.0 V have some features that are not present on the oxidative scans, probably due to the oxidation of a product formed during the reduction of water/oxygen. The anodic window also

decreases significantly with increasing water content.

The quantitative effect of water impurities on the electrochemical window of twelve RTILs is given in Table 5.2. Ferrocene was added to the system as an internal standard so as to determine the anodic and cathodic limits relative to the Fc/Fc^+ potential for the quantitative data.[16] The electrochemical window (in volts) *vs.* Fc/Fc^+ is recorded in vacuum-dried conditions, atmospheric conditions, and wet conditions at (298, 318 and 338) K. The magnitudes of the electrochemical windows are defined by current densities (j) of 1 mA cm^{-2} and 5 mA cm^{-2}. These current densities are chosen to be quite low and should facilitate a realistic electrochemical window size, particularly for gas sensing at very low concentrations of analyte.

Table 5.2: Effect of atmospheric moisture on the electrochemical window of twelve RTILs. Electrochemical window limits *vs.* Fc/Fc^+ at current densities (j) of 1 mA cm^{-2} (j=1) and 5 mA cm^{-2} (j=5). Vacuum-dried: dried under vacuum for 90 min. Atmospheric: used straight from the bench without any attempt at drying or purification. Wet: in a water-sat. atmosphere at temperatures (298, 318 and 338) K.

	E(Vacuum-dried)/V		E(Atmospheric)/V		E(Wet at 298 K)/V		E(Wet at 318 K)/V		E(Wet at 338 K)/V	
RTIL	j=1	j=5	j=1	j=5	j=1	j=5	j=1	j=5	j=1	j=5
$[P_{14,6,6,6}][FAP]$	5.2	5.4	3.2	4.0	1.8	2.6	1.6	2.1	0.8	2.0
$[C_4mpyrr][NTf_2]$	4.2	5.2	3.0	4.6	2.0	2.8	2.0	2.9	1.2	1.4
$[C_6mim][FAP]$	4.6	4.8	3.0	3.7	2.5	3.3	2.4	2.7	1.6	2.6
$[C_4mim][NTf_2]$	4.3	5.0	2.9	3.5	2.8	3.7	2.4	2.9	1.4	2.5
$[C_4dmim][NTf_2]$	4.7	5.2	3.3	4.4	2.9	3.8	2.4	3.1	1.4	2.5
$[N_{6,2,2,2}][NTf_2]$	4.7	5.4	2.3	4.6	2.2	3.4	1.9	2.5	1.7	1.7
$[C_4mim][PF_6]$	4.8	5.0	3.9	4.5	2.6	3.1	1.7	2.9	1.6	1.9
] $[C_2mim][NTf_2]$	4.2	4.6	2.8	3.7	2.6	3.2	1.4	2.5	0.7	1.6
$[C_4mim][BF_4]$	4.6	5.1	2.4	4.0	2.0	3.6	2.4	3.2	2.3	2.8
$[C_4mim][I]$	2.0	2.2	1.9	2.2	1.6	1.8	0.0	0.5	0.0	0.0
$[C_4mim][OTf]$	4.2	5.1	3.3	4.8	2.7	4.2	1.5	2.7	1.3	2.8
$[C_6mim][Cl]$	3.0	3.3	2.9	3.3	2.4	2.8	2.4	2.3	1.4	1.4

It can be seen that most of the RTILs have electrochemical windows of *ca.* 4.2 to 5.4 V in vacuum-dried conditions, with the widest window seen in $[P_{14,6,6,6}][FAP]$. Increasing the amount of water impurities has the biggest effect on the electrochemical window of $[P_{14,6,6,6}][FAP]$, which has a window that decreases from 5.2 V when purged to 0.8 V in wet conditions at 338 K. $[FAP]^-$ ionic liquids generally possess very wide electrochemical windows as the $[FAP]^-$ anion is believed to be the most stable to oxidation.[7] The water uptake for these ionic liquids is much less than that of the RTILs containing other anions as can be seen from Table 5.1. Slightly wider electrochemical windows are observed for $[NTf_2]^-$ anions compared to $[BF_4]^-$ and $[PF_6]^-$ in vacuum-dried conditions at current density 5 mA/cm^{-2}, although the difference is not significant, being only of the order of 0 to 400 mV. The electrochemical windows of these anions are comparable at current density 1 mA cm^{-2}. The RTILs with the smallest electrochemical window are $[C_4mim][I]$ and $[C_6mim][Cl]$ due to the relatively low oxidation of the halide ion. The decrease in electrochemical window of all twelve RTILs from vacuum-dried conditions to wet conditions at 338 K is significant, and to the order of 1.6 to 4.4 V.

The anodic and cathodic potentials *vs.* the Fc/Fc^+ internal reference are listed in Table 5.3 for current density 1 mA cm^{-2}, and Table 5.4 for current density 5 mA cm^{-2}. Potential values are listed for vacuum-dried and atmospheric conditions. This is important when selecting an IL for an electrochemical experiment because the redox signals of an analyte must fall within the electrochemical window of the RTIL, and this can be conveniently quantified using an internal reference. This table is particularly useful for experiments employing RTILs as electrolyte sensors, as one can select an RTIL with a suitable electrochemical window *vs.* ferrocene where the analytes' signals will be clearly visible.

Table 5.3: Anodic and cathodic potentials *vs.* Fc/Fc^+ for electrochemical window of twelve RTILs at current density 1 mA cm^{-2}. Vacuum-dried: dried under vacuum for 90 min. Atmospheric: used straight from the bench without any attempt at drying or purification.

	Vacuum-dried			Atmospheric		
RTIL	E(Cathodic)/V	E(Anodic)/V	E(Total)/V	E(Cathodic)/V	E(Anodic)/V	E(Total)/V
$[P_{14,6,6,6}][FAP]$	-2.7	+2.5	5.2	-1.5	+1.7	3.2
$[C_4mpyrr][NTf_2]$	-2.8	+1.4	4.2	-1.4	+1.6	3.0
$[C_6mim][FAP]$	-2.6	+2.0	4.6	-1.3	+1.7	3.0
$[C_4mim][NTf_2]$	-2.5	+1.8	4.3	-1.3	+1.6	2.9
$[C_4dmim][NTf_2]$	-2.5	+2.2	4.7	-1.5	+1.8	3.3
$[N_{6,2,2,2}][NTf_2]$	-2.6	+2.1	4.7	-1.4	+1.9	2.3
$[C_4mim][PF_6]$	-2.7	+2.1	4.8	-1.7	+2.2	3.9
$[C_2mim][NTf_2]$	-2.2	+2.0	4.2	-1.2	+1.6	2.8
$[C_4mim][BF_4]$	-2.6	+2.0	4.6	-1.1	+1.3	2.4
$[C_4mim][I]$	-2.0	+0.0	2.0	-1.9	+0.0	1.9
$[C_4mim][OTf]$	-2.6	+1.6	4.2	-1.6	+1.7	3.3
$[C_6mim][Cl]$	-2.6	+0.4	3.0	-2.4	+0.5	2.9

Table 5.4: Anodic and cathodic potentials *vs.* Fc/Fc^+ for electrochemical window of twelve RTILs at current density 5 mA cm^{-2}. Vacuum-dried: dried under vacuum for 90 mins. Atmospheric: used straight from the bench without any attempt at drying or purification.

	Vacuum-dried			Atmospheric		
RTIL	E(Cathodic)/V	E(Anodic)/V	E(Total)/V	E(Cathodic)/V	E(Anodic)/V	E(Total)/V
$[P_{14,6,6,6}][FAP]$	-2.8	+2.6	5.4	-1.9	+2.1	4.0
$[C_4mpyrr][NTf_2]$	-3.2	+2.0	5.2	-2.0	+2.6	4.6
$[C_6mim][FAP]$	-2.4	+2.4	4.8	-1.7	+2.0	3.7
$[C_4mim][NTf_2]$	-2.7	+2.3	5.0	-1.5	+2.0	3.5
$[C_4dmim][NTf_2]$	-2.7	+2.5	5.2	-2.1	+2.3	4.4
$[N_{6,2,2,2}][NTf_2]$	-3.0	+2.4	5.4	-2.4	+2.2	4.6
$[C_4mim][PF_6]$	-2.9	+2.1	5.0	-2.1	+2.4	4.5
$[C_2mim][NTf_2]$	-2.4	+2.2	4.6	-2.0	+1.7	3.7
$[C_4mim][BF_4]$	-2.8	+2.3	5.1	-2.0	+2.0	4.0
$[C_4mim][I]$	-2.1	+0.1	2.2	-2.0	+0.1	2.1
$[C_4mim][OTf]$	-2.8	+2.3	5.1	-2.6	+2.2	4.8
$[C_6mim][Cl]$	-2.7	+0.6	3.3	-2.7	+0.6	3.3

5.3 Conclusions

The effect of water on the electrochemical windows of RTILs has been studied in twelve different ionic liquids. The water content of each ionic liquid in different conditions (vacuum-dried, atmospheric and wet) was quantified, and a large variation in water uptake was observed. This variation in water content was mostly due to the identity of the anions in the ionic liquids and adhered to the following trend: $[FAP]^- > [NTf_2]^- > [PF_6]^- > [BF_4]^- > [OTf]^-$ > halides. A reduction in the electrochemical window at both the cathodic and anodic limits with increasing water content in each ionic liquid was observed. The decrease of the electrochemical windows has been measured against a standard internal reference couple, and the anodic and cathodic potentials *vs.* Fc/Fc^+ internal reference were presented under vacuum-purged and air-equilibrated conditions. This will aid the selection of RTILs for various electrochemical experiments, including the following body of work for the fabrication of a gas sensor for H_2S employing RTILs as the electrolyte. In the next two chapters we observe the voltammetry of H_2S in a variety of dry RTILs and note some differences in solubility and diffusion for each RTIL, as well as some differences in the diffusion layer of H_2S in RTILs compared to conventional solvents.

References

[1] Widegren, J. A.; Saurer, E. M.; Marsh, K. N. and Magee, J. W., *J. Chem. Thermodyn.*, 2005, **37**, 569–575.

[2] Widegren, J. A.; Laesecke, A. and Magee, J. W., *Chem. Commun.*, 2005, pages 1610–1612.

[3] Kelkar, M. and Maginn, E., *J. Phys. Chem. B*, 2007, **111**(18), 4867–4876.

[4] Silvester, D. S. and Compton, R. G., *Z. Phys. Chem.*, 2006, **220**, 1247–1274.

[5] Schröder, U.; Wadhawan, J. D.; Compton, R. G.; Marken, F.; Suarez, P. A. Z.; Consorti, C. S.; de Souza, R. F. and Dupont, J., *New J. Chem.*, 2000, **24**, 1009–1015.

[6] Buzzeo, M. C.; Hardacre, C. and Compton, R. G., *ChemPhysChem*, 2006, **7**, 176–180.

[7] Ignat′ev, N.; Welz-Biermann, U.; Kucheryna, A.; Bissky, G. and Willner, H., *J. Fluorine Chem.*, 2005, **126**, 1150–1159.

[8] Buzzeo, M. C.; Klymenko, O. V.; Wadhawan, J. D.; Hardacre, C.; Seddon, K. R. and Compton, R. G., *J. Phys. Chem. A*, 2003, **107**, 8872–8878.

[9] Broder, T. L.; Silvester, D. S.; Aldous, L.; Hardacre, C. and Compton, R. G., *J. Phys. Chem. B*, 2007, **111**, 7778–7785.

[10] Silvester, D. S.; Aldous, L.; Hardacre, C. and Compton, R. G., *J. Phys. Chem. B*, 2007, **111**, 5000–5007.

[11] Barrosse-Antle, L.; Silvester, D. S.; Aldous, L.; Hardacre, C. and Compton, R. G., *J. Phys. Chem. C*, 2008, **112**, 3398–3404.

[12] O' Mahony, A.; Silvester, D. S.; Aldous, L.; Hardacre, C. and Compton, R. G., *J. Phys. Chem. C*, 2008, **112**, 7725–7730.

[13] Wadhawan, J. D.; Schröder, U.; Neudeck, A.; Wilkins, S. J.; Compton, R. G.; Marken, F.; Consorti, C. S.; de Souza, R. F. and Dupont, J., *J. Electroanal. Chem.*, 2000, **493**, 75–83.

[14] Kakiuchi, T. and Tsujioka, N., *Electrochem. Commun.*, 2003, **5**, 253–256.

[15] Roznіecka, E.; Shul, G.; Sirieix-Plenet, J.; Gaillon, L. and Opallo, M., *Electrochem. Commun.*, 2005, **7**, 299–304.

[16] Rogers, E. I.; Silvester, D. S.; Poole, D. L.; Aldous, L.; Hardacre, C. and Compton, R. G., *J. Phys. Chem. C*, 2008, **112**, 2729–2735.

[17] Rivera-Rubero, S. and Baldelli, S., *J. Am. Chem. Soc.*, 2004, **126**(38), 11788–11789.

[18] Friere, M. G.; Santos, L. M. N. B. F.; Fernandes, A. M.; Coutinho, J. A. P. and Marrucho, I. M., *Fluid Phase Equilib.*, 2007, **261**, 449–454.

[19] Huddleston, J. G.; Visser, A. E.; Reichert, W. M.; Willauer, H. D.; Broker, G. A. and Rogers, R. D., *Green Chem.*, 2001, **3**, 156–164.

[20] Kato, H.; Nishikawa, K. and Koga, Y., *J. Phys. Chem. B*, 2008, **112**, 2655–2660.

[21] Endres, F.; MacFarlane, D. R. and Abbot, A., *Electrodeposition from Ionic Liquids*, Wiley, Weinheim Germany, 2008.

Chapter 6

The Reduction of Hydrogen Sulfide in Room Temperature Ionic Liquids

The electrochemical reduction of 1 atm. H_2S gas has been studied at a platinum microelectrode (10 μm diameter) in five RTILs: [C_2mim][NTf_2], [C_4mpyrr][NTf_2], [C_4mim][OTf], [C_4mim][NO_3] and [C_4mim][PF_6]. In all five RTILs, a chemically irreversible reduction peak was observed on the reductive sweep, followed by one or two oxidative peaks on the reverse scan. The oxidation peaks were assigned to the oxidation of HS^- and adsorbed hydrogen. In addition, a small reductive peak was observed prior to the large wave in [C_2mim][NTf_2] only, which may be due to the reduction of a sulfur impurity in the gas. Potential-step chronoamperometry was carried out on the reduction peak of H_2S revealing diffusion coefficients of 3.2, 4.6, 2.4, 2.7 and 3.1 $\times$ 10^{-10} m^2 s^{-1} and solubilities of 529, 236, 537, 438 and 230 mM in [C_2mim][NTf_2], [C_4mpyrr][NTf_2], [C_4mim][OTf], [C_4mim][NO_3] and [C_4mim][PF_6] respectively. The solubilities of H_2S in RTILs are much higher than that reported in conventional molecular solvents, suggesting that RTILs may be very favourable gas sensing media for H_2S detection.

6.1 Introduction

The focus of this Chapter is on the electrochemical reduction of H_2S gas, which is of major importance in the petrochemical industry, and whose toxicity has necessitated the development of monitoring devices.[1,2] The electrochemistry of H_2S has been well documented in various protic and aprotic solvents.[1,3–9] Most of these reports have predominantly focused on the oxidative features of H_2S on Pt electrodes.[4–6,8,9] A reduction wave for H_2S has been reported in aprotic solvents such as molten sulfide[9] (in the presence of H_2), and MeCN containing TEAP.[8] However, the mechanism for the reduction peak was not fully investigated, but some general observations were made. Banks and Winnick[9] conducted experiments for removing H_2S at high temperatures in purified molten Na_2S/K_2S on a graphite working electrode in the presence of hydrogen gas. They found high cathodic currents which were "steady-state" at low scan rates, becoming more transient at higher scan rates. Evans *et al.*[8] also briefly examined the reduction of H_2S at platinum electrodes in an MeCN/TEAP, showing a large "steady-state" peak followed by a transient oxidative peak on the reverse sweep, but did not suggest the identity of the peaks.

In addition to mechanistic studies, the solubility of H_2S has been reported in various solvents *e.g.* *n*-alkanes,[10] ethylene glycol,[11] acetone,[11] acetic acid,[11] chlorobenzene,[11] methanol and RTILs.[2,12] Information about gas solubilities is important for process design calculations in petrochemical industries, and the higher solubilities reported for RTILs compared to conventional solvents suggest scope for using RTILs as favourable gas sensing media.

This Chapter focuses on the detailed electrochemical reduction of H_2S in RTILs at Pt electrode (10 μm diameter) in five ionic liquids with different anions and cations (the structures of which are given in Chapter 4, Figure 4.2). A mechanism for the reduction of H_2S is suggested, and diffusion coefficients and solubilities have been calculated, providing some insight into the possible use of RTILs as H_2S gas sensing electrolyte media.

6.2 Results and Discussion

6.2.1 The Reduction of Hydrogen Sulfide in Various RTILs

The electrochemical reduction of H_2S has been examined in five different ionic liquids, namely $[C_2mim][NTf_2]$, $[C_4mpyrr][NTf_2]$, $[C_4mim][OTf]$, $[C_4mim][NO_3]$ and $[C_4mim][PF_6]$. Each ionic liquid showed featureless baselines when purged in a vacuum for 90 minutes, and hence were chosen as suitable solvents for electrochemical experiments.

6.2.1.1 Cyclic Voltammetry of H_2S in RTILs

Cyclic voltammetry for the reduction of a saturated solution of hydrogen sulfide (1 atm.) in all five ionic liquids on a Pt microelectrode (diameter 10μm) at a range of scan rates from 200 mV s^{-1} to 4000 mV s^{-1} is shown in Figure 6.1, in order of increasing viscosity of the RTIL (34, 89, 90, 266 and 371 cP respectively). The voltammograms were typically scanned from +1.0 V to -2.6 V *vs.* Pt quasi-reference electrode. In all five RTILs, a large reduction peak was observed, with one or two anodic peaks observed on the reverse sweep; the peaks are labeled in Figure 6.1 as peaks (I), (II) and (III). In four of the RTILs studied, the reduction peak, (I), observed at *ca.* -1.5 V to -2.5 V appears to be "steady-state"-like at lower scan rates, and becomes more transient at higher scan rates (peak (I) is transient at all scan rates studied in $[C_4mpyrr][NTf_2]$).

Common in all five RTILs, the oxidative back-peak (II) is very prominent, and its peak current increases systematically with scan rate. The wide peak separation between peaks (I) and (II) (*ca.* 1.8 V in all ionic liquids) suggests that peak (II) is more likely to be the oxidation of a product following the reduction of H_2S, and not part of a direct redox couple with peak (I). In three of the ionic liquids studied, there is also evidence of the appearance of a shoulder on peak (II), labeled peak (III), and the identity of all three peaks will be discussed in Section 6.2.1.2.

The peak currents obtained for the reductive peak (I) in this Chapter were difficult to

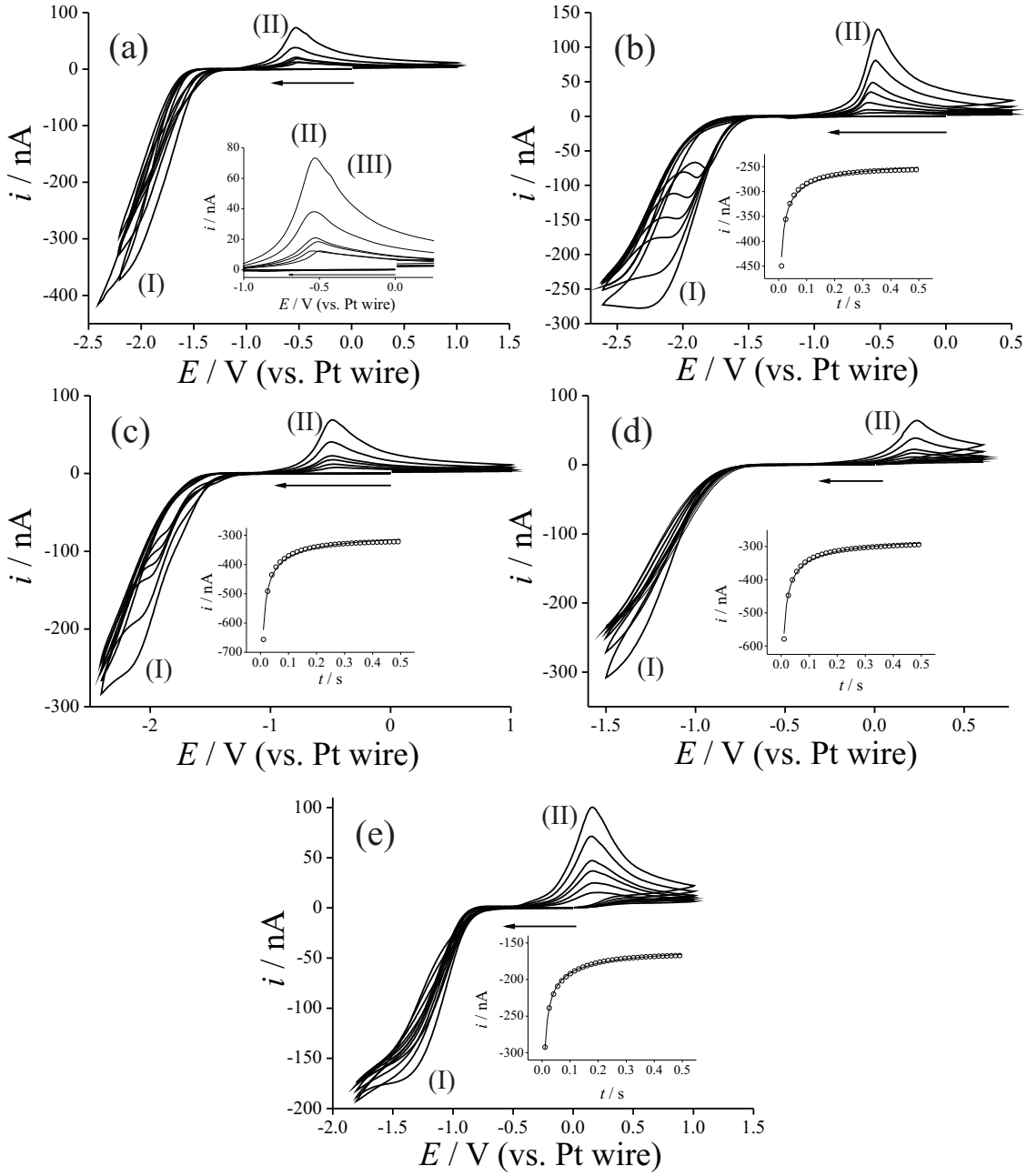


Figure 6.1: Cyclic voltammetry for the reduction of 1 atm. H_2S on a 10 μm diameter Pt electrode at 298 K, at scan rates of 200, 400, 700, 1000, 2000 and 4000 mV s^{-1} in the following ionic liquids: (a)[C_2mim][NTf_2], (b)[C_4mpyrr][NTf_2], (c)[C_4mim][OTf], (d)[C_4mim][NO_3], and (e)[C_4mim][PF_6].

determine, so a plot of peak current *vs.* square root scan rate could not be used to suggest if the process is diffusion controlled. However, the magnitude of the diffusion coefficients (*ca.* 10^{-10} m^2 s^{-1}, see later) suggest that the voltammetry observed is intermediate of micro/macro-electrode behaviour, according to the following inequality:

$$\nu \leq \frac{RTD}{nFr_{\mathrm{d}}{}^2} \tag{6.1}$$

(where ν is the scan rate, R is the universal gas constant, T the absolute temperature, D is the diffusion coefficient, F the Faraday constant, and r the radius of the disc). True steady-state behaviour can only be observed at scan-rates of less than *ca.* 250 mV s^{-1} (taking a typical diffusion coefficient of 3.0×10^{-10} m^2 s^{-1}). The scan rates studied in this Chapter (200 mV s^{-1} to 4000 mV s^{-1}) suggests that the voltammetry studied in this Chapter is between the region of pure micro- and pure macro-electrode behaviour.

There is also no evidence of a reaction of H_2S with the RTIL, or significant fouling of the electrode after the reduction of H_2S, since the electrochemical response of the ionic liquid after removal of H_2S appeared the same as that before the introduction of gas. This is consistent with that observed by Pomelli *et al.*, who showed that ionic liquids remained chemically unchanged following release of the H_2S.[2] The next section discusses the possible identity of peaks (I), (II) and (III).

6.2.1.2 Identity of Peaks (I), (II) and (III)

The reductive peak (I) is attributed to direct reduction of H_2S at the electrode surface to HS^-. The oxidative back peak (II) appears at potential of *ca.* -0.5 V to 0.4 V *vs.* Pt on the reverse scan, and is separated from peak (I) by *ca.* 1.8 V in all RTILs. Peak (II) is unlikely to be a back-peak from the re-oxidation of H_2S^-, but rather an oxidation of a reaction product following the electron transfer. The most likely identity for peak (II) is the oxidation of HS^-, probably

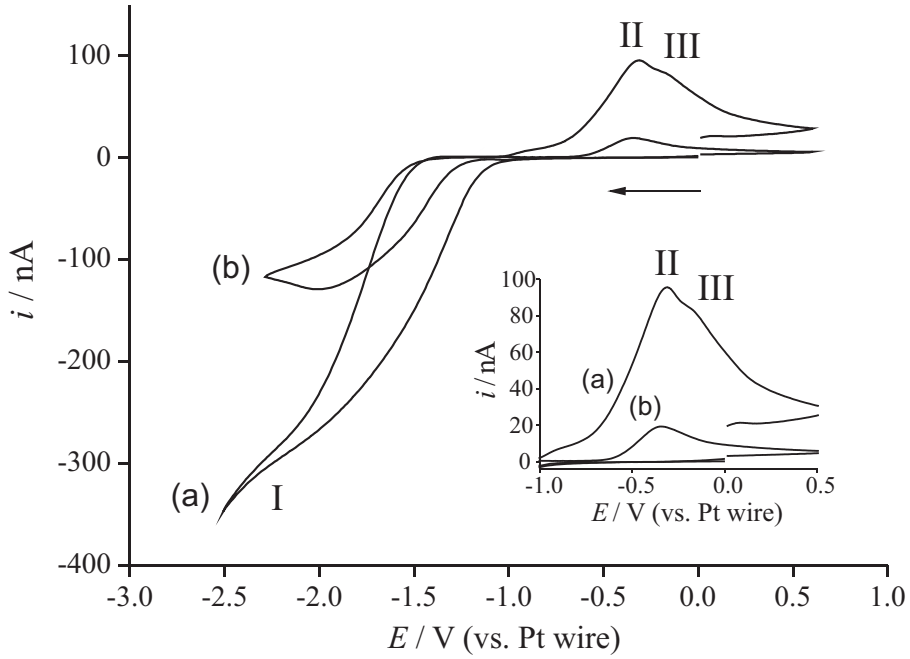


Figure 6.2: Cyclic voltammetry for the reduction of H_2S in [C_4mim][OTf] on (a) a Pt electrode (10 μm diameter), and (b) a Au electrode (5 μm diameter) at a scan rate of 4000 mV s^{-1} at 298 K.

to S. A shoulder peak (III) was also observed at a less negative potential in [C_2mim][NTf_2], [C_4mim][OTf] and [C_4mim][PF_6], which is believed to be the oxidation of adsorbed hydrogen. The oxidation of adsorbed hydrogen has been previously observed following the reduction of the ammonium ion in RTILs[13] at a potential of *ca.* -800 mV (in [C_4mim][OTf]) *vs.* the Fc/Fc^+ stable internal reference couple. The peak positions obtained from this Chapter for the reduction of H_2S on a 10 μm diameter Pt electrode are summarized in Table 6.1. Peak (III) appears at a position of *ca.* -800 mV *vs.* Fc/Fc^+, similar to that observed following the reduction of the ammonium ion.[13] In order to support this suggestion, the reduction of H_2S was also studied on a gold electrode, since hydrogen has previously been shown to be electrochemically active on Pt, but inactive on Au electrodes in RTILs.[14,15] Figure 6.2 shows cyclic voltammetry at 4000 mV s^{-1} for the reduction of 1 atm. H_2S in [C_4mim][OTf] on (a) Pt (10 μm diameter), and (b) Au (5 μm diameter) electrodes.

The peak positions on the Au electrode are also included in Table 6.1 for comparison, and

shows that peak (II) appears in the same place on both electrodes, but peak (III) is absent. This supports the identity of peak (III) as the oxidation of adsorbed hydrogen.

Table 6.1: Comparison of the peak positions *vs.* Fc/Fc^+ of peaks (I), (II) and (III) following the reduction of H_2S at Pt electrode (10 μm diameter) and Au electrode (5 μm diameter) in $[C_4mim][OTf]$ at scan rate 4000 mV s^{-1} and 298 K.

Electrode	(I)/mV	(II)/mV	(III)/mV	(IV)
Pt	-2500	-650	-800	-1700
Au	-2300	-650	n/a	n/a

The charge under peak (III) was calculated to be 2.7 $\times$ 10^{-10} mol cm^{-2}, which gives a surface coverage of 1.7 $\times$ 10^{14} atoms cm^2, corresponding to *ca.* 0.1 monolayers. Therefore, the following general mechanism is proposed:

Peak (I):

$$H_2S + e^- \rightarrow HS^- + H\bullet_{(ads)} (\text{or } \frac{1}{2}H_2) \tag{6.2}$$

Peak (II)

$$HS^- - e^- \rightarrow H\bullet_{(ads)} (\text{or} \frac{1}{2}H_2) + S \tag{6.3}$$

Peak (III):

$$H\bullet_{(ads)} - e^- \rightleftharpoons H^+ (\text{or } HNTf_2) \tag{6.4}$$

6.2.1.3 Potential Step Chronoamperometry

A potential step was carried out on the reductive wave (I) of H_2S in order to calculate the solubility and diffusion coefficients in each ionic liquid. The potential was stepped from a position of zero current to a potential more negative than the reductive wave, and the current was measured for 0.5 seconds. Some representative chronoamperomentric transients are shown as a series of circles together with the theoretical fit (solid line) in in the insets to Figure 6.1. The experimental data were fitted to the Shoup and Szabo expression,[16] and the diffusion coefficients

and solubilities obtained are summarized in Table 6.2. The diffusion coefficients are of the same order of magnitude as the gases O_2,[17] NO_2,[18] H_2[14] and SO_2[19] gases in RTILs, and one order of magnitude larger than solid species in RTILs (*cf.* 5.34×10^{-11} m^2 s^{-1} for ferrocene in $[C_2mim][NTf_2]$), suggesting that the large reduction peak (I) is due to H_2S gas.

Table 6.2: Chronoamperometric data obtained from theoretical fitting to the Shoup and Szabo[16] expression for the electrochemical reduction of H_2S in different ionic liquids at 298 K.

Ionic Liquid	η at 293 K/cP	$D_{H_2S}/\times 10^{-10}$ m^2s^{-1}	c/mM	$Dc/\times 10^{-10}$ Mm^2s^{-1}
$[C_2mim][NTf_2]$	34	3.2 ($\pm$0.9)	529 ($\pm$116)	1693
$[C_4mpyrr][NTf_2]$	89	4.6 ($\pm$0.2)	236 ($\pm$13)	1086
$[C_4mim][OTf]$	90	2.4 ($\pm$0.1)	537 ($\pm$33)	1289
$[C_4mim][NO_3]$	266	2.7 ($\pm$0.3)	438 ($\pm$48)	1183
$[C_4mim][PF_6]$	371	3.1 ($\pm$0.5)	230 ($\pm$32)	713

According to the Stokes-Einstein relation[20] in Equation 6.5, for a simple diffusing species, a linear relationship is expected between the diffusion coefficients (D) and the inverse of viscosity. This relationship is commonly followed in conventional molecular solvents, and also for organic molecules,[21] ferrocene[22] and cobaltocenium hexafluorophosphate[22] in RTILs.

$$D = \frac{k_B T}{6\eta\pi\alpha} \tag{6.5}$$

where k_B is the Boltzmann constant, T is the temperature and α is the hydrodynamic radius of the diffusing species. A plot of the diffusion coefficient of H_2S *vs.* the inverse of viscosity shows no obvious linear relationship, suggesting that the Stokes-Einstein relation given in Equation 6.5 does not apply, probably because H_2S is too small a molecule. This observation is consistent with that observed for O_2,[23] H_2[15] and SO_2[19] gases in RTILs.

The solubilities of H_2S were calculated to be 529 mM, 236 mM, 537 mM, 438 mM and 230 mM in $[C_2mim][NTf_2]$, $[C_4mpyrr][NTf_2]$, $[C_4mim][OTf]$, $[C_4mim][NO_3]$ and $[C_4mim][PF_6]$ respectively. It is clear that the nature of the anion slightly influences the solubility of H_2S,

and appears to be of the order: [OTf]>[NTf_2]>[NO_3]>[PF_6]. These solubility values are much larger than those reported for oxygen and hydrogen in RTILs (*ca.* 4-12 mM[17] and 3-10 mM[15] respectively), and comparable to the solubility of SO_2 in RTILs (*ca.* 250-3500 mM).[19]

Table 6.3 shows the solubilities of H_2S in several RTILs reported by Pomelli *et al.*[2] using NMR spectroscopy. The solubilities of H_2S in other common organic solvents[10,11,24] are also given in Table 6.3. The solubility values in RTILs are clearly much greater than that in organic solvents, suggesting that RTILs may be very favourable as H_2S gas sensing media. The differences in the solubility values in RTILs reported by Pomelli *et al.*[2] compared to those reported in this Chapter (Table 6.2) may reflect the different conditions used by Pomelli *et al.*[2] (*e.g.* 14 atm. pressure, compared to 1 atm. used in this Chapter).

Table 6.3: Literature values for the solubility of H_2S in various ionic liquids and conventional molecular solvents at 298K.

Ionic liquid	Solubility[§]/mM	Solvent	Solubility[†]/mM
[C_2mim][NTf_2][2]	18,200	*n*-hexane[10]	42.9
[C_2mmim][NTf_2][2]	17,800	*n*-decane[10]	48.8
[C_4mim][BF_4][2]	17,900	*n*-dodecane[10]	52.1
[C_4mim][OTf][2]	15,600	Acetone[11]	75.0
[C_4mim][PF_6][2]	12,700	Acetic Acid[11]	29.5
[C_4mim][NTf_2][2]	11,800	Chlorobenzene[11]	53.2
[C_4mmim][NTf_2][2]	11,200	Methanol[11]	28.4

[§] at 14 atm. [†] at 1 atm.

Since the diffusion coefficients and solubilities shown in Table 6.2 vary somewhat with the solvent, the product of the two variables was calculated, and is presented in the final column in Table 6.2. The RTIL with the highest *Dc* value will give rise to the highest curent response *via* the Clark-cell approach,[17] and is therefore likely to be the most suitable medium for gas sensing. As can be seen in Table 6.2, all five ionic liquids examined in this Chapter have relatively high *Dc* values, suggesting that they may all be suitable for H_2S gas sensing. The least viscous RTIL, [C_2mim][NTf_2], appears to be the most sensitive of the five RTILs studied. [C_4mpyrr][NTf_2],

$[C_4mim][OTf]$ and $[C_4mim][NO_3]$ give intermediate responses, and $[C_4mim][PF_6]$ gives the lowest current response, as is expected from the larger viscosity.

6.2.1.4 Reduction of H_2S in $[C_2mim][NTf_2]$: Additional Voltammetric Features

The reduction of hydrogen sulfide has been discussed in detail in section 6.2.1. However, in $[C_2mim][NTf_2]$ an additional reduction feature was observed. A second reductive peak, at a potential -1.5 V, was seen prior to the large reductive feature described in section 7.2.1.1. This peak (IV) is quite small and is often masked by the magnitude of peak I. The reduction peak (IV), observed at -1.5 V in $[C_2mim][NTf_2]$, is "steady-state" in nature, and a typical voltammogram is shown in Figure 6.3 at a scan rate of 4000 mV s^{-1}.

In order to suggest the identity of this peak, further experiments were performed. Since there is only H_2S present in solution, there are a limited number of species (H^+, S, HS^-) which could give rise to such a peak. Therefore, the electrochemistry of both H^+ (in the form of $H[NTf_2]$), and elemental sulfur was studied. Since the reference electrode material used in this study is not stable to changes within the solution, a ferrocene internal reference couple was also added.

The reduction of 126 mM $H[NTf_2]$ (as a source of H^+) was carried out in $[C_2mim][NTf_2]$, and is presented in Figure 6.3(a) at scan rate 100 mV s^{-1} on a Pt electrode of diameter 10 μm, and is compared with a voltammogram of H_2S in the same ionic liquid *vs.* ferrocene. The peak position of the reduction of $H[NTf_2]$ is *ca.* 0.7 V *vs.* Fc/Fc^+, compared peak (IV) at *ca.* 1.7 V *vs.* Fc/Fc^+, suggesting that peak (IV) is not due to the reduction of $H[NTf_2]$. Next, the reduction of elemental sulfur was studied. Figure 6.3(b) shows the reduction of sulfur in $[C_2mim][NTf_2]$ on a Pt electrode (diameter 10 μm) at a scan rate of 100 mV s^{-1}, overlaid on the reduction peak (IV), with ferrocene added as an internal reference couple. The peak potential for the reduction of sulfur *vs.* Fc/Fc^+ is *ca.* 1.70 V. We therefore speculate that peak (IV) (from H_2S reduction) may be the reduction of elemental sulfur, present in as an impurity in the gas.

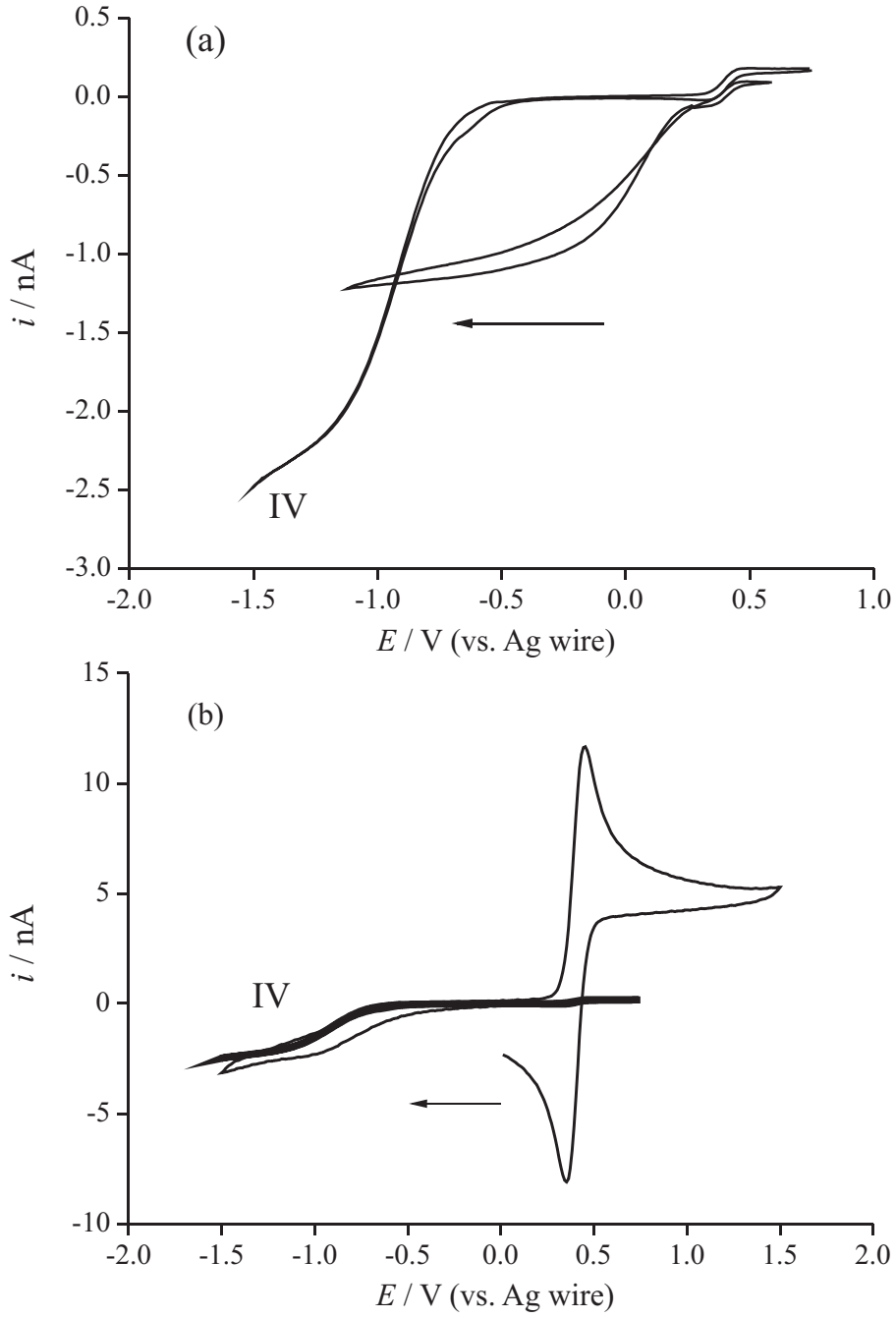


Figure 6.3: Cyclic voltammetry for the reduction of (a) H_2S (peak IV) and 126 mM $H[NTf_2]$ and (b) H_2S and elemental sulfur (bold line) in $[C_2mim][NTf_2]$ at Pt electrode (10 μm diameter) *vs.* the Fc/Fc^+redox couple at a scan rate of 4000 mV s^{-1} and temperature of 298 K.

6.3 Conclusions

The electrochemical reduction of 1 atm. H_2S has been studied in five RTILs. In all five solvents, a large "steady-state"-like reductive wave was observed at *ca.* -1.5 V to -2.5 V, which became transient at higher scan rates, and was attributed to the reduction of H_2S to HS^-. The two anodic peaks present on the back-scan were attributed to the oxidation of HS^- and adsorbed hydrogen, both products formed from the reduction of H_2S. From chronoamperometry, solubilities and diffusion coefficients for the reduction of H_2S were calculated in each RTIL, and H_2S gas was found to be very soluble in RTILs compared to conventional solvents, suggesting the possibility of using RTILs as favourable gas-sensing media. In addition, a further reductive wave (at a less negative potential to the reduction of H_2S) was also observed in $[C_2mim][NTf_2]$, and was thought to be due to the reduction of a sulfur impurity present in the gas. This has important implications in the analytical sensing of H_2S gas, and in understanding the reductive mechanism.

Chapter 7 aims to optimise this high solubility of H_2S in RTILs and observe the oxidative features of H_2S voltammetrically. The oxidation of H_2S was not clearly observed in this chapter due to the magnitude of oxidative peak of HS^-, and the high concentration of H_2S gas in the system. Therefore, 1% H_2S gas (with N_2 fill) was studied in several RTILs to see if a clearer oxidation peak was observed.

References

[1] Lawrence, N. S.; Davis, J.; Marken, F.; Jiang, L.; Jones, T. G. J.; Davies, S. N. and Compton, R. G., *Sens. Actuators, B*, 2000, **69**, 189–192.

[2] Pomelli, C.; Chiappe, C.; Vidis, A.; Laurenczy, G. and Dyson, P., *J. Phys. Chem. B*, 2007, **111**(45), 13014–13019.

[3] Opekar, F. and Bruckenstein, S., *Anal. Chem.*, 1984, **56**(8), 1206–1209.

[4] Chin, D. T. and Howard, P. D., *J. Electrochem. Soc.*, 1986, **133**(12), 2447–2450.

[5] Ramasubramanian, N., *J. Electroanal. Chem.*, 1975, **64**, 21–37.

[6] Najdeker, E. and Bishop, E., *J. Electroanal. Chem.*, 1973, **41**, 79–87.

[7] Berberova, N. and Shinkar, E., *Russ. Chem. Bull.*, 2000, **49**, 1178–1184.

[8] Evans, J.; Blount, H. and Ginnard, C. R., *J. Electroanal. Chem.*, 1975, **59**, 169–175.

[9] Banks, E. K. and Winnick, J., *J. Appl. Electrochem.*, 1986, **16**, 583–590.

[10] King, M. B. and Al-Najjar, H., *Chem. Eng. Sci.*, 1977, **32**, 1241–1246.

[11] Short, I.; Sahgal, A. and Hayduk, W., *J. Chem. Eng. Data*, 1983, **28**, 63–66.

[12] Jou, F.-Y. and Mather, A., *Internat. J. Thermophys.*, 2007, **28**, 490–495.

[13] Ji, X.; Banks, C. E.; Silvester, D. S.; Aldous, L.; Hardacre, C. and Compton, R. G., *Electroanalysis*, 2007, **19**, 2194–2201.

[14] Silvester, D. S.; Aldous, L.; Hardacre, C. and Compton, R. G., *J. Phys. Chem. B*, 2007, **111**, 5000–5007.

[15] Silvester, D. S.; Ward, K. R.; Aldous, L.; Hardacre, C. and Compton, R. G., *J. Electroanal. Chem.*, 2008, **618**, 53–60.

[16] Shoup, D. and Szabo, A., *J. Electroanal. Chem.*, 1982, **140**, 237–245.

[17] Buzzeo, M. C.; Klymenko, O. V.; Wadhawan, J. D.; Hardacre, C.; Seddon, K. R. and Compton, R. G., *J. Phys. Chem. A*, 2003, **107**, 8872–8878.

[18] Broder, T. L.; Silvester, D. S.; Aldous, L.; Hardacre, C. and Compton, R. G., *J. Phys. Chem. B*, 2007, **111**, 7778–7785.

[19] Barrosse-Antle, L.; Silvester, D. S.; Aldous, L.; Hardacre, C. and Compton, R. G., *J. Phys. Chem. C*, 2008, **112**, 3398–3404.

[20] Compton, R. G. and Banks, C. E., *Understanding Voltammetry*, World Scientific, 2007.

[21] Evans, R. G.; Klymenko, O. V.; Price, P. D.; Davies, S. G.; Hardacre, C. and Compton, R. G., *ChemPhysChem*, 2005, **6**, 526–533.

[22] Rogers, E. I.; Silvester, D. S.; Poole, D. L.; Aldous, L.; Hardacre, C. and Compton, R. G., *J. Phys. Chem. C*, 2008, **112**, 2729–2735.

[23] Evans, R. G.; Klymenko, O. V.; Saddoughi, S. A.; Hardacre, C. and Compton, R. G., *J. Phys. Chem. B*, 2004, **108**, 7878–7886.

[24] Koschel, D.; Coxam, J.-Y. and Majer, V., *Ind. Eng. Chem. Res.*, 2007, **46**(4), 1421–1430.

Chapter 7

The Oxidation of Hydrogen Sulfide in Room Temperature Ionic Liquids

The electrochemical oxidation of H_2S gas has been studied at a platinum microelectrode (10 μm diameter) in five RTILs: [C_4mim][OTf], [C_4dmim][NTf_2], [C_4mim][PF_6], [C_6mim][FAP] and [$P_{14,6,6,6}$][FAP]. In four of the RTILs ([C_4dmim][NTf_2], [C_4mim][PF_6], [C_6mim][FAP] and [$P_{14,6,6,6}$][FAP]), no clear oxidative signal was observed. In [C_4mim][OTf], a chemically irreversible oxidation peak was observed on the oxidative sweep with no signal seen on the reverse scan. The oxidative signal showed an adsorptive stripping peak type followed by near steady-state limiting current behavior. Potential-step chronoamperometry was carried out on the reductive wave giving a diffusion coefficient and solubility of 1.6×10^{-10} m^2 s^{-1} and 7 mM respectively (at 25^{o}C). Using these data the oxidation signal was modelled kinetically assuming adsorption preceding oxidation and that the adsorption was approximately Langmuirian. The oxidation step was described by an electrochemically fully irreversible Tafel law / Butler-Volmer formalism. The modelling indicated a substantial buildup of H_2S in the double layer in excess of the coverage that would be expected for a monolayer of chemisorbed H_2S, reflecting high solubility of the gas in [C_4mim][OTf] and possible attractive interactions with $[OTf]^-$ anions accumulated at the electrode at potentials positive of the potential of zero charge. Solute enrichment of the double layer in the solution adjacent of the electrode appears a novel feature of RTIL electrochemistry.

7.1 Introduction

In the present Chapter we consider the oxidation of H_2S and report voltammetry of an adsorbed electroactive species. Accordingly we have developed the theory of the linear sweep voltammetry of such processes at microdisc electrodes. With a knowledge of the solubility of H_2S in $[C_4mim][OTf]$ and its diffusion coefficient in this medium the model permits the inference of the extent of adsorption of H_2S. This model shows that unless there is significant accumulation of H_2S at the RTIL-Pt interface, giving local interfacial concentrations over and above those in bulk solution, then the predicted currents are significantly lower than measured. Accordingly, prior to oxidation we infer that the equivalent of several monolayers of gas must be present at the interface under equilibrated conditions. This is difficult to reconcile with chemisorption of H_2S, so we suggest that the double layer at the RTIL-Pt interface is enriched by the H_2S, reflecting both the high solubility of the gas and other possible attractive interactions with the $[OTf]^-$ anion likely to present as alternate layers with the $[C_4mim]^+$ cation at the interface.[1,2] Such multilayer physisorption of a species potentially mirrors behavior at the gas/solid interface (eg. N_2 on graphite) and also represents a significant physical difference between electrochemistry in RTILs as compared to conventional solvent media.

7.2 Results and Discussion

7.2.1 The Oxidation of Hydrogen Sulfide in Various RTILs

The oxidation of 1% H_2S was examined in five different RTILs: $[C_4mim][OTf]$, $[C_4dmim][NTf_2]$, $[C_4mim][PF_6]$, $[C_6mim][FAP]$ and $[P_{14,6,6,6}mim][FAP]$. Each ionic liquid showed featureless baselines when purged in a vacuum for 90 min. and each has favorable physical properties with respect to water content.[3] $[C_6mim][FAP]$ and $[P_{14,6,6,6}mim][FAP]$ were chosen as they contain the $[FAP]^-$ anion, which is considered highly hydrophobic, and these ionic liquids show little water

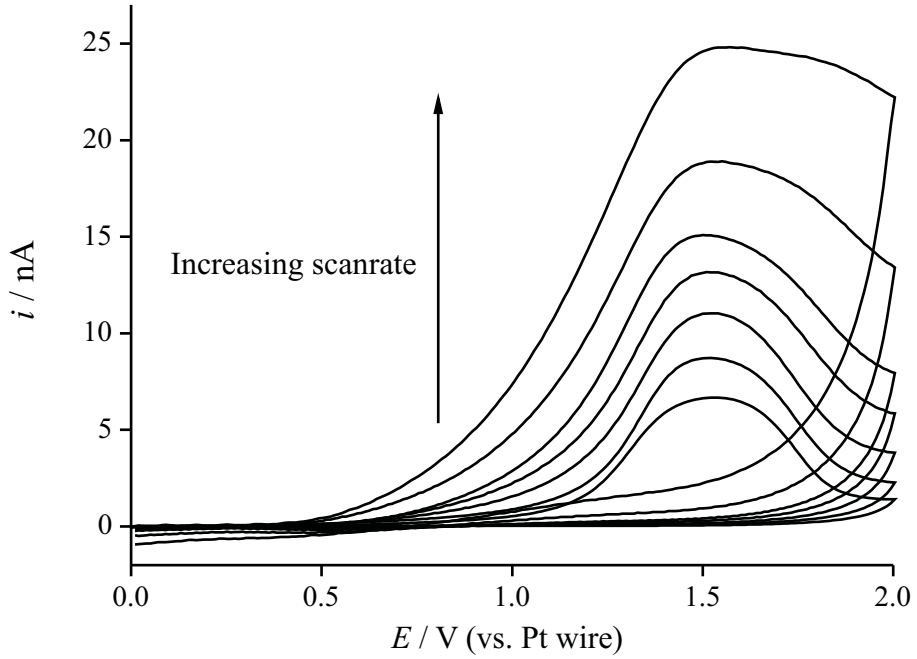


Figure 7.1: Cyclic voltammetry for the oxidation of 1 atm. 1% H_2S on a 10 μm diameter Pt electrode at 298 K, at scan rates of 100, 200, 400, 700, 1000, 2000 and 4000 mV s^{-1} in $[C_4mim][OTf]$.

uptake under atmospheric conditions.[3] $[C_4dmim][NTf_2]$ and $[C_4mim][PF_6]$ were chosen because they have the widest anodic windows under atmospheric conditions out of 12 RTILs studied.[3]

7.2.1.1 Cyclic Voltammetry of H_2S in RTILs

Cyclic voltammetry for the oxidation of a 1% solution of hydrogen sulfide (with N_2 fill at 1 atm.) was carried out on a Pt microelectrode (diameter 10μm) at scan rates from 100 mV s^{-1} to 4000 mV s^{-1}. The voltammograms are typically scanned from 0 V to 2.8 V *vs.* a Pt quasi-reference electrode. In $[C_4mim][OTf]$, a large oxidation peak was observed for scan rates 100 mV s^{-1} to 4000 mV s^{-1}, shown in Figure 7.1. The peak position of H_2S is calculated *vs.* the IUPAC recommended Fc/Fc^+ redox[4] couple in $[C_4mim][OTf]$, and is found to be +1.6 V.

The peak appears to be an adsorptive stripping peak, and increases systematically with scan rate. After the adsorptive peak, the current does not return to its baseline value, but approaches a steady state especially at low scan rates, suggesting that diffusive uptake by the surface is

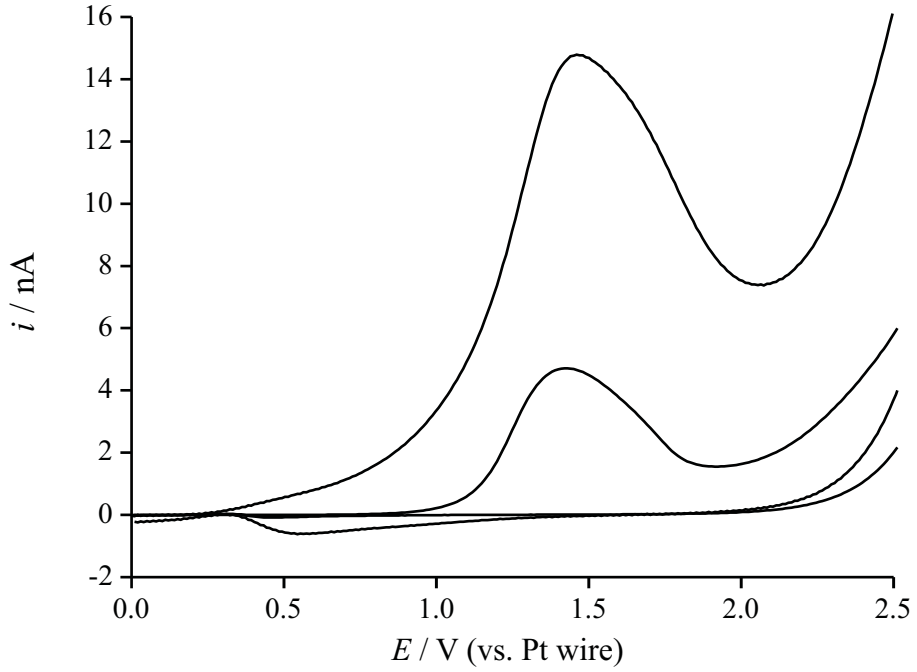


Figure 7.2: Cyclic voltammetry for the oxidation of 1% H_2S in [C_4mim][OTf] on a Pt electrode (10 μm diameter) at scan rates of 100 mV s^{-1} and 1000 mV s^{-1} at 298 K.

taking place after stripping. This feature increases with scan rate since under these conditions stripping is not completed until more positive potentials are attained, and this is clearly seen in Figure 7.2 for scan rates of 100 mV s^{-1} and 1000 mV s^{-1}. The signal also appears chemically irreversible as shown by the absence of any back peak following the oxidation, at all scan rates studied.

This oxidation peak is not a common feature to all five RTILs. Figure 7.3 shows the voltammetry of 1% H_2S in (a)[C_4dmim][NTf_2], (b)[C_4mim][PF_6], (c)[C_6mim][FAP], (d)[$P_{14,6,6,6}$mim][FAP], and (e)[C_4mim][OTf]. The dashed line signifies the voltammetry of the ionic liquid only, where no analyte is present. Previously, in Chapters 3 and 5, we have seen that RTIL electrochemistry is susceptible to halide and water impurities.[3,5] However, we see in Figure 7.3 that the voltammetry of the ionic liquid only is clean and shows a featureless baseline. Therefore we believe that any halide or water impurities are negligible. The solid line shows the voltammetry of 1% H_2S in each ionic liquid. Of the five RTILs examined, this clear adsorptive peak is only

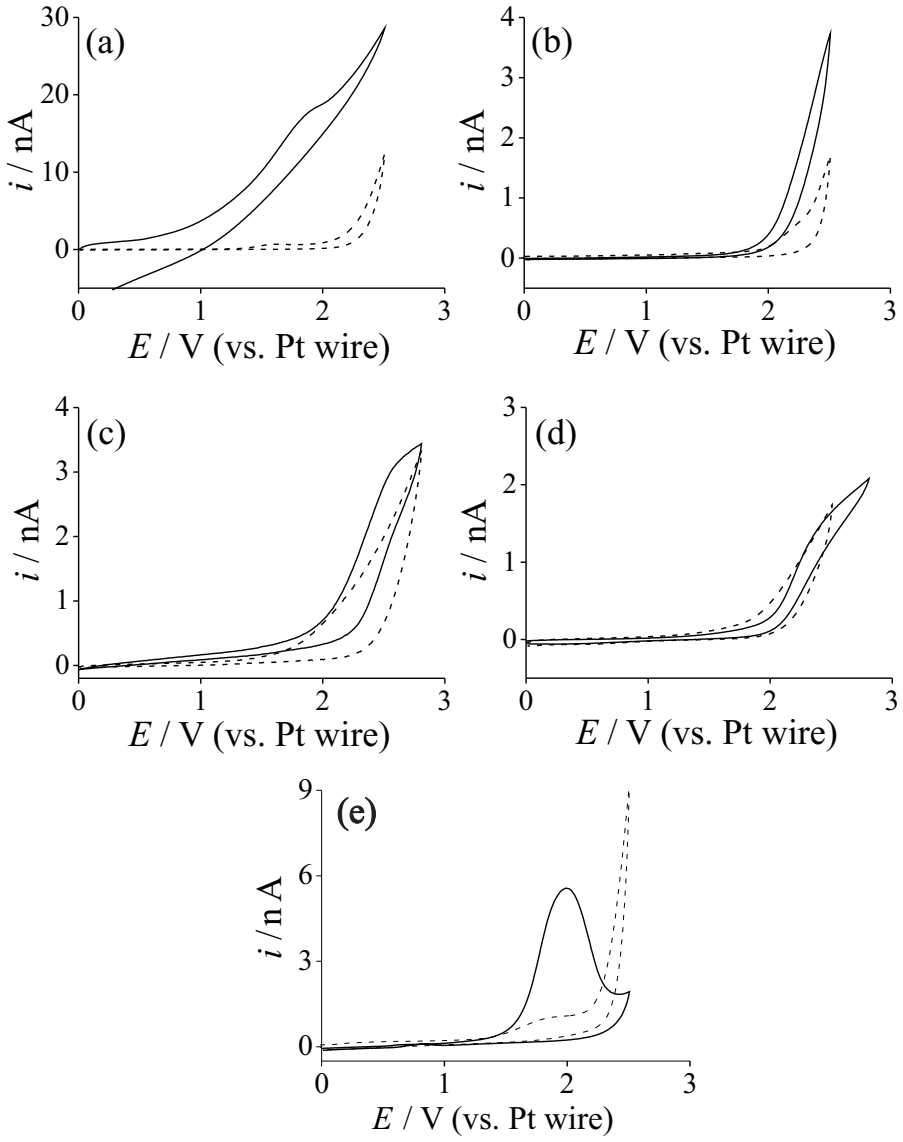


Figure 7.3: Cyclic voltammetry for the oxidation of 1 atm. H_2S on a 10 μm diameter Pt electrode at 298 K, at scan rate 100 mV s^{-1} in the following ionic liquids: (a)[C_4dmim][NTf_2], (b)[C_4mim][PF_6], (c)[C_6mim][FAP], (d)[$P_{14,6,6,6}$mim][FAP] and (e)[C_4mim][OTf]. *Dotted line* : CV of RTIL only where no analyte is present. *Solid line* : CV of 1% H_2S in RTIL.

seen in [C_4mim][OTf]. This may be due to the fact that the $[OTf]^-$ anion has favorable ionic interactions with the H_2S molecule, whereas the other anions ($[NTf_2]^-$, $[PF_6]^-$ and $[FAP]^-$) lack such an extensive interactions. The $[OTf]^-$ anion is known to hydrogen-bond strongly to water due to the presence of an SO_3^- group,[6] and this may be a factor for favorable interactions with H_2S.

We suggest that this leads to an accumulation of H_2S in the double layer of the Pt/RTIL

interface. To further support this conclusion, we integrated the area under the H_2S oxidation peak and found the surface coverage of H_2S to be substantially greater than one monolayer. To develop this idea further we consider the quantitative model outlined in the next section.

7.2.1.2 Simulation of Oxidation of H_2S in [C_4mim][OTf]

As an approximation, the oxidation of surface-bound H_2S (=A) was modelled by Edmund J. F. Dickinson, a current D.Phil student at the University of Oxford and has previously been published.,[7] and described according to the following reaction scheme:

$$\mathrm{A\,(soln)} \rightleftarrows \mathrm{A\,(ads)} \tag{7.1}$$

$$\mathrm{A\,(ads)} \rightarrow \mathrm{Products} + n\mathrm{e}^- \tag{7.2}$$

where the first step (adsorption) is modelled kinetically according to a Langmuir isotherm, and the second step (oxidation) is assumed to be irreversible and to generate products which are inert to all further reaction. n is assumed to be 2 for the oxidation of H_2S with the products being S and $2H^+$, with the H^+ likely bound to the $[OTf]^-$ anion.

The adsorption step is characterized by a rate of adsorption k_{ads} / mol^{-1} cm^3 s^{-1}, an equilibrium constant K_{eqm} / mol^{-1} cm^3, and a maximum surface coverage of $\mathrm{A_{(ads)}}$ Γ_{max} / mol cm^{-2}, such that the proportional coverage $\Theta = \Gamma/\Gamma_{\mathrm{max}}$ takes values between 0 and 1. The oxidation step is correspondingly characterized by a rate of oxidation k_{ox} / s^{-1}, which is described by an irreversible Tafel law / Butler-Volmer formalism :

$$k_{\mathrm{ox}} = k^0 \exp\left(\frac{\beta F}{RT}(E - E_{\mathrm{f}}^{\ominus})\right) \tag{7.3}$$

where β is the transfer coefficient defined in the oxidative direction and can take values between 0 and 1.

This mechanism is modelled for cyclic voltammetry at a microdisc electrode by numerical solution of the diffusion equation (Equation 7.4) across a 2D cylindrical simulation space, shown in Figure 7.4.

$$\frac{\partial c_{\mathrm{A}}}{\partial t} = D_{\mathrm{A}} \left(\frac{\partial^2 c_{\mathrm{A}}}{\partial z^2} + \frac{1}{r}\frac{\partial c_{\mathrm{A}}}{\partial r} + \frac{\partial^2 c_{\mathrm{A}}}{\partial r^2} \right) \tag{7.4}$$

The simulation space is bounded at $z_{\max} = 6\sqrt{D_{\mathrm{A}} t}$ and $r_{\max} = r_{\mathrm{d}} + 6\sqrt{D_{\mathrm{A}} t}$, at which points the concentration of A is assumed to be equal to its bulk value; these boundaries have been characterized as sufficiently exceeding the diffusive depletion layer at all times.[8] At $t = 0$, the initial conditions set the concentration of A equal to its bulk value everywhere in solution, and the surface coverage of adsorbed material on the electrode is set equal to its Langmuirian equilibrium value:

$$\Theta_{\mathrm{eq}} = \frac{K_{\mathrm{eqm}} c_{\mathrm{A}}^*}{1 + K_{\mathrm{eqm}} c_{\mathrm{A}}^*} \tag{7.5}$$

The mechanism then yields the following electrode surface boundary conditions for the solution of Equation 7.4:

$$\frac{\partial \Theta}{\partial t} = k_{\mathrm{ads}}(1 - \Theta) c_{\mathrm{A},0} - (k_{\mathrm{des}} + k_{\mathrm{ox}})\Theta \tag{7.6}$$

$$\frac{D_{\mathrm{A}}}{\Gamma_{\max}} \left.\frac{\partial c_{\mathrm{A}}}{\partial z}\right|_{z=0} = k_{\mathrm{ads}}(1 - \Theta) c_{\mathrm{A},0} - k_{\mathrm{des}}\Theta \tag{7.7}$$

noting that k_{ox} has a potential dependence described by Equation 7.3 and that k_{des} is described as:

$$k_{\mathrm{des}} = \frac{k_{\mathrm{ads}}}{K_{\mathrm{eqm}}} \tag{7.8}$$

Additionally, a zero-flux boundary condition is set at the insulating surface and at the symmetry boundary, and bulk concentration is set at the limits of the simulation space:

$$z = 0,\ r > r_{\mathrm{d}} \qquad \frac{\partial c_{\mathrm{A}}}{\partial z} = 0 \tag{7.9}$$

$$r = 0 \qquad \frac{\partial c_{\mathrm{A}}}{\partial r} = 0 \tag{7.10}$$

$$r = r_{\max};\ z = z_{\max} \qquad c_{\mathrm{A}} = c_{\mathrm{A}}^{*} \tag{7.11}$$

To solve Equation 7.4 numerically, it is made dimensionless and then discretized in space using the alternating direction implicit (ADI) method,[9] across an expanding space grid adapted from that used by Gavaghan.[10] The time grid is regular and employed 1000 time steps per unit RT/F of the CV; applied potential is altered at each time step at a rate given by the scan rate for the experiment, v. The resulting set of simultaneous equations is solved at each timestep using the Thomas (tri-diagonal matrix) algorithm,[11] for which the non-linear terms in the electrode surface boundary conditions must be linearized via the approximation:[12]

$$A'B' \approx A'B + AB' - AB \tag{7.12}$$

where A' and B' are implicit (next half-time step) concentration terms and A and B are explicit concentration terms respectively. This approximation has an error of $O(\Delta(D_{\mathrm{A}}t)^2)$: all simulation parameters were converged to within 0.2% accuracy for observed current. All simulations were programmed in C++ and run on a desktop computer with a 3 GHz Intel Pentium 4 processor and 500 MB of RAM, with running times of 10-15 minutes per voltammogram being typical for highest accuracy. The determination of best fit between experiment and simulation was done by eye, within 1 to 5% error, with use of multiple scan rates to decrease the error.

The current is retrieved at each timestep via numerical integration of the rate of oxidative consumption of the adsorbed species across the electrode, using the trapezium rule across all space points:

$$i = 2\pi n F\, \Gamma_{\max} k_{\mathrm{ox}} \int_{0}^{r_{\mathrm{d}}} \Theta\, r\, \mathrm{d}r \tag{7.13}$$

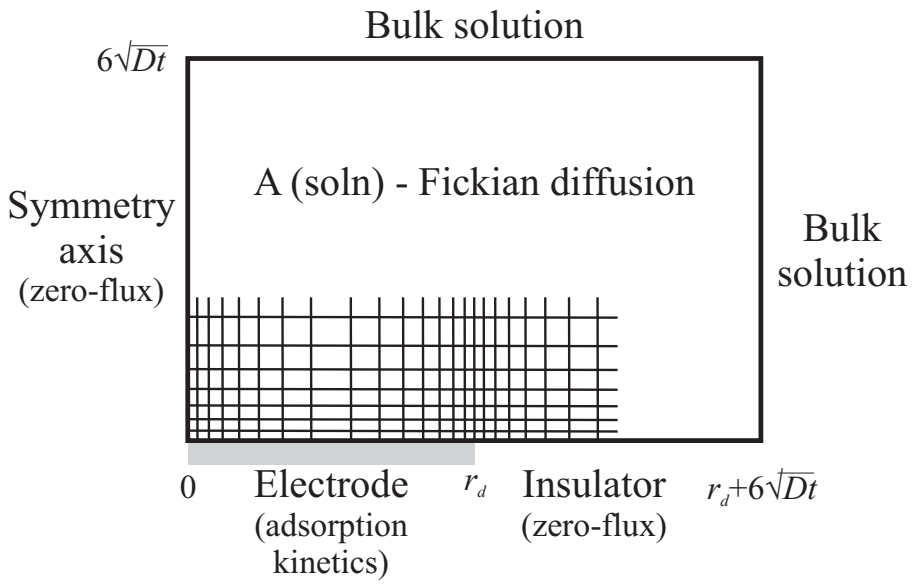


Figure 7.4: 2D cylindrical simulation space used for microdisc electrode as a numerical solution of the diffusion equation.

7.2.1.3 Comparison of Theory and Experiment for the Oxidation of H_2S

The above model was used to simulate the oxidative signal of 1% H_2S to confirm, or otherwise, the mechanism by which this oxidation occurs. To reduce the number of parameters to be optimized in the model, the diffusion coefficient and bulk concentration of 1% H_2S in [C_4mim][OTf] were obtained by potential step chronoamperometry on the reductive wave seen in Figure 7.5. Note that, consistent with the mechanism proposed, the size of the approximate steady state current flowing after the oxidative wave was of the same order of magnitude as the reduction wave at 100 mV s^{-1} but *ca.* 2-4 times larger increasing with scan rate. This reflects first the number of electrons transferred (one for the reductive and two for the oxidative wave), and second, the fact that there is both incomplete stripping at the fast scan rates plus re-adsorption of more H_2S during the oxidative scan.

A potential step was carried out on the reductive wave of H_2S in order to measure the solubility and diffusion coefficients in the ionic liquid. The potential is stepped from a position of zero current to a potential more negative than the reductive wave, and the current recorded for 0.5 s. A representative chronoamperometric transient is shown as a series of circles, together

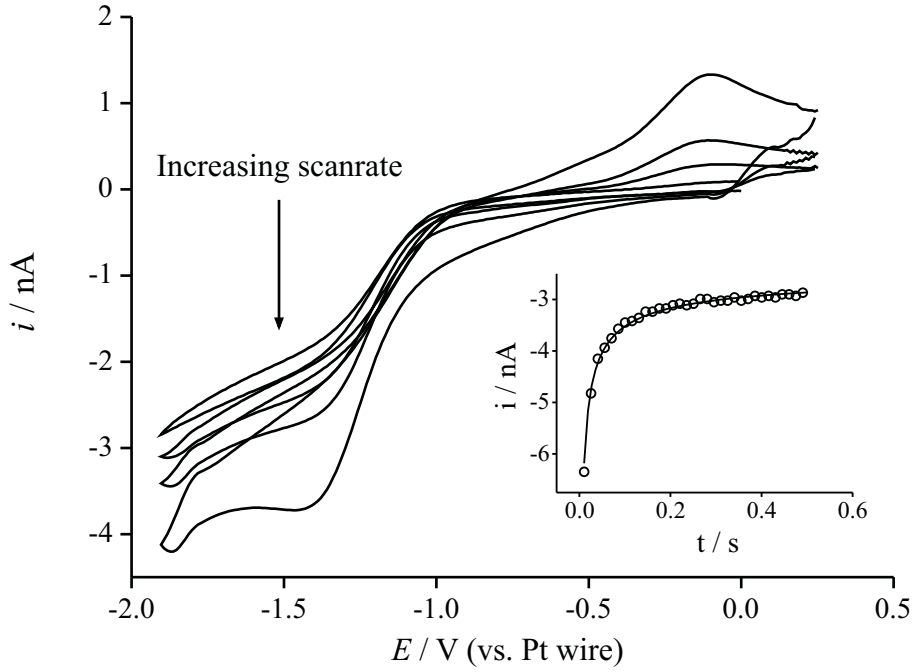


Figure 7.5: Cyclic voltammetry for the reduction of 1% H_2S in [C_4mim][OTf] at Pt electrode (10 μm diameter) at a scan rates of 100, 400, 1000 and 4000 mV s^{-1} and temperature of 298 K. *Inset* : Chronoamperometry for the reductive wave of 1% H_2S in [C_4mim][OTf]

with the theoretical fit, a solid line, in the inset to Figure 7.5. The experimental data are fitted to the Shoup and Szabo expression,[13] and the diffusion coefficient and solubility value obtained are found to be 1.60($\pm$0.02)$\times 10^{-10}$ m^2 s^{-1} and 7.00($\pm$0.05) mM respectively. The diffusion coefficient is similar to that found for pure H_2S,[14] and for the gases O_2,[15] NO_2,[16] H_2[17] and SO_2[18] in RTILs, and one order of magnitude larger than typical dissolved solids in RTILs (5.34×10^{-11} m^2 s^{-1} for ferrocene in [C_2mim][NTf_2]).

These values are used for simulation of the oxidative signals of 1% H_2S at scan rates 100 mV s^{-1} to 4000 mV s^{-1}. Note: chronoamperometry on the oxidative wave of 1% H_2S did not fit the Shoup and Szabo expression as expected since the presence of significant adsorbed material would be neglected in the Shoup and Szabo model.

Given that the output of the potential step chronoamperometry on the reduction wave fixes values for the solubility and the diffusion coefficient, there are four main variables for the simulation of the oxidation voltammetry of H_2S: k_{ads} / mol^{-1} cm^3 s^{-1}, an equilibrium

constant K_{eqm} / mol^{-1} cm^3, and a maximum surface coverage of $A_{(ads)}$ Γ_{max} / mol cm^{-2} which characterise the rate of adsorption in Equation 7.2, and k_{ox} / s^{-1} which characterises the oxidation step in Equation 7.3. Note: k_{ox} is related to k^0 as per Equation 7.2, and k^0 is the parameter that is varied in the simulation program. The maximum surface coverage (Γ_{max} / mol cm^{-2}) is fixed as being that for a monolayer of sulfur atoms, calculated using the van der Waals radius of sulfur[19] in a cubic formation: this value was calculated as 1.3×10^{-9} mol cm^{-2}. The transfer coefficient (β) was calculated from the experimental data using a Tafel plot[20] and set as 0.175. The number of electrons was set as 2 and the scan rate is 100 mV s^{-1}.

Figure 7.6 shows the variation of voltammetry with k_{ads} at a scan rate of 100 mV s^{-1}. k_{ads} was varied from 91 to 9.1×10^9 mol^{-1} cm^3 s^{-1}. The inset of Figure 7.6 shows lower values of k_{ads} with the main graph showing the higher values. K_{eqm} was set at 1 mol^{-1} cm^3, and k^0 was set at 6.4×10^2 s^{-1}. The signal increases with k_{ads}: when k_{ads} is small, A(*soln*) stays almost constant at the surface, and diffusion is hence negligible. The voltammetry is then controlled only by k_{ox} and by the coverage of adsorbed analyte. At higher rates of k_{ads} (shown in Figure 7.6) and when desorption is comparatively slow, typical diffusion-controlled microelectrode voltammetry is observed.

Figure 7.7 shows the variation of K_{eqm} / mol^{-1} cm^3 from 1 to 1×10^4 mol^{-1} cm^3. k_{ads} was set at 9.1×10^3 mol^{-1} cm^3 s^{-1}, and k^0 was set at 6.4×10^2 s^{-1}. The voltammetric signal increases. This behavior is Langmuirian, and related to the surface coverage of adsorbed material. According to Equation 7.5, as K_{eqm} increases, the proportional surface coverage will tend toward a maximum of 1, so that all available sites on the electrode surface will be filled. Hence maxima for the limiting and peak currents are observed.

Figure 7.8 shows the effect of variation of k_{ox}. k^0 was varied from 6.4×10^{-4} to 6.4×10^4 s^{-1}. k_{ads} was set at 9.1×10^{15} mol^{-1} cm^3 s^{-1} and K_{eqm} was set at 1×10^6 mol^{-1} cm^3. According to Equation 7.3, at higher values of k_{ox}, the peak potential becomes more negative. k^0 is increased

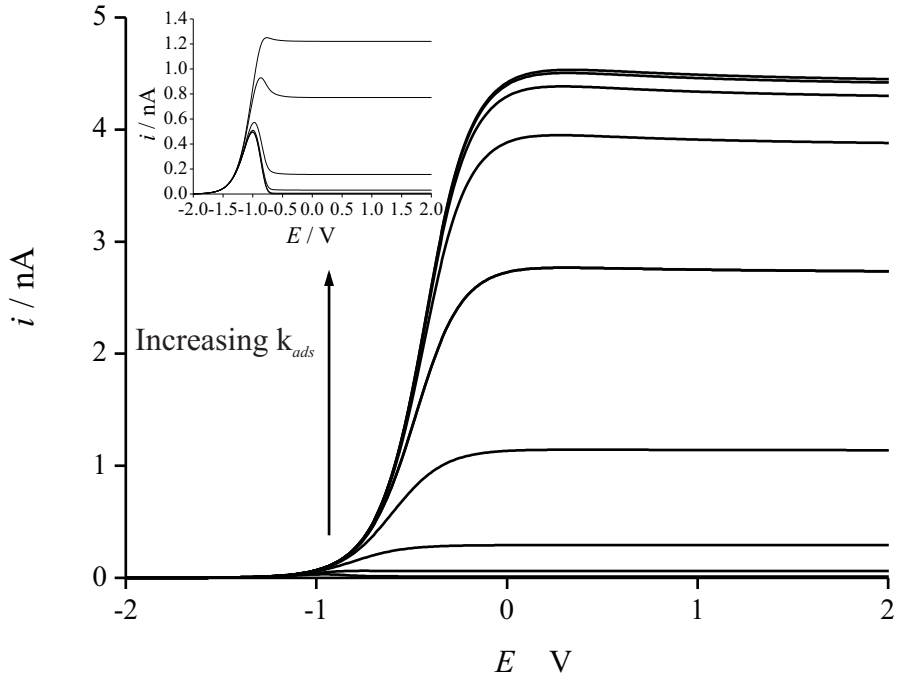


Figure 7.6: Simulated voltammetry for oxidation at a microelectrode at scan rate of 100 mV s^{-1} varying k_{ads} from 9.1×10^{1} to 9.1×10^{9} mol^{-1} cm^3 s^{-1}. *Inset*: k_{ads}=5×10^{-4} to 3×10^{-1} mol^{-1} cm^3 s^{-1}. K_{eqm}=1 mol^{-1} cm^3, k^0=6.4×10^{2} s^{-1}. Maximum surface coverage (Γ_{max})=1.3×10^{-9} mol cm^{-2}, transfer coefficient (β)=0.175.

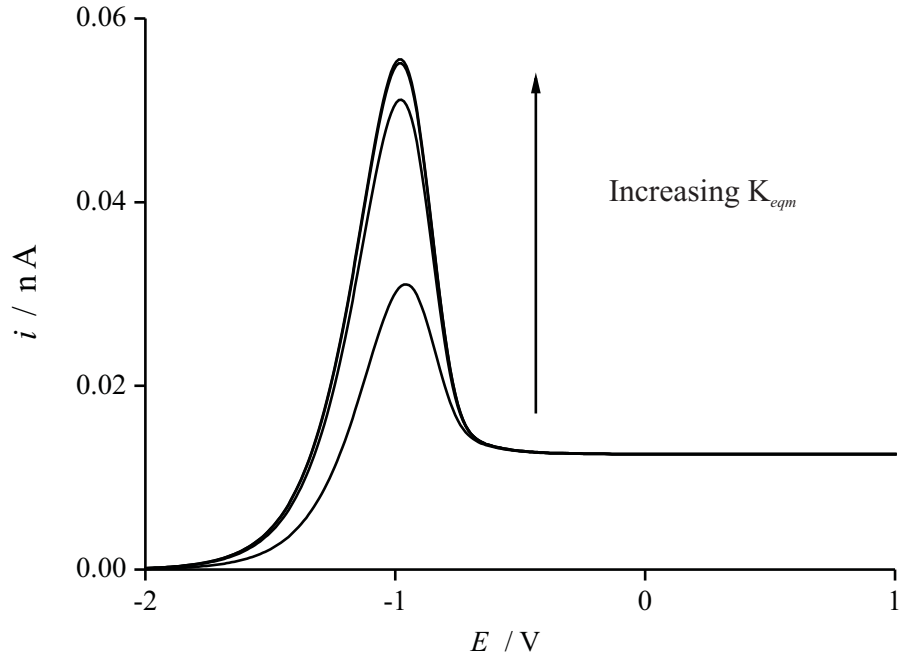


Figure 7.7: Simulated voltammetry for oxidation at a microelectrode at scan rate of 100 mV s^{-1} varying K_{eqm} from 1 to 1×10^{4} mol^{-1} cm^3. k_{ads}=9.1×10^{3} mol^{-1} cm^3 s^{-1}, k^0 =6.4×10^{2} s^{-1}. Maximum surface coverage (Γ_{max})=1.3×10^{-9} mol cm^{-2}, transfer coefficient (β)=0.175.

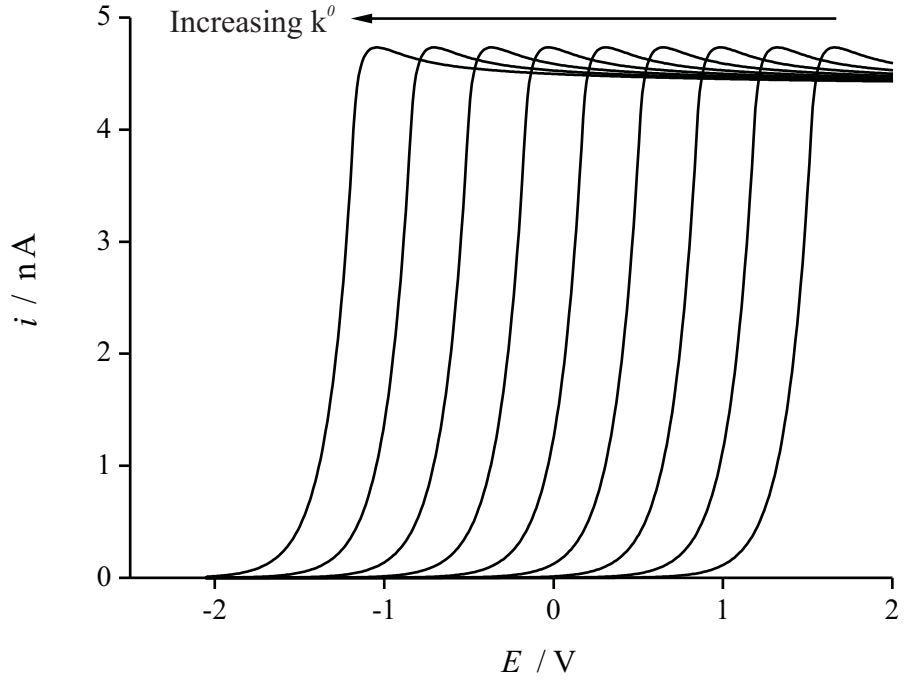


Figure 7.8: Simulated voltammetry for oxidation at a microelectrode at scan rate of 100 mV s^{-1} varying k_{ox}. k^0 varied from 6.4×10^{-4} to 6.4×10^{4} s^{-1}. k_{ads}=9.1×10^{15} mol^{-1} cm^3 s^{-1}, K_{eqm}=1×10^{6} mol^{-1} cm^3. Maximum surface coverage (Γ_{max})=1.3×10^{-9} mol cm^{-2}, transfer coefficient (β)=0.175.

so that the observed potential of the voltammetry fits the experimental results.

Returning to the experimental data reported above: in Figure 7.9 we compare the experimental data (solid line) and the theoretical data (dashed line) for the oxidation of 1% H_2S at scan rates of 100 and 1000 mV s^{-1}. In order to attempt to model the experimental data, the values of k_{ads} and K_{eqm} used throughout (9.1×10^{15} mol^{-1} cm^3 s^{-1} and 1×10^{6} mol^{-1} cm^3 respectively) were those that gave a maximum achievable current. k_0 is set as 6.4×10^{2} s^{-1}, the surface coverage value for the theoretical data is 1.3×10^{-9} mol cm^{-2} and the transfer coefficient (β) is 0.175. We also adopted the measured values for the diffusion coefficient and the solubility of H_2S ($1.60(\pm0.02)\times10^{-10}$ m^2 s^{-1} and 7.00($\pm$0.05) mM respectively). The experimental data signal at 100 mV s^{-1} give a peak current of 6.7 nA. The maximum achievable peak current for the theoretical data at the same scan rate is 4.8 nA. While the magnitude of the peak current for the theoretical model is comparable with that of the experimental scan for 100 mV s^{-1}, the wave

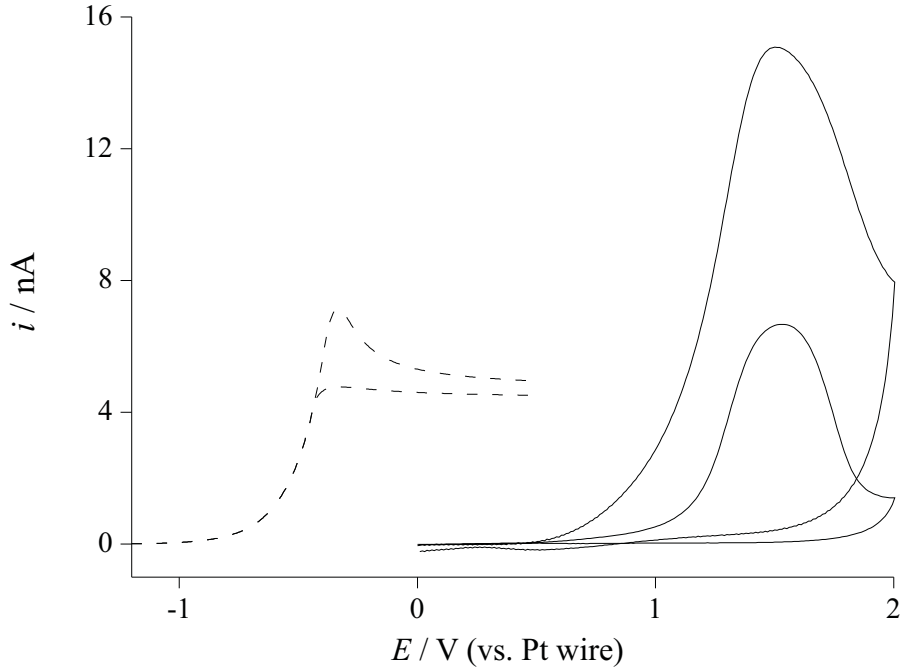


Figure 7.9: Comparison of cyclic voltammetry for the oxidation of H_2S in [C_4mim][OTf] at Pt electrode (10 μm diameter, solid line) and simulation of oxidative waves at highest achievable peak currents (dashed line) at scan rates 100 and 1000 mV s^{-1}. k_{ads}=9.1×10^{15} mol^{-1} cm^3 s^{-1}, K_{eqm}=1×10^6 mol^{-1} cm^3, k^0 =6.4×10^2 s^{-1}. Maximum surface coverage (Γ_{max})=1.3×10^{-9} mol cm^{-2}, transfer coefficient (β)=0.175.

shape differs substantially. The theoretical model appears diffusional, whereas the experimental model shows much more at an 'adsorptive stripping peak' at 1.5 V with diffusional behavior at a more positive potential. The theoretical scan at 1000 mV s^{-1} resembles the shape of the experimental scan for the same scan rate. However, the current for the stripping peak and the current for the steady-state behavior in the theoretical model do not scale to match precisely the currents of the experimental data.

The only variable remaining to be adjusted is the maximum surface coverage. Increasing the value of the surface coverage would imply multilayers of H_2S at the electrode surface which is one possibility, and this would in turn increase the current output of the simulation to match that of the experimental results. The other possibility is chemisorption, which can only lead to a monolayer coverage of the electrode surface. Hitherto, it was taken to be the coverage of a monolayer of sulfur atoms as calculated by the van der Waals radius[19] of sulfur since this

corresponds to a maximum signal from a chemisorbed layer. The fact that the current output for the simulation under this regime is much less than that of the experimental output likely suggests that a H_2S enriched double layer is responsible for the enhanced magnitude of the peak current. We have already mentioned that H_2S is highly soluble in $[C_4mim][OTf]$, and that the $[OTf]^-$ anion readily hydrogen-bonds with water, possibly accounting for this high solubility and large oxidative signals. This factor may be responsible for a H_2S-enriched double layer with significant quantities of H_2S in the solution adjacent to the electrode, which would give rise to the results seen for the oxidation of H_2S in RTILs.

7.3 Conclusions

The electrochemical oxidation of H_2S has been studied in five RTILs. In four of the solvents no clear oxidative peak was observed. In [C_4mim][OTf], an adsorptive stripping peak was observed followed by a steady-state signal at a more positive potential. No signal was observed on the reverse sweep. The signal was simulated as a two-step, two-electron reaction scheme. The first step (adsorption) was modelled kinetically according to a Langmuir isotherm, and the second step (oxidation) was assumed to be electrochemically irreversible and generated products which were inert to all further reaction, most likely by dissolving in the RTIL medium. Given values of the H_2S solubility and diffusion coefficient can be accurately found by using potential step chronoamperometry and that the maximum monolayer coverage of adsorbed H_2S on the surface can be estimated, the fact that currents bigger than predicted are observed even if k_{ads} and K_{eqm} are optimally large indicate either multilayer adsorption at the electrode surface, or a substantial build up of H_2S at the interface. This represents a new insight for RTIL electrochemistry: in effect the double layer of the RTIL in the presence of dissolved H_2S leads to excess H_2S in the vicinity at the interfacial region.

This behaviour in RTILs once again shows the high solubility of H_2S in these media. While this bodes well for the fabrication of a gas sensor, the fact that adsorption of H_2S at the electrode surface results in fouling of the electrode means that either a cleaning procedure for the electrode surface needs to be implemented, or the detection of H_2S at lower potentials must be studied. The latter is possible with the use of a mediating species. This would lead to less or no fouling of the electrode surface, and possibly prevent the interference of other electrochemically active impurities in the system. Many mediating species were studied, and the results are outlined in Chapter 11. In the course of this study, the electrochemical behaviour of many species in RTILs was observed for the first time at the platinum electrode. The following three chapters outline the behaviour of some of these species in RTILs, and show features such as species

kinetics (Chapter 8), varying reactions of species in different RTILs (Chapter 9), and selectivity of RTILs towards electrochemical activity of different species (Chapter 10). We begin with the kinetics of DMPD in $[C_4mim][BF_4]$, and examine comproportionation of the dication with the neutral species with theoretical simulation.

References

[1] Flatte, M. E.; Kornyshev, A. A. and Urbakh, M., *J. Phys.: Condens. Matter*, 2008, **20**, 073102/1–073102/9.

[2] Parka, J.-E.; Mommaa, T. and Osaka, T., *Electrochim. Acta*, 2007, **52**, 5914–5923.

[3] O' Mahony, A. M.; Silvester, D. S.; Aldous, L.; Hardacre, C. and Compton, R. G., *J. Chem. Eng. Data*, 2008, **53**, 2884–2891.

[4] Rogers, E. I.; Silvester, D. S.; Poole, D. L.; Aldous, L.; Hardacre, C. and Compton, R. G., *J. Phys. Chem. C*, 2008, **112**, 2729–2735.

[5] Silvester, D. S. and Compton, R. G., *Z. Phys. Chem.*, 2006, **220**, 1247–1274.

[6] Llewellyn Lancaster, N. and Welton, T., *J. Org. Chem.*, 2004, **69**, 5986–5992.

[7] O' Mahony, A. M.; Dickinson, E. J. F.; Aldous, L.; Hardacre, C. and Compton, R. G., *J. Phys. Chem. C*, 2009, **113**, 10997–11002.

[8] Svir, I. B.; Klymenko, O. V. and Compton, R. G., *Radiotekhnika*, 2001, **118**, 92.

[9] Peaceman, J. W. and Rachford, H. H., *J. Soc. Indust. Appl. Math.*, 1955, **3**, 28–41.

[10] Gavaghan, D. J., *J. Electroanal. Chem.*, 1998, **456**, 1–12.

[11] Atkinson, K. E., *Elementary Numerical Analysis*, John Wiley and Sons, New York, 3rd ed., 2004.

[12] Britz, D., *Digital Simulation in Electrochemistry*, Springer-Verlag, Berlin, 3rd ed., 2005.

[13] Shoup, D. and Szabo, A., *J. Electroanal. Chem.*, 1982, **140**, 237–245.

[14] O' Mahony, A.; Silvester, D. S.; Aldous, L.; Hardacre, C. and Compton, R. G., *J. Phys. Chem. C*, 2008, **112**, 7725–7730.

[15] Buzzeo, M. C.; Klymenko, O. V.; Wadhawan, J. D.; Hardacre, C.; Seddon, K. R. and Compton, R. G., *J. Phys. Chem. A*, 2003, **107**, 8872–8878.

[16] Broder, T. L.; Silvester, D. S.; Aldous, L.; Hardacre, C. and Compton, R. G., *J. Phys. Chem. B*, 2007, **111**, 7778–7785.

[17] Silvester, D. S.; Aldous, L.; Hardacre, C. and Compton, R. G., *J. Phys. Chem. B*, 2007, **111**, 5000–5007.

[18] Barrosse-Antle, L.; Silvester, D. S.; Aldous, L.; Hardacre, C. and Compton, R. G., *J. Phys. Chem. C*, 2008, **112**, 3398–3404.

[19] Bondi, A., *J. Phys. Chem.*, 1964, **68**, 441.

[20] Compton, R. G. and Banks, C. E., *Understanding Voltammetry*, World Scientific, 2007.

Chapter 8

Kinetics and Thermodynamics of Redox Processes in Room Temperature Ionic Liquids: The Use of Voltammetry. The Disproportionation of Radical Cations of DMPD in $[C_4mim][BF_4]$.

The voltammetry of DMPD in the RTIL $[C_4mim][BF_4]$, is studied, by means of microdisc voltammetry, over a wide range of voltage scan-rates incorporating the transition from linear to convergent diffusion. Two voltammetric waves were recorded corresponding to the formation of the radical cation $DMPD^{\bullet+}$ and dication $DMPD^{2+}$; both are stable on the voltammetric timescale. Double potential step chronoamperometry was used to measure the diffusion coefficients of DMPD and $DMPD^{+}$. These values, in conjunction with simulations of the cyclic voltammetry, permit the inference of the equilibrium constant and kinetics for the comproportionation of DMPD and $DMPD^{2+}$ forming $DMPD^{\bullet+}$ to be studied.

8.1 Introduction

RTILs have led to substantial synthetic innovations in both academic[1–3] and industrial[4] contexts. However, unlike reactions in the latter media, the measurement of reaction parameters, both kinetic and thermodynamic, has lagged and comparatively less data is available to guide the planning and interpretation of chemistry in the RTIL environment.

Voltammetry, at least in principle, offers an experimentally simple yet accurate route into the quantitative measurement of both kinetic and thermodynamic data. For example, in the case of an arbitrary species, A, which can undergo oxidation to species B and C:

$$\mathrm{A} - \mathrm{e}^- \rightleftharpoons \mathrm{B} \quad (E^{\ominus}_{\mathrm{f,A/B}}) \tag{8.1}$$

$$\mathrm{B} - \mathrm{e}^- \rightleftharpoons \mathrm{C} \quad (E^{\ominus}_{\mathrm{f,B/C}}) \tag{8.2}$$

if two separate voltammetric features are attributable to these processes then their analysis can give information about the comproportionation reaction:[5]

$$\mathrm{A} + \mathrm{C} \rightleftharpoons 2\mathrm{B} \tag{8.3}$$

where, specifically, the formal potentials $E^{\ominus}_{\mathrm{f,A/B}}$ and $E^{\ominus}_{\mathrm{f,B/C}}$ will provide information about the equilibrium constant:

$$K_{\mathrm{eqm}} = \frac{[\mathrm{B}]^2}{[\mathrm{A}][\mathrm{C}]} \tag{8.4}$$

and $\Delta G^{\ominus}$ for reaction 8.3:

$$\Delta G^{\ominus} = -RT\ln(K_{\mathrm{eqm}}) = -F(E^{\ominus}_{\mathrm{f,B/C}} - E^{\ominus}_{\mathrm{f,A/B}}) \tag{8.5}$$

The kinetics of reaction 8.3 may sometimes be discernible from the precise voltammetric waveshapes and their separation.[6] However, in the context of voltammetry using large planar electrodes ('macroelectrodes'), Savéant has shown, in a paper long regarded as a classic,[7] that if species A, B and C have identical diffusion coefficients, D_A, D_B and D_C, then the voltammetry is completely insensitive to the rate of comproportionation. The same is true of voltammetry recorded under diffusional modes other than linear.[5] Only if there is an appreciable disparity in the diffusion coefficients can the kinetics of reaction 8.3 become apparent in the voltammetry. Accordingly, voltammetry has been relatively little used in the context of measuring comproportionation kinetics except in so far that it has been coupled to spectroscopic methods, such as ESR[7] and UV/visible spectroscopy.[8] At the heart of this neglect is the fact that, in most aqueous and non-aqueous systems, species A, B and C often have closely similar diffusion coefficients unless they are structurally very dissimilar.

As electrochemical research using RTILs as solvents[9–15] has matured it has become apparent that, unlike conventional solvents such as DMF, DMSO and acetonitrile, the difference in diffusion coefficients between structurally similar species in a redox couple is not always insignificant. An extreme example, discovered by Buzzeo,[16] is that of the oxygen/superoxide (O_2/O_2^-) couple in which the anion has a diffusion coefficient *ca* 30 times smaller than the neutral parent in the RTIL $[N_{6222}][N(Tf)_2]$. Work by Evans[10] and by Hapiot[17] have shown that even for aromatic molecules, such as DPPD, the diffusion coefficients differ significantly between the neutral parent and the corresponding radical cation and dication despite close structural similarity. Analyte ions of higher charge typically diffuse less rapidly due to electrostatic interaction with the ions in the solvent. As a consequence it can be anticipated that, in ionic liquids, voltammetric analysis can be used as a means of obtaining information about the rate of comproportionation in solution.

In this Chapter we consider the oxidation of DMPD in the ionic liquid $[C_4mim][BF_4]$ (struc-

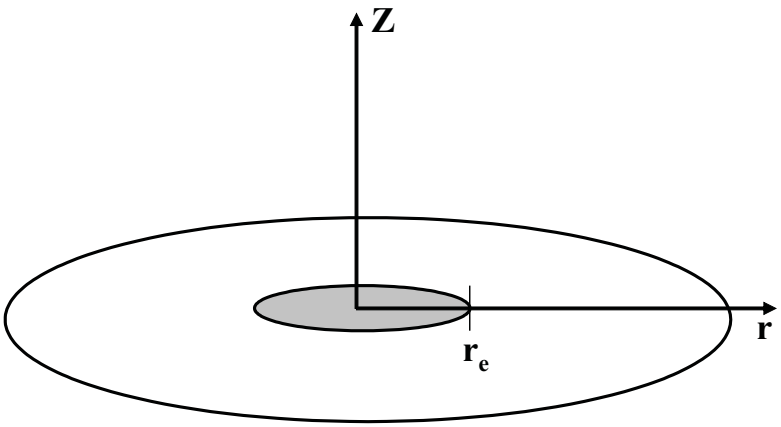


Figure 8.1: Circular disc electrode inlaid on an insulating support.

tures outlined in Chapter 4), using a microdisc electrode. The theory in this Chapter has been outlined and simulations carried out by Stephen R. Belding, a current D.Phil student at the University of Oxford. The experimental work has been carried out by Edward O. Barnes, a current undergraduate student at the University of Oxford, under the supervision of the author. The resulting work has been already published.[18]

It is shown that comparison between experimental and simulated data can be used to extract both kinetic and thermodynamic data including information about comproportionation. Also noted is the value of double potential step chronoamperometry in elucidating the diffusion coefficients of DMPD and $DMPD^{\bullet+}$.[12]

8.2 Theory

We consider an EE reaction at a microdisc electrode (Figure 8.1), as defined by Equations 8.1 and 8.2, where we additionally allow for comproportionation (Equation 8.3).

The heterogeneous rate constants for the first two steps are $k^0_{A/B}$ and $k^0_{B/C}$ respectively. The homogeneous rate constant for comproportionation is k_{comp} and for disproportionation is k_{disp}.

Table 8.1: Dimensional parameters.

Dimensional Parameter	**Definition**
$\alpha_{X/Y}$	Transfer coefficient for $X - e^- \rightleftharpoons Y$ / unitless
c_X	Concentration of species X / mol m^{-3}
$c_{X,0}$	Concentration of species X at the electrode surface / mol m^{-3}
c_X^*	Concentration of species X in bulk solution / mol m^{-3}
D_X	Diffusion coefficient of species X / m^2 s^{-1}
E	Applied potential / V
$E^{\ominus}_{f,X/Y}$	Formal reduction potential for $X - e^- \rightleftharpoons Y$ / V
$k^0_{X/Y}$	Electrochemical rate constant for $X - e^- \rightleftharpoons Y$ / m s^{-1}
k_{comp}	Rate constant for comproportionation / dm^3 mol^{-1} s^{-1}
k_{disp}	Rate constant for disproportionation / dm^3 mol^{-1} s^{-1}
i	Current / A
j	Flux across the electrode / mol m^2 s^{-1}
r	Radial coordinate / m
t	Time / s
v	Scan-rate / V s^{-1}
z	Axial coordinate / m

The equilibrium constant for Equation 8.3 is therefore $K_{eqm} = \frac{k_{comp}}{k_{disp}}$. Specifically we consider the case of cyclic voltammetry.

$$\frac{\partial c_A}{\partial t} = D_A \left(\frac{\partial^2 c_A}{\partial r^2} + \frac{1}{r}\frac{\partial c_A}{\partial r} + \frac{\partial^2 c_A}{\partial z^2} \right) + k_{disp} {c_B}^2 - k_{comp} c_A c_C \tag{8.6}$$

$$\frac{\partial c_B}{\partial t} = D_B \left(\frac{\partial^2 c_B}{\partial r^2} + \frac{1}{r}\frac{\partial c_B}{\partial r} + \frac{\partial^2 c_B}{\partial z^2} \right) - 2\left(k_{disp} {c_B}^2 - k_{comp} c_A c_C \right) \tag{8.7}$$

$$\frac{\partial c_C}{\partial t} = D_C \left(\frac{\partial^2 c_C}{\partial r^2} + \frac{1}{r}\frac{\partial c_C}{\partial r} + \frac{\partial^2 c_C}{\partial z^2} \right) + k_{disp} {c_B}^2 - k_{comp} c_A c_C \tag{8.8}$$

where all symbols are defined in Table 8.1.

8.2.1 Cyclic Voltammetry

In the cyclic voltammetry experiment, the applied potential, E, is swept from an initial value, E_i, to a more oxidising value, E_f, and then back to the initial value. The value of E is therefore calculated at any time on the forward sweep using Equation 8.9 and on the reverse sweep using Equation 8.10, where v is the voltage scan-rate and t is the time:

$$E_{\text{forward}} = E_{\text{i}} + vt \tag{8.9}$$

$$E_{\text{reverse}} = 2E_{\text{f}} + E_{\text{i}} - vt \tag{8.10}$$

When $t > 0$, $z = 0$ and $r \leq r_{\text{e}}$, the boundary conditions are the Butler-Volmer conditions describing species A and C and conservation of mass for species B:

$$\begin{aligned}
D_{\text{A}}\left(\frac{\partial c_{\text{A}}}{\partial z}\right)_0 = \quad & k^0_{\text{A/B}} c_{\text{A},0} \exp\left(-\alpha_{\text{A/B}} \frac{F(E - E^{\ominus}_{\text{f,A/B}})}{RT}\right) \\
& - k^0_{\text{A/B}} c_{\text{B},0} \exp\left((1-\alpha_{\text{A/B}}) \frac{F(E - E^{\ominus}_{\text{f,A/B}})}{RT}\right) \\
D_{\text{B}}\left(\frac{\partial c_{\text{B}}}{\partial z}\right)_0 = \quad & -D_{\text{A}}\left(\frac{\partial c_{\text{A}}}{\partial z}\right)_0 - D_{\text{C}}\left(\frac{\partial c_{\text{C}}}{\partial z}\right)_0 \\
D_{\text{C}}\left(\frac{\partial c_{\text{C}}}{\partial z}\right)_0 = \quad & -k^0_{\text{B/C}} c_{\text{B},0} \exp\left(-\alpha_{\text{B/C}} \frac{F(E - E^{\ominus}_{\text{f,B/C}})}{RT}\right) \\
& + k^0_{\text{B/C}} c_{\text{C},0} \exp\left((1-\alpha_{\text{B/C}}) \frac{F(E - E^{\ominus}_{\text{f,B/C}})}{RT}\right)
\end{aligned}$$

The remaining boundary conditions are:

$t = 0$, all r, all z	$c_{\text{A}} = c^*_{\text{A}}$	$c_{\text{B}} = 0$	$c_{\text{C}} = 0$
$t > 0$, $r > r_{\text{e}}$, $z = 0$	$\frac{\partial c_{\text{A}}}{\partial z} = 0$	$\frac{\partial c_{\text{B}}}{\partial z} = 0$	$\frac{\partial c_{\text{C}}}{\partial z} = 0$
$t > 0$, all r, $z \to \infty$	$\frac{\partial c_{\text{A}}}{\partial z} = 0$	$\frac{\partial c_{\text{B}}}{\partial z} = 0$	$\frac{\partial c_{\text{C}}}{\partial z} = 0$
$t > 0$, $r \to \infty$, all z	$\frac{\partial c_{\text{A}}}{\partial r} = 0$	$\frac{\partial c_{\text{B}}}{\partial r} = 0$	$\frac{\partial c_{\text{C}}}{\partial r} = 0$
$t > 0$, $r = 0$, all z	$\frac{\partial c_{\text{A}}}{\partial r} = 0$	$\frac{\partial c_{\text{B}}}{\partial r} = 0$	$\frac{\partial c_{\text{C}}}{\partial r} = 0$

8.2.2 Computational Details

The problem is generalised by means of a transformation into non-dimensional form using a conventional set of normalised parameters (defined in Table 8.3). The resulting set of normalised diffusion equations were derived by Belding *et al.*[5] The boundary conditions given in the previous sections are readily formulated in terms of normalised variables using the definitions given in

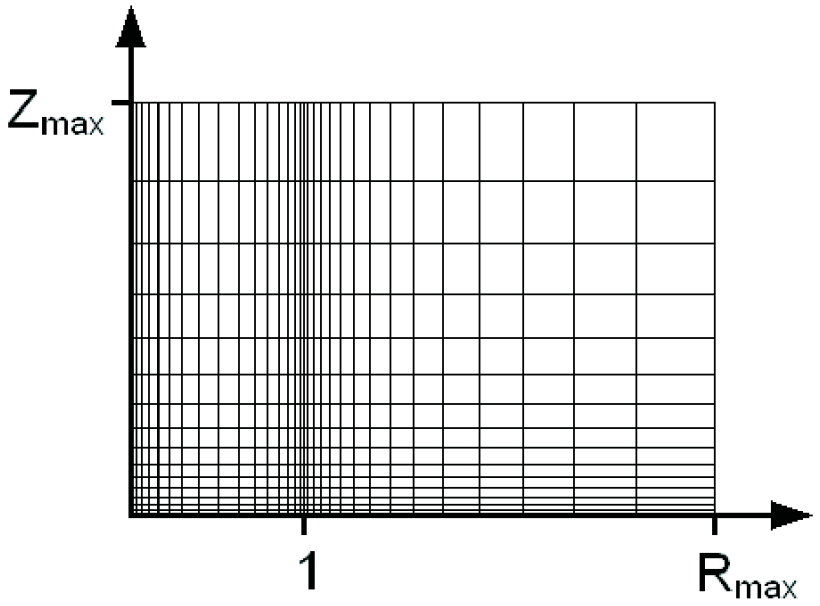


Figure 8.2: Discretised grid used in the simulations (some points have been removed for clarity).

Table 8.3. The problem is then discretised using the ADI method[19,20] and solved numerically using the iterative Newton-Raphson scheme.[21] The discretised spatial mesh is analogous to that reported by Gavaghan[22](Figure 8.2) and converged to within 0.1 %. Each temporal increment is optimised during runtime such that convergence to within 0.01 % is obtained. As the temporal mesh becomes denser, the simulation becomes more accurate. Varying the density of the mesh and comparison of a feature of the voltammogram to an analytical solution allows accuracy of 0.1 % over the shortest possible time. The time grid employed 200 time steps per unit RT/F of the CV. All programs were written in C++ and compiled using a Borland compiler. The simulations were run on a desktop PC with a processor speed of 2.83 GHz and 3.25 GB of RAM. Approximately 20 min of CPU time were required to simulate a single voltammogram. The determination of best fit between experiment and simulation is done by eye and is within a 1 to 5% error. Use of multiple scan rates decreases the error.

8.3 Results and Discussion

8.3.1 Chronoamperometry

Double potential step chronoamperometric transients at the platinum electrode (10 μm diameter) were achieved using a sample time of 0.01 s. A solution of approximately 20 mM DMPD in $[C_4mim][BF_4]$ was pretreated by holding the potential at a point of zero current for 20 s, after which the potential was stepped to a position after the oxidative peak for DMPD corresponding to transport controlled diffusion, and the current measured for 5 s. The potential was then stepped to a position after the reductive peak for $DMPD^{\bullet+}$ corresponding to transport controlled diffusion, and the current response measured for a further 5 s. In order to extract diffusion coefficients and solubility data from these transients, the first potential step was fitted using the nonlinear curve fitting function in the software package Origin 7.0 (Microcal Software Inc.) according to the following equations proposed by Shoup and Szabo[23] outlined in Chapter 4, where D_{DMPD} is the diffusion coefficient for DMPD and c_{DMPD} is the initial concentration of parent species. The value of the parameter $D_{\mathrm{DMPD}^{\bullet+}}$ was elucidated by fitting the transient for the second potential step using simulation software developed by Klymenko *et al.*[12]

The fitted transient is shown in Figure 8.3 and the corresponding values of c_{DMPD}, D_{DMPD} and $D_{\mathrm{DMPD}^{\bullet+}}$ recorded in Table 8.2. It is important to note the value of $c_{\mathrm{DMPD}} = 19.5$ mM obtained from fitting the chronoamperometric transient to the Shoup and Szabo equation is in good agreement with the value of $c_{\mathrm{DMPD}} \approx 20$ mM used in the experiment. As noted in other situations,[16] despite structural similarity between DMPD and $DMPD^{\bullet+}$, the discrepancy in diffusion coefficients is not insignificant. It is important to note that the potentials applied over the course of the double-step experiment are not sufficient to bring about transfer of a second electron ($DMPD^{\bullet+} - e^- \rightleftharpoons DMPD^{2+}$). The concentration of $D_{\mathrm{DMPD}^{2+}}$ in solution is negligible and, consequently, comproportionation cannot occur: Figure 8.3 is independent of the effects of comproportionation regardless of the values of D_{DMPD}, $D_{\mathrm{DMPD}^{\bullet+}}$ and $D_{\mathrm{DMPD}^{2+}}$.

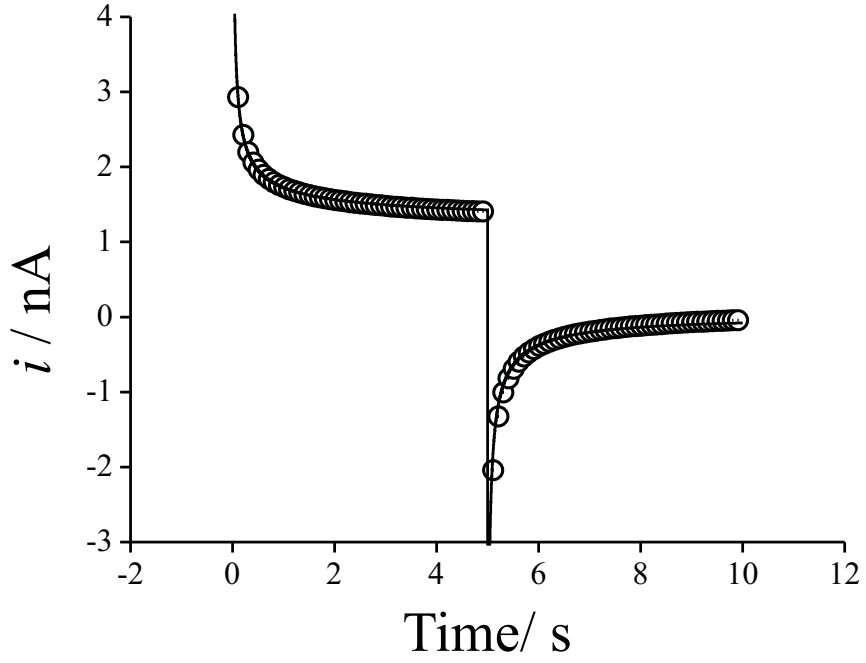


Figure 8.3: Chronoamperometric fit: —, experiment; ∘, simulation.

Table 8.2: Fitted data for DMPD in [C_4 mim][BF_4].

Parameter	**Experimental Value**
$\alpha_{\mathrm{DMPD/DMPD^{\bullet+}}}$	(0.5 ± 0.1)
$\alpha_{\mathrm{DMPD^{\bullet+}/DMPD^{2+}}}$	(0.5 ± 0.1)
c_{DMPD}	(19.5 ± 1.0) mM
$E^{\ominus}_{\mathrm{f,DMPD/DMPD^{\bullet+}}}$	$(0.205 \pm 0.01$ V *vs* Pt
$E^{\ominus}_{\mathrm{f,DMPD^{\bullet+}/DMPD^{2+}}}$	(0.745 ± 0.01) V *vs* Pt
$k^0_{\mathrm{DMPD/DMPD^{\bullet+}}}$	≥ 0.01 cm s^{-1}
$k^0_{\mathrm{DMPD^{\bullet+}/DMPD^{2+}}}$	(0.001 ± 0.002) cm s^{-1}
D_{DMPD}	$(2.0 \pm 0.1) \times 10^{-7}$ cm^2 s^{-1}
$D_{\mathrm{DMPD^{\bullet+}}}$	$(1.1 \pm 1) \times 10^{-7}$ cm^2 s^{-1}
$D_{\mathrm{DMPD^{2+}}}$	$(7 \pm 0.1) \times 10^{-8}$ cm^2 s^{-1}
k_{comp}	(250 ± 150) dm^3 mol^{-1} s^{-1}
$\Delta G^{\ominus}_{\mathrm{comp}}$	-52.1 kJ mol^{-1}

8.3.2 Cyclic Voltammetry

The kinetic and thermodynamic parameters of the two redox couples were elucidated by means of cyclic voltammetry. The oxidation of DMPD was examined in [C_4mim][BF_4]. Cyclic voltammetry for the oxidation of 20 mM DMPD was carried out on a Pt microelectrode (diameter 10μm) at scan rates ranging from 10 mV s^{-1} to 1 V s^{-1}. The voltammograms are typically

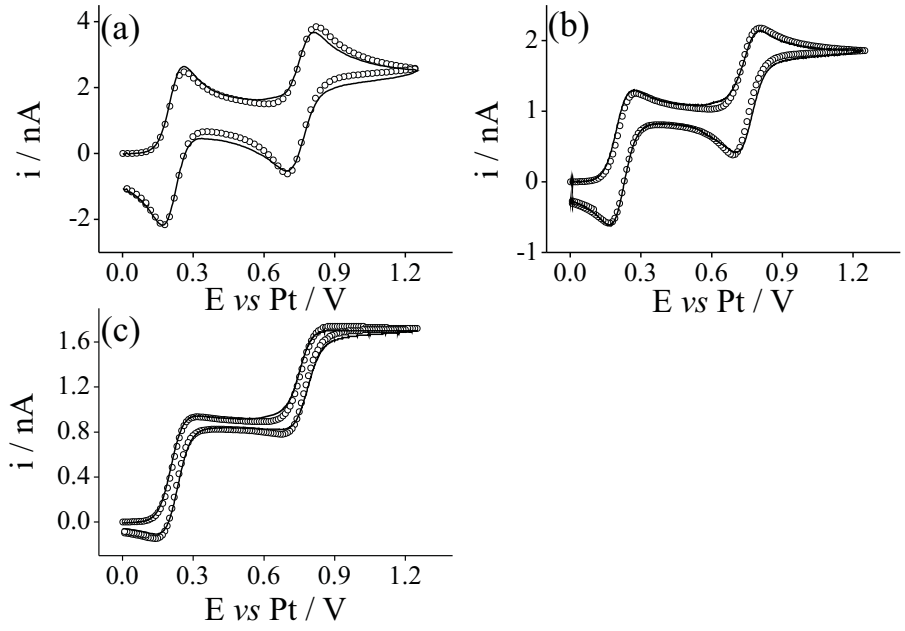


Figure 8.4: Voltammetric fits: —, experiment; ∘, simulation ($k_{\text{comp}} = 250$ dm^3 mol^{-1} s^{-1}). (a) 1000 mV s^{-1}(b) 100 mV s^{-1}(c) 10 mV s^{-1}.

scanned from 0 V to 1.5 V *vs.* a Pt quasi-reference electrode. Two oxidation peaks were observed for scan rates 10 mV s^{-1} to 1 V s^{-1}, shown in Figure 8.4 at potentials 0.4 V and 0.9 V. These correspond, respectively, to the oxidation of DMPD to DMPD$^{\bullet+}$ and DMPD^{2+}. Both electron transfers are chemically reversible as indicated by the presence of two back peaks. The reliability of the fitting procedure was ensured by fitting the voltammograms over a wide range of scan-rates (2 orders of magnitude). The fitted voltammograms are shown in Figure 8.4 and the corresponding data quoted in Table 8.2.

The onset of electrochemical reversibility occurs in RTILs at much lower values of the electrochemical rate constant compared to other non-aqueous solvents. For example, in a classic paper by Amatore,[24] electrochemical rate constants as high as 4 cm s^{-1} could be distinguished voltammetrically in acetonitrile. The reason for this discrepancy lies in the high viscosity of ionic liquid solvents (e.g. $\mu_{[\text{C}_4\text{mim}][\text{BF}_4]} = 112$ mPas at 25°C[25]) compared to other non-aqueous solvents (e.g. $\mu_{\text{acetonitrile}} = 34$ mPas at 25°C[26]). Mass transport is more likely to be rate limiting in solvents of greater viscosity. The rate constant for the first electron trans-

Table 8.3: Normalised parameters.

Normalised Parameter	**Definition**
J	$\frac{i}{Fc_{\mathrm{A}}^{*}D_{\mathrm{A}}r_{\mathrm{e}}}$
K^{0}	$\frac{k^{0}r_{\mathrm{e}}}{D_{\mathrm{A}}}$
K_{comp}	$\frac{k_{\mathrm{comp}}c_{\mathrm{A}}^{*}r_{\mathrm{e}}^{2}}{D_{\mathrm{A}}}$
K_{disp}	$\frac{k_{\mathrm{disp}}c_{\mathrm{A}}^{*}r_{\mathrm{e}}^{2}}{D_{\mathrm{A}}}$
θ	$\frac{F(E-E_{\mathrm{f}}^{\ominus})}{RT}$
R	$\frac{r}{r_{\mathrm{e}}}$
σ	$\frac{r_{\mathrm{e}}^{2}Fv}{D_{\mathrm{A}}RT}$
τ	$\frac{D_{\mathrm{A}}t}{r_{\mathrm{e}}^{2}}$
x	$\frac{c_{\mathrm{X}}}{c_{\mathrm{X}}^{*}}$
x_{0}	$\frac{c_{\mathrm{X},0}}{c_{\mathrm{X}}^{*}}$
Z	$\frac{z}{r_{\mathrm{e}}}$

fer ($\mathrm{DMPD} - e^{-} \rightleftharpoons \mathrm{DMPD}^{\bullet+}$) is electrochemically reversible on the voltammetric timescale ($k^{0}_{\mathrm{DMPD/DMPD}^{\bullet+}} \geq 0.01$ cm s^{-1}) while the second ($\mathrm{DMPD}^{\bullet+} - e^{-} \rightleftharpoons \mathrm{DMPD}^{2+}$) is quasi-reversible ($k^{0}_{\mathrm{DMPD}^{\bullet+}/\mathrm{DMPD}^{2+}} = (0.001 \pm 0.002)$ cm s^{-1}).

The comproportionation of DMPD and DMPD^{2+} to form $\mathrm{DMPD}^{\bullet+}$ is thermodynamically downhill. Using Equation 8.5 and the data in Table 8.2, $\Delta G^{\ominus} = -52.1$ kJ mol^{-1}. However, from the Table 8.2, comproportionation is slow on the voltammetric timescale ($k_{\mathrm{comp}} = 250$ dm^{3} mol^{-1} s^{-1}). When DMPD is oxidised, the lone electron pair on each nitrogen atom makes an increased contribution to the resonance within the aromatic ring: the double bond character of each C-N bonds increases. The rearrangement energy for the electron transfer is substantial and leads to a small value of the rate constant as laid out in Marcus theory.[27,28]

In a recent paper[5] it was shown that, in the limit of electrochemical reversibility, the presence of diffusionally controlled comproportionation can be discerned only at high scan-rates when the diffusion coefficients of the species (D_{DMPD}, $D_{\mathrm{DMPD}^{\bullet+}}$ and $D_{\mathrm{DMPD}^{2+}}$) are significantly different such that $D_{\mathrm{DMPD}^{\bullet+}}/D_{\mathrm{DMPD}} > 1.5$ and $D_{\mathrm{DMPD}^{2+}}/D_{\mathrm{DMPD}} > 1.5$ or $D_{\mathrm{DMPD}^{\bullet+}}/D_{\mathrm{DMPD}} < 0.75$ and $D_{\mathrm{DMPD}^{2+}}/D_{\mathrm{DMPD}} < 0.75$. It is important to note that this conclusion refers to a comparison between $k_{\mathrm{comp}} = 0$ dm^{3} mol^{-1} s^{-1} and *diffusion control*. For an arbitrary value of k_{comp}

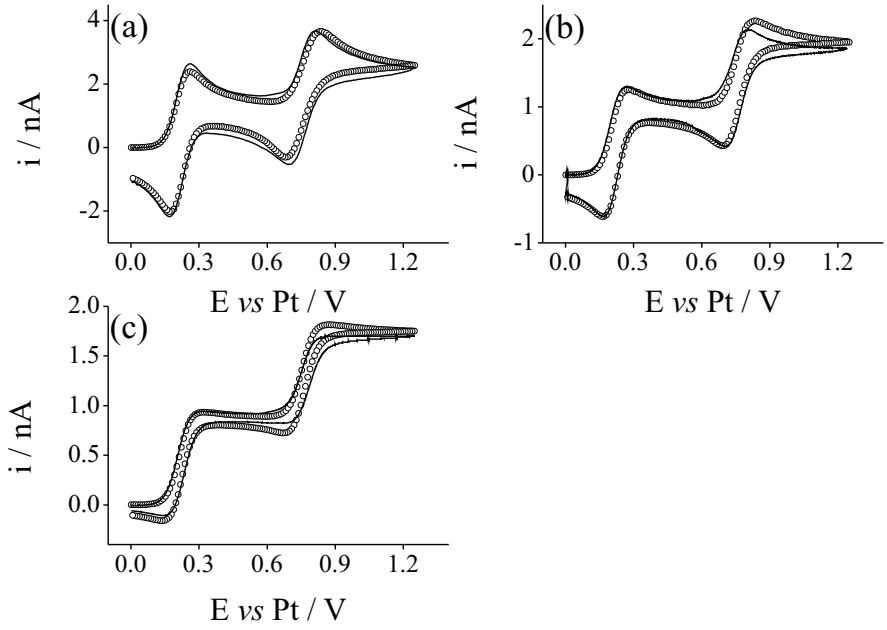


Figure 8.5: Voltammetric fits: —, experiment; ∘, simulation ($k_{\text{comp}} = 0$ dm^3 mol^{-1} s^{-1}). (a) 1000 mV s^{-1}(b) 100 mV s^{-1}(c) 10 mV s^{-1}.

the aforementioned conditions for the observation of comproportionation are neither necessary nor sufficient. Figure 8.5 shows a comparison between the experimental voltammograms at a range of scan rates and the simulated transients corresponding to the data in Table 8.2 with $k_{\text{comp}} = 0$ dm^3 mol^{-1} s^{-1}.

It is clear that, for the present system, the occurrence of comproportionation *can* be identified voltammetrically and the discrepancy between $k_{\text{comp}} = 0$ dm^3 mol^{-1} s^{-1} and $k_{\text{comp}} = 250$ dm^3 mol^{-1} s^{-1} increases with decreasing scan-rate. At low scan-rates a steady-state voltammetric response is obtained while at high scan-rates comproportionation is outrun on the voltammetric timescale. Therefore, in each case, the presence of comproportionation cannot be discerned from the voltammetry. For DMPD in [C_4 mim][BF_4], the effect of comproportionation is not expected to be apparent in the limit of very low scan-rates.

8.4 Conclusions

In this Chapter, simulation studies have been used to show that comproportionation, in which DMPD reacts homogeneously with $DMPD^{2+}$ ($DMPD + DMPD^{2+} \rightleftharpoons 2DMPD^{\bullet+}$), can be discerned for the 2 electron oxidation of DMPD in the ionic liquid [C_4 mim][BF_4]. In addition, the kinetic and thermodynamic parameters of the reaction were elucidated by means of double potential step chronoamperometry and cyclic voltammetry. This Chapter outlines the advantage of high viscosity of RTILs in discerning the kinetics of a reaction.

The ability of RTILs to interact with a species is also of interest. In the following two Chapters, the interaction of RTILs with species in solution is explored and shows that a change in the anion of the RTIL can alter the electrochemical reactions of species in solution which might be useful for differing purposes of detection of the analyte species. The next Chapter outlines the effect of the anion of an RTIL on the reversibility of the voltammetry of catechol and dopamine.

References

[1] Wang, Y.; Sun, Y.; Yu, L. and Zeng, Z., *Shenyang Yaoke Daxue Xuebao*, 2006, **23**, 432–434.

[2] Mallakpour, S. and Kolahdoozan, M., *Polym. J.*, 2008, **40**, 513–519.

[3] Silvester, D. S. and Compton, R. G., *Z. Phys. Chem.*, 2006, **220**, 1247–1274.

[4] Ignat′ev, N.; Welz-Biermann, U.; Kucheryna, A.; Bissky, G. and Willner, H., *J. Fluorine Chem.*, 2005, **126**, 1150–1159.

[5] Belding, S. R.; Baron, R.; Dickinson, E. J. F. and Compton, R. G., *J. Phys. Chem. C*, 2009, **113**, 16042–16050.

[6] Barnes, A. S.; Rogers, E. I.; Streeter, I.; Aldous, L. and Hardacre, C.and Compton, R. G., *J. Phys. Chem. B*, 2008, **112**, 7560–7565.

[7] Andrieux, C. P.and Savéant, J. M., *J. Electroanal. Chem.*, 1970, **28**, 339–348.

[8] Amatore, C.; Maisonhaute, E. and Simonneau, G., *Electrochem. Commun.*, 2000, **2**, 81–84.

[9] Belding, S. R.; Rogers, E. I. and Compton, R. G., *J. Phys. Chem. C*, 2009, **113**, 4202–4207.

[10] Evans, R. G.; Klymenko, O. V.; Price, P. D.; Davies, S. G.; Hardacre, C. and Compton, R. G., *ChemPhysChem*, 2005, **6**, 526–533.

[11] Paddon, C. A.; Silvester, D. S.; Bhatti, F. L.; Donohoe, T. J. and Compton, R. G., *Electroanalysis*, 2007, **19**, 11–22.

[12] Klymenko, O. V.; Evans, R. G.; Hardacre, C.; Svir, I. B. and Compton, R. G., *J. Electroanal. Chem.*, 2004, **571**, 211–221.

[13] Zigah, D.; Ghilane, J.; Lagrost, C. and Hapiot, P., *J. Phys. Chem. B*, 2008, **112**, 14952–14958.

[14] Endres, F. and Zein El Abedin, S., *PhysChemChemPhys*, 2006, **8**, 2101–2116.

[15] Hapiot, P. and Lagrost, C., *Chem. Rev.*, 2008, **108**, 2238–2264.

[16] Buzzeo, M. C.; Klymenko, O. V.; Wadhawan, J. D.; Hardacre, C.; Seddon, K. R. and Compton, R. G., *J. Phys. Chem. A*, 2003, **107**, 8872–8878.

[17] Ghilane, J.; Lagrost, C. and Hapiot, P., *Anal Chem*, 2007, **79**, 7383–7391.

[18] Barnes, E. O.; O' Mahony, A. M.; Belding, S. R. and Compton, R. G., *J. Chem. Eng. Data*, 2010, **55**, 2219–2224.

[19] Britz, D., *Digital Simulation in Electrochemistry*, Springer-Verlag, Berlin, 3 ed., 2005.

[20] Heinze, J., *J. Electroanal. Chem.*, 1981, **124**, 73–86.

[21] Press, W. H.; Teukolsky, S. A.; Vetterling, W. T. and Flannery, B. P., *Numerical Recipes: The Art of Scientific Computing*, Cambridge University Press, 2007.

[22] Gavaghan, D. J., *J. Electroanal. Chem.*, 1998, **456**, 1–12.

[23] Shoup, D. and Szabo, A., *J. Electroanal. Chem.*, 1982, **140**, 237–245.

[24] Amatore, C.; Bonhomme, F.; Bruneel, J.-L.; Servant, L. and Thouin, L., *J. Electroanal. Chem.*, 2000, **484**, 1–17.

[25] Okoturo, O. O. and VanderNoot, T. J., *J. Electroanal. Chem.*, 2004, **568**, 167–181.

[26] Cunningham, G. P.; Vidulich, G. A. and Kay, R. L., *J. Chem. Eng. Data*, 1967, **12**, 336–337.

[27] Compton, R. G. and Banks, C. E., *Understanding Voltammetry*, World Scientific, 2007.

[28] Marcus, R. A., *J. Chem. Phys.*, 1956, **24**, 966–978.

Chapter 9

The Electrochemical Oxidation of Catechol and Dopamine on Platinum in $[C_2mim][NTf_2]$ and $[C_4mim][BF_4]$: Adsorption Effects in Ionic Liquid Voltammetry

The electrochemical oxidation of catechol and dopamine has been studied at a platinum micro-electrode (10 μm diameter) in two RTILs: $[C_2mim][NTf_2]$ and $[C_4mim][BF_4]$. For catechol in $[C_2mim][NTf_2]$, an electrochemically quasi-reversible oxidation peak was observed at 1.1 V *vs.* Pt with a back peak at 0.4 V *vs.* Pt. This is assigned to the two-electron oxidation of catechol to doubly protonated o-benzoquinone. Double-step chronoamperometry gave a diffusion coefficient for the catechol and the oxidised species which is 3.8×10^{-11} m^2 s^{-1} for both. For catechol in $[C_4mim][BF_4]$, a two-electron oxidation wave was observed at 1.0 V *vs.* Pt with no back peak. Another peak at less positive potential was also observed at 0.6 V *vs.* Pt in $[C_4mim][BF_4]$ but not in $[C_2mim][NTf_2]$ which is assigned to the adsorption of electrochemically formed neutral o-benzoquinone on the platinum electrode. The oxidised protonated o-benzoquinone is suggested to be deprotonated by the $[BF_4]^-$ anion, but not by the $[NTf_2]^-$ anion: hence adsorption of the neutral species at the platinum electrode, not the charged species. For dopamine in both RTILs, two chemically irreversible oxidation peaks were observed at 0.75 V and 1.1 V *vs.* Pt, and assigned to the oxidation of dopamine to the corresponding semi-quinone and the quinone. Potential-step chronoamperometry was carried out on the oxidation waves of dopamine in $[C_2mim][NTf_2]$ and the diffusion coefficient of species in solution was calculated to be 6.85 $\times 10^{-12}$ m^2 s^{-1} and confirmed that the waves corresponded to one and two electron processes. A third wave was observed at 1.8 V *vs.* Pt which is attributed to the oxidation of the amine group to a radical cation with likely subsequent follow up chemistry. In $[C_4mim][BF_4]$ a peak at less positive potential was observed for dopamine, similar to catechol which is assigned to the

adsorption of the neutral quinone species on the platinum electrode formed by the reaction of the removal of protons from the oxidised dopamine with the $[BF_4]^-$ anion.

9.1 Introduction

Catecholamines such as dopamine are particularly interesting phenols due to their biological role. Dopamine is a neurotransmitter in humans and plays a well-documented role in the function of the nervous, cardiovascular and renal systems.[1–3] It is shown that people diagnosed with Parkinson's disease show a significant, if not complete depletion of dopamine in the central nervous system.[4] Therefore, dopamine is of interest both as a disease marker and in pharmaceuticals.

The two-electron oxidation of catechol and dopamine in aqueous solvent have been well documented by Hubbard *et al.*, who have intensively studied the chemisorption of various phenols at polycrystalline platinum electrodes, focusing on the orientation of adsorbed layers.[5–11] In their work they have found that many factors affect the orientation and mode of attachment of phenols to the platinum surface, such as analyte molecular structure, analyte concentration, electrode potential, nature of the electrolyte anion and temperature.[8]

Although there are now many studies of electrode processes in RTILs reported[12–15] it is the case that almost exclusively these focus on reactions in which products and reactants are solution phase. Little evidence has emerged hitherto to suggest that chemisorption plays a significant role in electrolytic reactions in RTILs. Exceptions to this observation include the reduction of dichlorine[16] and also the oxidation of hydrogen sulphide.[17] In the former case chemisorption was recorded by an unusual scan rate dependency whereby the voltammetry signal decreased with increased scan rate. In the latter case, significant accumulation of H_2S in the double layer was inferred voltammetrically as outlined in Chapter 7. In this Chapter we explore the voltammetry of catechol and dopamine at platinum electrodes where in aqueous solutions significant adsorption effects have been noted, as described above. In an ionic liquid containing $[BF_4]^-$ anions, adsorption will be seen to occur since it is the case that the two-electron oxidation product of catechol can lose protons to form the neutral o-benzoquinone which can adsorb whereas in the $[NTf_2]^-$ liquid solution this does not happen and the protonated

benzoquinone does not adsorb due to its charged nature.

9.2 Results and Discussion

The oxidations of catechol and dopamine were examined in $[C_4mim][BF_4]$ and $[C_2mim][NTf_2]$. Each ionic liquid showed featureless baselines in the absence of the solutes when purged in a vacuum for 90 min.

These ionic liquids were chosen due to their differing anions. It was expected that the $[BF_4]^-$ anion would have a different effect than the $[NTf_2]^-$ anion both on any adsorption processes given that the $[BF_4]^-$ is known to react with protons to form HF and BF_3[18,19] and the observations of Hubbard with respect to the high anion sensitivity of quinone adsorption in aqueous media[8] and also on the solution phase species owing to the differing capacities for interactions with the two analytes studied.[20] There may also be a difference in reactivity due to the slight difference in the cation in each ionic liquid, however it is the effect of the anion which would primarily account for any differences observed in the chemistry.

9.2.1 Cyclic Voltammetry of Catechol in RTILs

9.2.1.1 Catechol in $[C_2mim][NTf_2]$

Figure 9.1 shows cyclic voltammetry of 20 mM catechol in $[C_2mim][NTf_2]$ at platinum electrode (diameter 10μm) for scan rates 100 mV s^{-1} to 4000 mV s^{-1} in potential range 0.0 V to 2.0 V *vs.* Pt. The voltammetry shows an oxidative peak at approximately 1.1 V *vs.* Pt. The peak is steady-state at lower scan rates and becomes more transient at higher scan rates. This is due to the transition from convergent to more planar diffusion showing intermediate behaviour of micro/macroelectrode electrochemistry.[21] On reversal of the scan at 2.0 V *vs.* Pt the voltammogram decreases to zero current for the steady-state voltammetry at lower scan rates. At higher scan rates, a back peak is seen at approximately 0.4 V *vs.* Pt. This peak increases with scan

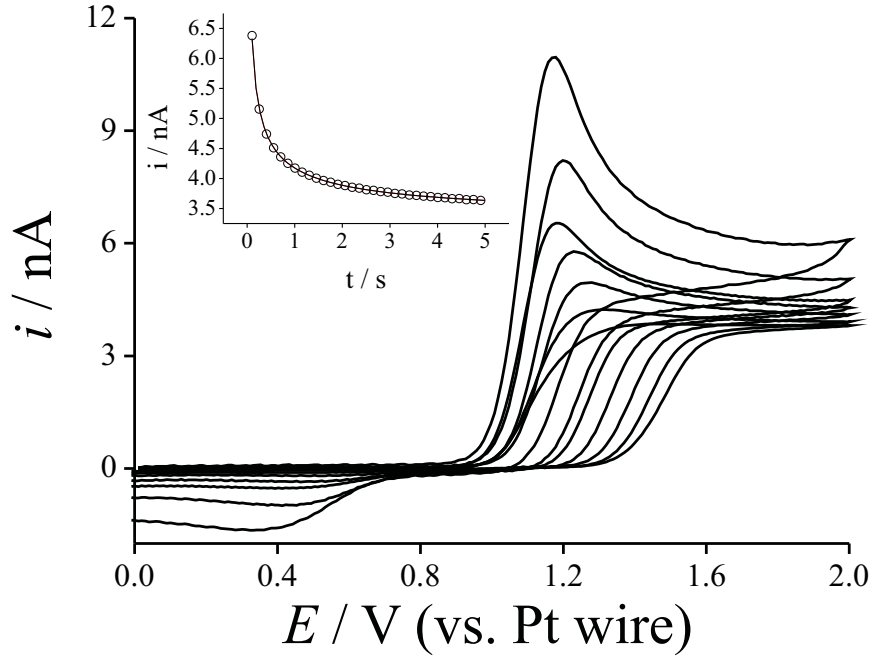


Figure 9.1: Cyclic voltammetry for the oxidation of 20 mM catechol in $[C_2mim][NTf_2]$ at Pt electrode (10 μm diameter) at a scan rates of 100, 200, 400, 700, 1000, 2000 and 4000 mV s^{-1} and temperature of 298 K. *Inset* : Chronoamperometry for the oxidative wave of 20 mM catechol in $[C_2mim][NTf_2]$. $D = 3.8 \times 10^{-11}$ m^2 s^{-1}, $nc = 40$ mM..

rate. This behaviour has also been observed at a glassy carbon electrode in aprotic solvents such as MeCN[22,23] and acetate buffer.[24] The shape of the back peak, and the fact that it is separated from the forward peak by 700 mV suggests that the oxidation is electrochemically quasi-reversible.

Chronoamperometry was employed to infer the mechanism of the oxidation. If the mechanism is diffusion controlled, the chronoamperometry allows us to calculate the diffusion coefficient of the species and the number of electrons transferred. A potential step was carried out beyond the oxidative wave of the catechol from 0.0 V (corresponding to no faradaic current) to 1.6 V *vs*. Pt and the current was measured for 5 s (*inset* Figure 9.1). The experimental data (circles) was theoretically fitted (solid line) to the Shoup and Szabo expression.[25] The diffusion coefficient obtained for catechol in $[C_2mim][NTf_2]$ was calculated to be 3.84×10^{-11} m^2 s^{-1}. The chronoamperometric fitting also gave the *nc* value (no. of electrons $\times$ concentration) which was 40 mM. This indicates a 2-electron transfer since the concentration of catechol was 20 mM,

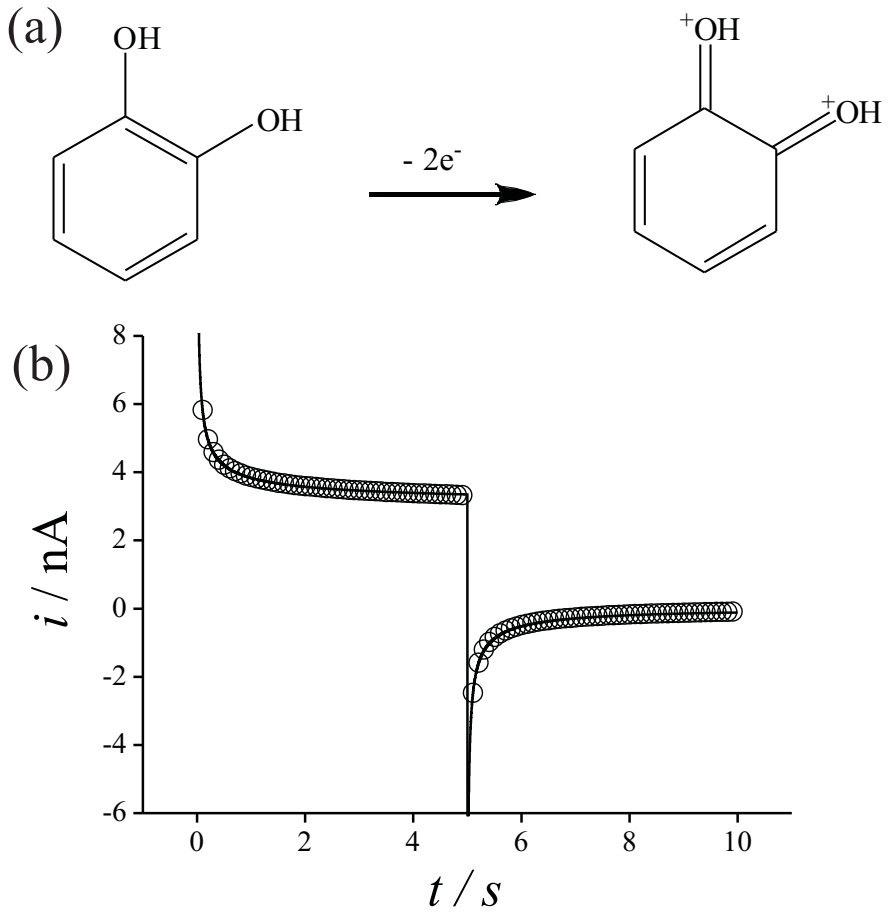


Figure 9.2: (a) Mechanism for the 2-electron, 2-proton oxidation of catechol to doubly protonated o-benzoquinone in $[C_2mim][NTf_2]$. (b) Double step chronoamperometry for oxidation of 20 mM catechol in $[C_2mim][NTf_2]$ at Pt electrode (10 μm diameter). $D_{cat} = 3.8 \times 10^{-11}$ m^2 s^{-1}, $D_{benz} = 3.8 \times 10^{-11}$ m^2 s^{-1}, $nc = 40$.

so $c = 20$ mM and $n = 2$. This result implies that the oxidation of catechol is diffusion-controlled at the potential of 1.6 V and is directly oxidised to the doubly protonated o-benzoquinone. The fact that the oxidative signal was reproducible with potential cycling shows that no protons are lost to form H_2, so the oxidised species is doubly protonated. Therefore we infer the process to be that of Figure 9.2(a).

To further support this conclusion, double-step chronoamperometry was carried out on the oxidative wave to calculate the diffusion coefficient of the oxidised catechol species. The potential was stepped from 0.0 V (no faradaic current) to 1.6 V *vs*. Pt to oxidise the catechol to doubly protonated o-benzoquinone and then stepped back to 0.0 V to reduce the oxidised

species back to catechol. The transient obtained is shown in Figure 9.2 (b) (circles). The diffusion coefficient (D_{cat}) and *nc* of catechol were determined from analysis of the experimental data for the first potential step using Shoup and Szabo approximation.[25] A computer simulation was used to model the second potential step to give the diffusion coefficient of doubly protonated o-benzoquinone (D_{benz}). The value for D_{cat} was calcuated to be 3.8×10^{-11} m^2 s^{-1} as before, and the value for D_{benz} was calculated to also be 3.8×10^{-11} m^2 s^{-1}. The experimental data (circles) fits the simulation data (solid line) well, showing that the oxidation and reduction processes are diffusion controlled. The ratio of $(D_{\mathrm{cat}})/D_{\mathrm{benz}}) \approx 1$ suggesting that both species diffuse at the same rate through the ionic liquid media,. The oxidised species is charged, which in ionic media usually results in slower diffusion as reported by Rogers *et al.*[26] However, the positive charge on the doubly protonated o-benzoquinone is very likely substantially delocalised around the aromatic ring, so that ionic interactions between the oxidised species and the solvent would be diminished.

The reductive voltammetry of catechol was also examined in [C_2mim][NTf_2]. The reduction of catechol was observed as a steady-state wave at approximately -1.1 V *vs.* Pt, and the current increased with increasing scan rate. This is attributed to the direct reduction of the catechol in the RTIL. Figure 9.3 shows the cyclic voltammetry of 20 mM catechol in [C_2mim][NTf_2] at scan rate 1000 mV s^{-1} in the potential range of 2.0 V to -2.0 V. The forward scan shows an oxidative wave at potential 1.1 V *vs.* Pt which is attributed to the direct oxidation of catechol to a doubly-protonated o-benzoquinone discussed above. On the reverse sweep, a reductive wave is observed at potential 0.5 V *vs.* Pt which is attributed to the reverse reaction of the oxidation. At a more negative potential on the reverse scan, a further reductive wave is observed at -1.4 V *vs.* Pt. This wave is attributed to the direct reduction of the catechol to a double-negatively charged semi-quinone. This signal is not due to any chemistry caused by the oxidation of the catechol, which is outlined in the *inset* of Figure 9.3, which shows the direct reduction of catechol

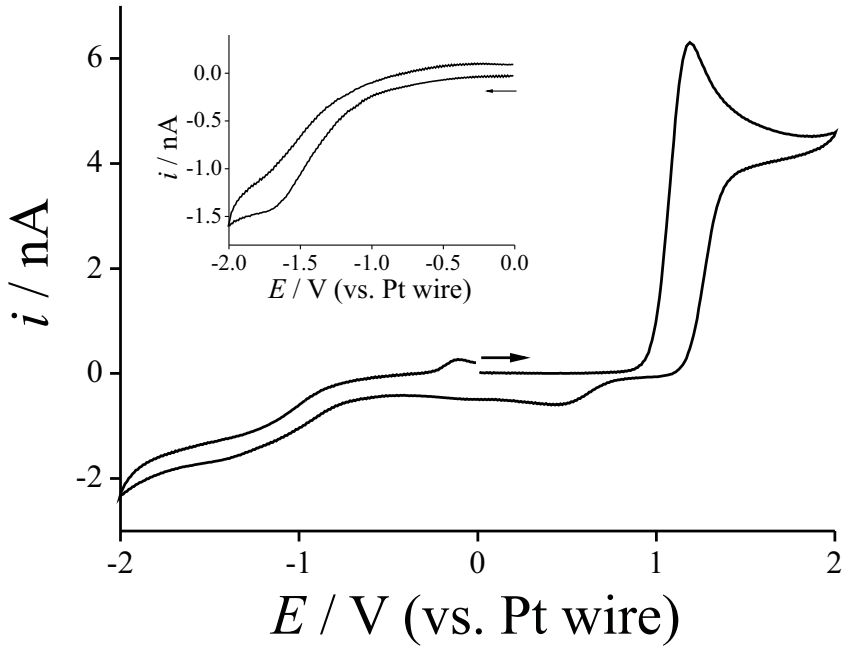


Figure 9.3: Cyclic voltammetry for the oxidation of 20 mM catechol in $[C_2mim][NTf_2]$ at Pt electrode (10 μm diameter) at a scan rate 1000 mV s^{-1} and temperature of 298 K.

in $[C_2mim][NTf_2]$ without ever scanning positively, in the potential range of 0.0 V to -2.0 V. This voltammetric feature was not examined further in this work as the difference in oxidative features in two different RTILs was mainly of interest.

9.2.1.2 Catechol in $[C_4mim][BF_4]$

Cyclic voltammetry for the oxidation of a 20 mM solution of catechol was also carried out in $[C_4mim][BF_4]$ in potential range 0.0 V to 1.5 V *vs.* Pt at scan rates 100 mV s^{-1} to 4000 mV s^{-1}, shown in Figure 9.4. The ionic liquid $[C_4mim][BF_4]$ differs greatly to $[C_2mim][NTf_2]$ with respect to properties such as hydrophobicity which is mainly due to the nature of the anion,[27] so any change in the electrochemical oxidation of catechol in a $[BF_4]^-$ RTIL compared with a $[NTf_2]^-$ RTIL is not unexpected. Voltammetry shows a prewave peak at approx. 0.6 V *vs.* Pt which is steady-state at lower scan rates, followed by another larger oxidative wave at approx. 1.0 V *vs.* Pt. This second wave is steady-state at lower scan rates and becomes more transient at higher scan rates due to variation from convergent to linear diffusion. This wave is attributed to a two-

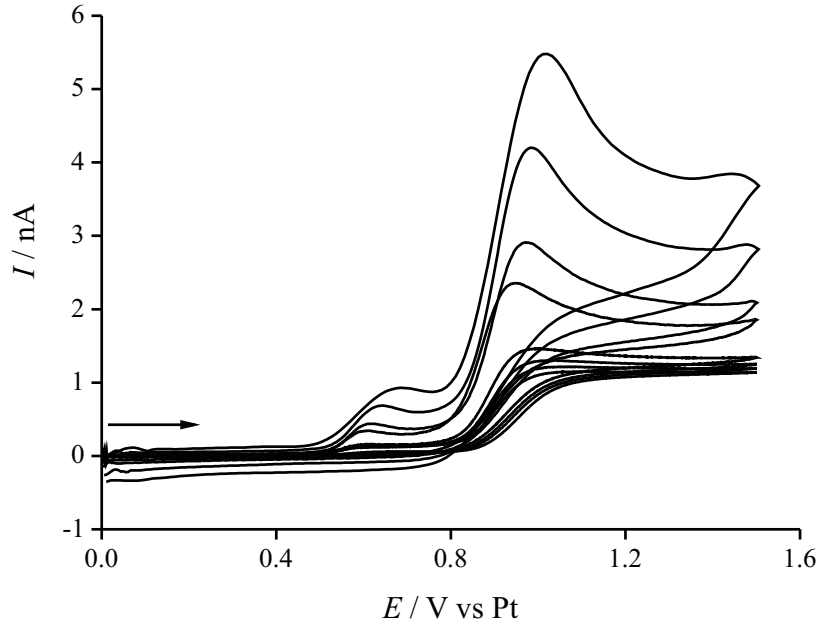


Figure 9.4: Cyclic voltammetry for the oxidation of 20 mM catechol in $[C_4mim][BF_4]$ at Pt electrode (10 μm diameter) at a scan rates of 10, 25, 50, 100, 500, 1000, 2500 and 5000 mV s^{-1} and temperature of 298 K.

electron oxidation of catechol to doubly protonated o-benzoquinone as seen in $[C_2mim][NTf_2]$. On reversal of the scan at 1.5 V *vs*. Pt the voltammetry decreases to zero current at all scan rates studied (10 - 5000 mVs^{-1}), and no back peak is observed under any conditions studied. This suggests that the oxidation of catechol in this medium is fully chemically irreversible.

We suggest an EC mechanism for catechol in $[C_4mim][BF_4]$, where catechol undergoes a two-electron oxidation to form doubly protonated o-benzoquinone, observed in Figure 9.4 at potential 1.0 V *vs*. Pt.

Since no back peak is observed, no reduction back to catechol occurs. Rather, the anion of the RTIL ($[BF_4]^-$), reacts with the protons to form HBF_4, which then decomposes to HF and BF_3.[18] Remaining then in solution is neutral o-benzoquinone, which undergoes a follow up reaction, likely a Diels-Alder reaction[28] with other neutral species in solution. Some neutral o-benzoquinone species in solution adsorbs onto the Pt surface[6,9] where it again likely undergoes a Diels-Alder reaction with other o-benzoquinone species to form a monolayer of product, which is observed as a prewave in Figure 9.4 at 0.6 V *vs*. Pt. The mechanism is outlined in Figure 9.5.

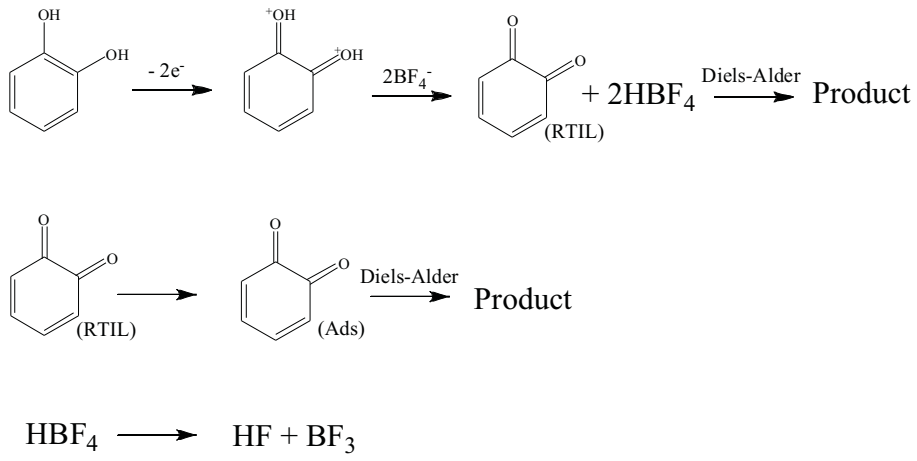


Figure 9.5: Mechanism for the 2-electron, 2-proton oxidation of catechol to doubly protonated o-benzoquinone in $[C_4mim][BF_4]$ and reaction of $[BF_4]^-$ anion with protons.

It is noteworthy that, while the electron transfer process is seen to precede the proton transfer process in this mechanism, that work has been carried out by Costentin *et al.* observing concerted proton and electron transfers (CPET), whereby a small value for the transfer coefficient (<0.5)can indicate the occurrence of this process.[29] The value for the transfer coefficient (β) in the case of Figure 9.4 is 0.28, which may indicate the occurrence of CPET, if solvent dipole reorganisation is not significant.

The charge under the prewave was measured and calculated to be 2.8×10^{-10} C, resulting in a surface coverage of 1.7 nmol cm^{-2} for a two-electron process. The adsorptive behaviour of benzoquinone is well documented by Hubbard *et al.* in aqueous media at a platinum electrode (area 0.07 cm^2), whereby the aromatic ring is coordinated parallel to the Pt surface resulting in a monolayer.[6,9] The surface coverage of the benzoquinone on the platinum surface in aqueous media was calculated by Hubbard *et al.* to be 0.6 nmol cm^{-2} where the aromatic ring is adsorbed parallel to the electrode. While the surface coverage of benzoquinone in $[C_4mim][BF_4]$ is higher than in aqueous media, this may be due to different orientation of species adsorption on the electrode surface due to differing solvent, a point also noted by Hubbard.

To further support this conclusion, cyclic voltammetry was carried out on varying concentrations of catechol in $[C_4mim][BF_4]$. Figure 9.6 shows cyclic voltammetry of 5, 10 and 20 mM

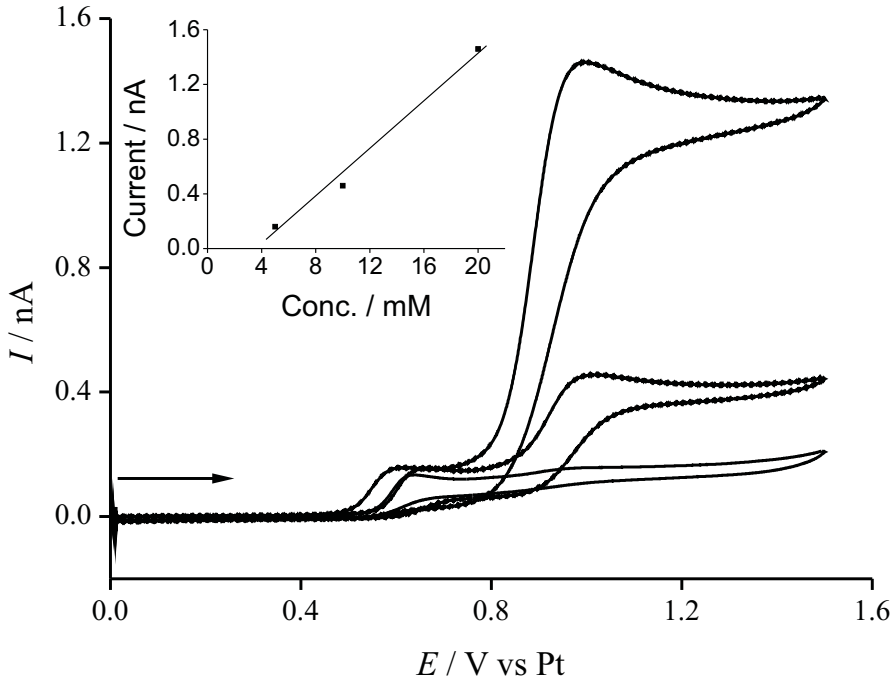


Figure 9.6: Cyclic voltammetry for the oxidation of 5, 10 and 20 mM catechol in $[C_4mim][BF_4]$ at Pt electrode (10 μm diameter) at a scan rate 100 mV s^{-1} and temperature of 298 K. *inset*: Concentration (mM) *vs.* peak current (nA) for oxidation wave at 1.0 V.

catechol in $[C_4mim][BF_4]$ at scan rate 100 mV s^{-1} in potential range 0.0 V to 1.5 V *vs.* Pt. The prewave is observed at approximately 0.6 V *vs.* Pt. It is steady-state at this scan rate, and does not increase with increasing concentration, while the oxidative wave, seen at 1.0 V does increase with increasing concentration. This supports the conclusion that the prewave is due to adsorption.[30] The *inset* of Figure 9.6 shows that the current of the oxidative wave at 1.0 V increases linearly with increasing concentration.

The presence of water in the system had very little effect on the oxidation of catechol. When excess water was added to the system, the current of the oxidative scan increased, due to a decrease in viscosity. The electrochemical window of the RTIL was also decreased.

The voltammetry of catechol in RTILs was used as a 'fingerprint' to interpret the voltammetry of dopamine which contains an orthoquinone moiety also. Similar electrochemical behaviour is expected for the oxidation of dopamine since the structure of both molecules is similar, and the voltammetry of dopamine is interpreted in Section 9.2.2

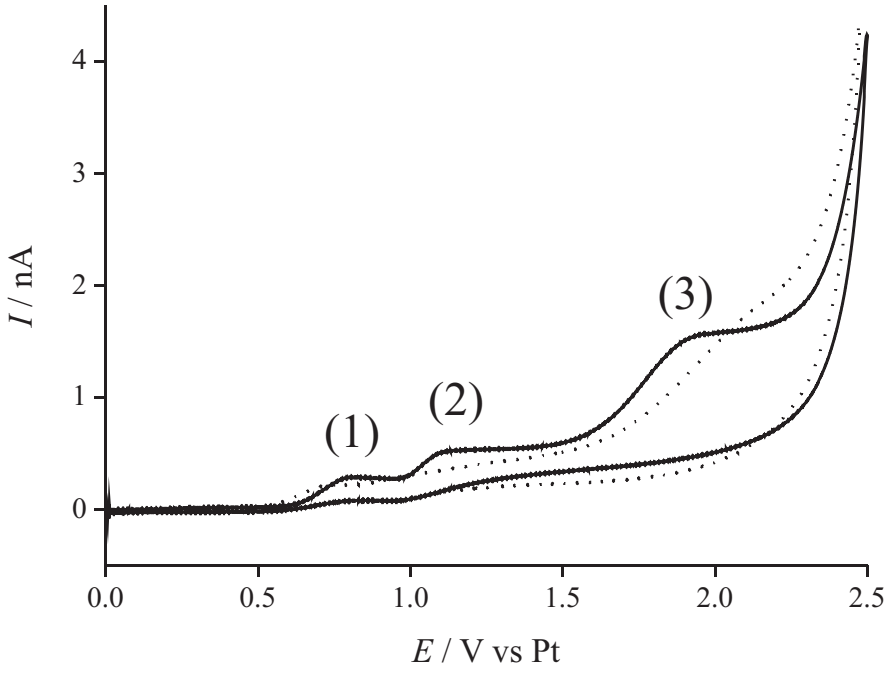


Figure 9.7: Cyclic voltammetry for the oxidation of 10 mM dopamine in $[C_2mim][NTf_2]$ at Pt electrode (10 μm diameter) at a scan rate 100 mV s^{-1} and temperature of 298 K. *Solid line*: first scan of oxidation of dopamine; *dotted line*: subsequent scans of oxidation of dopamine.

9.2.2 Cyclic Voltammetry of Dopamine in RTILs

Cyclic voltammetry for the oxidation of a 10 mM solution of dopamine was carried out on a Pt microelectrode (diameter 10μm) at scan rate 100 mV s^{-1} in $[C_2mim][NTf_2]$ and $[C_4mim][BF_4]$. The voltammograms are typically scanned from 0 V to 2 V *vs*. a Pt quasi-reference electrode.

9.2.2.1 Dopamine in $[C_2mim][NTf_2]$

Figure 9.7 shows the oxidation of dopamine in $[C_2mim][NTf_2]$ at the platinum electrode at scan rate 100 mV s^{-1} in potential range 0.0 V to 2.4 V *vs*. Pt. The solid line denotes the first oxidative scan of dopamine in ionic liquid, and the dotted line denotes subsequent scans. The voltammetry shows three waves are present in this scan, wave 1 at 0.75 V, wave 2 at 1.1 V and wave 3 at 1.8 V *vs*. Pt. The reversal of the voltammogram shows no back peak is present, therefore we assume that this reaction is electrochemically irreversible.

The first wave at 0.75 V *vs*. Pt is attributed to the one-electron oxidation of dopamine which

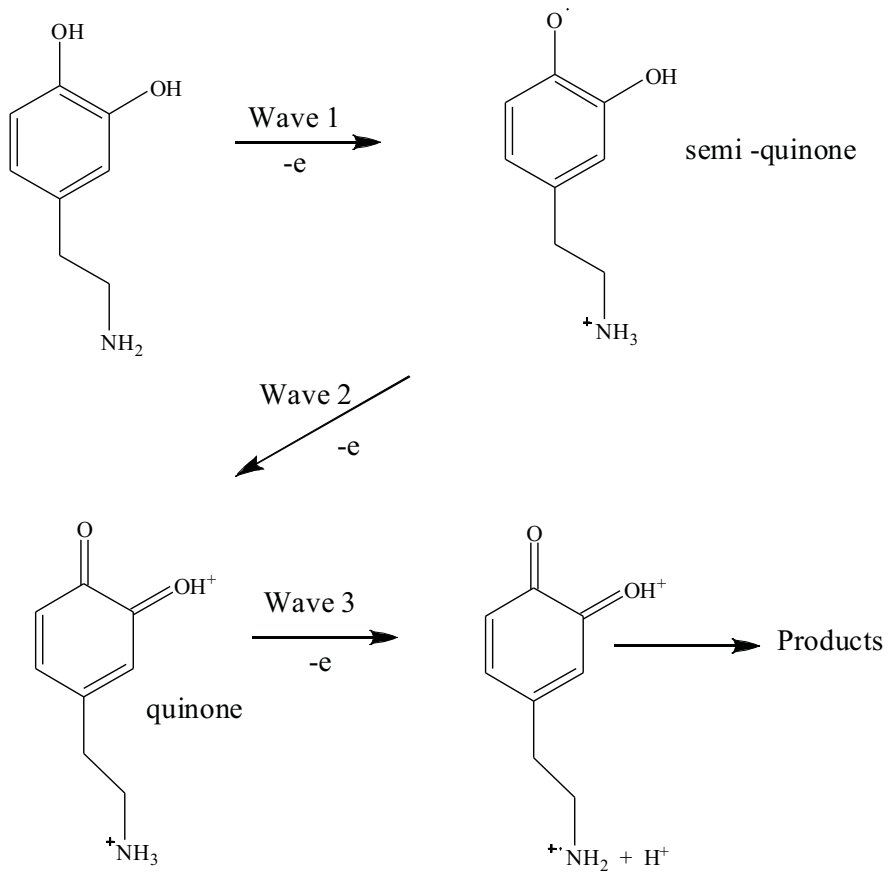


Figure 9.8: Mechanism for the 2-electron, 2-proton oxidation of dopamine to a semi-quinone and a protonated quinone and formation of an amine radical cation.

results in the formation of a semi-quinone. The proton is not lost to solution, but rather is likely taken up by the amine group. The second wave at potential 1.1 V *vs*. Pt is attributed to a second one-electron oxidation which results in a protonated quinone. Both of these oxidation signals occur at potentials similar to that of catechol, therefore we assume similar processes, that is a two-electron oxidation of dopamine to a quinone. However, the third wave at 1.9 V occurs at a potential much more positive than any signal seen in catechol oxidation, and thus we assume that this signal is due to the protonated amine group. Therefore we propose that the third wave is due to the loss of a proton to solution, formation of a radical cationic amine group and likely follow up chemistry. The outline of this mechanism is presented in Figure 9.8.

Chronoamperometric data were recorded of the first wave, and then both waves. A potential step was carried out on the first oxidative wave of dopamine from 0.0 V (corresponding to no

faradaic current) to 0.8 V *vs*. Pt and the current was measured for 5 s. The experimental data was theoretically fitted to the Shoup and Szabo expression.[25] The diffusion coefficient obtained for dopamine in $[C_2mim][NTf_2]$ was calculated to be 6.8×10^{-12} m^2 s^{-1}. The chronoamperometric fitting also gave the *nc* value (no. of electrons $\times$ concentration) which was 11 mM. A potential step was also carried out on the first two oxidative waves of dopamine from 0.0 V to 1.2 V *vs*. Pt and the current was measured for 5 s. The data was again fitted to the Shoup and Szabo expression.[25] The diffusion coefficient obtained was calculated to be 6.9×10^{-12} m^2 s^{-1} and the *nc* value was 20 mM. This indicates a 2-electron transfer for both waves since the *nc* value for dopamine doubled from oxidation of the first wave to the second, indicating that $n = 1$ for wave 1, $n = 2$ for wave 2 and $c = 10$ mM. The diffusion coefficient has not changed from the one-electron to the two-electron oxidation which is expected as the species in solution is the same. This result implies that the oxidation of dopamine is diffusion-controlled for each wave at the potentials used in the chronoamperometry and that in the second wave catechol is oxidised to the protonated o-benzoquinone.

The oxidation of dopamine was also observed in $[C_4mim][BF_4]$ to see if similar disparities for the oxidation of species between these two RTILs was observed for dopamine as well as catechol.

9.2.2.2 Dopamine in $[C_4mim][BF_4]$

In Section 9.2.1 it is noted that in aqueous solution, the adsorption of o-benzoquinone onto a platinum surface is dependent on various factors such as identity of the anion of the electrolyte, and that no adsorption of o-benzoquinone onto the Pt surface was observed in $[C_2mim][NTf_2]$. The same behaviour applies for dopamine. Figure 9.9 presents the voltammetry of dopamine in $[C_4mim][BF_4]$ at scan rate 100 mV s^{-1} in potential range 0.0 V to 2.0 V *vs*. Pt.

The solid line represents the first oxidative scan of dopamine in RTIL. The dotted line represents subsequent scans. Four oxidative waves are visible in this scan, and they appear at

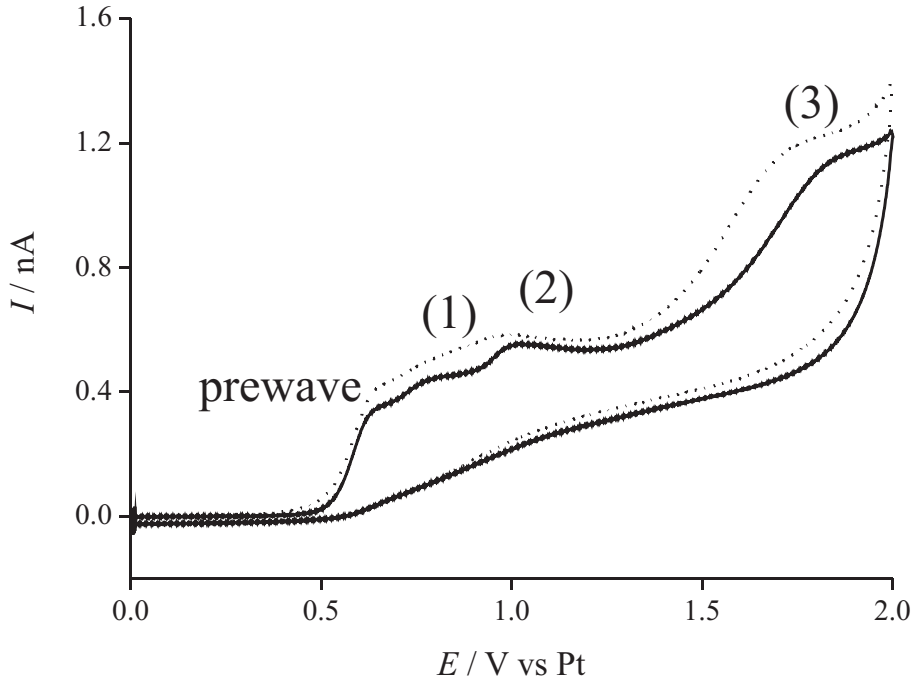


Figure 9.9: Cyclic voltammetry for the oxidation of 10 mM dopamine in $[C_4mim][BF_4]$ at Pt electrode (10 μm diameter) at a scan rate 100 mV s^{-1} and temperature of 298 K. *Solid line*: first scan of oxidation of dopamine; *dotted line*: subsequent scans of oxidation of dopamine.

potentials 0.6 V, 0.75 V, 1.1 V and 1.8 V *vs.* Pt. Wave 1 is attributed to the one-electron oxidation of dopamine to a semi-quinone, wave 2 is attributed to the two-electron oxidation of the catechol to a protonated quinone, and wave 3 is attributed to the oxidation of the amine to a cation radical which likely reacts further. This behaviour is similar to that seen for dopamine in the ionic liquid $[C_2mim][NTf_2]$. However, another prewave at 0.6 V *vs.* Pt is visible which was not observed in $[C_2mim][NTf_2]$. This wave is attributed to the adsorption of a chemically formed species onto the platinum surface. As with the oxidation of catechol to doubly protonated o-benzoquinone in $[C_4mim][BF_4]$, the $[BF_4]^-$ anion reacts with the protonated benzoquinone formed after the second oxidation process, leaving an unstable o-benzoquinone species in solution. This species adsorbs onto the Pt electrode surface where it then likely undergoes a Diels-Alder reaction with other o-benzoquinone species in solution to form a product. This chemisorption is observed as a prewave at potential 0.6 V *vs.* Pt.

This work presents a reliable method for the detection of catechol and dopamine in room

temperature ionic liquids. The RTIL can be altered to achieve differing reactions at the electrode surface for small concentrations of each analyte. The variation of the surface chemistry might be useful for differing purposes of detection of the analyte species. The mechanisms for the oxidation of catechol and dopamine are also presented in detail elucidating the method of oxidation for simple phenol species (catechol) and slightly more complicated phenol species (dopamine), which may assist future understanding of electrochemistry of even more complicated phenol species.

9.3 Conclusions

The electrochemical oxidation of catechol and dopamine has been studied in two RTILs. Catechol and dopamine showed a two-electron oxidation in $[C_2mim][NTf_2]$; catechol showed one electrochemically quasi-reversible diffusion-controlled oxidative wave to form a doubly protonated quinone with corresponding reductive wave at a peak separation of 700 mV, dopamine showed two irreversible oxidative waves for oxidation to the semi-quinone and the protonated quinone, and a further oxidation wave for the amine group to a radical cation. Chronoamperometric transients were taken of each and diffusion coefficients of catechol and dopamine were found to be 3.8×10^{-11} m^2 s^{-1} and 6.8×10^{-12} m^2 s^{-1} respectively. Voltammetry of catechol and dopamine in $[C_4mim][BF_4]$ showed an adsorptive peak at a less positive potential to the oxidative peak(s) seen in $[C_2mim][NTf_2]$, and this is attributed to the adsorption of the neutral benzoquinone species in solution onto the bare platinum surface. This difference between electrochemical behaviour in each RTIL is due to the identity of the anion; with $[BF_4]^-$ the anion can react and remove protons from the oxidised electrochemical reaction product leaving a neutral molecule which can adsorb on platinum. In contrast with $[NTf_2]^-$ the protons remain on the oxidised species which is positively charged and does not adsorb.

In the next Chapter, we further examine the selective reactions of different anions in RTILs in another biological species, that of nicotinamide adenine dinucleotide (NADH). We observed selective reaction of the anion of the RTIL with the proton of the reduced form of this species which can promote or prevent electrochemical oxidation from occurring.

References

[1] Lupu, S.; Lete, C.; Marin, M.; Totir, N. and Balaure, P. C., *Electrochim. Acta*, 2009, **54**, 1932 – 1938.

[2] Zhao, Y.; Gao, Y.; Zhan, D.; Liu, H.; Zhao, Q.; Kou, Y.; Shao, Y.; Li, M.; Zhuang, Q. and Zhu, Z., *Talanta*, 2005, **66**, 51 – 57.

[3] Chernyshov, D. V.; Shvedene, N. V.; Antipova, E. R. and Pletnev, I. V., *Anal. Chim. Acta*, 2008, **621**, 178 – 184.

[4] Safavi, A.; Maleki, N.; Moradlou, O. and Tajabadi, F., *Anal. Biochem.*, 2006, **359**, 224 – 229.

[5] Stern, D.; Salaita, G.; Lu, F.; McCargar, J.; Batina, N.; Frank, D.; Laguren-Davidson, L.; Lin, C.-H.; Walton, N.; Gui, J. and Hubbard, A., *Langmuir*, 1988, **4**, 711–722.

[6] Soriaga, M. P. and Hubbard, A. T., *J. Am. Chem. Soc.*, 1982, **104**, 3937–3945.

[7] Soriaga, M. P.; Wilson, P. H.; Hubbard, A. T. and Benton, C. S., *J. Electroanal. Chem.*, 1982, **142**, 317 – 336.

[8] Hubbard, A. T.; Stickney, J. L.; Soriaga, M. P.; Chia, V. K. F.; Rosasco, S. D.; Schardt, B. C.; Solomun, T.; Song, D.; White, J. H. and Wieckohski, A., *J. Electroanal. Chem.*, 1984, **168**, 43 – 66.

[9] Soriaga, M. P.; White, J. H.; Song, D.; Chia, V. K. F.; Arrhenius, P. O. and Hubbard, A. T., *Inorg. Chem.*, 1985, **24**, 73–79.

[10] Batina, N.; Frank, D. G.; Gui, J. Y.; Kahn, B. E.; Lin, C.-H.; Lu, F.; McCargar, J. W.; Salaita, G. N.; Stern, D. A.; Zapien, D. C. and Hubbard, A. T., *Electrochim. Acta*, 1989, **34**, 1031 – 1044.

[11] Salaita, G. N.; Laguren-Davidson, L.; Lu, F.; Walton, N.; Wellner, E.; Stern, D. A.; Batina, N.; Frank, D. G.; Lin, C.-H.; Benton, C. S. and Hubbard, A. T., *J. Electroanal. Chem.*, 1988, **245**, 253 – 273.

[12] Marsh, K. N.; Deev, A.; Wu, A. C.-T.; Tran, E. and Klamt, A., *Korean J. Chem. Eng.*, 2002, **19**, 357–362.

[13] Buzzeo, M. C.; Evans, R. G. and Compton, R. G., *ChemPhysChem*, 2004, **5**, 1106–1120.

[14] Silvester, D. S. and Compton, R. G., *Z. Phys. Chem.*, 2006, **220**, 1247–1274.

[15] Endres, F. and Zein El Abedin, S., *PhysChemChemPhys*, 2006, **8**, 2101–2116.

[16] Huang, X.-J.; Silvester, D. S.; Streeter, I.; Aldous, L.; Hardacre, C. and Compton, R. G., *J. Phys. Chem. C*, 2008, **112**, 19477–19483.

[17] O' Mahony, A. M.; Dickinson, E. J. F.; Aldous, L.; Hardacre, C. and Compton, R. G., *J. Phys. Chem. C*, 2009, **113**, 10997–11002.

[18] Villagrán, C.; Deetlefs, M.; Pitner, W. R. and Hardacre, C., *Anal. Chem.*, 2004, **76**, 2118–2123.

[19] Hapiot, P. and Lagrost, C., *Chem. Rev.*, 2008, **108**, 2238–2264.

[20] Evans, R. G.; Klymenko, O. V.; Hardacre, C.; Seddon, K. R. and Compton, R. G., *J. Electroanal. Chem.*, 2003, **556**, 179–188.

[21] Barnes, A. S.; Rogers, E. I.; Streeter, I.; Aldous, L. and Hardacre, C.and Compton, R. G., *J. Phys. Chem. B*, 2008, **112**, 7560–7565.

[22] Astudillo, P.; Tiburcio, J. and Gonzalez, F., *J. Electroanal. Chem.*, 2007, **604**, 57–64.

[23] Lawrence, N. S.; Davis, J.; Jiang, L.; Jones, T.; Davies, S. and Compton, R., *Electroanalysis*, 2001, **13**, 432–436.

[24] Lawrence, N. S.; Davis, J.; Marken, F.; Jiang, L.; Jones, T. G. J.; Davies, S. N. and Compton, R. G., *Sens. Actuators, B*, 2000, **69**, 189–192.

[25] Shoup, D. and Szabo, A., *J. Electroanal. Chem.*, 1982, **140**, 237–245.

[26] Rogers, E. I.; Silvester, D. S.; Poole, D. L.; Aldous, L.; Hardacre, C. and Compton, R. G., *J. Phys. Chem. C*, 2008, **112**, 2729–2735.

[27] O' Mahony, A. M.; Silvester, D. S.; Aldous, L.; Hardacre, C. and Compton, R. G., *J. Chem. Eng. Data*, 2008, **53**, 28842891.

[28] Dory, Y. L.; Roy, A.-L.; Soucy, P. and Deslongchamps, P., *Organic Letters*, 2009, **11**, 1197–1200.

[29] Costentin, C.; Evans, D. H.; Robert, M.; Savéant, J. M. and Singh, P. S., *J. Am. Chem. Soc.*, 2005, **127**, 12490–12491.

[30] Rogers, E. I.; Huang, X.-J.; Dickinson, E. J. F.; Hardacre, C. and Compton, R. G., *J. Phys. Chem. C*, 2009, **113**, 17811–17823.

Chapter 10

Selecting Room Temperature Ionic Liquids to Optimize Voltammetric Responses. The Oxidation of NADH in $[C_2mim][NTf_2]$ and $[C_4mim][PF_6]$

The electrochemistry of nicotinamide adenine dinucleotide in its reduced form (NADH) was examined in two RTILs: $[C_2mim][NTf_2]$ and $[C_4mim][PF_6]$. The oxidation of NADH has previously been studied in aqueous solution where it follows the pathway: one-electron oxidation to the $NADH^{\bullet+}$ radical cation, deprotonation to produce the neutral $NAD^{\bullet}$ radical, then oxidation to the NAD^+ cation. The electrochemistry of NADH was examined in $[C_2mim][NTf_2]$ and $[C_4mim][PF_6]$ at the bare Pt electrode (10 μm diameter): in $[C_2mim][NTf_2]$ no oxidation was observed; in $[C_4mim][PF_6]$ an oxidative signal was observed at potential 1.4 V *vs.* Ag, which likely followed the pathway described above, where upon formation of the $NADH^{\bullet+}$ radical cation, the $[PF_6]^-$ anion (unlike the $[NTf_2]^-$ anion) reacts with the proton to form HPF_6 which then decomposes to HF and PF_5. This demonstrates the tuneability of RTILs whereby the choice of one anion in an RTIL over another can promote a reaction. PVF was studied as a mediator for NADH detection in both $[C_2mim][NTf_2]$ and $[C_4mim][PF_6]$ to attempt to lower the potential at which NADH can be detected and decrease electrode fouling. The Pt electrode was modified with PVF and the oxidation of PVF to PVF^+ was observed in $[C_2mim][NTf_2]$ and $[C_4mim][PF_6]$, but no mediation of NADH oxidation was observed.

10.1 Introduction

The electrochemical oxidation of NADH is of great interest in the field of biosensors since there are approximately 300 dehydrogenases which are dependent on NADH and its oxidised form NAD^+.[1] The dehydrogenases catalyze the oxidation of a variety of species, such as alcohol, lactate, glucose, aldehyde, and carbohydrate, that are of interest from the analytical and biological point of view.[2] The electrochemical oxidation of NADH has been the subject of numerous studies related to the development of amperometric biosensors. However there are some problems with the electrochemical detection of NADH which include the large overvoltage encountered for NADH oxidation at ordinary electrodes.[1,2] Consequently, considerable effort has been made to identify new electrode materials and new methods that will overcome the high potential for NADH oxidation. In particular, recently RTILs are being used to modify electrodes for use as biosensors for detection of NADH[3] and other species such as horseradish peroxidase.[4] The modification of electrodes supporting carbon nanotubes with RTILs is of particular recent interest for obtaining thermodynamic and kinetic data about DNA and its detection.[5–7]

In this Chapter we examine the oxidation of NADH in two different RTILs $[C_2mim][NTf_2]$ and $[C_4mim][PF_6]$ at the bare Pt electrode. We observe the effect of the different anions on the electrochemical features of NADH and examine the tuneability of RTILs for use as solvents in sensors where the variation of the anion in an RTIL can promote a reaction or prevent it from occurring.

We also examine the possible use of a modified platinum electrode (10 μm diameter) with PVF as a mediator for NADH detection in order to lower the potential at which it can be detected. While mediation of NADH detection at modified electrodes has been widely observed in aqueous solvent,[2,3,8–10] and specifically using ferrocene-based mediators,[11–13] this has not been attempted before using RTIL as solvent to the best of our knowledge.

Although the use of PVF-modified electrodes for NADH detection has not been achieved

in this Chapter, a new insight into the use of RTILs as solvents in biosensors is presented which demonstrates the tuneability of RTILs in electrochemical reactions whereby the desired voltammetric signal is attained by changing the anion on the RTIL (to $[PF_6]^-$ from $[NTf_2]^-$). In particular the oxidation of NADH produces protons and we suggest that it is the irreversible reaction of these with $[PF_6]^-$ but not with $[NTf_2]^-$ which drives the reaction in one RTIL but not the other. Proton release often accompanies oxidation reactions and so this insight may have generic significance for the implementation of such processes in RTIL solvents. In this way, $[PF_6]^-$ containing RTILs might be viewed as permitting proton releasing oxidations much as in water whereas the switch to $[NTf_2]^-$ RTILs would give behaviour more akin to solvents such as MeCN.

10.2 Experimental: Electrode Modification with PVF

The electrode surface was modified using two different methods. The first method was electrochemical modification. PVF was electrodeposited in its oxidised form as poly(vinylferricenium) perchlorate onto the platinum disc electrode from a solution of 0.1 M TBAP/DCM solution containing 1 mM concentration of PVF by maintaining the working electrode potential at 0.7 V for 300 s. The electrode was removed from the polymer-containing DCM solution, shaken to remove any adhering solution and examined using cyclic voltammetry in MeCN solution containing 0.1 M TBAP in which redox forms of PVF are insoluble. The electrode was removed from the TBAP/MeCN solution and allowed to dry. The platinum electrode was further modified with a section of disposable micropipette tip into which 20 μL RTIL was placed. The PVF-modified electrode was examined using cyclic voltammetry in the RTIL.

The second method of electrode modification was casting the polymer onto the electrode surface. The working electrode was prepared via a solvent evaporation method. The polymer was dissolved in DCM to a concentration of 20 mM and then a known amount of solution was

dropped onto the working electrode surface. The electrode was then set up in the T-cell and purged under vacuum until the DCM had evaporated and left a film of PVF on the electrode surface. 20 μL RTIL was dropped onto the electrode and the PVF-modified electrode was examined using cyclic voltammetry. It is worth noting that this method does not guarantee an exact amount of PVF on the electrode surface, as the working electrode is surrounded by glass onto which some of the PVF is cast. The reproducibility of voltammetric signals from system to system was $\pm$ 50%

10.3 Results and Discussion

10.3.1 The Oxidation of NADH in RTILs at Platinum Electrodes

The oxidation of NADH has previously been observed in aqueous media[1] and follows the pathway:

$$\mathrm{NADH} - \mathrm{e}^- \rightarrow \mathrm{NADH}^{\bullet +} \tag{10.1}$$

$$\mathrm{NADH}^{\bullet +} \overset{-H^+}{\rightarrow} \mathrm{NAD}^{\bullet} \tag{10.2}$$

$$\mathrm{NAD}^{\bullet} - \mathrm{e}^- \rightarrow \mathrm{NAD}^+ \tag{10.3}$$

where NADH is oxidised to produce the radical cation (Equation 10.1), which then deprotonates to produce the neutral radical (Equation 10.2), which then is immediately oxidised to the cation at the electrode surface (Equation 10.3).[1]

The electrochemistry of NADH was studied on the bare platinum electrode in $[C_2mim][NTf_2]$ and $[C_4mim][PF_6]$.

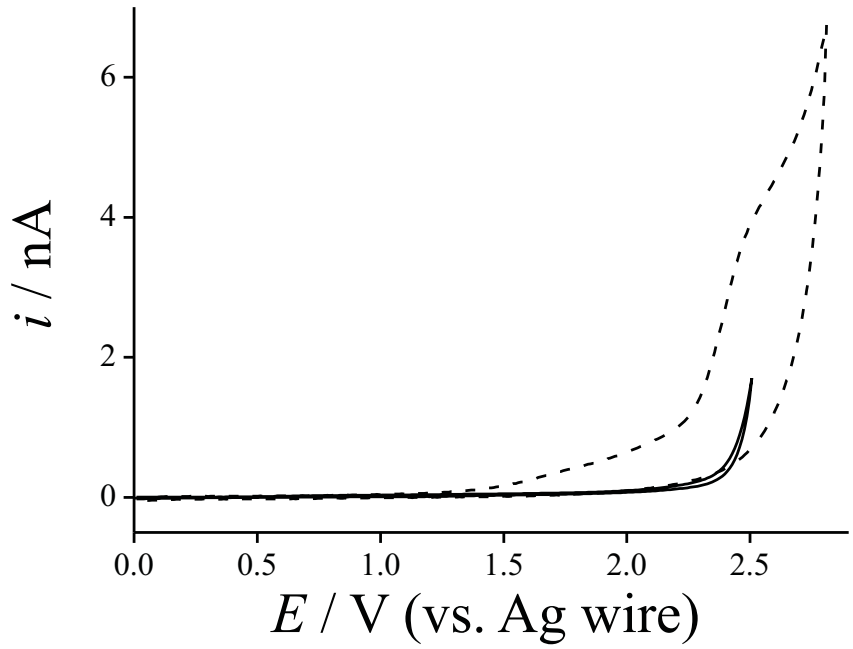


Figure 10.1: Cyclic voltammetry for the oxidation of NADH in $[C_2mim][NTf_2]$ at Pt electrode (10 μm diameter) at a scan rate 100 mV s^{-1} and temperature of 298 K. *Solid line*: oxidation of NADH in $[C_2mim][NTf_2]$; *dotted line*: Oxidation of $[C_2mim][NTf_2]$.

10.3.1.1 NADH in $[C_2mim][NTf_2]$

Figure 10.1 shows the cyclic voltammetry of NADH in $[C_2mim][NTf_2]$ at the bare platinum electrode (diameter 10μm) *vs.* Ag at scan rate 100 mV s^{-1}. The dashed line is the voltammetry of $[C_2mim][NTf_2]$ only in the potential range of 0.0 to 2.9 V, and the solid line is the voltammetry of 20 mM NADH in $[C_2mim][NTf_2]$ in the potential range of 0.0 to 2.5 V.

The voltammetric sweep for $[C_2mim][NTf_2]$ only (dashed line) at the Pt electrode shows a featureless baseline after purging under vacuum for approximately 90 min, until the onset of the oxidation of the anion at approximately 1.5 V. The voltammetric sweep for NADH in $[C_2mim][NTf_2]$ (solid line) also shows a featureless baseline again until what is assumed to be the onset of oxidation of the anion at approximately 2.3 V. The voltammogram is reversed at potential 2.5 V, and no faradaic current is observed on the reverse scan either. Thus we observe no oxidation of NADH to NAD^+ in this ionic liquid. This is likely due to the lack of interaction of the proton which would arise from the oxidation of NADH with the RTIL anion, $[NTf_2]^-$.

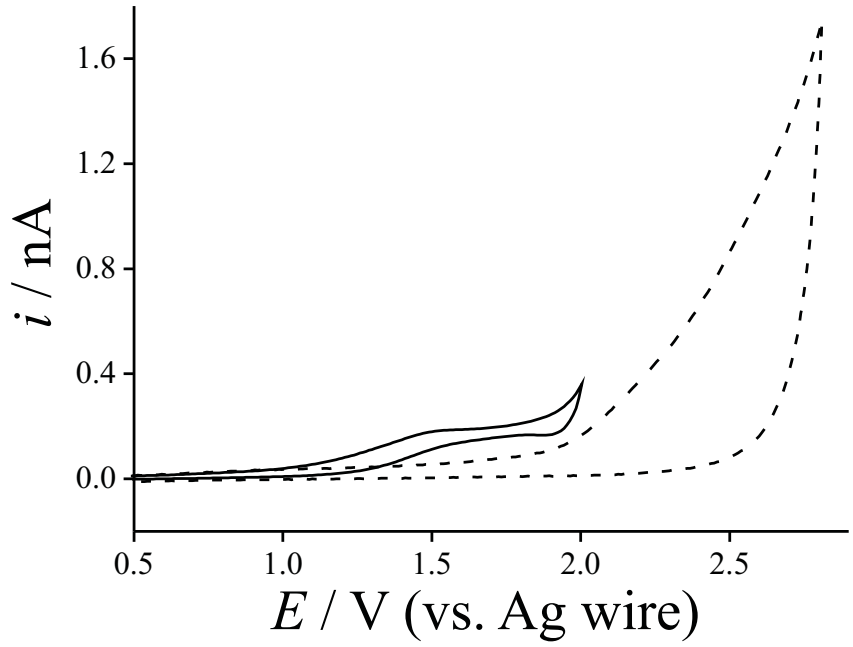


Figure 10.2: Cyclic voltammetry for the oxidation of NADH in $[C_4mim][PF_6]$ at Pt electrode (10 μm diameter) at a scan rate 100 mV s^{-1} and temperature of 298 K. *Solid line*: oxidation of NADH in $[C_4mim][PF_6]$; *dotted line*: Oxidation of $[C_4mim][PF_6]$.

This prevents the reaction from occurring. Similar behaviour has previously been noted with respect to the oxidation of catechol in RTILs.[14] The oxidation of catechol in RTILs forms doubly-protonated o-benzoquinone. In $[C_2mim][NTf_2]$, this is a chemically reversible process since the protons in the doubly protonated o-benzoquinone do not interact with the $[NTf_2]^-$ anion. We next turned to the possibility of using an RTIL solvent containing the anion, $[PF_6]^-$, which interacts more strongly with H^+.[14]

10.3.1.2 NADH in $[C_4mim][PF_6]$

Figure 10.2 shows the oxidation of NADH in $[C_4mim][PF_6]$ at the bare platinum electrode (diameter 10μm) *vs.* Ag at scan rate 100 mV s^{-1}. The dashed line is the voltammetry of $[C_4mim][PF_6]$ only in the potential range of 0.5 to 2.9 V, and the solid line is the voltammetry of NADH in $[C_4mim][PF_6]$ in the potential range of 0.5 to 2.0 V.

The signal for $[C_4mim][PF_6]$ only (dashed line) shows a featureless baseline after approximately 90 min purging under vacuum until the onset of the oxidation of the anion at approx-

imately 2.0 V *vs.* Ag. The signal for NADH shows zero faradaic current until approximately 1.4 V *vs.* Ag where the steady-state oxidation wave of NADH is observed. The potential is reversed at 2.0 V and the current returns to a point of zero faradaic current. The oxidation peak is broad and is likely attributed to a two-electron oxidation of NADH to NAD^+ similar to previous observations in aqueous media.[1] The wave is steady-state at lower scan rates and becomes more transient at higher scan rates. No back peak is observed at any scan rate studied (100 - 4000 mV s^{-1}). This suggests that the oxidation of NADH in this medium is fully chemically irreversible, so that no reduction of oxidised NADH occurs. Rather, the anion of the RTIL reacts with protons to form HPF_6, which decomposes irreversibly which is known to happen in this RTIL.[15–17] Therefore we suggest the following possible mechanism:

$$NADH - e^- \rightarrow NADH^{\bullet +} \tag{10.4}$$

$$NADH^{\bullet +} \rightarrow NAD^{\bullet} + \text{"}HPF_6\text{"} \tag{10.5}$$

$$\text{"}HPF_6\text{"} \rightarrow \text{Products} \tag{10.6}$$

$$NAD^{\bullet} - e^- \rightarrow NAD^+ \tag{10.7}$$

where NADH is oxidised in $[C_4mim][PF_6]$ to NAD^+ in a two-electron oxidation. The proton is lost to the RTIL anion, $[PF_6]^-$, and the NAD^+ undergoes further reactions.

The oxidation of different concentrations of NADH at the bare Pt electrode was also studied. Figure 10.3 shows the cyclic voltammetry of NADH in $[C_4mim][PF_6]$ at the bare Pt electrode (diameter 10 μm) *vs.* Ag at scan rate 100 mV s^{-1} for concentrations 7, 10 and 14 mM, in the potential range of 0.0 to 2.0 V. The voltammetric sweep for $[C_4mim][PF_6]$ only (dashed line) at the Pt electrode shows a featureless baseline after purging under vacuum for approximately 90 min.

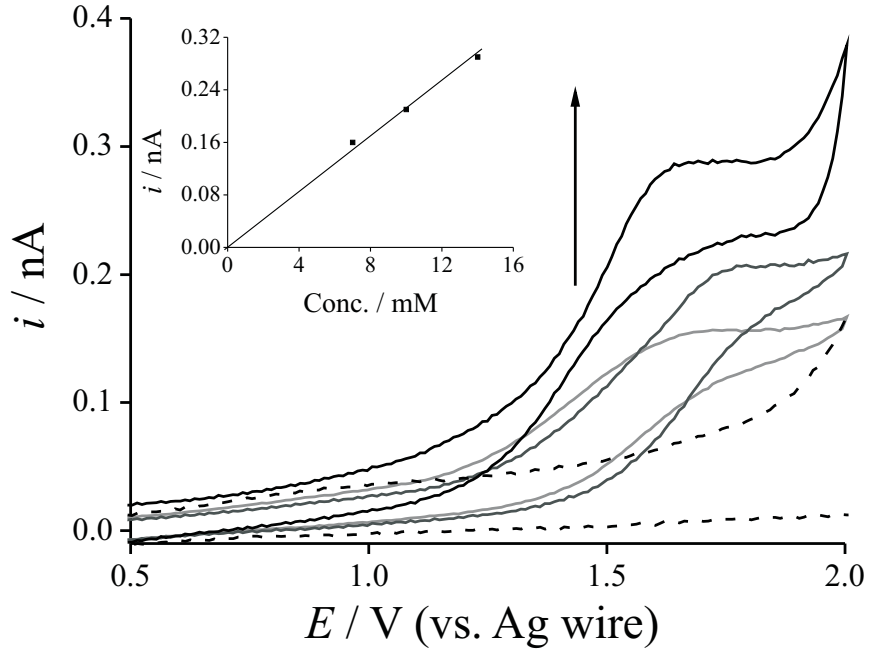


Figure 10.3: Cyclic voltammetry for the oxidation of NADH in $[C_4mim][PF_6]$ at bare Pt electrode (diameter 10 μm) at 100 mV S^{-1} at concentrations 7, 10, and 14 mM. *inset*: concentration / mM *vs.* peak current / nA for oxidation of NADH in $[C_4mim][PF_6]$.

The voltammetric sweep for increasing concentrations of NADH (solid line) shows an oxidative wave at approximately 1.7 - 1.8 V *vs.* Ag. This is attributed to the two-electron oxidation of NADH to the NAD^+ cation. The signal increases with increasing concentration seen in the inset of Figure 10.3. The diffusion coefficient for NADH in $[C_4mim][PF_6]$ was calculated from the peak current of the steady-state signal for NADH oxidation to be 5.5×10^{-12} m^2 s^{-1}. This value is consistent with diffusion of species in RTILs.[14] It was noted that with increasing concentration of NADH, the onset of electrode fouling occurred, likely due to interactions of the NAD^+ cation. We carried out chronoamperometry on the oxidative wave of NADH by applying a potential step from 0.0 V (zero faradaic current) to 1.8 V (point after faradaic current) and attempted to fit the model to the Shoup and Szabo expression. However, this microcoulometric method is only suitable for simple electron processes, and the model would not fit the experimental data. Thus we conclude that other processes aside from the two-electron oxidation of NADH are taking place.

By tuning the nature of the RTIL, the oxidation of NADH can be promoted ($[PF_6]^-$) or prevented ($[NTF_2]^-$). It was also of interest to explore the possibility of modifying the electrode surface to realise the same process.

10.3.2 Electrochemistry of NADH at PVF-modified Electrodes

The mediated detection of NADH was next attempted at a PVF-modified Pt electrode in the RTILs $[C_2mim][NTf_2]$ and $[C_4mim][PF_6]$. The mediation of NADH with ferrocene and ferrocene compounds has previously been observed in aqueous solution.[11–13] This results in the detection of NADH at lower potential allowing less interference from other species and decreases electrode fouling. We therefore modified the bare Pt electrode with PVF to carry out this experiment.

10.3.2.1 Modification of Platinum Electrode with PVF

PVF was electrochemically immobilised onto the electrode surface in the first method outlined in Section 10.2. Voltammetry was obtained for the reduction of $PVF^+ClO_4^-$ modified Pt electrode in MeCN containing 0.1 M TBAP and in the RTIL $[C_4mim][PF_6]$. However, this method of electrochemically adsorbing PVF onto a platinum electrode is not always reliable. Other experiments have shown that after modification of the electrode and characterisation in MeCN, the electrochemical signal can be lost when MeCN is removed and RTIL is added. As well as this, a stable signal is not always attained. The current magnitude can vary from scan to scan, therefore this is not a reliable method for the deposition of PVF onto a platinum electrode surface for use with RTILs.

Accordingly another method of electrode modification was sought and that is casting the PVF onto the electrode surface using solvent evaporation as outlined in Section 10.2. Figure 10.4 shows the voltammetry of a cast PVF modified electrode in $[C_2mim][NTf_2]$ and $[C_4mim][PF_6]$ in the potential ranges of -0.1 to 0.8 V and -0.2 V to 1.0 V respectively at scan rate 100 mV s^{-1}.

The voltammetry in $[C_2mim][NTf_2]$ in Figure 10.4(a) shows an oxidative peak at approxi-

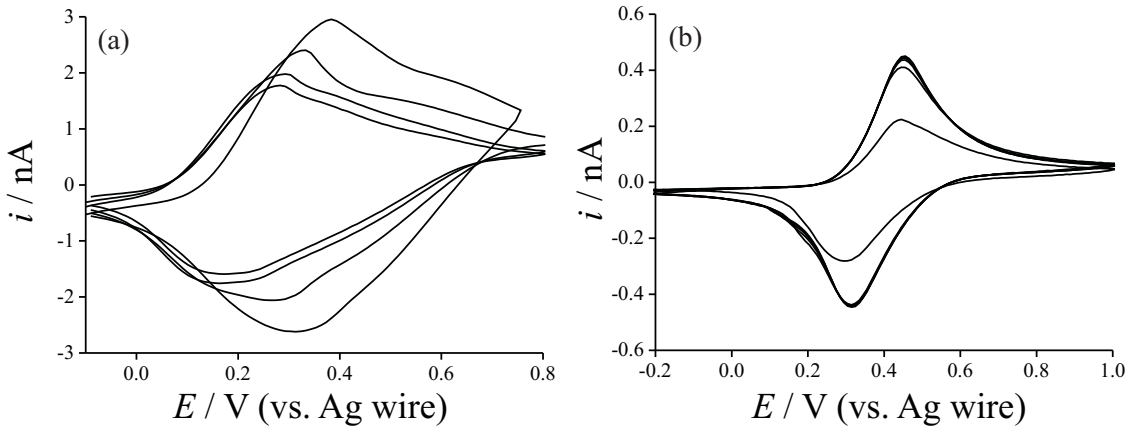


Figure 10.4: Cyclic voltammetry for the oxidation of PVF-modified electrode using solvent evaporation method (120 μL of 20 mM PVF in DCM) in (a) [C_2mim][NTf_2] and, (b) [C_4mim][PF_6] at Pt electrode (10 μm diameter) at a scan rate of 100 mV s^{-1} and temperature of 298 K.

mately 0.2 to 0.4 V *vs*. Ag which is attributed to the oxidation of PVF to PVF^+. The potential shift in the peak current signals for the oxidation and reduction is attributed to potential drift caused by the use of a quasi-reference electrode. The signal increases with increasing number of scans until it reaches a maximum current which has previously been noted by Bard *et al*.[18,19]

The voltammetry in [C_4mim][PF_6] in Figure 10.4(b) shows an oxidative peak at 0.45 V *vs*. Ag which is also attributed to the direct oxidation of PVF to PVF^+. The scan is reversed at 1.0 V and a back peak is observed at potential 0.35 V *vs*. Ag which is attributed to the reduction of PVF^+ to PVF. As with the voltammetry in [C_2mim][NTf_2], the signal increases with increasing number of scans until it reaches a maximum peak current where it remains for subsequent scans. This method of electrode modification was used for mediation of NADH oxidation in RTILs, as described next.

10.3.2.2 The Attempted Oxidation of NADH in [C_2mim][NTf_2] and [C_4mim][PF_6] at PVF-modified Electrodes

The platinum working electrode was modified with PVF using the solvent evaporation method outlined in Section 10.2.

The cyclic voltammetry of PVF-modified platinum electrode in [C_2mim][NTf_2] was carried

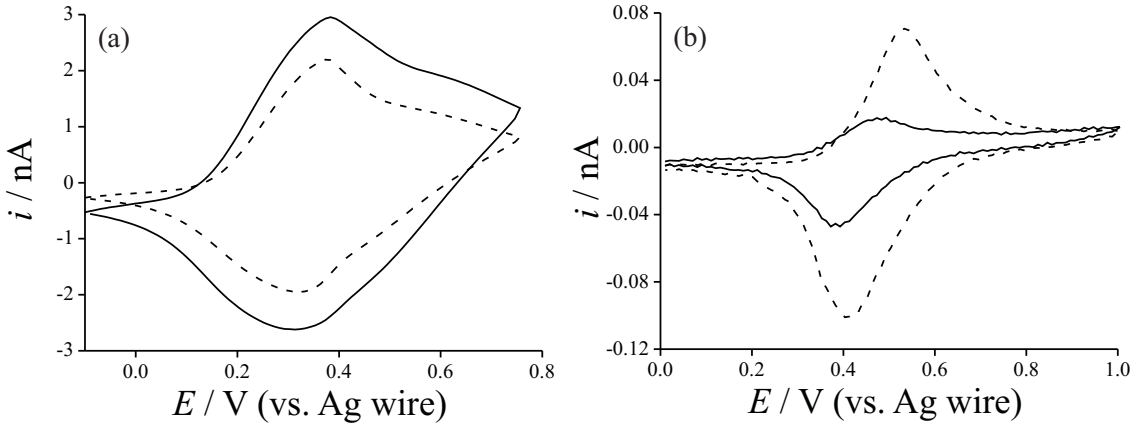


Figure 10.5: Cyclic voltammetry for the oxidation of PVF-modified electrode with added excess NADH in (a) $[C_2mim][NTf_2]$ and, (b) $[C_4mim][PF_6]$ at Pt electrode (10 μm diameter) at a scan rate of 100 mV s^{-1} and temperature of 298 K.

out as per Section 10.3.2.1. Cyclic voltammetry shows oxidative and reductive signals at 0.4 V and 0.3 V *vs.* Ag respectively shown in Figure 10.5(a) denoted by the solid line. The peak current for the oxidative and reductive waves are 3.0 and -2.6 nA respectively. NADH was added to $[C_2mim][NTf_2]$ at the electrode and cyclic voltammetry was carried out. Cyclic voltammetry also shows an oxidative signal at 0.4 V *vs.* Ag and a reductive signal at 0.3 V *vs.* Ag shown in Figure 10.5(a) denoted by the dashed line. The peak currents for the oxidative and reductive waves are approximately 2.2 and -2.0 nA respectively. These data show no increase in the peak current for the oxidation and reduction of PVF in $[C_2mim][NTf_2]$ with the addition of NADH showing that no mediation had taken place.

Cyclic voltammetry of PVF-modified platinum electrode (10 μm diameter) in $[C_4mim][PF_6]$ was also carried out as per Section 10.3.2.1. The voltammogram shows an oxidative wave at approximately 0.48 V *vs.* Ag on the forward scan and a back peak at 0.38 V *vs.* Ag, shown in Figure 10.5(b) denoted by a solid line. The peak current for the oxidative and reductive waves are 0.2 and -0.4 nA respectively. NADH was added to $[C_4mim][PF_6]$ and cyclic voltammetry was carried out. The forward scan shows a peak at approximately 0.53 V *vs.* Ag and a reductive peak was observed at potential 0.43 V *vs.* Ag shown in Figure 10.5(b) denoted by a dashed line. The peak currents for the oxidative and reductive waves are approximately 0.07 and -

0.1 nA respectively. These data show an increase in the peak current for the oxidation and reduction of PVF in $[C_4mim][PF_6]$ with the addition of NADH. However, this does not suggest that mediation is taking place. For mediation to take place, the oxidative peak current should increase, not the reductive. The change in signal may indirectly reflect the presence or absence of NADH, for example via accumulation in the film modifying the transport within it. The increase in signal for PVF may also be due to increased cycling. In aqueous systems, an increase in current for PVF immobilised on the Pt electrode surface has previously been observed.[19] The drift in the peak potentials is due to the quasi-reference Ag electrode. Thus we conclude that mediated detection of NADH using PVF-modified electrodes in RTILs has not been achieved.

10.4 Conclusions

The detection of NADH at the bare Pt electrode in RTILs was achieved. The oxidation of NADH was examined in two RTILs, $[C_4mim][PF_6]$ and $[C_2mim][NTf_2]$: in $[C_2mim][NTf_2]$ no oxidation for NADH was observed, attributed to the lack of interaction between the RTIL anion $[NTf_2]^-$ and the proton released if NADH is to be oxidised; in $[C_4mim][PF_6]$ the two-electron oxidation of NADH to NAD^+ was observed at 1.4 V *vs.* Ag where NADH was oxidised to form the radical cation $NADH^{\bullet+}$, $[PF_6]^-$ was thought to react with this species to form $NADH^{\bullet}$ and HPF_6, which likely degrades to HF and PF_5. This demonstrates the tuneability of RTILs where by the choice of the anion in the solvent can allow or prevent a chemical reaction.

The mediated detection of NADH at a modified electrode in RTILs was attempted. The Pt working electrode was modified with PVF through solvent evaporation. The modified electrode was characterised in $[C_2mim][NTf_2]$ and $[C_4mim][PF_6]$ using cyclic voltammetry which showed the one-electron oxidation of PVF to PVF^+. NADH was added to each system but no mediation was observed.

The oxidation of NADH at the bare Pt electrode in $[C_4mim][PF_6]$ has been realised. It appears that tuning the solvent rather than tailoring the electrode surface is a more helpful strategy for voltammetric detection in RTILs, at least in the case of NADH. This presents a new insight into the use of RTILs in bioelectrochemical measurements. The detection of NADH in RTIL solvent has not been previously reported. This presents an alternative electrochemical sensor for NADH detection coupled with the benefits of using RTILs as a solvent. It also represents insight into the tuneability of an anion within the solvent system to promote an electrochemical reaction. This can be useful in a wide variety of sensors both for selective sensing and analyte fingerprinting.

In the next Chapter, we return to the fabrication of a gas sensor for H_2S and examine the mediated detection of this gas. Species studied in this Chapter, as well as Chapters 8 and 9

were relevant to the use of mediated detection of H_2S since DMPD, catechol and PVF were all examined as mediator candidates. The successes or failures of these mediating species are discussed in the next Chapter. However this Chapter and Chapters 8 and 9 outline the interesting voltammetric features of these species in RTILs in their own right, and have produced useful electrochemical features for selective detection of species in RTILs as well as interesting kinetic features of species in RTILs.

References

[1] Banks, C. E. and Compton, R. G., *Analyst*, 2005, **130**, 1232–1239.

[2] Shan, C.; Li, F.; Yuan, F.; Yang, G.; Niu, L. and Zhang, Q., *Nanotech.*, 2008, **19**, 285601–285607.

[3] Kachoosangi, R. T.; Musameh, M. M.; Abu-Yousef, I.; Yousef, J. M.; Kanan, S. M.; Xiao, L.; Davies, S. G.; Russell, A. and Compton, R. G., *Anal. Chem.*, 2009, **81**, 435–442.

[4] Long, J.; Silvester, D. S.; Wildgoose, G.; Surkus, A.-E.; Flechsig, G.-U. and Compton, R. G., *Bioelectrochem.*, 2008, **74**, 183–187.

[5] Xie, Y.-N.; Wang, S.-F.; Zhang, Z.-L. and Pang, D.-W., *J. Phys. Chem. B*, 2008, **112**, 9864–9868.

[6] Zhang, X.; Jiao, K. and Wang, X., *Electroanalysis*, 2008, **20**, 1361–1366.

[7] Zhang, W.; Yang, T.; Zhuang, X.; Guo, Z. and Jiao, K., *Biosensors and Bioelectronics*, 2009, **24**, 2417–2422.

[8] Mano, N.; Theinpont, A. and Khun, A., *Electrochem. Commun.*, 2001, **3**, 585–589.

[9] Wang, Q.; Tang, H.; Xie, Q.; Tan, L.; Zhang, Y.; Li, B. and Yao, S., *Electrochim. Acta*, 2007, **52**, 6630–6637.

[10] Zhao, Y.; Liu, H.; Kou, Y.; Li, M.; Zhu, Z. and Q., Z., *Electrochem. Commun.*, 2007, **9**, 2457–2462.

[11] Bu, H.-Z.; Mikkelson, S. and English, A., *Anal. Chem.*, 1998, **70**, 4320–4325.

[12] Pandey, P.; Upadhyay, S.; Upadhyay, B. and Pathak, H., *Anal. Bioch.*, 1998, **260**, 195–203.

[13] Serban, S. and El Murr, N., *Biosensors and Bioelectronics*, 2004, **20**, 161–166.

[14] Barnes, E. O.; O' Mahony, A. M.; Aldous, L.; Hardacre, C. and Compton, R. G., *J. Electroanal. Chem.*, 2010, **646**, 11–17.

[15] Shvedene, N.; Chernyshov, D. V. and Pletnev, I. V., *Russ. J. Gen. Chem.*, 2008, **78**, 2507–2520.

[16] Baker, G. and Baker, S., *Aust. J. Chem.*, 2005, **58**, 174–177.

[17] Khachatryan, K.; Smirnova, S.; Torocheshnikove, I.; Shvedene, N.; Formanovsky, A. and Pletnev, I. V., *Anal. Bioanal. Chem.*, 2005, **381**, 464–470.

[18] Peerce, P. and Bard, A. J., *J. Electroanal. Chem.*, 1980, **112**, 97–115.

[19] Merz, A. and Bard, A. J., *J. Am. Chem. Soc.*, 1978, **100**, 3222–3223.

Chapter 11

The Mediated Detection of Hydrogen Sulfide in Room Temperature Ionic Liquids

The detection of H_2S via electrochemical oxidation was studied using several electron transfer or other mediators in various RTILs with the aim of fabricating an amperometric gas sensor. Each mediator was characterised in at least two RTILs, and H_2S was added to each system to observe if any mediation took place. Five of the mediators were unsuccessful: DMPD, catechol, ferrocene, potassium ferrocyanide and PVF. The last, successful, mediator characterised was 3,5-tert-butyl-o-benzoquinone. Cyclic voltammetry was carried out on the mediator in $[C_2mim][NTf_2]$. A reductive wave was observed and attributed to the two-electron reduction of the mediator. No oxidative signal was observed. H_2S gas (1% H_2S gas with 99% N_2 fill) was flowed through the system and cyclic voltammograms were carried out scanning negatively, then positively. A decrease in the reductive wave of the mediator was observed after the addition of H_2S, and an oxidative signal was observed when scanning positively. This is due to the reaction between the mediator and H_2S whereby a 1,2-hydroxy-3,5-tert-butyl-4-thiol-benzene is formed. This reaction is reversible and on purging the system with N_2, the original reductive signal of the mediator was recovered. This system represents a renewable gas sensor for H_2S over limited exposure times whereby the decrease in the reduction current of the mediator, and the onset of a new oxidative signal can both be utilized as analytical signals. This system was also tested for lower concentrations of H_2S (200 ppm H_2S with N_2 fill).

11.1 Introduction

The mediated detection of H_2S has been well studied. A large body of work exists examining the mediated detection of H_2S at glassy carbon (GC) electrodes in aqueous solution using a diverse range of mediators such as catechol, dopamine, hydroquinone and DMPD,[1,2] as well as diphenylamine derivatives in various aqueous buffer solutions.[2–4] The immobilization of an anthracene/ferrocene copolymer onto basal plane pyrolytic graphite (BPPG) electrode, and the use of ferrocene sulfonates at the platinum electrode were also examined for the mediated detection of H_2S.[5,6] In some of these cases, such as for ferrocene, mediation of H_2S detection takes place in the following manner:

$$M - e^- \rightarrow M^+ \tag{11.1}$$

$$2M^+ + H_2S \rightarrow 2M + 2H^+ + S \tag{11.2}$$

where the mediator (M) is oxidised and a voltammetric signal is observed (Equation 1); upon the addition of H_2S the oxidised mediator (M^+) is reduced (Equation 2), which then allows it to be reoxidised and thus increases the observed voltammetric signal. Higher concentrations of H_2S augment this effect and the voltammetric signal increases with concentration. In other cases, such as for catechol and hydroquinone, mediation of H_2S detection takes place in the following manner:

$$H_2Q - 2e^- - 2H^+ \rightleftharpoons Q \tag{11.3}$$

$$Q + H_2S \rightarrow H_2P \tag{11.4}$$

$$H_2P - 2e^- - 2H^+ \rightleftharpoons P \tag{11.5}$$

where H_2Q is the catechol or hydroquinone mediator which is oxidised to form a quinoid, Q (Equation 11.3). The addition of H_2S will chemically react with this species to form the thiol derivative of the catechol or hydroquinone mediator, H_2P, (Equation 11.4), which itself is electrochemically active. Reoxidation of H_2P (Equation 11.5) will then cause an increase in the oxidation signal which is augmented by higher concentrations of H_2S.

A limitation associated with these sensors is the aqueous electrolyte used. A gas sensor 'lifetime' is determined by how quickly the electrolyte dries up. Aqueous electrolytes cannot survive high temperatures and pressures. However, RTILs can survive dramatic temperature and pressure changes and remain physically and chemically unchanged due to negligible volatility.[7] For this reason, several of these mediators were examined in RTILs for H_2S detection.

The species 3,5-tert-butyl-o-benzoquinone has also been previously examined as a mediator for the detection of H_2S in aqueous buffers of varying pH at the GC electrode using square-wave voltammetry.[8] The mediated detection of H_2S using this species was observed, but not in the manner of previous mediating species. In this case, the mediator and analyte reacted chemically to form an adduct, which yields a new voltammetric signal. The initial voltammetric signal of the mediator decreases due to consumption during the chemical reaction.

In this Chapter we present the mediated detection of H_2S with 3,5-tert-butyl-o-benzoquinone in the RTIL, $[C_2mim][NTf_2]$, at the platinum electrode using cyclic voltammetry. We report similar findings to those of Giovanelli *et al.* using reductive cyclic voltammetry, and examine in detail the chemical reaction between the mediator and the H_2S gas. We also report the prospect of a renewable gas sensor for H_2S over certain time limits showing that part of this chemical reaction is reversible. This particular feature is the most attractive within this system as it presents the possibility of a practical, viable, re-usable gas sensor, including notably the

attractive properties of the use of RTILs as solvents.

11.2 Experimental: Dissolving Mediators in RTILs

DMPD was directly dissolved in $[C_4mim][BF_4]$ at concentration 20 mM. For addition of catechol and ferrocene to the RTIL, a drop (20 μL) of 20 mM catechol or ferrocene in MeCN was added to the RTIL in the cavity and purged under vacuum to remove the MeCN. Potasssium ferrocyanide was also directly dissolved in excess in $[C_4mpyrr][NTf_2]$. PVF was immobilised onto the electrode surface via the solvent evaporation method. The polymer was dissolved in DCM to a concentration of 20 mM and then a known amount of solution was dropped onto the working electrode surface. The electrode was then set up in the T-cell and purged under vacuum until the DCM had evaporated and left a film of PVF on the electrode surface. 20 μL $[C_4mim][PF_6]$ was dropped onto the electrode and the PVF-modified electrode was examined using CV. 3,5-tert-butyl-o-benzoquinone was directly dissolved in $[C_2mim][NTf_2]$ at concentration 20 mM. Smaller concentrations of the species were achieved by diluting the solution with pure $[C_2mim][NTf_2]$.

Experiments diluting hydrogen sulfide gas (1.01% H_2S nitrogen fill) to a concenatration of 200ppm were carried out using a gas mixer which consists of two volume gauges, one for hydrogen sulfide, and another for N_2 (oxygen free). Each gas passes through the volume gauge at a specific rate and into a mixing tube where they are mixed to the desired concentration. The mixture is then flowed through the T-cell.

11.3 Results and Discussion

The mediated detection of H_2S in RTILs has been carried out in this work in an effort to construct a gas sensor which possesses all the benefits of RTILs as solvents, and to decrease the potential at which H_2S is detected. The regeneration of the gas sensor is also important for the fabrication of a reusable sensor for practical viability. Several mediating species were tested in

a range of RTILs, with one candidate achieving success.

11.3.1 Attempted Detection of H_2S in RTILs Using Several Mediating Species

Figure 11.1(a)-(e) shows the attempted mediated detection of H_2S using the following mediators: DMPD, catechol, ferrocene, potassium ferrocyanide and PVF respectively, in a range of RTILs. Each of these species have been utilized as mediators in aqueous systems, particularly DMPD and ferrocene or ferrocene-based species for the mediated detection of H_2S.[1,2,4–6,9,10]

Figure 11.1(a) shows the attempted mediation of H_2S 100% using 20 mM DMPD in the ionic liquid $[C_4mim][BF_4]$. The mediator was dissolved directly in the RTIL. The voltammetry of DMPD in RTILs has previously been observed[11] (and outlined in Chapter 8), and yielded two reversible oxidative signals for the oxidation of DMPD to $DMPD^{\bullet+}$ and $DMPD^{\bullet+}$ to $DMPD^{2+}$. In Figure 11.1(a), the solid line denotes the presence of DMPD only in the RTIL. A cyclic voltammogram was taken of DMPD in the potential range of 0.0 to 2.0 V. On the forward scan two oxidative peaks were observed at potentials 0.4 V and 1.0 V *vs.* Pt, denoting the oxidation of DMPD to $DMPD^{\bullet+}$ and $DMPD^{\bullet+}$ to $DMPD^{2+}$ respectively. The scan was reversed at 2.0 V and the reductions of $DMPD^{2+}$ and $DMPD^{\bullet+}$ were observed at 1.0 V and 0.38 V *vs.* Pt respectively. H_2S was flowed through the T-cell for *ca.* 40 minutes. A cyclic voltammogram was then taken in the potential range of 0.0 to 1.5 V. As before, on the forward scan, two signals for the oxidation of DMPD and $DMPD^{\bullet+}$ were observed at 0.3 and 1.0 V *vs.* Pt respectively. While the current increased a little (+0.12 nA for DMPD oxidation and +0.24 nA for $DMPD^{\bullet+}$ oxidation), the magnitude of this increase was not significant enough to suggest that any useful mediation was taking place. Rather this increase is likely due to the change in viscosity of the RTIL due to the presence of the highly RTIL-soluble H_2S gas.[12–14]

Three other mediating species, catechol, ferrocene and potassium ferrocyanide were also dissolved in the RTILs $[C_4mim][BF_4]$, $[C_2mim][NTf_2]$, and $[C_4mim][PF_6]$ respectively using sol-

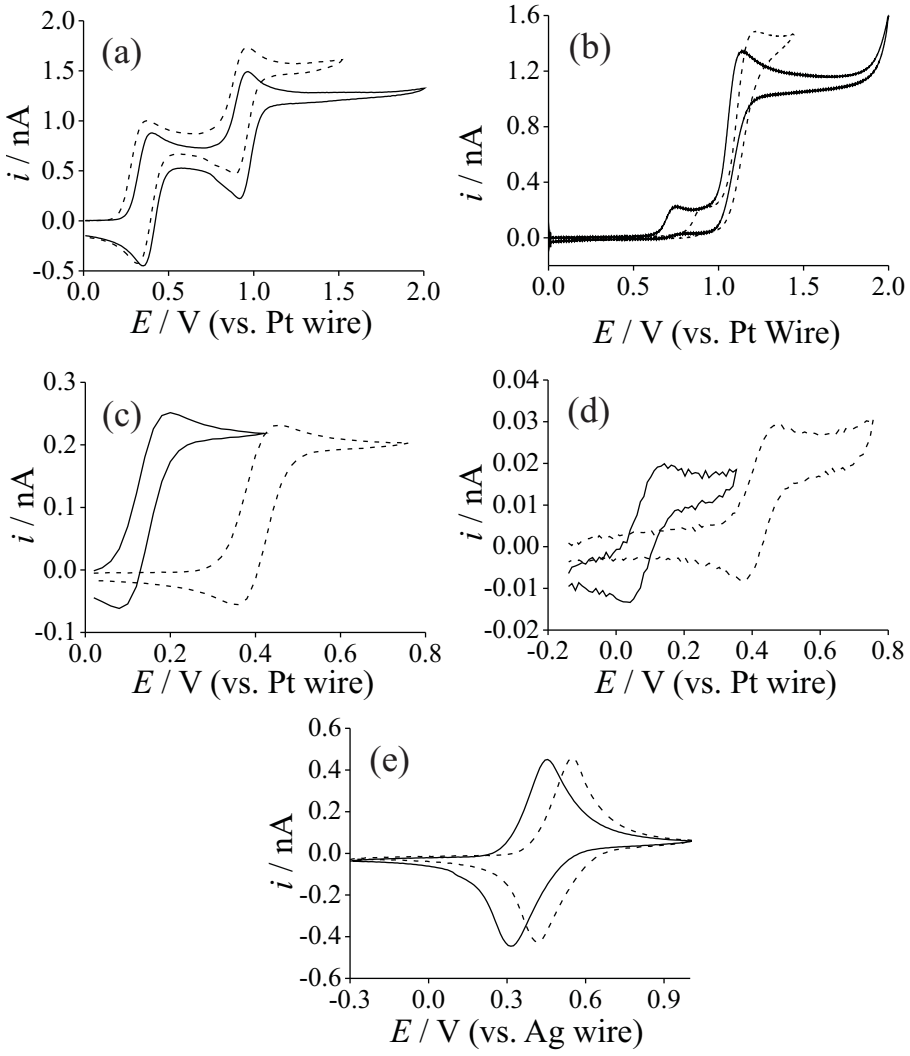


Figure 11.1: Cyclic voltammetry for the oxidation of (a) 20 mM DMPD in $[C_4mim][BF_4]$ (solid line) + H_2S 100% (dotted line), (b) 20 mM catechol in $[C_4mim][BF_4]$ (solid line) + H_2S 100% (dotted line), (c) 10 mM Ferrocene in $[C_2mim][NTf_2]$ (solid line) + H_2S 1% (dotted line), (d) excess Potassium Ferrocyanide in $[C_4mpyrr][NTf_2]$ (solid line) + H_2S 1% (dotted line), and (e) PVF in $[C_6mim][PF_6]$ (solid line) + H_2S 1% (dotted line), at Pt electrode (10 μm diameter) at a scan rate 100 mV s^{-1} and temperature of 298 K.

vent evaporation outlined in Section 11.2, and mediated H_2S detection was attempted using each. Figure 11.1(b), (c) and (d) show the voltammetry of each of these species in RTILs denoted by the solid lines. The voltammetry of catechol, ferrocene and potassium ferrocyanide in RTILs has already been outlined in previous literature.[15–17] The oxidation of 20 mM catechol in $[C_4mim][BF_4]$ was observed in Figure 11.1(b) in the potential range of 0.0 to 2.0 V. On the forward scan, the electrochemically irreversible oxidation of catechol to a doubly-protonated

benzoquinone species was observed at potential 1.1 V *vs.* Pt. This species reacted with the $[BF_4]^-$ anion of the ionic liquid to form HBF_4 and orthoquinone. The adsorption of the orthoquinone species onto the Pt electrode surface was observed as a prewave at the less positive potential of 0.7 V *vs.* Pt. This voltammetry has previously been observed in Chapter 9. H_2S 100% was flowed through the T-cell for 40 minutes and a cyclic voltammogram was taken in the potential range of 0.0 to 1.5 V. A shift was observed in the electrochemical signals on the forward scan for the oxidation of catechol to orthoquinone at 1.2 V *vs.* Pt, and the adsorption of the orthoquinone species onto the electrode surface at 0.9 V *vs.* Pt. This is due to the use of a quasi-reference electrode in the system. A slight increase in the oxidation of catechol at 1.2 V *vs.* Pt was observed, but as with DMPD, the increase was not significant enough to constitute mediation, rather a change in the viscosity of the RTIL due to the presence of H_2S.

Similar behaviour was observed for attempted mediation using ferrocene and potassium ferrocyanide whereby the current in the oxidative signals increased slightly with the presence of H_2S, but not significantly, and can be attributed to changes in viscosity.

The attempted mediation of H_2S detection was also carried out using PVF as a mediator and is shown in Figure 11.1(e). PVF was immobilised directly onto the electrode surface using solvent evaporation methods outlined in Chapter 10 and has been published.[18] Figure 11.1(e) shows the oxidation of PVF in $[C_4mim][PF_6]$ in the potential range of -0.3 V to 0.95 V. The forward scan shows the oxidation of PVF to PVF^+ at 0.4 V *vs.* Ag , and the reverse scan shows the reduction of PVF^+ to PVF at 0.3 V *vs.* Ag. H_2S gas (1% H_2S with 99% N_2 fill) was flowed through the cell for *ca.* 40 minutes and a cyclic voltammogram was taken in the potential range of -0.3 V to 0.95 V. The oxidation peak of PVF to PVF^+ is observed at potential 0.55 V *vs.* Ag and the reduction of PVF^+ to PVF at 0.45 V *vs.* Ag. A shift in the potential of the electrochemical signals was observed as before due to the use of a quasi-reference electrode. No increase was observed in the oxidative and reductive signals on addition of H_2S to the T-cell showing that

no mediation has taken place. Unlike the previous systems observed in Figures 11.1(a)-(d) even a slight increase in the electrochemical signals was not observed for the voltammetric signals of PVF due to change in viscosity of the RTIL. This is likely because PVF was immobilised directly onto the electrode surface and not free to diffuse throughout the entire RTIL, therefore changes in viscosity would not influence diffusion of PVF in this system.

Of these five mediators tested, none were likely to be practically useful for the mediated detection of H_2S in RTILs, despite some having previously been so in aqueous solution. Therefore a further mediator was utilized and is discussed in Section 11.3.2.

11.3.2 The Successful Detection of H_2S in $[C_2mim][NTf_2]$ using 3,5-tert-butyl-o-benzoquinone as a Mediator

Figure 11.2 shows the structure of 3,5-tert-butyl-o-benzoquinone, the next species examined as a mediator for H_2S detection. This species was directly dissolved in the RTIL $[C_2mim][NTf_2]$ as per Section 11.2.

The reaction of H_2S with 3,5-tert-butyl-o-benzoquinone has previously been observed in aqueous solution by Giovanelli *et al.*[8] In the present work we suggest a similar mechanism in the RTIL $[C_2mim][NTf_2]$. This is outlined in Figure 11.2. The mediator 3,5-tert-butyl-o-benzoquinone (a), reacts with H_2S in the RTIL to form the di-substituted 1,2-hydroxybenzene species (b) shown in Step 1. This species can be electrochemically reduced or oxidised. On forming, the di-substituted 1,2-hydroxybenzene species reacts with the parent mediator and is oxidised back to a thiol-substituted benzoquinone species (c) shown in Step 2. The parent species itself is reduced to a di-substituted 1,2-hydroxybenzene species (d). The newly formed benzoquinone species is then free again to react with H_2S to form 2,4-thiol-3,5-tertbutyl-o-benzoquinone (e) shown in Step 3. The following work outlines voltammetric features to support this mechanism in RTILs.

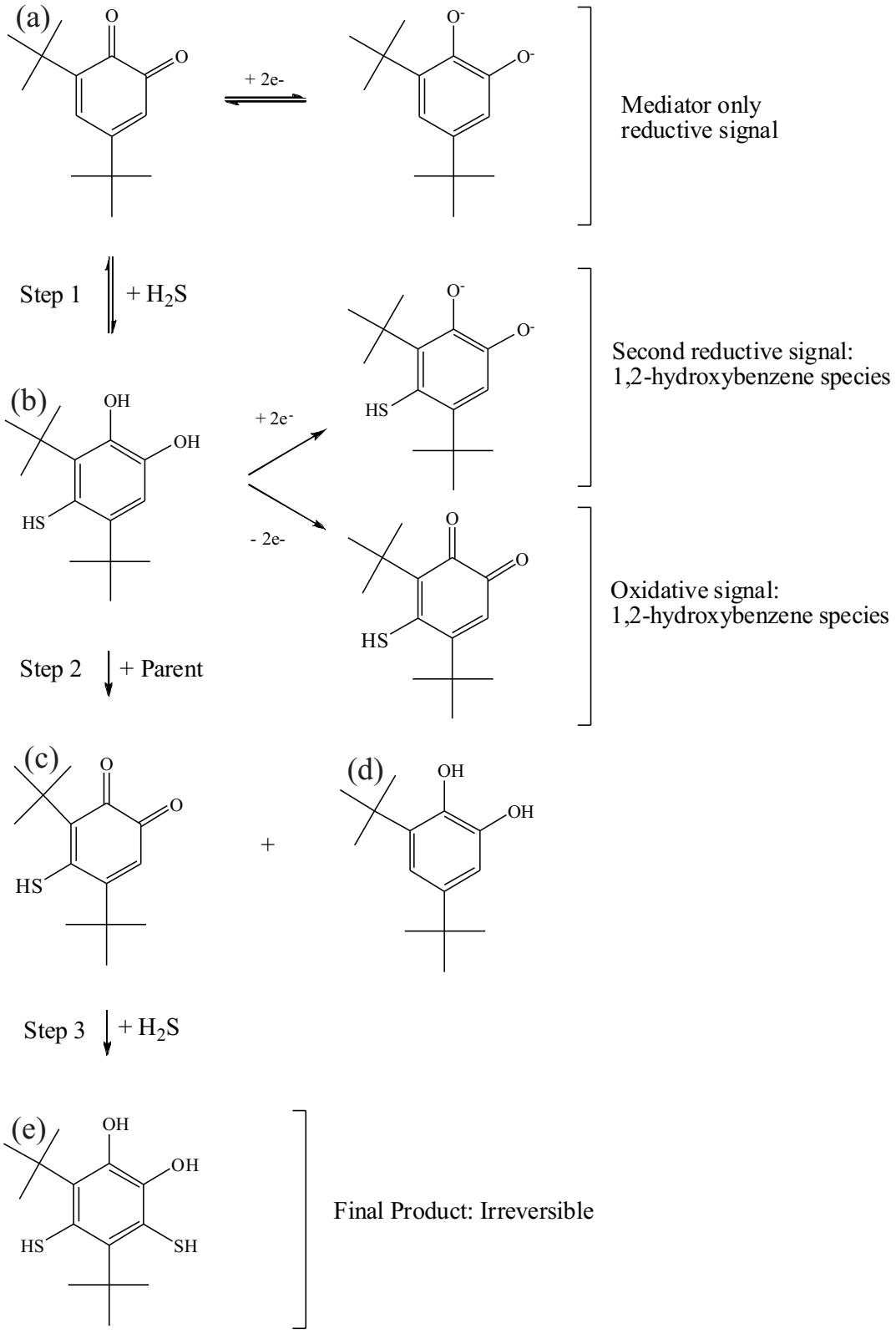


Figure 11.2: Reaction mechanism between 3,5-tert-butyl-o-benzoquinone and H_2S in $[C_2mim][NTf_2]$.

11.3.2.1 Reduction of H_2S in $[C_2mim][NTf_2]$ Using 3,5-tert-butyl-o-benzoquinone as a Mediator over Short Times

Figure 11.3 shows the cyclic voltammograms for the reduction of different concentrations of the mediator 3,5-tert-butyl-o-benzoquinone. Figure 11.3(a) shows the reduction of 20 mM mediator in $[C_2mim][NTf_2]$ in the potential range of 0.0 V to -1.1 V, denoted by the solid line. A signal is observed at -0.9 V *vs.* Pt on the forward scan. This is attributed to the direct two-electron reduction of the mediator outlined in Figure 11.2. The cyclic voltammogram is reversed at potential -1.1 V and an oxidative signal is observed at -0.85 V *vs.* Pt which is attributed to the re-oxidation of the reduced species. A potential step was carried out on the reductive wave of the mediator from 0.0 V (corresponding to no faradaic current) to -0.95 V *vs.* Pt and the current was measured for 5 s. The experimental data was theoretically fitted to the Shoup and Szabo expression.[19] The diffusion coefficient obtained for the mediator in $[C_2mim][NTf_2]$ was calculated to be 1.4×10^{-11} m^2 s^{-1}. The chronoamperometric fitting also gave the *nc* value (no. of electrons $\times$ concentration) which was 36 mM. This indicates a 2-electron transfer since the concentration of mediator dropped onto the electrode was *ca.* 20 mM, so $c = 18$ mM and $n = 2$. The reductive signal for the mediator is observed in Figure 11.3(b)-(d) also for concentrations 2mM, 5mM and 10mM mediator respectively at potential -0.75 V *vs.* Pt, denoted by the solid lines.

H_2S gas (1% H_2S with 99% N_2 fill) was flowed into each of these systems for 10-15 minutes. Figure 11.3(a) shows cyclic voltammetry after the addition of H_2S denoted by the dotted line in the potential range of 0.0 V to -1.3 V. On the forward scan, a reductive signal is observed at potential -0.53 V *vs.* Pt (current -0.13 nA), and at a more negative potential a further signal is observed at -1.0 V *vs.* Pt (current -0.59 nA). The first signal is attributed to the direct reduction of the mediator only. The shift in potential from -0.9 V to -0.7 V *vs.* Pt is attributed to the effect of H_2S on the quasi-reference electrode. It has been confirmed, using the IUPAC-recommended

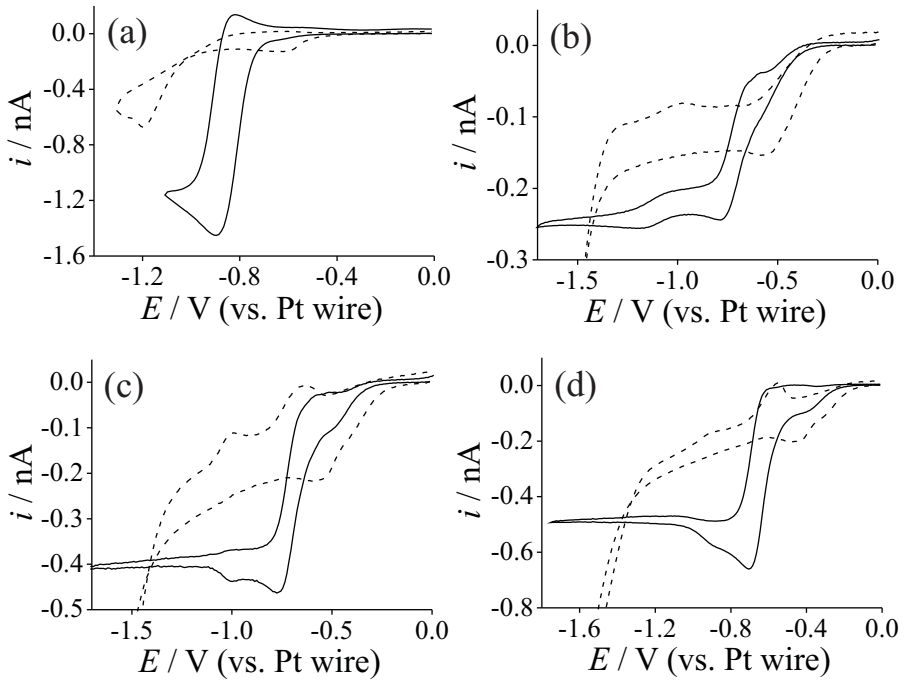


Figure 11.3: Cyclic voltammetry for the reduction of (a) 20 mM, (b) 2 mM, (c) 5 mM (d) 10 mM 3,5-tert-butyl-o-benzoquinone (solid line) and 10-15 mins H_2S 1% flow (dotted) at Pt electrode (10 μm diameter) at a scan rate 100 mV s^{-1} and temperature of 298 K.

Fc/Fc^+ redox couple as an internal reference,[16] that this signal is due to the reduction of the mediator only. The decrease in the mediator only signal is attributed to the consumption of the mediator with H_2S over time.

The next reductive signal at a potential of -1.0 V *vs.* Pt is assigned to the reduction of the product formed as a result of the reaction between the mediator and H_2S, which is outlined in Step 2 of Figure 11.2. Figure 11.3(b)-(d) also shows cyclic voltammograms for the addition of H_2S after 10-15 minutes exposure for 2, 5 and 10 mM mediator respectively, denoted by the dashed lines. In each case, a potential shift and current decrease of the signal of the mediator is observed. The signal for the product of the reaction is not as clear for these smaller concentrations of 3,5-tert-butyl-o-benzoquinone as with 20 mM concentration. This is likely due to lower currents of the signal and relatively higher currents of the direct reduction of H_2S at the Pt electrode, the onset of which is observed at *ca.* -1.5 V *vs.* Pt.

After 10-15 minutes exposure to H_2S, the t-cell was purged with nitrogen gas for approxi-

mately 60 minutes. Figure 11.4(a) shows the initial cyclic voltammogram taken of the mediator only in the potential range of 0.0 V to -1.1 V denoted by the solid line. It also shows the cyclic voltammogram taken after 60 minutes N_2 purging in the potential range of 0.0 V to -1.3 V denoted by the dashed line. This signal shows an increase in the current of the mediator signal from -0.13 nA (after 10 minutes exposure to H_2S) to 1.29 nA (after 60 minutes N_2 purging), which is a near 100% recovery of the initial signal of the mediator before any exposure to H_2S. It should be noted that the reaction times quoted in this work are subject only to the system examined and the need to equilibrate the gas in a relatively large volume of electrolyte. In a practical sensor, a thin layer of electrolyte would diminish this reaction time substantially. The recovery of the initial current of the mediator signal is one of the most promising aspects of the use of this mediator for the detection of H_2S since a sensor incorporating this system can be used, treated, and re-used, making it very attractive as a practical sensor. In Figure 11.4(b)-(d) similar behaviour is observed whereby the current of the reductive signal of the mediator is recovered after exposure to H_2S through N_2 purging (dashed line), to the initial current of the mediator before exposure to H_2S (solid line) for three concentrations of mediator species (2, 5 and 10 mM).

Therefore we attribute Step 1 of Figure 11.2 to be reversible within the timescales presented in these experiments. This system represents a viable sensor for H_2S detection since a clear change in voltammetry is observed and the sensor can be treated for re-use. To confirm that the mechanism outline in Step 1 of Figure 11.2 is accurate, further experiments were carried out in Section 11.3.2.2.

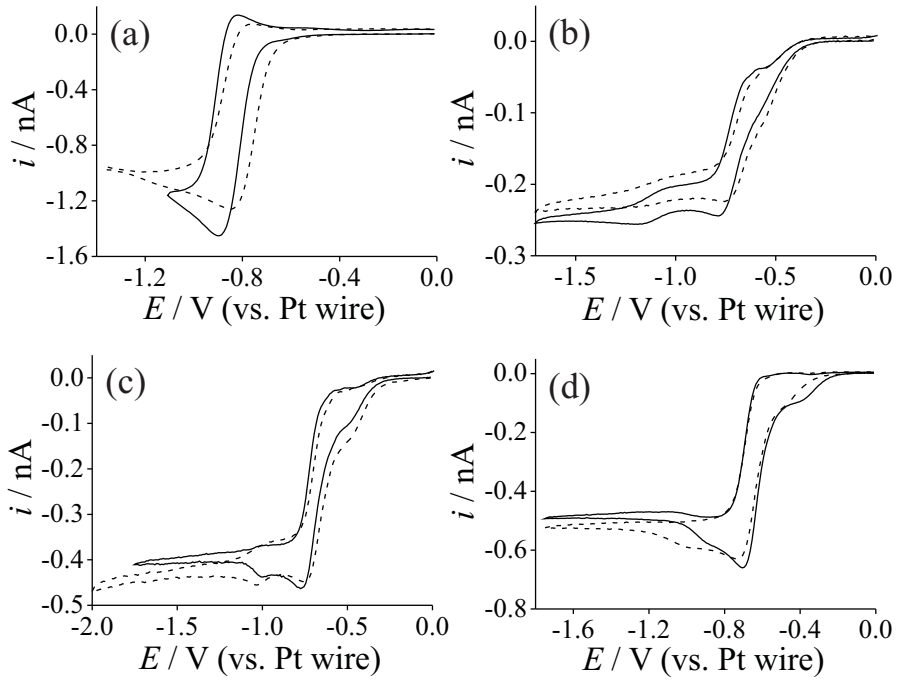


Figure 11.4: Cyclic voltammetry for the reduction of (a) 20 mM, (b) 2 mM, (c) 5 mM (d) 10 mM 3,5-tert-butyl-o-benzoquinone (solid line) and 60 mins N_2 flow (dotted) after H_2S exposure at Pt electrode (10 μm diameter) at a scan rate 100 mV s^{-1} and temperature of 298 K.

11.3.2.2 Oxidative and Reductive Features of H_2S in $[C_2mim][NTf_2]$ and 3,5-tert-butyl-o-benzoquinone Mediator over Long Times

Figure 11.2 outlines the reaction between H_2S the the mediator 3,5-tert-butyl-o-benzoquinone. Step 1 shows the formation of a substituted 1,2-dihydroxybenzene species which reduces at a potential more negative to that of the mediator. The mediator itself is partly consumed in the reaction. It is noteworthy that the partial consumption of the mediating species is not a limitation to this system since it can be overcome in a practical sensor by using a mediator-saturated solution in contact with the electrode. To further examine Step 1 of Figure 11.2, cyclic voltammetry was carried out to observe the oxidative signal of the product assumed to be a substituted 1,2-dihydroxybenzene. Figure 11.5(a) shows the voltammetry of 2 mM 3,5-tert-butyl-o-benzoquinone and added H_2S gas $[C_2mim][NTf_2]$ in the potential range of -1.5 V to +1.5 V. A cyclic voltammogram was taken on 2 mM of the mediator in $[C_2mim][NTf_2]$ from 0.0 V to -1.5 V, then reversed and scanned to 2.0 V, and finally reversed again and scanned

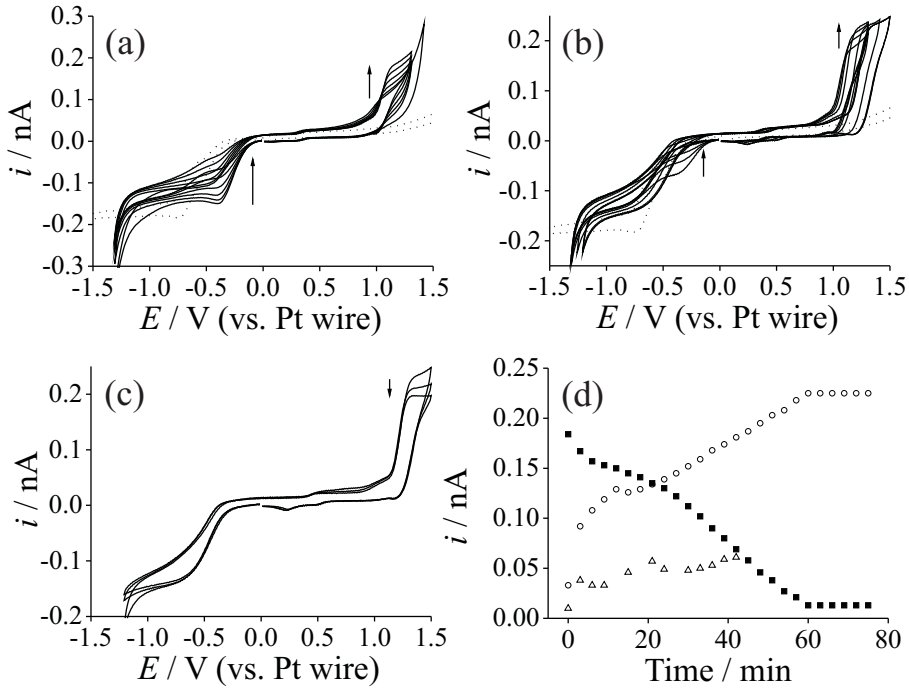


Figure 11.5: (a) Cyclic voltammetry for the reduction and oxidation of 2 mM 3,5-tert-butyl-o-benzoquinone (dotted) and 6-42 mins H_2S 1% exposure(solid); (b) Cyclic voltammetry for the reduction and oxidation of 2 mM 3,5-tert-butyl-o-benzoquinone (dotted) and 42-78 mins H_2S 1% exposure(solid); (c) Cyclic voltammetry for the reduction and oxidation of 2 mM 3,5-tert-butyl-o-benzoquinone after 78 mins H_2S 1% exposure(solid) for 0, 15 and 60 mins N_2 purging; (d) Time/min *vs.* current/nA for the reduction of 3,5-tert-butyl-o-benzoquinone from 6-78 mins. (■), for the oxidation of 1,2-hydroxyquinone species after reduction(○) and for the oxidation of 1,2-hydroxyquinone species without reduction (△).

back to 0.0 V. Figure 11.5(a) shows this scan denoted by the dotted line. On the negative sweep the reductive signal for the mediator only is observed at potential -0.75 V *vs.* Pt at current -0.185 nA. On the positive sweep (from 0.0 V to 2.0 V) no voltammetric signals are observed.

H_2S gas (1% H_2S gas with 99% N_2 fill) is introduced into the system and cyclic voltammograms are taken at regular time intervals in the potential range of -1.3 V to +1.3 V in a similar manner to that of the mediator only. Figure 11.5(a) shows the decrease of the mediator signal on the negative sweep from 6 - 42 mins, denoted by the solid lines. The reductive signal of the mediator has shifted potential to -0.4 V *vs.* Pt and decreases to -0.1 nA over 42 mins. On the reverse sweep, the onset of a new signal is observed at potential 1.0 V *vs.* Pt. This is attributed to the oxidation of a 1,2-dihydroxybenzene species formed when the H_2S and the

mediator react as outlined in Step 1 of Figure 11.2. Similar behaviour of the structurally similar molecule catechol in $[C_2mim][NTf_2]$ was previously observed,[15] supporting the theory that a 1,2-dihydroxybenzene species is formed. Over time this signal increases as the mediator signal decreases.

This reaction was observed over a long period of time. Figure 11.5(b) shows cyclic voltammograms of the mediator and added H_2S from 42 to 78 mins taken at regular intervals in the potential range of -1.3 V to +1.4 V. On the forward scan the complete consumption of the mediator signal is observed over time at -0.4 V *vs.* Pt. This is due to the chemical reaction of 3,5-tert-butyl-o-benzoquinone with H_2S gas. At a more negative potential, the onset of a signal at -0.6 V *vs.* Pt is observed. This is attributed to the reduction of a species formed due to the reaction of the parent mediator with the 1,2-dihydroxybenzene species outlined in Figure 11.2 Step 2. The parent species and the 1,2-dihyroxybenzene species undergo reduction and oxidation respectively when they react together to form 3,5-tert-butyl-4-thiol-o-benzoquinone (Figure 11.2(c)) and 3,5-tert-butyl-1,2-dihydroxybenzene (Figure 11.2(d)). The former species is available for further reaction with H_2S to form the final product. The voltammetric signal observed at -0.6 V *vs.* Pt is attributed to the reduction of this final product.

This chemical reaction is irreversible. After 78 mins exposure to H_2S, N_2 gas was pumped through the T-cell to purge it of H_2S. Figure 11.5(c) shows cyclic voltammograms of the mediator/H_2S system (after 78 mins H_2S exposure) for N_2 purging of 0, 15 and 60 mins. These cyclic voltammograms were taken in the range of -1.2 V to +1.5 V. The forward scan shows a reduction peak at -0.6 V *vs.* Pt which is attributed to the reduction of the final reaction product outlined in Figure 11.2. With 60 mins of N_2 purging the signal remains unchanged indicating an irreversible chemical reaction. The oxidative scan shows little change in the oxidative peak of the 1,2-dihydroxybenzene species at 1.2 V *vs.* Pt, again indicating an irreversible chemical reaction. The slight decrease in this signal over 0 to 60 mins N_2 purging is attributed to the

removal of excess H_2S from the system, the direct oxidation of which proceeds directly after the oxidation of 1,2-dihydroxybenzene,[14] and the presence of which alters the viscosity of the RTIL slightly.[12,13]

Figure 11.5(d) shows the change in the modulus of the current of the reductive mediator signal (■) and the change in the current of the oxidative 1,2-dihydroxybenzene species (○) over time. Initially (0-20 mins) each signal changes until the rate of change slows. This change is attributed to Step 1 of the mechanism outlined in Figure 11.2 which is chemically reversible. After 20 mins, the rate of change of each signal increases again until the reductive signal reaches a minimum, and the oxidative signal reaches a maximum. This is attributed to the further reaction of the 1,2-dihydroxybenzene species with the parent mediator until the parent is completely consumed leaving only the final product shown in Step 3 of Figure 11.2.

Also shown in Figure 11.5(d) is a third signal (△) which shows the change in the oxidative signal over time in the potential range of 0.0 V to 1.5 V without ever scanning reductively. This signal increases much more slowly than that of the oxidative signal after reduction (○). This shows that while the mediator and H_2S do react to form the 1,2-dihydroxybenzene species regardless of voltammetric cycling, however voltammetric cycling can activate the electrode towards the oxidation of this species.

3,5-tert-butyl-o-benzoquinone has been presented as a suitable mediator for H_2S detection in RTILs. The reductive voltammetry changes, due to consumption of the mediator and formation of an adduct. The decrease of the reductive signal and the onset of an oxidative signal are both viable markers for the presence of H_2S. Also, within certain time limits, this chemical reaction is reversible whereby a recovery of the initial mediator signal is observed after purging the cell with N_2 over a period of time, allowing re-use of the sensor. Therefore this species is a suitable mediator for detection of H_2S as it incorporates the benefit of a re-usable sensor and all the attractive properties of RTILs. In the next section, a scale-down of H_2S concentration

to 200 ppm was carried out to observe whether this sensor can operate at low levels of H_2S.

11.3.2.3 The Mediated Detection of Low Concentrations of H_2S in RTILs

Figure 11.6 shows the mediated detection of H_2S gas (200 ppm H_2S with N_2 fill) in $[C_2mim][NTf_2]$ using the mediator 3,5-tert-butyl-o-benzoquinone (2 mM). Cyclic voltammetry was carried out on 2 mM 3,5-tert-butyl-o-benzoquinone in $[C_2mim][NTf_2]$ only (dotted line). The two-electron reduction of the mediator was observed at -0.73 V *vs.* Pt on the forward scan. The scan was reversed at -1.5 V and an oxidative sweep was carried out to potential 1.5 V. No oxidative voltammetric features were observed. The scan was reversed again at 1.5 V and cycled to 0.0 V. H_2S 1% was mixed with N_2 to a concentration of 200 ppm in the method outlined in Chapter 4 and flowed through the system. Cyclic voltammograms were taken at regular time intervals in the potential range of -1.2 V to 1.2 V. The scan was cycled from 0.0 V to -1.2 V, and the reduction of the mediator was observed at -0.59 V *vs.* Pt, the current of which decreased slightly over time suggesting that H_2S was reacting with the mediator to form the 1,2-hydroxybenzene species outlined in Figure 11.2(b). The scan was reversed at -1.2 V and scanned to 1.2 V. Initially, no oxidative signal for the 1,2-hydroxybenzene species. After 140 mins of H_2S flow however, a signal was observed on the oxidative scan at 1.0 V *vs.* Pt shown in Figure 11.6 (solid line).

This is attributed to the oxidation of the 1,2-hydroxybenzene species formed by chemical reaction of H_2S and 3,5-tert-butyl-o-benzoquinone. As previously mentioned in Section 11.3.2.1, the reaction times quoted in this work reflect the cell used which contains a relatively large volume of electrolyte: faster response times are expected with a real sensor. Therefore, at very low concentrations of H_2S, chemical reaction with the mediator occurs to decrease the reductive mediator signal and cause the onset of an oxidative signal not present before the addition of H_2S.

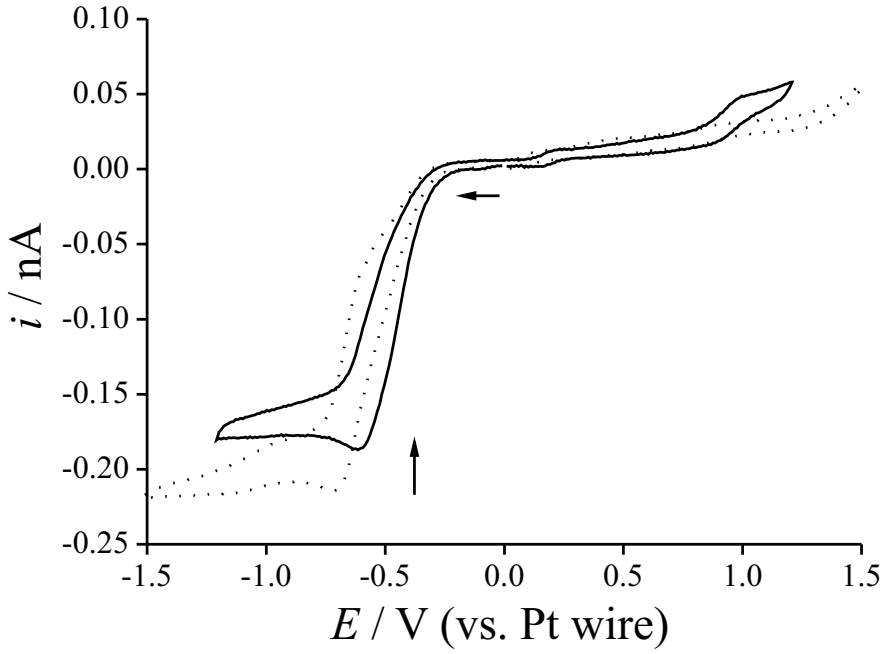


Figure 11.6: Cyclic voltammetry for the reduction and oxidation of 2 mM 3,5-tert-butyl-o-benzoquinone in $[C_2mim][NTf_2]$ (dotted) and the reduction and oxidation of added H_2S 200 ppm for 140 mins flow at Pt electrode (10 μm diameter) at a scan rate 100 mV s^{-1} and temperature of 298 K.

11.4 Conclusions

The mediated detection of H_2S has been attempted in RTILs using six different mediators: DMPD, catechol, ferrocene, potassium ferrocyanide, PVF and 3,5-tert-butyl-o-benzoquinone. Of the six attempts, only the use of 3,5-tert-butyl-o-benzoquinone was successful in the mediated detection of H_2S.

This mediator reacts with H_2S in $[C_2mim][NTf_2]$ outlined in Figure 11.2, to form a 1,2-hydroxyquinone species which can be reduced or oxidised. During this process, the reductive signal of the mediator decreases due to consumption by this chemical reaction. This decrease in signal in itself is a viable analytical signal for use as a sensor. The oxidation of the formed 1,2-hydroxyquinone is also a viable analytical signal within a gas sensor since before addition of the H_2S, the oxidative voltammetric sweep of the mediator shows a featureless baseline, and upon addition of H_2S, an electrochemical signal is observed. This reaction is reversible over

short times (0 - 20 mins), by purging the system with N_2, which is an attractive feature for a practical gas sensor as the system can be re-used.

At longer times (20 mins), a further chemical reaction occurs between the 1,2-hydroxybenzene species and the parent mediator whereby the parent is reduced by the 1,2-hydroxybenzene species, which itself is oxidised to a tri-substituted o-benzoquinone species. This new species is available again for reaction with H_2S to form a final product of 2,4-thiol-3,5-tert-butyl-o-benzoquinone. This final reaction is chemically irreversible when the system is purged with N_2 for any period of time.

This mechanism is also true for lower concentrations of H_2S, and while the reaction times are relatively long, these times are related only to the high-volume electrolyte cells used in this work, not to real sensors.

Therefore, a viable practical method of H_2S detection is possible using the mediating species 3,5-tert-butyl-o-benzoquinone, which possesses attractive features such as re-usability, decrease in signal potential, and all the attractive features associated with the use of RTILs.

This concludes work for the fabrication of a practical sensor for H_2S detection. Chapter 5 allows us to select a suitable RTIL for particular experiments based on physical properties such as viscosity and water affinity. Chapters 6 and 7 allow us to understand H_2S processes in RTILs as well as at the electrode surface. While attempting to decrease the potential at which H_2S is detection, several species were employed as mediators for H_2S detection. The voltammetry of some of these species (DMPD, catechol and PVF) show interesting voltammetry in RTILs at the Pt electrode in their own right and this voltammetry was studied in Chapters 8, 9 and 10. Finally, this Chapter shows the success of one mediating species, 3,5-tertbutyl-o-benzoquinone in RTILs for the fabrication of a practical H_2S sensor.

In the next Chapter, we deviate from H_2S detection in favour of observing electrochemistry of ferrocene in RTILs at ring-recessed disc microelectrodes in generator-collector mode. This work

allows us to utilize the high viscosity and slow conductivity encountered in RTILs to study the potential-step voltammetric transients of ferrocene at microdisc arrays in generator mode, and microring arrays in collector mode. This Chapter also outlines the fabrication of ring-recessed disc microelectrodes.

References

[1] Lawrence, N. S.; Davis, J.; Jiang, L.; Jones, T.; Davies, S. and Compton, R., *Electroanalysis*, 2001, **13**, 432–436.

[2] Lawrence, N. S.; Davis, J.; Jiang, L.; Jones, T. G. J.; Davies, S. N. and Compton, R. G., *Electroanalysis*, 2001, **13**, 143–148.

[3] Lawrence, N. S.; Thompson, M.; Davis, J.; Jiang, L.; Jones, T. G. J. and Compton, R. G., *Mikrochim. Acta*, 2001, **137**, 105–110.

[4] Thompson, M.; Lawrence, N. S.; Davis, J.; Jiang, L.; Jones, T. G. J. and Compton, R. G., *Sens. Actuators, B*, 2002, **87**, 33–40.

[5] Lawrence, N. S.; Tustin, G. J.; Faulkner, M. and Jones, T. G. J., *Electrochim. Acta*, 2006, **52**, 499–503.

[6] Robinson, K. and Lawrence, N. S., *Electroanalysis*, 2006, **18**, 677–683.

[7] Silvester, D. S. and Compton, R. G., *Z. Phys. Chem.*, 2006, **220**, 1247–1274.

[8] Giovanelli, D.; Lawrence, N. S.; Jiang, L.; Jones, T. G. J. and Compton, R. G., *Anal. Lett.*, 2003, **36**, 2941–2959.

[9] Lawrence, N. S.; Davis, J.; Jiang, L.; Jones, T.; Davis, S. and Compton, R. G., *Analyst*, 2000, **125**, 661–663.

[10] Banks, C. E.; Yashina, A. S.; Tustin, G. J.; Lafitte, V. G. H.; Jones, T. G. J. and Lawrence, N. S., *Electroanalysis*, 2007, **19**, 2518–2522.

[11] Barnes, E. O.; O' Mahony, A. M.; Belding, S. R. and Compton, R. G., *J. Chem. Eng. Data*, 2010, **55**, 2219–2224.

[12] Barrosse-Antle, L. E.; Aldous, L.; Hardacre, C.; Bond, A. M. and Compton, R. G., *J. Phys. Chem. C*, 2009, **113**, 7750–7754.

[13] Zhao, C.; Bond, A. M.; Compton, R. G.; O' Mahony, A. M. and Rogers, E. I., *Anal. Chem.*, 2010, **82**, 3856–3861.

[14] O' Mahony, A. M.; Dickinson, E. J. F.; Aldous, L.; Hardacre, C. and Compton, R. G., *J. Phys. Chem. C*, 2009, **113**, 10997–11002.

[15] Barnes, E. O.; O' Mahony, A. M.; Aldous, L.; Hardacre, C. and Compton, R. G., *J. Electroanal. Chem.*, 2010, **646**, 11–17.

[16] Rogers, E. I.; Silvester, D. S.; Poole, D. L.; Aldous, L.; Hardacre, C. and Compton, R. G., *J. Phys. Chem. C*, 2008, **112**, 2729–2735.

[17] Wadhawan, J. D.; Schröder, U.; Neudeck, A.; Wilkins, S. J.; Compton, R. G.; Marken, F.; Consorti, C. S.; de Souza, R. F. and Dupont, J., *J. Electroanal. Chem.*, 2000, **493**, 75–83.

[18] O' Mahony, A. M.; Hardacre, C. and Compton, R. G., *J. Electrochem. Soc.*, 2010, **157**, F49–F53.

[19] Shoup, D. and Szabo, A., *J. Electroanal. Chem.*, 1982, **140**, 237–245.

Chapter 12

Micro arrays of ring-recessed disc electrodes in transient generator-collector mode: theory and experiment

The fabrication, characterisation and use of arrays of ring-recessed disc microelectrodes is reported. This devices are operated in generator-collector mode with a disc acting as generator and the ring as the collector. In this Chapter, experiments and simulations relating to time of flight experiments in which material electrogenerated at a disc is diffusionally transported to the ring are reported. Analysis of the current transient measured at the latter when it is potentiostatted at a value to ensure diffusionally controlled "collection" is shown to sensitively reflect the diffusion coefficients of the species forming the redox couple being driven at the generator electrode. The method is applied to the Fc/Fc^{+} couple in the room temperature ionic liquid $[N_{6,2,2,2}][NTf_2]$ and the results found to agree with independent measurements.

12.1 Introduction

Recently, a general theoretical framework to study diffusional mass transport at a new type of microelectrode array particularly suited for generator-collector experiments was presented.[1] That new geometry consisted on an array of ring-recessed disc microelectrode arrays, distributed on a planar substrate. Here, the fabrication of these devices is presented and their application to the estimation of diffusion coefficients from bipotentiostatic time-of-flight experiments in ionic liquids is presented. Time of flight experiments with electrochemical detection and generation were shown to be a general method for determination of diffusional coefficients.[2–5]

Disc-ring structures may be preferable to double band structures in generator-collector experiments because the generator electrode is completely surrounded by the collector electrode, so less generated material is lost by diffusion to the solution bulk, and collection efficiencies are consequently higher. In the case of microband electrodes, these losses are mostly overcome using triple band and interdigitated structures. Therefore, up until now, generator-collector experiments at microelectrodes were performed at double[6] and triple[7] band, or interdigitated microband structures.[8,9] Regular interdigitated microbands are necessarily fabricated using microfabrication techniques based on photolithography, and their minimum geometric features are limited by the optical resolution of the photolithographic step. The most common photolithographic equipment is able to achieve resolutions of a few microns or, at most, around the micron. Electron beam lithography coupled to nanoimprint lithography allows the fabricatication of devices presenting sub-micrometric features, but these techniques are still rather uncommon due to the high cost of the required equipment and the need for very clean fabrication environments.

In this Chapter we demonstrate the fabrication of a new device based on disc-ring structures, using standard microfabrication techniques, and where the gap between disc and ring is below the resolution of the photolithographic step. To achieve this, the discs are fabricated recessed with respect to the rings, so the gap between them is controlled by the recess height. This height

is nothing else than the thickness of a layer of dielectric material, in the present case a silicon oxide layer, that provides electrical insulation between the discs and the rings above them. Since the deposition of this dielectric layer is independent of the photolithographic step, it is possible in principle to grow very thin layers of oxide over the metal layer featuring the discs, so that nanometric scale gaps can be obtained between discs and rings, regardless of the resolution of our aligner. Another great advantage of this approach is that, since discs and rings are actually on different planes, it is possible to fabricate controlled arrays of identical disc-ring sets. This approach is not common and has never been applied for fabrication of ring-disc arrays, but has been once used to produce interdigitated array electrodes[10,11] and single microcavity device with a ring-generator and tubular nanoband-collector electrode.[12] This is important because although the only disc-ring microelectrodes reported to date are coplanar, the fabrication of regular arrays seems an important challenge, if not impossible, due to the way in which they are produced.[13–16]

In previous work, it was demonstrated that this type of device is highly efficient, and allows for steady-state collection efficiencies above 90%, comparable with those obtained at interdigitated microbands. In this Chapter we apply the diffusion domain approach used before for simulation of current responses from arrays of ring-recessed disc electrodes[1] and other arrays of electrodes[17,18] to aid in the determination of diffusion coefficients from potential step experiments at arrays of ring-recessed disc electrodes in generator-collector mode where potential on the disc is stepped from the value corresponding to no current to one of diffusion controlled electrolysis whilst the ring is potentiostated to reverse the electrolysis and convert the disc product back to starting material. Three different behaviour zones can be clearly distinguished during generator-collector experiments on fully reversible redox couples. First, at very short times, diffusion to the generator microdisc is mainly planar, because the recessed nature of the microdisc eliminates the possibility of edge diffusion to it. When the material generated by the

disc reaches the ring electrode, it is converted back to the starting material and diffuses back towards the disc. After this equilibration period, a true steady-state current is achieved both at the microdisc and the microring electrodes. The duration of this so-called equilibration period is important when the diffusion coefficients of the reduced and oxidised species are different, and the current during this time is extremely sensitive to the ratio of diffusion coefficients. Another important advantage of these devices compared to conventional disc microelectrode arrays is that the steady state currents achieved are true steady state current regardless of the experiment duration, even if the array of disc-ring systems is very densely packed, since the cycling of material between disc and ring reduces the overlap of the diffusional fields of adjacent electrodes.

The fabrication of the ring-recessed disc microelectrode arrays was carried out by Dr. F. Javier Del-Campo, IMB-CNM. CSIC, Campus de la Universidad Autonoma de Barcelona, Bellaterra 08193, Spain. The theoretical and mathematical models for this Chapter were outlined by Denis Menshykau, a D.Phil. student at Oxford University. The experimental work was carried out by the author.

12.2 Theoretical model

12.2.1 The model of electrode surface

We consider an electrode with an idealized surface as shown in Figure 12.1. The surface is composed of an "array" of ring-recessed disc electrodes in which the discs are recessed relative to the surrounding rings. The disc electrode act as a "generator" electrode and ring electrode as a "collector" electrode. Material is assumed to reach the disc electrode via diffusion through the cylindrical well above it and negligibly otherwise.

The diffusion of the electrochemically active species is complicated because it is intrinsically a three dimensional problem. However, the problem can be simplified by noting that each cylindrical well belongs to a diffusionally independent region known as a diffusion domain.[17,19]

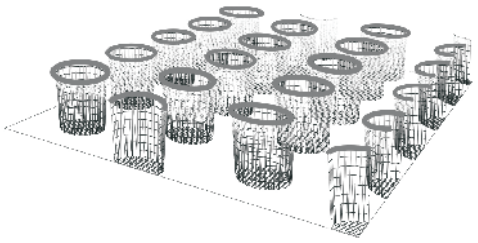


Figure 12.1: Schematic diagram of the electrode surface

The diffusional domain approximation treats these zones as being cylindrical with a ring-recessed disc electrode center situated at the axis of symmetry, thus reducing the problem to one of only two dimensions. The approximation is illustrated in Figure 12.2. Figure 12.2(a) and (b) show the surface in Cartesian coordinates and Figure 12.2(c) identifies the unit cell in cylindrical coordinates (r, z). The cylindrical radial coordinate, r, is defined as the distance from the axis of symmetry that runs through the center of the electrode domain. The cylindrical domain is of equal area to the hexagonal unit cell. The total current from the macroelectrode "array" is given by simple multiplication of the current from a single diffusion domain times the total number of domains N_{p}. Recently it was shown that two dimensional simulations in conjunction with the diffusion domain approach gives results indistinguishable from full three dimensional simulations.[20]

12.2.2 Mathematical model

Equation 12.1 shows the electron transfer reaction at the generator electrode considered in these numerical simulations. Equation 12.2 shows the corresponding and reverse electron transfer reaction at the collector electrode. Both species A and B are assumed soluble, but only species

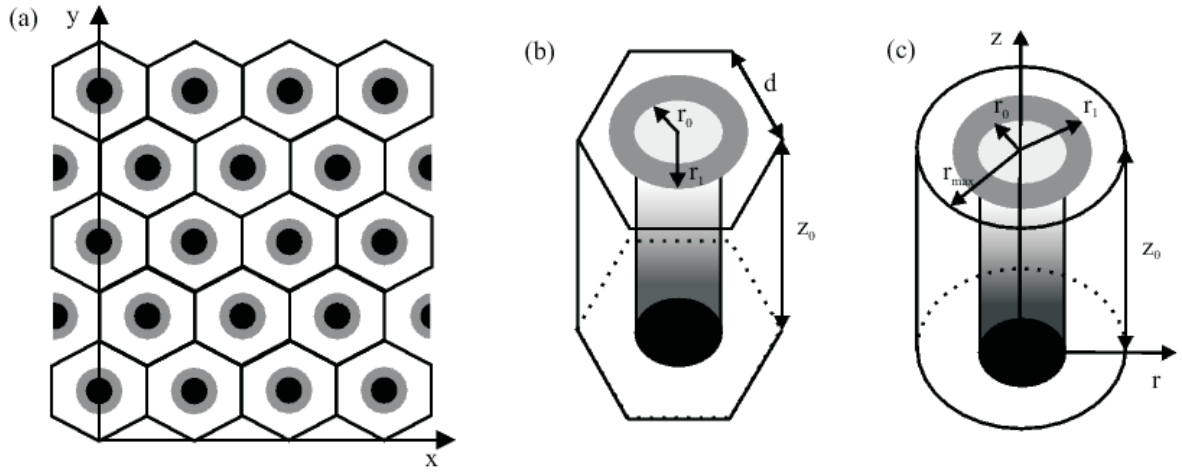


Figure 12.2: (a)Schematic diagram of the unit cell for an array of ring-recessed electrodes; (b) single unit cell in Cartesian coordinates; (c) equivalent diffusion domain in cylindrical coordinates

A is assumed to be present in the bulk solution.

$$\text{Disc} : \text{A} + \text{e}^- \rightleftharpoons \text{B} \tag{12.1}$$

$$\text{Ring} : \text{B} - \text{e}^- \rightleftharpoons \text{A} \tag{12.2}$$

The rate of electron transfer is described by the Butler-Volmer kinetics:

$$D_\text{A} \frac{\partial[\text{A}]}{\partial z}|_\text{el} = (k_\text{f}[\text{A}] - k_b[\text{B}])|_\text{el} \tag{12.3}$$

where k_f and k_b are given by Equations 12.4 and 12.5, consequently and $D_\text{A} \frac{\partial[\text{A}]}{\partial z}|_\text{el}$ is the diffusional flux of species A to the electrode surface along path Z.

$$k_\text{f} = k^0 \exp\left(-\frac{\alpha F}{RT}(E - E_\text{f}^\ominus)\right) \tag{12.4}$$

$$k_\text{b} = k^0 \exp\left(\frac{(1-\alpha) F}{RT}(E - E_\text{f}^\ominus)\right) \tag{12.5}$$

where $E_f^{\ominus}$ is the formal potential of the A/B couple and k^0 is the standard rate constant of electron transfer. We next consider the potential step experiment applied to the reduction of A at the disc electrode and we assume that the step is big enough to assume that the concentration of A is zero at the disc surface. We also assume that the potential at the ring is held at a sufficiently positive value, that the concentration of B is zero at the ring. Species A and B might have different or equal diffusion coefficients. We consider both cases separately.

Equal diffusion coefficients. At each point in solution the concentration of species A and B must satisfy the mass conservation law:

$$[\mathrm{A}] + [\mathrm{B}] = [\mathrm{A}]_0 \tag{12.6}$$

where $[\mathrm{A}]_0$ is the bulk concentration of A. In this case the concentration profile of species A may be simulated independently from that of B. Mass transport in cylindrical coordinates is described by Fick's second law of diffusion given by Equation 12.7

$$\frac{\partial[\mathrm{A}]}{\partial t} = D_\mathrm{A}\left(\frac{\partial^2[\mathrm{A}]}{\partial r^2} + \frac{1}{r}\frac{\partial[\mathrm{A}]}{\partial r} + \frac{\partial^2[\mathrm{A}]}{\partial z^2}\right) \tag{12.7}$$

Unequal diffusion coefficients. In case of unequal diffusion coefficients mass conservation law 12.6 is not fulfilled and mass transport Equation 12.7 for species A should be accompanied by the mass transport law for the species B:

$$\frac{\partial[\mathrm{B}]}{\partial t} = D_\mathrm{B}\left(\frac{\partial^2[\mathrm{B}]}{\partial r^2} + \frac{1}{r}\frac{\partial[\mathrm{B}]}{\partial r} + \frac{\partial^2[\mathrm{B}]}{\partial z^2}\right) \tag{12.8}$$

Note that here we assume that the solution is fully supported[21] and Fick's second law of diffusion adequately describes mass transport in fully supported media when migration can be neglected and if the length scale of the device is higher than 10 nm.

The model is normalized with use of the dimensionless parameters which are listed in Table 12.1. Mass transport in cylindrical coordinates is given by the dimensionless version of Equations 12.7 and 12.8:

$$\frac{\partial a}{\partial \tau} = \frac{\partial^2 a}{\partial R^2} + \frac{1}{R}\frac{\partial a}{\partial R} + \frac{\partial^2 a}{\partial Z^2} \tag{12.9}$$

$$\frac{\partial b}{\partial \tau} = D_\mathrm{r}\left(\frac{\partial^2 b}{\partial R^2} + \frac{1}{R}\frac{\partial b}{\partial R} + \frac{\partial^2 b}{\partial Z^2}\right) \tag{12.10}$$

The boundary conditions for Equations 12.9 and 12.10 are summarized in Table 12.2.

Table 12.1: Dimensionless parameters used for numerical simulation.

Parameter	Expression normalized to r_0
Radial coordinate	$R = r/r_0$
Normal coordinate	$Z = z/r_0$
Time	$\tau = \frac{Dt}{r_0^2}$
Scan rate	$\sigma = \frac{Fvr_0^2}{RTD}$
Potential	$\theta = \frac{F(E-E_\mathrm{f}^0)}{RT}$
Concentration of species A	$a = [\mathrm{A}]/[\mathrm{A}]_0$
Concentration of species B	$b = [\mathrm{B}]/[\mathrm{A}]_0$
Pore depth	$L_\mathrm{cyl} = \frac{z_0}{r_0}$
Outer radius of collector ring	$R_1 = \frac{r_1}{r_0}$
Radius of diffusion domain	$R_\mathrm{max} = \frac{r_\mathrm{max}}{r_0}$
Diffusion coefficient ratio	$D_\mathrm{r} = \frac{D_\mathrm{B}}{D_\mathrm{A}}$
Electrode current	$j = \frac{-i}{4FD[\mathrm{A}]_0 r_0}$

Table 12.2: Boundary and initial conditions.

Boundary	Condition
Initial concentration	$a = 1$
Bulk solution concentration	$a = 1$
Concentration at generator electrode	$a = 0$
Concentration at collector electrode	$b = 0$
Boundary condition at generator and collector electrodes	$\frac{\partial a}{\partial Z} = -D_\mathrm{r}\frac{\partial b}{\partial Z}$
Axis of symmetry and insulator surface	$\frac{\partial a}{\partial R} = 0$
Diffusion domain border	$\frac{\partial a}{\partial R} = 0$
Insulator surface	$\frac{\partial a}{\partial Z} = 0$

12.3 Experimental and computational details

12.3.1 Instrumentation

The electrode diameter of a 10μm Pt microdisc electrode was calibrated electrochemically by analyzing the potential-step voltammetry of a 2 mM solution of Fc in MeCN containing 0.1 M TBAP, with a diffusion coefficient for ferrocene 2.3×10^{-5} cm^2 s^{-1} at 298 K.[22]

The electrodes were housed in a glass cell "T-cell" designed for investigating microsamples of ionic liquids under a controlled atmosphere.[23,24] The working electrode was modified with a section of disposable micropipette tip to create a small cavity above the disc into which a drop (20 μL) of ionic liquid and a drop (20 μL) of 5 mM Fc in acetonitrile was placed. The RTIL solution was purged under vacuum (Edwards High Vacuum Pump, Model ES 50) for *ca.* 90 minutes, which served to remove trace atmospheric moisture naturally present in the RTIL, and evaporate the acetonitrile so that a concentration of 5 mM Fc remained in the RTIL.

An array of ring-recessed disc electrodes was used to compare the theoretical generator/collector model outline in Section 12.2.2 with experimental data. The electrode array was rinsed well with water and dried with nitrogen. The Fc/$[N_{6,2,2,2}][NTf_2]$ solution used at the platinum electrode was removed from the cavity above the disc using a micropipette and dropped onto the surface of the electrode array. Experiments were performed in a faraday cage at room temperature.

12.3.2 Microdisc and Micro Array Chronoamperometric Experiments

Chronoamperometric transients at the platinum electrode (10 μm diameter) were achieved using a sample time of 0.01 s. After pre-equilibration for 20 seconds, the potential was stepped from a position of zero current to a chosen potential after the oxidative peak of ferrocene, and the current was measured for 5 s. The software package Origin 7.0 (Microcal Software Inc.) was used to fit the experimental data as outlined in Chapter 4.

Double potential step chronoamperometric transients at the platinum electrode (10 μm di-

ameter) were achieved using a sample time of 0.01 s also outlined in Chapter 4.

Bipotentiostat chronoamperometry was performed on the ring-recessed disc electrode array to oxidise and reduce Fc. The microdisc array was used as a generator electrode to oxidise Fc to Fc^+, and the microring array was used as the collector electrode to reduce Fc^+ to Fc. The solution was pretreated by holding potential at a pont of zero current for 20 s, after which the potential on the microdisc array was stepped to potential after the oxidative peak for Fc. The current was measured for 0.5 s at a sample time of 0.001 s, and then for 20 s at a sample time of 0.004 s. Simultaneously the potential was stepped back to a point after the reduction of Fc^+ to Fc on the microring array. The current was measured under the same conditions as that of the microdisc array.

12.3.3 Array fabrication procedure

Microelectrode arrays were fabricated using standard photolithographic techniques as follows. A 1 micron thick layer of thermal oxide was grown on 4-inch diameter silicon wafers to provide electrical insulation to the microelectrodes (Figure 12.3.1). Next the bottom metal layer was deposited by sputtering (Figure 12.3.2). This metal layer consisted of 25 nm Ti, 25 nm Ni and 125 nm Au. The Titanium was used to promote adhesion of the gold over the silicon oxide. Nickel was used as a diffusion barrier to avoid contamination of the gold by titanium due to the high temperatures achieved during sputtering. Next, a positive photoresist was deposited by spin coating over the gold. This photoresist was developed after contact-UV insolation through a clear field mask (Figure 12.3(a)). Following this, the bottom metal areas and the contacts were defined in a wet-etching step (Figure 12.3.3). The excess photoresist was stripped once these patterns had been defined, and a thin silicon oxide layer (*ca.* 1 micron) was grown over the wafers (Figure 12.3.4). This oxide layer provided electrical insulation and provided the separation between the discs and the rings in the final device. Following the deposition of the

intermediate oxide layer, a second metal layer was deposited and patterned in the same way as the previous one (Figure 12.3.5-6). The only special feature of this second metal layer was that it featured "holes" corresponding to the underlaying microdiscs (Figure 12.3(b)). This way the top gold layer will also be used as mask during the final etching steps. Following this second metallisation, a passivation layer was deposited over the wafers to provide electrical insulation to the devices. This passivation layer consisted of 200nm of silicon oxide and 400 nm of silicon nitride (Figure 12.3.7).

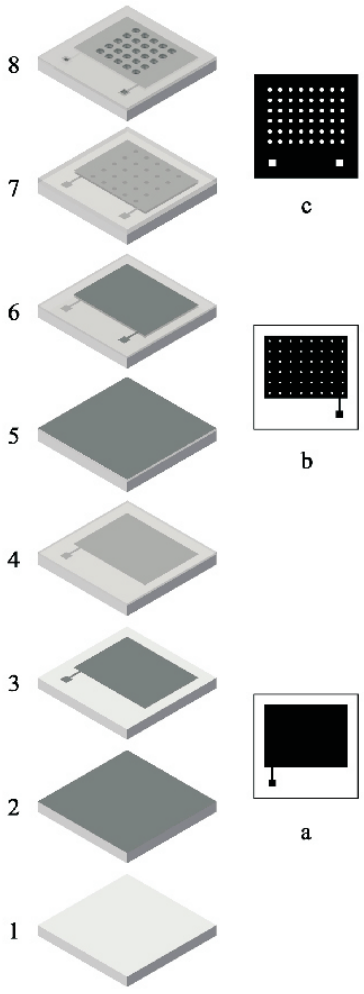


Figure 12.3: Diagrammatic representation of main steps in the fabrication process (1-8) and mask types used (a-c).

The next steps of the fabrication were critical, as it involved opening the contacts and defining

the rings and discs in the top and bottom metal levels, respectively.

A positive photoresist was spin coated over the surface of the nitride face of the wafers. A dark field chromium mask featuring discs was used to pattern the microrings on the top metal layer (Figure 12.3(c)). After the photoresist was developed, the silicon nitride and oxide over the top metal layer was etched by reactive ion etching, RIE. During this step, the top metal layer served as mask and thus the intermediate oxide layer between metal levels could also be etched (Figure 12.3.8). The trouble with this approach is that the RIE may damage the gold and therefore the time of attack must be carefully controlled in order not to "burn" the top metal level. As a result of this and also of the fact that the different passivating layers present slight inhomogeneities depending on the position of the wafer in various ovens, intermediate silicon oxide is not successfully removed from all the disc-ring systems, and hence there are a low number of active microdiscs compared to more common microelectrode arrays. After the RIE step, the excess resin was stripped in acetone and the wafers thoroughly rinsed in deionised water. The wafers were then diced into individual chips, which were subsequently attached, wire-bonded and encapsulated on suitable print circuit board strips.

12.3.4 Computational procedure

Because of the symmetry of the model, the mass transport Equations 12.7 and 12.8 and its accompanying conditions (Table 12.2) were solved in the two dimensional space in the region $0 < R < R_{\max}$ and $Z > 0$. The bulk solution condition is implemented at a distance $6\sqrt{\tau_{\max} * max\{1, D_{\mathrm{r}}\}}$ from the highest point of the electrode, where $\tau_{\max}$ is the time scale of experiment. Beyond this the effects of diffusion are not important on the experimental voltammetric timescale.[25,26] The modeling of the ring-recessed disc electrode is complicated by the presence of singularities at the boundaries between electrodes and insulators. To calculate the precise values of the current at the electrodes a rectangular expanding grid, similar to that used

in previous simulations of electrodes with complicated surfaces[27–30] was utilised. The expanding grid is defined by Equations 12.11-12.14 and the schematic view of the grid is presented in Figure 12.4.

$$R_{i+1} - R_i = h_i \tag{12.11}$$

$$Z_{i+1} - Z_i = k_i \tag{12.12}$$

$$h_i = \gamma_R \times h_{i-1} \tag{12.13}$$

$$k_i = \gamma_Z \times k_{i-1} \tag{12.14}$$

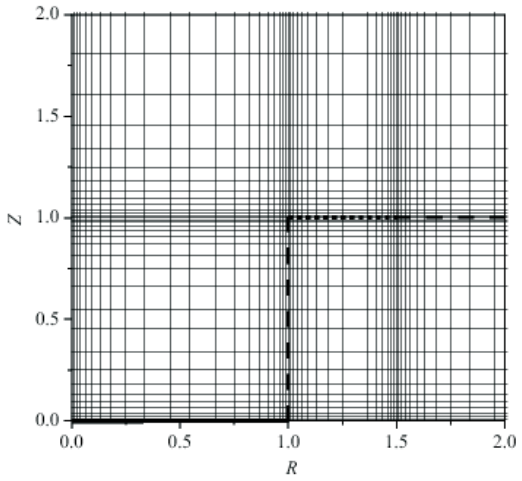


Figure 12.4: Expanding grid used in this Chapter (some lines excluded for clarity). The generator electrode is shown in solid black, the collector electrode is in black squares and the insulator is in black dashes

Furthermore if the distance separating the disc from the ring is small, very fine time steps are required to calculate accurate values of current. Standard values of the mesh used in computations were $h_0 = k_0 = 10^{-5}$ and $\gamma_R = \gamma_Z = 1.125$. An expanding time grid is also used; time steps were calculated each time in agreement with the expression:

$$min(\tau_k \tau^m, \gamma_\tau \delta\tau) \tag{12.15}$$

where, standard values of parameters are $\tau_k = 0.001, m = 0.65, \gamma_\tau = 1.01$ and initial time step is $\delta\tau = 10^{-10}$. To check the convergence of the simulation procedure, numerous simulations were run with different space grids and time steps. The calculated current converges with a decrease of the space step and time step. The whole range of parameters were tested to achieve an accuracy of 0.2%. To validate the procedure, a comparison to the known results for a flat macrodisk were made. The alternating direction implicit finite difference method[31] was used in conjunction with the Thomas algorithm[32] to solve the discretized form of the mass transport Equations 12.9 and 12.10. The program was written in C++ on a desktop PC with a processor speed of 2.4 GHz and 2 GB of RAM. Simulation times were approx. 10 mins. Determination of the best fit between experiment and simulation was done by eye, within an error of 1 to 5%.

The dimensionless current at a generator and collector electrodes of cylindrical symmetry was calculated with formula 12.16 and 12.17 respectively.

$$j = \frac{\pi}{2} \int_0^1 j' R \mathrm{d}R \tag{12.16}$$

$$j = \frac{\pi}{2} \int_1^{R_1} j' R \mathrm{d}R \tag{12.17}$$

$j' = \frac{\partial a}{\partial Z}$ was calculated with a three point approximation.[33]

12.4 Results and Discussion

12.4.1 Isolated Ring-Recessed disc Electrodes: Theory

Equal diffusion coefficients. Figure 12.5 shows current transients and concentration profiles calculated on ring-recessed disc electrodes. At short times ($\tau < 10^{-4}$) diffusion to the generator electrode (disc) is planar (Figure 12.5(b)) and the current corresponds to that predicted by the Cottrell equation; no current is at that time observed on the ring (generator) electrode. At $\tau > 10^{-3}$ the electrogenerated species B reaches the collector electrode (Figure 12.5(c)) and

an increase of current on it is observed. However, the diffusion to the collector electrode is still planar and the current scales inversely with square root of time. With further increase of time the thickness of the diffusional layer increases (Figure 12.5(d)) and the current on the collector electrode grows. Current on the generator electrode is not described by the Cottrell equation anymore but decays slowly because of the convergent diffusion. At very long times ($\tau > 10^3$) steady state currents are observed at both generator and collector electrodes and the concentration profile does not changes over the the time (Figure 12.5(e)).

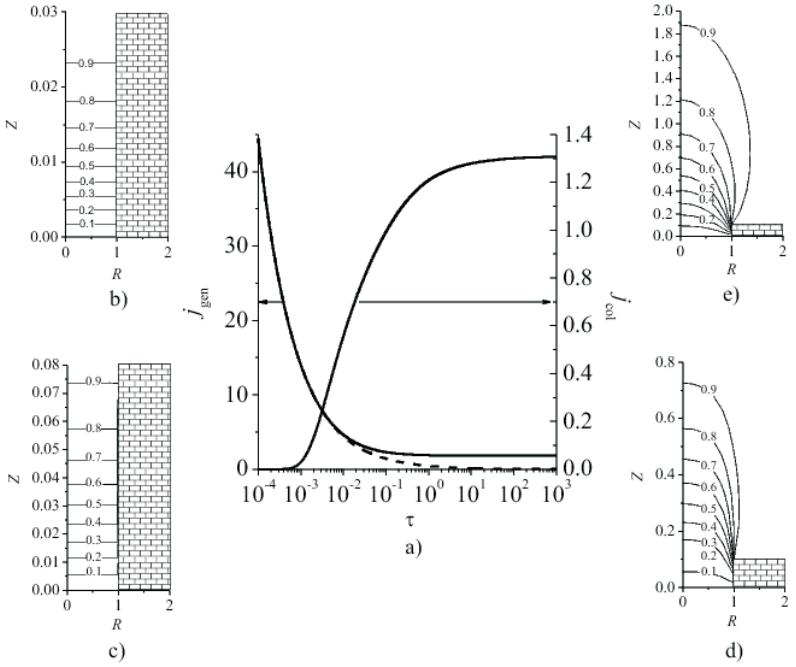


Figure 12.5: a) Calculated dimensionless current at generator and collector electrodes (solid lines) versus dimensionless time in the potential step experiment, dashed line represents current transient given by the Cottrell equation, $L_{\mathrm{cyl}} = 0.1$. b), c), d), e) Concentration profile at $\tau = 10^{-4}$, 10^{-3}, 0.1, 100 correspondingly

Figure 12.6 shows the influence of the cylinder depth L_{cyl} on the current transients on the generator and collector electrodes. An increase of ring to disc separation causes an increase of time scale for which the generator electrode behaves as a macroelectrode. This is because the sides of the well surrounding the disc constrain the diffusion to being one dimensional, similar

behavior was observed before on the disc recessed electrodes.[20,34–36]At the same time increase of the parameter L_{cyl} causes increased delay of the current appearing at the collector electrode. Increasing the cylinder depths/recess heights have a decreasing effect on the steady state current both on generator and collector electrodes.

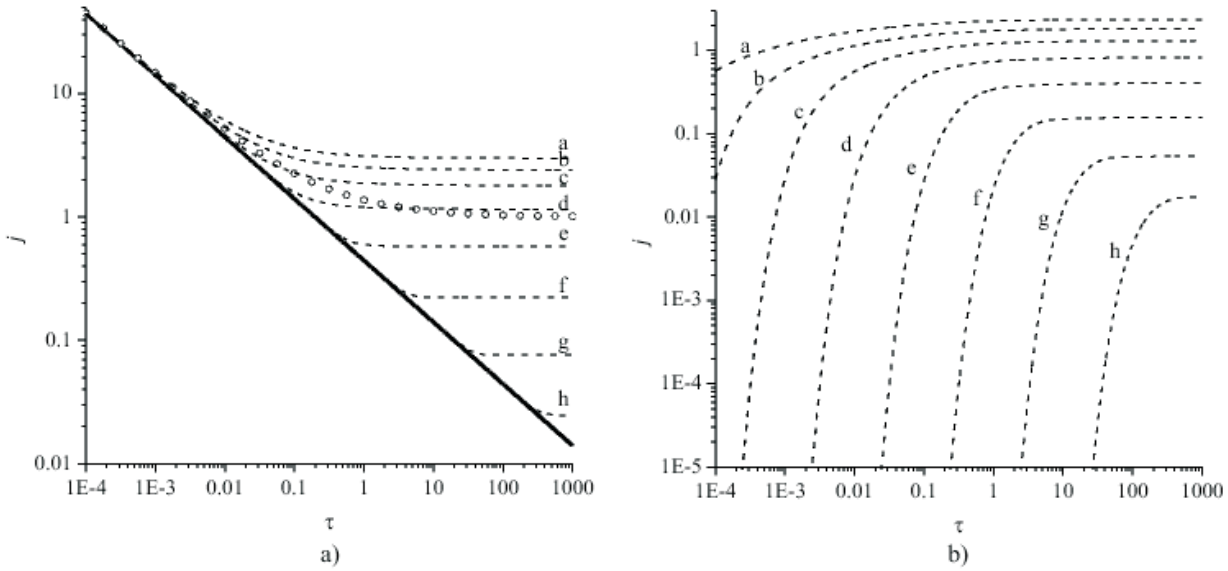


Figure 12.6: Absolute value of calculated dimensionless current at generator a) and collector b) versus dimensionless time in the potential step experiment, single electrode, $R_1 = 1.1$. Solid and dotted lines corresponds to current at macro- and microelectrodes. Dashed lines represents current at recessed generator-collector electrodes with L_{cyl} =0.01 a, 0.032 b, 0.1 c, 0.32 d, 1 e, 3.2 f, 10 g, 32 h.

Unequal Diffusion Coefficients. Figure 12.7 shows current transients calculated for the case of unequal diffusional coefficients. Current transitions on both generator and collector electrodes is sensitive to the ratio of the diffusion coefficients D_{r}. If the diffusion coefficient of the reduced species B is less than that of the initial form A, then the current at the generator electrode will show a "delay" compared with the case of equal diffusion coefficients. The current on the generator electrode goes through a minimum and before it reaches the steady state value if the diffusion coefficient of reduced species B is less than that of the initial form. If the

diffusion coefficient of the reduced form is higher than that of oxidised then it reaches collector electrode faster than in case of equal diffusion coefficients. Consequently current at the collector electrode rises faster (time of flight $\sim L_{\mathrm{cyl}}^2/D_{\mathrm{r}}$). However supply of electroactive species to generator electrode is limited by the slow diffusion of oxidised form (time of flight $\sim L_{\mathrm{cyl}}^2$). Slow generation of reduced specie on the disc electrode causes a decrease of current on collector electrode, consequently the current on it goes through the maximum until the steady state is reached. The value of the steady state current on both generator and collector electrode depends on the geometry of the ring-disc electrode and on the diffusion coefficient of the initial species A, but is not affected by the value of the diffusion coefficients of reduced species B (D_{B}).

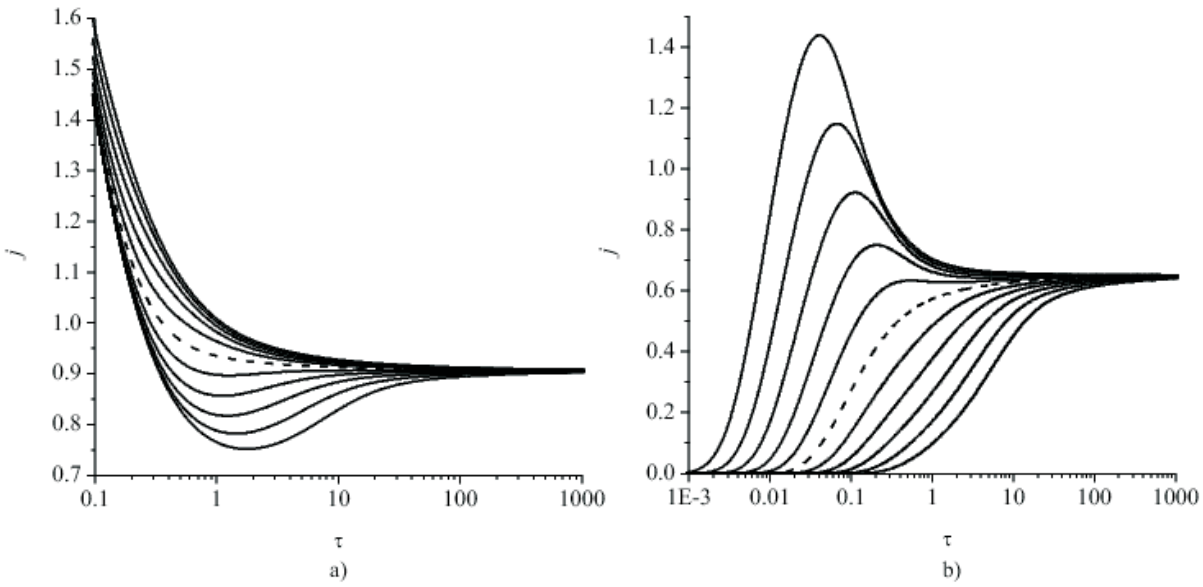


Figure 12.7: Absolute value of calculated dimensionless current at generator a) and collector b) electrodes versus dimensionless time in the potential step experiment, single electrode, $R_1 = 1.1$, $L_{\mathrm{cyl}} = 0.5$. Dashed line represents case of equal diffusion coefficients, solid lines represents results of modeling with unequal diffusion coefficients. D_{r} have values of 0.1, 0.16, 0.25, 0.40, 0.63, 1.6, 2.5, 4.0, 6.3, 10 from the lowest to the highest line.

12.4.2 Effect of the Array Density

Figure 12.8 shows the influence of the diffusion domain radius on the current transients. It is clear that the current on the generator electrode is almost independent of the diffusion domain radius. This is contrary to the behavior of a flat array of microelectrodes (in the absence of the collector) where the current dramatically depends on the diffusional domain radius[37] and timescale of the experiment. It was shown that the nano or microelectrode in the array with any separation of electrodes within the array can be assumed to be diffusionally independent, only for limited time, after which the array as a whole behaves as a macroelectrode[37] (see solid curves on Figure 12.8).

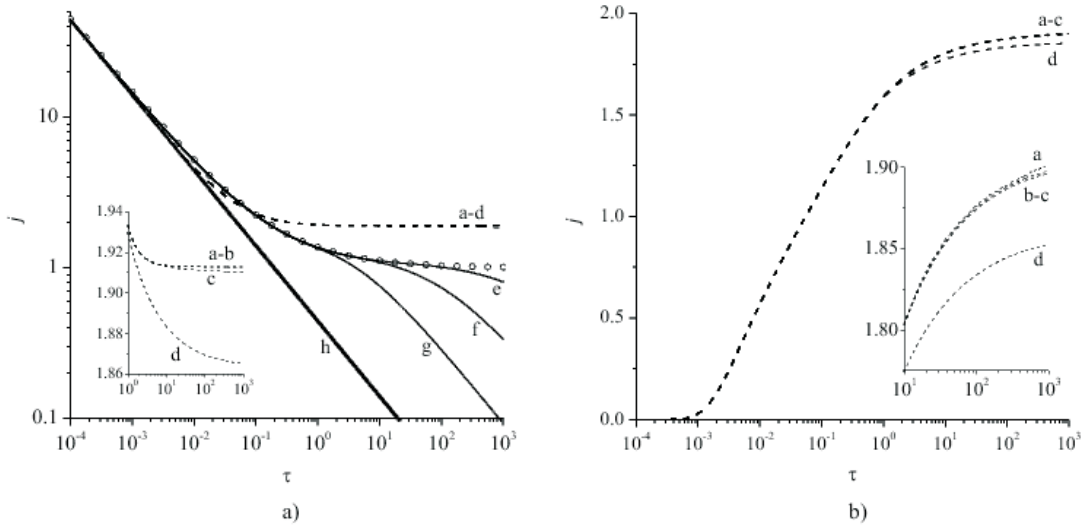


Figure 12.8: Influence of diffusional domain radius on current transients. $R_1 = 1.1$ and $L_{cyl} = 0.1$. a) circles corresponds to single microelectrode, solid line h corresponds to macroelectrode, solid lines g, f and e corresponds to microelectrodes in the array with $R_{max} = 5$, 10 and 13 correspondingly, dashed lines a and b, c, d represents current on generator at single recessed generator-collector device and the array of generator-collector device with R_{max} =10, 5 and 2 correspondingly. b) dashed lines a and b, c, d represents current on collector at single recessed generator-collector device and the array of generator-collector device with R_{max}=10, 5 and 2 correspondingly.

This dramatic difference can be understood in terms of the concentration profiles presented in Figure 12.9. This shows the concentration profile for an analyte at a flat microelectrode

array and also for ring-recessed disc electrode. The size of the diffusional layer on the array of flat microelectrodes increases with time, however on the generator-collector system it increases significantly only at very short times, which makes the microelectrodes in the array diffusionally independent at all but the very longest timescales of the experiment.

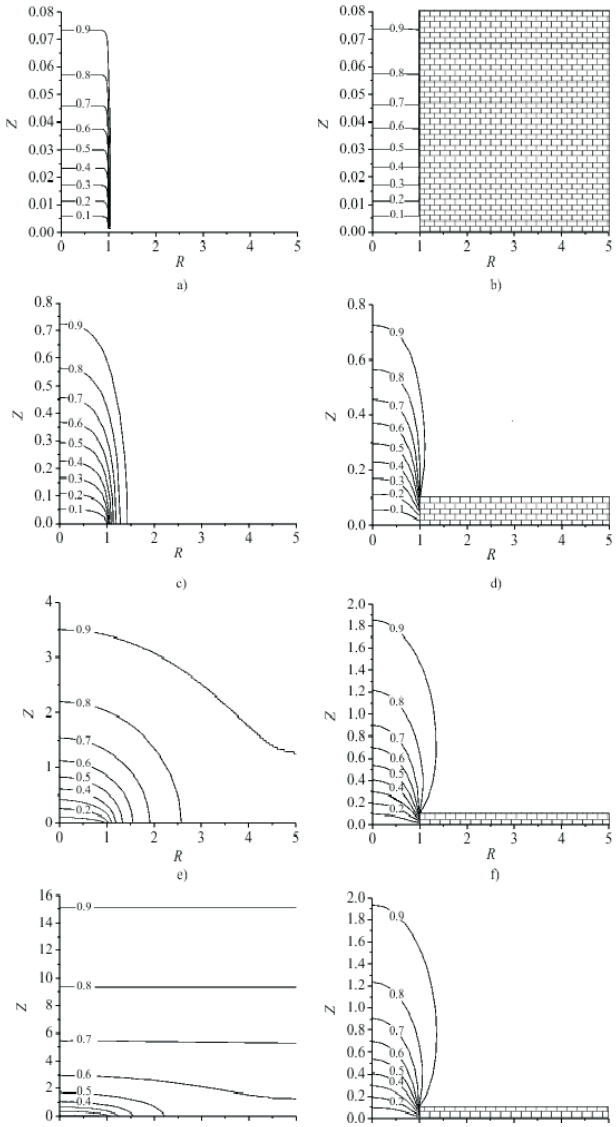


Figure 12.9: Simulated concentrations profiles, at array of microelectrodes (a), c), e), g)) and recessed generator-collector (b), d), f), h)): $\tau = 0.001$ a) and b), $\tau = 0.1$ c) and d), $\tau = 10$ e) and f), $\tau = 100$ g) and h)

In Table 12.3 duration and values of the steady state currents from an array of microdiscs and

an array of generator collector electrodes are presented. It is clear that the generator-collector electrodes have greater advantages over the ordinary arrays of microdiscs when the radius of the electrode is small as can be judged from Table 12.3. At these values of the radius, the duration of steady state currents on array of microelectrodes is too short, however on arrays of the generator-collector electrodes due to the diffusional independence of electrodes within the array the current does not deviate from the steady state value over time. Furthermore use of generator-collector electrodes allows dense packing of electrodes in the array without loss of the duration of steady state current.

Table 12.3: Steady state current and time of diffusional independence on discs electrodes and generator-collector electrodes* within the array.

		microdisc	
$\frac{d}{r_0}$	r_0=100 nm	r_0=1 μm	r_0=10 μm
5	6×10^{-5}; 1.5×10^{-7}**	6×10^{-3}; 1.5×10^{-8}	0.6; 1.5×10^{-9}
10	6×10^{-4}; 3.9×10^{-8}	0.04; 3.9×10^{-9}	4; 3.9×10^{-10}
50	0.055; 1.5×10^{-9}	5.5; 1.5×10^{-10}	550; 1.5×10^{-11}
		generator-collector	
$\frac{d}{r_0}$	r_0=100 nm	r_0=1 μm	r_0=10 μm
5	∞; 3×10^{-7}	∞; 3×10^{-8}	∞; 3×10^{-9}
10	∞; 7.4×10^{-8}	∞; 7.4×10^{-9}	∞; 7.4×10^{-10}
50	∞; 3×10^{-9}	∞; 3×10^{-10}	∞; 3×10^{-11}

Table 12.4: * Geometry of the generator collector electrode is definite by the next parameters L_{cyl}=0.1, $R_1 = R_{\max}$, area of the electrode array is 1 mm^2. ** The first number is time, s of diffusional independence of electrodes within the array, the second number is the values of current, A from the microelectrode array.

12.4.3 Array Characterisation

Figure 12.10 shows images of the fabricated array obtained to confirm its geometry. The ring-recessed disc microelectrode arrays were characterised by perfilometry using a P15 KLA Tencor instruments perfilometer mounting a low force head. The tip used was a 2mm diamond stylus tip with a 60 cone angle. These measurements allowed the determination of the various passivation layers. The height of the top nitride and oxide passivation layer was 710 +/- 50 nm, and the disc recess height relative to the rings was 1.50 microns Figure 12.10(a). In addition, confocal

microscopy was also used to obtain a 3D optical images of the devices shown in Figure 12.10(b). For these measurements, a PLμ non-contact confocal imaging profiler system attached to a Nikon microscope using a 50× magnification lens was employed, and controlled using PLμ proprietary software (Sensofar, Spain). The same software was used to analyse the images and extract topological data. Confocal measurements were in good agreement with perfilometric measurements. Optical microscopy was also used to verify the diameter of the discs and rings making up the arrays, which were 10 microns for disc diameter and 30 microns for ring diameter (Figure 12.10(b)). Figure 12.10(c) shows the whole array, the number of ring-recessed disc electrodes in the array is 130.

12.4.4 Experimental Validation

Diffusion coefficients measurements. Figure 12.11(a) shows a cyclic voltammogram of the oxidation and reduction of Fc and Fc^+ respectively in $[N_{6,2,2,2}][NTf_2]$ at 100 mV s^{-1} at 10 μm diameter Pt electrode the solution was purged under vacuum for 90 min. Fc is oxidized by one-electron to Fc^+ at a peak potential of +0.14 V *vs.* Ag, and reduced back to Fc at a peak potential of +0.05 V *vs.* Ag, corresponding to Equation 12.18.

$$[Fe(C_5H_5)_2] \rightleftharpoons [Fe(C_5H_5)_2]^+ + e^- \tag{12.18}$$

Double potential step chronoamperometry was carried out to calculate diffusion coefficients of Fc and its oxidized species, Fc^+. The potential was stepped from -0.1 V to +0.4 V to oxidise Fc to Fc^+, and then stepped back to -0.1 V to reduce Fc^+ to Fc. The transient obtained is shown as the solid line in Figure 12.11. The diffusion coefficient, D and concentration, c of neutral Fc was determined from analysis of the experimental data for the first potential step using Shoup and Szabo[38] approximations. A computer simulation program[39] was used to model the second potential step to give D_{Fc^+}. The value for D_{Fc} was calculated to be 10.0×10^{-12} m^2 s^{-1} which

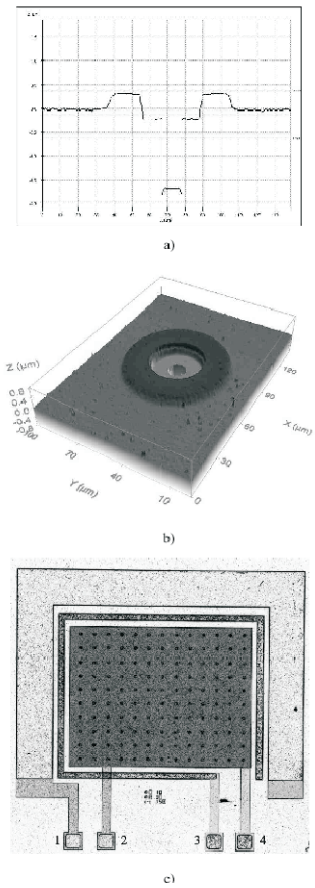


Figure 12.10: a) Perfolimetry profile. b) Confocal microscopy image showing, in detail, a typical ring-recessed disc electrode in an array. The disc diameter, which is also the ring inner diameter, is 10 microns. The ring outer diameter is 30 microns. The disc recess height is approximately 1.6 microns c) Optical microscope image of the chip type used in this Chapter. The chip features 4 electrodes. From left to right, 1 is a large electrode that can be used as auxiliary electrode. 2 corresponds to the recessed microdiscs, 3 is a thin microband intended for use as quasi-reference electrode and 4 connects to the top microring electrodes.

is consistent with previous observations reported for other RTILs.[40,41] The value for D_{Fc^+} was calculated to be 5.50×10^{-12} m^2 s^{-1}. The ratio $D_{Fc}/D_{Fc^+} \neq 1$, suggesting that the neutral Fc species diffuses more quickly than the charged Fc^+ species through the ionic liquid media, an effect similar to that observed for oxygen/superoxide in RTIL[42]

The same Fc/RTIL solution used to determine the above diffusion coefficient and concentration values, was dropped onto the electrode array surface. The solution had previously been purged under vacuum for 90 min. and was used without further degassing.

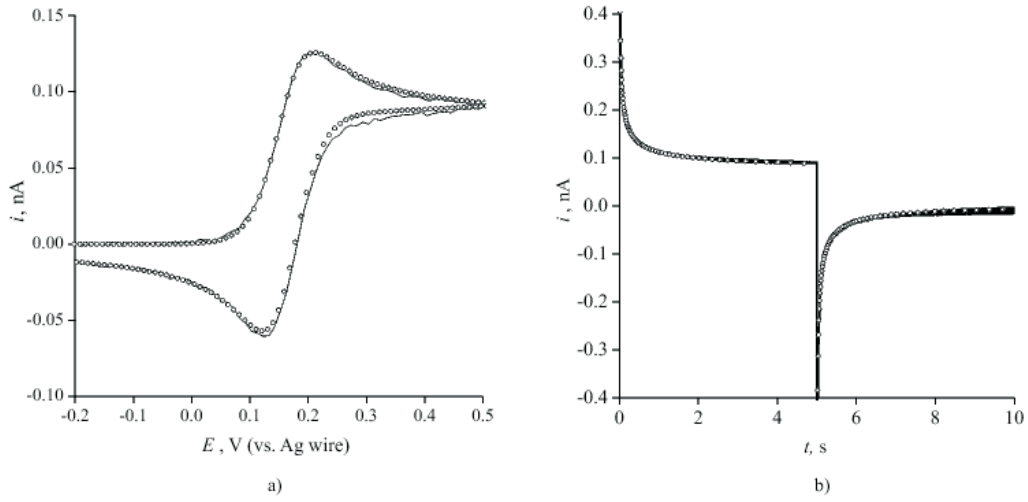


Figure 12.11: a) Cyclic voltammogram of ferrocene in $[N_{6,2,2,2}][NTf_2]$ at 10 μm Pt electrode *vs.* Ag wire at 100 mV $s^{-}1$. b)Double-step chronoamperometry of Fc in $[N_{6,2,2,2}][NTf_2]$ at microdisc platinum electrode (10 μm diameter) *vs.* silver wire for duration 5 s at sample time 0.01 s. Experimental data is shown as a line and theoretical fit is plotted as cycles.

Generator collector mode. The array was immersed in a solution of Fc of known concentration. Figure 12.12 shows a bipotentiostat chronoamperometric transients using the microdisc array as the generator and the microring array as the collector. The potential on the microdisc array was stepped from -0.1 V to +0.4 V to oxidise Fc to Fc^+ and potential on the microring array was kept at -0.1 V to reduce Fc^+ to Fc. The transients obtained are shown as the solid line in Figure 12.12. The diffusion coefficients of Fc and Fc^+ and the concentration of the Fc in solution have been previously determined at the platinum electrode and are known.

To model the transient at generator and collector electrode, diffusion coefficients and concentration values were used as determined in double step chronoamperometry shown in Figure 12.11. The geometry of the array were used as determined from microscopy (Figure 12.10) and the number of active generator-collector electrodes N were varied. The optimised value of active generator-collector microelectrodes was N=26. The fraction of the active electrodes is 20% which is less than the typical value of active electrodes in conventional microdisc electrodes arrays.[37,43] This is due to deficiencies in the final etching step of the fabrication process. Pre-

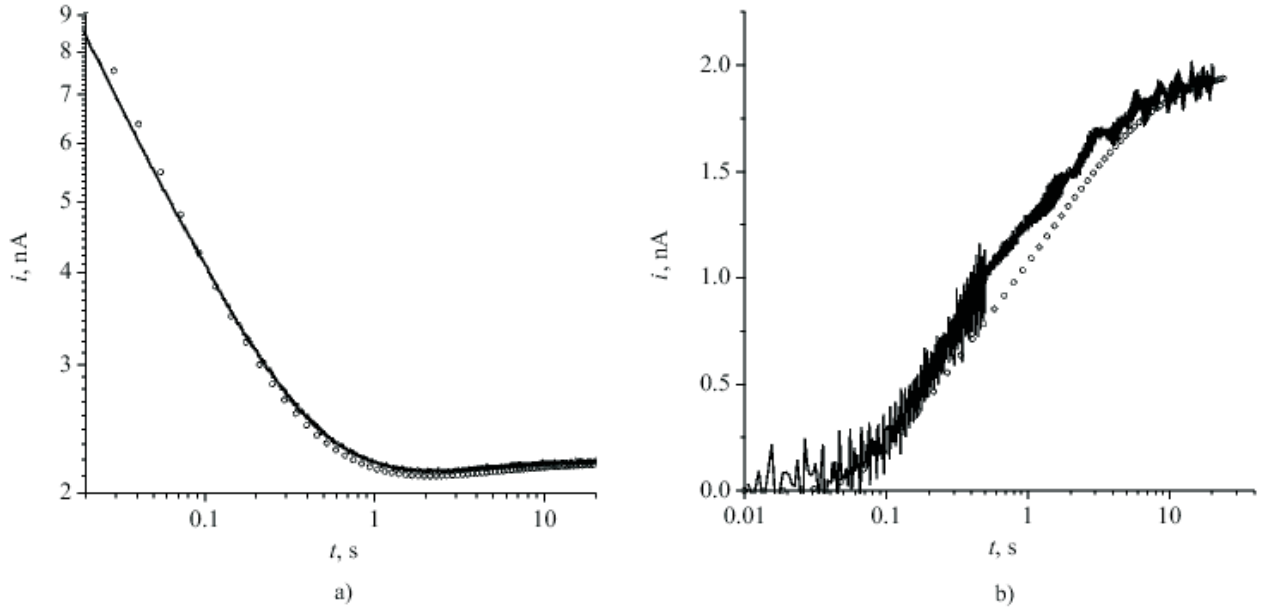


Figure 12.12: Bipotentiostat chronoamperometry of Fc in $[N_{6,2,2,2}][NTf_2]$ at ring-recessed disc electrode array for a) generator electrode and b) collector electrode, experimental data is shown as a line and theoretical fit is plotted as cycles. D_{Fc}=10.0×10^{-12}, D_{Fc^+}=5.50×10^{-12}

sumably, due to slight inhomogeneities in oxide layer thicknesses, the reactive ion etching has not been able to open all the microdiscs and hence the low active number. To show that the theoretical model presented above adequately describes fabricated arrays of the generator-collector electrodes in the presence of dead devices we consider different types of dead devices. Devices with an inactive ring and an inactive disc do not contribute to the recorded current and they do not distort current transients from neighbouring electrodes due to diffusional independence of the generator-collector system (Figure 12.8); devices with a dead disc and an active ring do not generate any current due to absence of electroactive species at the ring electrode; finally devices with an active disc only can distort the current, but voltammograms and current transients recorded at ring only and disc only modes suggest that the number of active rings is significantly higher than number of active discs, consequently the presence of such a devices is negligible. It is clear that the theoretical fit is in good agreement with the experimental data. Particularly, the theoretical fit represents well one-dimensional diffusion to microdisc at short times when

the Fc^+ has not yet reached the collector electrode (Figure 12.9(b)). It also describes well the region of times where diffusion is converged and Fc^+ reduced to Fc at the collector electrode and diffuses back to the generator (Figure 12.9(d) and (f)). The fit predicts the feature that current transient on the generator electrode goes through the minima and finally it gives accurate values of steady state current on generator and collector electrodes. This shows that two dimensional simulations in conjunction with the diffusion domain approach gives accurate description of a full three dimensional problem of mass transport at ring-recessed disc electrodes, taking into account sensitivity of current transients, particularly the depth of minima/maxima and the time of flight to the ratio of diffusion coefficients (Figure 12.7). Consequently we conclude that the method can be applied to simultaneous determination of diffusion coefficients of red/ox couple.

12.5 Conclusions

Three different time regimes are observed in a potential step experiment on ring-recessed disc electrode. First a rapid decrease of current on generator similar to that on macroelectrode and no-current on the collector is observed at short times. This is followed by the region where current at the collector grows and current at the generator "equilibrates". Finally a true steady state current is observed on both generator and collector electrodes. All three regions of behavior were observed experimentally on a fabricated array of generator-collector array. The theoretical fit agrees well with the experimental data, therefore diffusional domain approach can be used to model arrays of ring-recessed disc electrodes. Currents in the steady state mode are almost independent of the distance between electrodes in the array, but sensitive to the distance between disc and ring L_{cyl}. Steady state currents are also insensitive to the ratio of diffusional coefficients, but the modeling of current transients on the generator and collector electrodes allows the determination of diffusion coefficients to both oxidised and reduced forms simultaneously. The use of arrays of ring-recessed disc electrodes in generator-collector mode has advantages over conventional arrays of disc electrodes, such as higher currents at a single microelectode in an array. The number of electrodes on the array can also be increased, as smaller interelectrode distances are possible. As well as this, the discs in the array are not restricted by size as true steady-state behavior is observed over a wide range of scales.

References

[1] Menshykau, D.; del Campo, J. F.; Munoz, F. and Compton, R., *Sens. Actuators, B*, 2009, **138**, 362–367.

[2] Wittek, M.; Mller, G.; Johnson, M. and Majda, M., *Anal. Chem.*, 2001, **73**, 870–877.

[3] Amatore, C.; Sella, C. and Thouin, L., *J. Phys. Chem. B*, 2002, **106**, 11565–11571.

[4] Slowinska, K.; Feldberg, S. and Majda, M., *J. Electroanal. Chem.*, 2003, **554**, 61–69.

[5] Amatore, C.; Sella, C. and Thouin, L., *J. Electroanal. Chem.*, 2006, **593**, 194–202.

[6] Fosset, B.; Amatore, C.; Bartelt, J.; Michael, A. and Wightman, R., *Anal. Chem.*, 1991, **63**, 306–314.

[7] Fosset, B.; Amatore, C.; Bartelt, J. and Wightman, R., *Anal. Chem.*, 1991, **63**, 1403–1408.

[8] Niwa, O.; Morita, M. and Tabei, H., *Anal. Chem.*, 1990, **62**, 447–452.

[9] Aoki, K.; Morita, M.; Niwa, O. and Tabei, H., *J. Electroanal. Chem.*, 1988, **256**, 269–282.

[10] Niwa, O.; Morita, M. and Tabei, H., *J. Electroanal. Chem.*, 1989, **267**, 291–297.

[11] Ivanic, R.; Rehacek, V.; Novotny, I.; Breternitz, V.; Spiess, L.; Knedlik, C. and Tvarozek, V., *Vacuum*, 2001, **61**, 229–234.

[12] Vandaveer IV, W. R.; Woodward, D. J. and Fritsch, I., *Electrochim. Acta*, 2003, **48**, 3341–3348.

[13] Zhao, G.; Giolando, D. M. and Kirchhoff, J. R., *Anal. Chem.*, 1995, **67**, 1491–1495.

[14] Liljeroth, P.; Johans, C.; Slevin, C. J.; Quinn, B. M. and Kontturi, K., *Electrochem. Comm.*, 2002, **4**, 67–71.

[15] Harvey, S. L. R.; Parker, K. and O'Hare, D., *J. Electroanal. Chem.*, 2007, **610**, 122–130.

[16] Harvey, S. L. R.; Coxon, P.; Bates, D.; Parker, K. H. and O'Hare, D., *Sens. Actuators B*, 2008, **129**, 659–665.

[17] Amatore, C.; Saveant, J. M. and Tessier, D., *J. Electroanal. Chem.*, 1983, **147**, 39–51.

[18] Davies, T. J.; Moore, R. R.; Banks, C. E. and Compton, R. G., *J. Electroanal. Chem.*, 2004, **574**, 123–152.

[19] Brookes, B. A.; Davies, T. J.; Fisher, A. C.; Evans, R. G.; Wilkins, S. J.; Yunus, K.; Wadhawan, J. D. and Compton, R. G., *J. Phys. Chem. B*, 2003, **107**, 1616–1627.

[20] Guo, J. and Lindner, E., *Anal. Chem.*, 2009, **81**, 130–138.

[21] Dickinson, E. J. F.; Limon-Petersen, J. G.; Rees, N. V. and Compton, R. G., *J. Phys. Chem. C*, 2009, **113**, 11157–11171.

[22] Sharp, M., *Electrochim. Acta*, 1983, **28**, 301–308.

[23] Schröder, U.; Wadhawan, J. D.; Compton, R. G.; Marken, F.; Suarez, P. A. Z.; Consorti, C. S.; de Souza, R. F. and Dupont, J., *New J. Chem.*, 2000, **24**, 1009–1015.

[24] Silvester, D. S.; Aldous, L.; Hardacre, C. and Compton, R. G., *J. Phys. Chem. B*, 2007, **111**, 5000–5007.

[25] Svir, I. B.; Klymenko, O. V. and Compton, R. G., *Radiotekhnika*, 2001, **118**, 92.

[26] Bard, A. J. and Faulkner, L. R., *Electrochemical Methods: Fundamentals and Applications, 2nd ed.*, John Wiley and Sons: New York, 2001.

[27] Gavaghan, D. J., *J. Electroanal. Chem.*, 1998, **456**, 1–12.

[28] Dickinson, E. J. F.; Streeter, I. and Compton, R. G., *J. Phys. Chem. B*, 2008, **112**, 4059–4066.

[29] Dickinson, E. J. F.; Streeter, I. and Compton, R. G., *J. Phys. Chem. C*, 2008, **112**, 11637–11644.

[30] Davies, T. J. and Compton, R. G., *J. Electroanal. Chem.*, 2005, **585**, 63–82.

[31] Peaceman, J. W. and Rachford, H. H., *J. Soc. Indust. Appl. Math.*, 1955, **3**, 28–41.

[32] Atkinson, K. E., *Elementary Numerical Analysis*, John Wiley and Sons, New York, 3rd ed., 2004.

[33] Gavaghan, D. J., *J. Electroanal. Chem.*, 1997, **420**, 147.

[34] Amatore, C.; Oleinick, A. I. and Svir, I., *J. Electroanal. Chem.*, 2006, **597**, 77–85.

[35] Amatore, C.; Oleinick, A. I. and Svir, I., *Anal. Chem.*, 2009, **81**, 4397–4405.

[36] Menshykau, D. and Compton, R. G., *Langmuir*, 2009, **25**, 2519–2529.

[37] Menshykau, D.; Huang, X. J.; Rees, N. V.; Del Campo, F. J.; Munoz, F. and Compton, R. G., *Analyst*, 2009, **134**, 343–348.

[38] Shoup, D. and Szabo, A., *J. Electroanal. Chem.*, 1982, **140**, 237–245.

[39] Klymenko, O. V.; Evans, R. G.; Hardacre, C.; Svir, I. B. and Compton, R. G., *J. Electroanal. Chem.*, 2004, **571**, 211–221.

[40] Rogers, E. I.; Silvester, D. S.; Poole, D. L.; Aldous, L.; Hardacre, C. and Compton, R. G., *J. Phys. Chem. C*, 2008, **112**, 2729–2735.

[41] Evans, R. G.; Klymenko, O. V.; Price, P. D.; Davies, S. G.; Hardacre, C. and Compton, R. G., *ChemPhysChem*, 2005, **6**, 526–533.

[42] Evans, R. G.; Klymenko, O. V.; Saddoughi, S. A.; Hardacre, C. and Compton, R. G., *J. Phys. Chem. B*, 2004, **108**, 7878–7886.

[43] Ordeig, O.; Banks, C. E.; Davies, T. J.; Del Campo, J.; Mas, R.; Munoz, F. X. and Compton, R. G., *Analyst*, 2006, **131**, 440–445.

Overall Conclusions

The work presented in this thesis has evaluated RTILs as suitable solvents for gas sensing. RTILs have been evaluated in this work with respect to their physical properties, in particular, electrochemical window under various conditions and water uptake. A wide variation of water uptake was observed by varying the cations and anions that constitute various RTILs. This information has been presented along with variation of other physical properties such as viscosity and density in order to allow us choose an optimum RTIL for specific tasks.

RTILs have been examined as solvents for the detection of H_2S. The reduction and oxidation of H_2S has been observed in many different RTILs, and data such as diffusion coefficient and solubility are presented. The mediation of H_2S in RTILs has also been examined using a wide variety of mediators.

The electrochemistry of some of these potential mediators has been examined itself in RTILs, and interesting features are presented. In some cases, the mechanism of the oxidation of the target analyte has changed depending on the nature of the anion of the RTIL. In other cases, the oxidation of species was promoted or prevented in different RTILs depending on the nature of the anion.

Of various species used in the attempted mediation of H_2S, one species was successful, 3,5-tert-butyl-o-benzoquinone. The mechanism of the reaction of this mediator with H_2S, both chemical and electrochemical, was elucidated using cyclic voltammetry. Over relatively short times, the reaction of the mediator with H_2S is reversible, presenting a possible renewable gas sensor. Over longer times, further chemical reactions occur which are irreversible. For lower concentrations of H_2S, this timescale becomes longer, and thus 3,5-tert-o-benzoquinoe has been observed to be a suitable mediating species for detection of H_2S in RTILs.

Overall, RTILs have been shown to possess many favourable characteristics, and in some cases are seen as superior to conventional solvents, for gas sensing. Increased knowledge of

the many reactions of RTILs with different species is growing, and they are becoming viable alternatives to conventional volatile organic solvents in a variety of processes.

Typeset using LaTeX